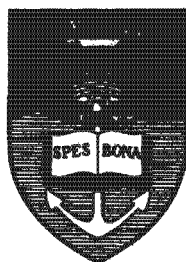


The copyright of this thesis vests in the author. No quotation from it or information derived from it is to be published without full acknowledgement of the source. The thesis is to be used for private study or non-commercial research purposes only.

Published by the University of Cape Town (UCT) in terms of the non-exclusive license granted to UCT by the author.



Ruthenium based Fischer-Tropsch Synthesis on Crystallites and Clusters of Different Sizes

From “Nano” to “Ångstrøm”

by

Cathrin Alexandra Welker

Dipl. Chem., University of Stuttgart, Germany

Thesis presented to the University of Cape Town
in fulfillment of the requirements
for the degree of

Doctor of Philosophy

Centre for Catalysis Research
Department of Chemical Engineering
University of Cape Town

Rondebosch

August 2007

"Ipsa scientia potestas est."

-Cicero

University of Cape Town

Acknowledgments

This work matured during the period January 2004-August 2007 at the Centre for Catalysis Research in the Department of Chemical Engineering at the University of Cape Town.

My gratitude belongs to my team of supervisors, A./Prof. Michael Claeys, Prof. Eric van Steen and Prof. John R. Moss for all their advices and help throughout my thesis. Special thanks to A./Prof. Michael Claeys for all his effort with the thesis corrections and just for always having, or rather making, time for me even if it was on a Sunday afternoon.

Thanks to Dr. Noko Phala for inducting me into the fascinating world of molecular modelling.

Many thanks to the “people behind the scenes”, like Mr. Mohamed Jaffer and Mrs. Miranda Waldron from the Electron Microscope Unit (University of Cape Town) or Mrs. Helen Divey, Ms. Stephanie LeGrange and Mrs. Suzanna Vasic from our in-house Main Laboratory. All your effort and help are highly appreciated.

I have to make special mention of all my colleagues from the Centre for Catalysis Research and the Organometallic Research Group: Elvera, Itai, Jurie, Pete, You Qi, Harry, Emma, Siya, Ramakrishna just to mention a few. There were so many of them and my University-life would have not been the same without all of them! Nelli, thanks for our co-operation at my old university. It was great fun to “cook” in the old labs again!

I would like to thank my sponsor, the “DST-NRF Centre of Excellence in Catalysis” (c*change), for supplying the money. Without their financial support this thesis would not have been possible!

Jako, you are definitively not forgotten! Thanks so much for the proof-reading, the listening when I was complaining and when I so desperately needed some support. I will never be able to make up for all of it!

Last, but certainly not least, many thanks to my family and friends back home in “good old Germany” for all their support even with all these kilometres between us. Endless thanks to my parents and to my brother Christian and my sister Nicole.

This thesis is dedicated to my beloved father who passed away in November 2005.

Synopsis

The Fischer-Tropsch synthesis is the catalytic conversion of hydrogen and carbon monoxide into higher hydrocarbons. Although ruthenium is the most active catalyst in Fischer-Tropsch synthesis, the lower cost metals iron and cobalt are used commercially. Generally, increased catalyst performance is achieved with increased metal surface area and dispersion, though recent literature reports that cobalt, iron and rhodium crystallites below a certain size in the nanometer range display lower metal surface area specific activity and a high methane selectivity. There have also been several attempts to investigate the possibility to conduct a homogeneously catalysed Fischer-Tropsch synthesis, which can be considered as an extreme case of metal dispersion.

The aim of this study is to investigate Fischer-Tropsch activity and selectivity on well-defined nano-sized ruthenium crystallites and supported organometallic clusters with varying nuclearity, and to compare/bridge the obtained findings by subdividing it into a) catalyst preparation and characterisation, b) Fischer-Tropsch performance of model catalyst (including post-reaction catalyst characterisation), and c) theoretical investigations of the feasibility of Fischer-Tropsch reactions on mono- and diatomic ruthenium complexes.

In **catalyst preparation**, model catalysts with narrow ruthenium crystallite sizes ranging from 2 to 10 nm were successfully prepared by applying the reverse micelle technique. Crystallite sizes remained largely unaffected upon reduction of the catalyst, emphasizing a stability in their model character. These catalyst systems prepared with the reverse micelle technique were ideally suited to investigate the effect of crystallite size during Fischer-Tropsch synthesis in the nanometer-sized ("heterogeneous") range. Additionally, for comparison with "heterogenized homogeneous" Fischer-Tropsch catalysts organometallic compounds with ruthenium nuclearity varying from 2 to 6 were synthesized and deposited on an alumina support.

The **Fischer-Tropsch activity and selectivity** were monitored continuously throughout the experiment. Nano-sized crystallites showed decreased activity in the Fischer-Tropsch synthesis for smaller crystallites both initially and at steady-state. Decreased methane selectivity, increased formation of longer chain hydrocarbons, and an increased olefin formation were obtained at steady-state on larger crystallites. The product obtained on small crystallites was richer in hydrogen with enhanced paraffin to olefin ratios and increased alcohol to aldehyde ratios.

The main findings regarding Fischer-Tropsch performance on the supported organometallic compounds were that formation of typical Fischer-Tropsch products (C_1 - C_4 hydrocarbons) were obtained on all clusters, indicating their ability for C-C bond formation and C-O bond cleavage. However, no direct evidence was found that gas phase carbon monoxide was activated for the formation of organic products. Product selectivities showed relatively high methane selectivity, low chain growth probabilities and high olefin selectivities.

By comparing initial cluster and steady-state crystallite activities as function of number of exposed metal atoms, it was noted that the two series connect almost continuously, which may indicate that the organometallic clusters are valuable model systems to study steps of product formation in Fischer-Tropsch synthesis.

Theoretical investigations on proposed reaction mechanisms illustrated that a minimum of two adjacent metal atoms is required for C-O bond cleavage and chain growth required for Fischer-Tropsch. The CO-insertion mechanism seems to be thermodynamically most feasible.

University of Cape Town

Contents

Contents	I
List of Figures	V
List of Tables	XIII
List of Schemes	XIV
Nomenclature	XVII
1 Introduction	1
2 Literature Review	3
2.1 Fischer-Tropsch Synthesis	3
2.1.1 General - History and Development	3
2.1.2 Stoichiometry of the Fischer-Tropsch Reaction	4
2.1.3 Fischer-Tropsch Products	5
2.1.3.1 Classification of Fischer-Tropsch Products	5
2.1.3.2 Fischer-Tropsch Product Distributions	6
2.1.4 Mechanisms in Fischer-Tropsch Synthesis	7
2.1.4.1 Alkyl Mechanism	7
2.1.4.2 Alkenyl Mechanism	7
2.1.4.3 Enol Mechanism	8
2.1.4.4 CO-Insertion Mechanism	9
2.1.5 Different Catalysts for Fischer-Tropsch Synthesis	9
2.1.6 Effect of Crystallite Size in Fischer-Tropsch Synthesis	10
2.1.7 Homogeneously Catalysed Fischer-Tropsch Synthesis	13
2.2 Catalyst Deactivation	15
2.2.1 Poisoning	15
2.2.2 Fouling	16
2.2.3 Thermal Degradation	17
2.2.4 Gas-solid and Solid-solid Reactions	19
2.3 Preparation Methods for Heterogeneous Catalyst Systems	20
2.3.1 Conventional Preparation Techniques	20
2.3.1.1 Impregnation Techniques	20
2.3.1.2 Precipitation Techniques	21
2.3.1.3 Synthesis from Organometallic Compounds	21
2.3.2 Microemulsion Technique	22
2.3.2.1 Definition of a Microemulsion	22

2.3.2.2	Preparation of Nano-particles	23
3	Scope of the Thesis	27
4	Experimental Methodology	29
4.1	Catalyst Preparation	29
4.1.1	Supported Nano-sized Crystallites	29
4.1.2	Supported Organometallic Compounds	30
4.1.2.1	Synthesis of Tetracarbonylbis(η^5 -cyclopentadienyl)-diruthenium $\text{Ru}_2(\text{CO})_4(\eta^5\text{-C}_5\text{H}_5)_2$	32
4.1.2.2	Synthesis of Tetracarbonylbis(η^5 -pentamethyl-cyclopentadienyl)- diruthenium $\text{Ru}_2(\text{CO})_4(\eta^5\text{-C}_5(\text{CH}_3)_5)_2$	33
4.1.2.3	Synthesis of μ -Carbonyl- μ -ethenylidene-bis[carbonyl- (η -cyclopentadienyl)ruthenium] $\text{Ru}_2(\text{CO})_2(\mu\text{-CO})(\mu\text{-CHCH}_3)(\eta^5\text{-C}_5\text{H}_5)_2$	33
4.1.2.4	Synthesis of Dodecacarbonyltriruthenium $\text{Ru}_3(\text{CO})_{12}$	34
4.1.2.5	Synthesis of Dodecacarbonyl-tetra(μ -hydrido)-tetraruthenium $\text{Ru}_4(\mu\text{-H})_4(\text{CO})_{12}$	34
4.1.2.6	Synthesis of μ_5 -Carbido-pentadecacarbonyl-pentaruthenium $\text{Ru}_5\text{C}(\text{CO})_{15}$	35
4.1.2.7	Synthesis of μ_6 -Carbido-heptadecacarbonyl-hexaruthenium $\text{Ru}_6\text{C}(\text{CO})_{17}$	36
4.1.2.8	Impregnation onto Alumina Support	37
4.2	Characterisation of Water-in-Oil Microemulsions	37
4.3	Characterisation of Support Material	37
4.4	Characterisation of Organometallic Compounds	37
4.4.1	Infrared Spectroscopy (IR)	37
4.4.2	Nuclear Magnetic Resonance Spectroscopy (NMR)	38
4.4.3	Thermogravimetric Analysis (TGA)	38
4.5	Characterisation of Supported Model Catalysts	38
4.5.1	Inductively Coupled Plasma Spectrometry (ICP)	38
4.5.2	Transmission Electron Microscopy (TEM)	38
4.5.3	CO-Chemisorption	39
4.5.4	X-Ray Diffraction Spectroscopy (XRD)	39
4.5.5	Temperature Programmed Reduction (TPR)	40
4.6	Fischer-Tropsch Synthesis Experiments	40
4.6.1	Reactor Set-up	40
4.6.2	Operation of the Fixed-Bed Reactor Set-up and Reaction Conditions	43
4.7	Analytical Procedures	45
4.7.1	Sampling Techniques	45
4.7.2	Analysis of Inorganic Compounds and Methane	45
4.7.3	Analysis of Volatile Organic Compounds (VOC's)	46
4.8	Data Work-up	48
4.8.1	Conversion, Yield and Selectivity	49
4.8.2	Turnover Frequency	49

5	Characterisation Results	51
5.1	Characterisation of the Reverse Micelle System and the Catalyst Support	51
5.1.1	Viscosity Measurements and Water-pool Size	51
5.1.2	Zetapotential of Support	53
5.2	Supported Nano-sized Crystallites	54
5.2.1	TEM Analysis of Supported Nano-sized Crystallites	54
5.2.2	Chemisorption Analysis of Supported Nano-sized Crystallites . . .	59
5.2.3	TPR Analysis of Supported Nano-sized Crystallites	60
5.2.4	Further Characterisation of Supported Nano-sized Crystallites . .	60
5.2.5	Summary of Characterisation Results of Alumina Supported Nano-sized Crystallites	62
5.3	Organometallic Model Catalysts	64
5.3.1	Thermal Stability of Unsupported Organometallic Clusters in Different Gases	64
5.3.2	Characterisation of Alumina Supported Organometallic Clusters .	66
6	Fischer-Tropsch Testing of Model Catalysts	67
6.1	Supported Nano-sized Crystallites	67
6.1.1	Fischer-Tropsch Activity	67
6.1.2	Product Formation	75
6.1.2.1	Methane Formation and Chain Growth	75
6.1.2.2	Olefin Formation	79
6.1.2.3	Formation of Oxygenates	88
6.1.2.4	Formation of Branched Products	89
6.1.3	Conclusions of Findings of Fischer-Tropsch Experiments on Supported Nano-sized Crystallites	90
6.2	Supported Organometallic Compounds	93
6.2.1	Fischer-Tropsch Activity	93
6.2.2	Product Formation	100
6.2.2.1	Methane Formation and Chain Growth	101
6.2.2.2	Olefin Formation	103
6.2.2.3	Does CO-activation take place on the supported organometallic compounds?	105
6.2.3	Conclusions of Findings of FT Experiments on Supported Organometallic Compounds	108
6.3	Nano- and Ångström-sized Crystallites/Clusters - Comparison and Discussion	110
7	Theoretical Feasibility of CO-Activation and FT Chain Growth on Mono- and Diatomic Ruthenium Compounds	115
7.1	Proposed Reaction Mechanisms	115
7.1.1	Monoatomic Reaction Mechanism	115
7.1.2	Diatomic Reaction Mechanism	118
7.2	Computational Details	119
7.3	Validity of the Theoretical Method	124
7.4	Monoatomic Reaction Mechanism	124
7.5	Diatomic Reaction Mechanism	127
7.6	Conclusions of Theoretical Investigations	130

8	Summary and Conclusions	131
9	Recommendations and Future Work	135
	References	137
A	Preparation and Characterisation of Model Catalysts	153
A.1	Chemicals for Model Catalyst Preparation	154
A.2	Metal Crystallite Size Distributions	155
A.3	Chemisorption Reading	158
A.4	Calculation of the Number of Exposed Surface Atoms	158
A.5	Theoretical Modelling of Reverse Micelle Size	160
A.6	Thermogravimetric Analysis	163
B	Fischer-Tropsch Performance Tests	165
B.1	TCD and FID Chromatograms	165
B.2	Tables of Selected Results	167
B.3	Additional Fischer-Tropsch Graphs	177
B.3.1	Supported Nano-sized Crystallites	177
B.3.2	Supported Organometallic Compounds	180
B.4	Additional Characterisation Data of Supported Organometallic Compounds	182
C	Theoretical Calculations	183
C.1	The Density Functional Theory	184
C.2	Calculation of Thermodynamic Data	185
C.3	Entropy of Reaction	187
C.3.1	Monoatomic Reaction Mechanisms	187
C.3.2	Diatomic Reaction Mechanisms	188
D	Curriculum Vitae	189
E	List of Publications	193

List of Figures

2.1	Schematic ternary-phase diagram of surfactant-oil-water system (Mabaso (2005)).	23
4.1	Ternary-phase diagram of water-PEGDE-n-hexane reverse micelle system indicating the stability region for the reverse micelles (as established by Mabaso (2005)) and the composition of the reverse micelle systems RM-1 to RM-13 used in this work. (Alphabetic codes correspond to the following catalysts: a: RM-1; b: RM-2; c: RM-3; d: RM-4; e: RM-5; f: RM-6; g: RM-7; h: RM-8; i: RM-9; j: RM-10; k: RM-11; l: RM-12; m: RM-13)	31
4.2	Structures of the different prepared organometallic compounds varying the number of ruthenium atoms from two to six. (<i>Note</i> : Chemical structures of Ru-4, Ru-5 and Ru-6 are shown below.)	32
5.1	Water-pool size, d_{wp} , as estimated by viscosity correlation equation by Cheng and Schachmann, and calculated using equation by Mabaso.	52
5.2	Zetapotential of alumina support as function of pH value.	53
5.3	TEM micrographs of four selected alumina supported nano-sized crystallites; <i>left</i> : after calcination, <i>right</i> : after reduction and passivation.	55
5.4	Crystallite size distributions of five selected calcined (<i>closed bars</i>) and reduced (<i>open bars</i>) alumina supported nano-sized crystallites as determined by means of TEM analysis. (For crystallite size distributions of remaining supported nano-sized crystallites see Appendix A.2, Figure A.1, p. 155.)	56
5.5	Average crystallite size of calcined catalyst and the corresponding water-pool size in the corresponding reverse micelle solution they were prepared from, as function of water-to-surfactant weight ratio; y-bars indicate width of distribution expressed as standard deviation.	58
5.6	Ternary-phase diagram of water-PEGDE-n-hexane reverse micelle system indicating the stability region for the reverse micelles (as established by Mabaso (2005)), the composition of the reverse micelle systems RM-1 to RM-13 used in this work and the resulting average crystallite sizes of the calcined catalysts (in nm). (Alphabetic codes correspond to the following catalysts: a: RM-1; b: RM-2; c: RM-3; d: RM-4; e: RM-5; f: RM-6; g: RM-7; h: RM-8; i: RM-9; j: RM-10; k: RM-11; l: RM-12; m: RM-13)	59
5.7	TPR patterns of the different alumina supported nano-sized crystallites.	61
5.8	XRD patterns of calcined sample RM-10 and pure alumina support, including reference patterns for metallic ruthenium and ruthenium dioxide.	62
5.9	First derivative of weight vs. temperature profile from TGA analysis for the different organometallic complexes in nitrogen.	65

6.1	<p><i>top</i>: Changes in turnover frequencies of volatile organic compounds in FT synthesis at 170°C/4 bar as function of time on stream for five selected alumina supported nano-sized ruthenium crystallites.</p> <p><i>bottom</i>: Maximal initial and average steady-state turnover frequencies of volatile organic compounds in FT synthesis versus average ruthenium crystallite size of fresh (1-3 minutes runtime) or, respectively, spent (steady-state) catalysts.</p> <p>(Note: Average crystallite sizes obtained from TEM micrographs of freshly reduced and spent catalysts.)</p> <p>($T_{\text{Reaction}} = 170^{\circ}\text{C}/225^{\circ}\text{C}$, $P = 4 \text{ bar}/20 \text{ bar}$, $\text{GHSV} = 7 \text{ ml(STP)}/(\text{min}\cdot\text{g}_{\text{cat}})$, $(\text{H}_2/\text{CO})_{\text{in}} = 2:1$)</p>	69
6.2	<p>TEM micrographs of four selected spent alumina supported nano-sized ruthenium crystallites after FT testing for five days at 170°C/4 bar (a to d) and, respectively, two selected spent catalysts after FT testing for five days at 225°C/20 bar (e and f).</p>	71
6.3	<p>Crystallite size distributions of five selected reduced (<i>open bars</i>) and spent (<i>closed bars</i>) alumina supported nano-sized crystallites after FT testing for five days at 170°C and 4 bar as determined by means of TEM analysis. (For crystallite size distributions of other model catalysts see Appendix A.2, Figure A.2, p. 157.)</p>	72
6.4	<p>Changes in turnover frequencies of volatile organic compounds in FT synthesis at 170°C/4 bar as function of time on stream for catalyst sample RM-2, with (●) and without (○) carbon monoxide pre-exposure after reduction prior to FT experiment.</p> <p>($T_{\text{Reaction}} = 170^{\circ}\text{C}$, $P = 4 \text{ bar}$, $\text{GHSV} = 7 \text{ ml(STP)}/(\text{min}\cdot\text{g}_{\text{cat}})$, $(\text{H}_2/\text{CO})_{\text{in}} = 2:1$)</p>	73
6.5	<p><i>top</i>: Changes in methane selectivities in volatile organic compounds in FT synthesis at 170°C/4 bar as function of time on stream for five selected alumina supported nano-sized ruthenium crystallites.</p> <p><i>bottom</i>: Average methane selectivities in volatile organic compounds in FT synthesis versus average ruthenium crystallite size of fresh (1-3 minutes runtime) or, respectively, spent (steady-state) model catalysts.</p> <p>(Note: Average crystallite sizes obtained from TEM micrographs of freshly reduced and spent catalysts.)</p> <p>($T_{\text{Reaction}} = 170^{\circ}\text{C}/225^{\circ}\text{C}$, $P = 4 \text{ bar}/20 \text{ bar}$, $\text{GHSV} = 7 \text{ ml(STP)}/(\text{min}\cdot\text{g}_{\text{cat}})$, $(\text{H}_2/\text{CO})_{\text{in}} = 2:1$)</p>	77
6.6	<p><i>top</i>: Changes in C_{5+}-selectivities in volatile organic compounds in FT synthesis at 170°C/4 bar as function of time on stream for five selected supported nano-sized ruthenium crystallites.</p> <p><i>bottom</i>: Average C_{5+}-selectivities in volatile organic compounds in FT synthesis versus average ruthenium crystallite size of fresh (1-3 minutes runtime) or, respectively, spent (steady-state) model catalysts.</p> <p>(Note: Average crystallite sizes obtained from TEM micrographs of freshly reduced and spent catalysts.)</p> <p>($T_{\text{Reaction}} = 170^{\circ}\text{C}/225^{\circ}\text{C}$, $P = 4 \text{ bar}/20 \text{ bar}$, $\text{GHSV} = 7 \text{ ml(STP)}/(\text{min}\cdot\text{g}_{\text{cat}})$, $(\text{H}_2/\text{CO})_{\text{in}} = 2:1$)</p>	78

- 6.7 *left*: Average steady-state methane selectivities in the total formed product in FT synthesis versus average crystallite size of spent (steady-state) model catalysts.
right: Average steady-state C₅₊-selectivities in the total formed product in FT synthesis versus average ruthenium crystallite size of spent (steady-state) model catalysts.
 (Note: Average crystallite sizes obtained from TEM micrographs of freshly reduced and spent catalysts.)
 (T_{Reaction} = 170°C/225°C, P = 4 bar/20 bar, GHSV = 7 ml(STP)/(min·g_{cat}), (H₂/CO)_{in} = 2:1) 79
- 6.8 Maximal initial and average steady-state turnover frequencies of C₂₊ hydrocarbons in the volatile organic compounds (C₂-C₉) in FT synthesis versus average ruthenium crystallite size of fresh (1-3 minutes runtime) or, respectively, spent (steady-state) catalysts.
 (Note: Average crystallite sizes obtained from TEM micrographs of freshly reduced and spent catalysts.)
 (T_{Reaction} = 170°C/225°C, P = 4 bar/20 bar, GHSV = 7 ml(STP)/(min·g_{cat}), (H₂/CO)_{in} = 2:1) 80
- 6.9 *top*: Changes in molar content of ethene in C₂ hydrocarbon-fraction in FT synthesis at 170°C/4 bar as function of time on stream for five selected alumina supported nano-sized ruthenium crystallites.
bottom: Average molar contents of ethene in C₂ hydrocarbon-fraction in FT synthesis as function of crystallite size of fresh (1-3 minutes runtime) or, respectively, spent model catalysts (steady-state).
 (Note: Average crystallite sizes obtained from TEM micrographs of freshly reduced and spent catalysts.)
 (T_{Reaction} = 170°C/225°C, P = 4 bar/20 bar, GHSV = 7 ml(STP)/(min·g_{cat}), (H₂/CO)_{in} = 2:1) 82
- 6.10 *top*: Changes in molar content of propene in C₃ hydrocarbon-fraction in FT synthesis at 170°C/4 bar as function of time on stream for five selected alumina supported nano-sized ruthenium crystallites.
bottom: Average molar contents of propene in C₃ hydrocarbon-fraction in FT synthesis as function of crystallite size of fresh (1-3 minutes runtime) or, respectively, spent model catalysts (steady-state).
 (Note: Average crystallite sizes obtained from TEM micrographs of freshly reduced and spent catalysts.)
 (T_{Reaction} = 170°C/225°C, P = 4 bar/20 bar, GHSV = 7 ml(STP)/(min·g_{cat}), (H₂/CO)_{in} = 2:1) 83
- 6.11 *top*: Changes in molar contents of pentenes in C₅-fraction of linear hydrocarbons in FT synthesis at 170°C/4 bar as function of time on stream for five selected alumina supported nano-sized ruthenium crystallites.
bottom: Average molar contents of pentenes in C₅-fraction of linear hydrocarbons in FT synthesis as function of crystallite size of fresh (1-3 minutes runtime) or, respectively, spent model catalysts (steady-state).
 (Note: Average crystallite sizes obtained from TEM micrographs of freshly reduced and spent catalysts.)
 (T_{Reaction} = 170°C/225°C, P = 4 bar/20 bar, GHSV = 7 ml(STP)/(min·g_{cat}), (H₂/CO)_{in} = 2:1) 84

- 6.12 Average molar contents of olefins in linear hydrocarbons in FT synthesis at 225°C/20 bar (steady-state) as function of carbon number on alumina supported nano-sized ruthenium crystallites.
($T_{\text{Reaction}} = 225^{\circ}\text{C}$, $P = 20$ bar, $\text{GHSV} = 7 \text{ ml(STP)}/(\text{min}\cdot\text{g}_{\text{cat}})$, $(\text{H}_2/\text{CO})_{\text{in}} = 2:1$) 85
- 6.13 *top*: Changes in molar contents of 1-pentene in linear C₅-olefins in FT synthesis at 170°C/4 bar as function of time on stream for five selected alumina supported nano-sized crystallites.
bottom: Average molar contents of 1-pentene in linear C₅-olefins in FT synthesis as function of crystallite size of fresh (1-3 minutes runtime) or, respectively, spent model catalysts (steady-state).
(Note: Average crystallite sizes obtained from TEM micrographs of freshly reduced and spent catalysts.)
($T_{\text{Reaction}} = 170^{\circ}\text{C}/225^{\circ}\text{C}$, $P = 4$ bar/20 bar, $\text{GHSV} = 7 \text{ ml(STP)}/(\text{min}\cdot\text{g}_{\text{cat}})$, $(\text{H}_2/\text{CO})_{\text{in}} = 2:1$) 87
- 6.14 Average steady-state molar contents of α -olefins in the corresponding fraction of linear olefins in FT synthesis at 225°C/20 bar at steady-state as function of carbon number for supported nano-sized ruthenium crystallites.
($T_{\text{Reaction}} = 225^{\circ}\text{C}$, $P = 20$ bar, $\text{GHSV} = 7 \text{ ml(STP)}/(\text{min}\cdot\text{g}_{\text{cat}})$, $(\text{H}_2/\text{CO})_{\text{in}} = 2:1$) 88
- 6.15 Average steady-state molar contents of oxygenates in the linear C₅-products (*left y-axis*) and average steady-state molar contents of 1-pentanol in C₅-oxygenates (*right y-axis*) in FT synthesis at 225°C/20 bar versus average ruthenium crystallite size of spent (steady-state) catalysts.
(Note: Average crystallite sizes were obtained from TEM micrographs of spent catalysts.)
($T_{\text{Reaction}} = 225^{\circ}\text{C}$, $P = 20$ bar, $\text{GHSV} = 7 \text{ ml(STP)}/(\text{min}\cdot\text{g}_{\text{cat}})$, $(\text{H}_2/\text{CO})_{\text{in}} = 2:1$) 90
- 6.16 Average steady-state molar ratios of branched to linear (iso/n) C₅ hydrocarbons in FT synthesis at 225°C/20 bar versus average ruthenium crystallite size of spent (steady-state) model catalysts.
(Note: Average crystallite sizes were obtained from TEM micrographs of spent catalysts.)
($T_{\text{Reaction}} = 225^{\circ}\text{C}$, $P = 20$ bar, $\text{GHSV} = 7 \text{ ml(STP)}/(\text{min}\cdot\text{g}_{\text{cat}})$, $(\text{H}_2/\text{CO})_{\text{in}} = 2:1$) 91
- 6.17 Gas chromatogram of product obtained after 2 minutes of testing compound Ru-6 in synthesis gas.
($T_{\text{Reaction}} = 170^{\circ}\text{C}$, $P = 4$ bar, $\text{GHSV} = 7 \text{ ml(STP)}/(\text{min}\cdot\text{g}_{\text{cat}})$, $(\text{H}_2/\text{CO})_{\text{in}} = 2:1$) 94
- 6.18 *top*: Changes in turnover frequencies of C₁-C₄ hydrocarbons in FT synthesis as function of time on stream for five selected alumina supported organometallic compounds.
bottom: Maximal initial turnover frequencies of C₁-C₄ hydrocarbons in FT synthesis versus initial number of exposed metal atoms on alumina supported organometallic compounds.
(Note: TOF was calculated from the initial cluster size.)
($T_{\text{Reaction}} = 170^{\circ}\text{C}$, $P = 4$ bar, $\text{GHSV} = 7 \text{ ml(STP)}/(\text{min}\cdot\text{g}_{\text{cat}})$, $(\text{H}_2/\text{CO})_{\text{in}} = 2:1$) 95
- 6.19 TEM micrographs of spent supported organometallic compounds after FT synthesis for five hours (a to d), and respectively five days (e and f). . . . 97

- 6.20 *top*: IR spectra for spent (after FT performance for 5 hrs) redissolved Ru-2c and fresh $\text{Ru}_2(\text{CO})_2(\mu\text{-CO})(\mu\text{-CHCH}_3)(\eta^5\text{-C}_5\text{H}_5)_2$ dissolved in methylene chloride.
bottom: IR spectra for spent (after FT performance for 5 hrs) redissolved Ru-3 and fresh $\text{Ru}_4(\mu\text{-H})_4(\text{CO})_{12}$ and $\text{Ru}_3(\text{CO})_{12}$ dissolved in methylene chloride. 98
- 6.21 MS histogram of organometallic compound found in the outlet flow of FT performance of Ru-2a. (*Note*: Spectrum indicates formation of monoatomic ruthenium complex containing a cyclopentadiene group and two CO-ligands.) 99
- 6.22 Average initial methane selectivities in the $\text{C}_1\text{-C}_4$ hydrocarbons between 1-3 minutes runtime in FT synthesis versus initial number of exposed metal atoms on alumina supported organometallic compounds.
 $(T_{\text{Reaction}} = 170^\circ\text{C}, P = 4 \text{ bar}, \text{GHSV} = 7 \text{ ml(STP)}/(\text{min}\cdot\text{g}_{\text{cat}}), (\text{H}_2/\text{CO})_{\text{in}} = 2:1)$ 101
- 6.23 Molar product contents (C_1 to C_4) obtained at 2 minutes runtime in FT tests as function of carbon number on alumina supported organometallic compounds (*left*: Ru-2a, Ru-2b and Ru-2c; *right*: Ru-3, Ru-4, Ru-5 and Ru-6).
 $(T_{\text{Reaction}} = 170^\circ\text{C}, P = 4 \text{ bar}, \text{GHSV} = 7 \text{ ml(STP)}/(\text{min}\cdot\text{g}_{\text{cat}}), (\text{H}_2/\text{CO})_{\text{in}} = 2:1)$ 102
- 6.24 Maximal initial turnover frequencies of $\text{C}_2\text{-C}_4$ hydrocarbons in FT synthesis tests versus initial number of exposed metal atoms on alumina supported organometallic compounds.
 $(T_{\text{Reaction}} = 170^\circ\text{C}, P = 4 \text{ bar}, \text{GHSV} = 7 \text{ ml(STP)}/(\text{min}\cdot\text{g}_{\text{cat}}), (\text{H}_2/\text{CO})_{\text{in}} = 2:1)$ 103
- 6.25 Average initial molar contents of ethene in C_2 hydrocarbons (*top*) and propene in C_3 hydrocarbons (*bottom*) between 1-3 minutes runtime in FT synthesis versus initial number of exposed metal atoms on alumina supported organometallic compounds.
 $(T_{\text{Reaction}} = 170^\circ\text{C}, P = 4 \text{ bar}, \text{GHSV} = 7 \text{ ml(STP)}/(\text{min}\cdot\text{g}_{\text{cat}}), (\text{H}_2/\text{CO})_{\text{in}} = 2:1)$ 104
- 6.26 Gas chromatogram of product obtained after 3 minutes of testing compound Ru-6 in pure hydrogen.
 $(T_{\text{Reaction}} = 170^\circ\text{C}, P = 4 \text{ bar}, \text{GHSV} = 7 \text{ ml(STP)}/(\text{min}\cdot\text{g}_{\text{cat}}))$ 107
- 6.27 Changes in turnover frequencies of $\text{C}_1\text{-C}_4$ hydrocarbons in FT synthesis as function of time on stream for catalyst sample Ru-3, in synthesis gas (●) and in hydrogen (○).
 $(T_{\text{Reaction}} = 170^\circ\text{C}, P = 4 \text{ bar}, \text{GHSV} = 7 \text{ ml(STP)}/(\text{min}\cdot\text{g}_{\text{cat}}), (\text{H}_2/\text{CO})_{\text{in}} = 2:1)$ 107
- 6.28 *top*: Maximal initial and average steady-state turnover frequencies in FT synthesis as function of number of exposed ruthenium atoms of fresh (1-3 minutes runtime) or, respectively, spent model catalysts (steady-state).
bottom: Maximal initial and average steady-state turnover frequencies of C_{2+} hydrocarbons in FT synthesis as function of number of exposed ruthenium atoms of fresh (1-3 minutes runtime) or, respectively, spent model catalysts (steady-state).
 $(T_{\text{Reaction}} = 170^\circ\text{C}, P = 4 \text{ bar}, \text{GHSV} = 7 \text{ ml(STP)}/(\text{min}\cdot\text{g}_{\text{cat}}), (\text{H}_2/\text{CO})_{\text{inlet}} = 2:1)$ 111
- 6.29 Average initial and steady-state methane contents in FT synthesis as function of number of exposed metal atoms of fresh (1-3 minutes runtime) or, respectively, spent model catalysts (steady-state).
 $(T_{\text{Reaction}} = 170^\circ\text{C}, P = 4 \text{ bar}, \text{GHSV} = 7 \text{ ml(STP)}/(\text{min}\cdot\text{g}_{\text{cat}}), (\text{H}_2/\text{CO})_{\text{inlet}} = 2:1)$ 112

6.30	<i>top</i> : Average initial and steady-state molar contents of ethene in the C ₂ -fraction in FT synthesis as function of number of exposed metal atoms of fresh (1-3 minutes runtime) or, respectively, spent model catalysts (steady-state).	
	<i>bottom</i> : Average initial and steady-state molar contents of propene in the C ₃ -fraction in FT synthesis as function of number of exposed metal atoms of fresh (1-3 minutes runtime) or, respectively, spent model catalysts (steady-state).	
	(T _{Reaction} = 170°C, P = 4 bar, GHSV = 7 ml(STP)/(min·g _{cat}), (H ₂ /CO) _{inlet} = 2:1)	114
7.1	Enthalpy of reaction, ΔH _{rxn} , in kJ/mol for the different intermediates proposed in the monoatomic reaction mechanisms <i>A</i> , <i>B</i> and <i>C</i> at 475 K.	126
7.2	Enthalpy of reaction, ΔH _{rxn} , in kJ/mol for the different intermediates proposed in the diatomic reaction mechanisms <i>A1</i> and <i>A2</i> leading to the generation of the chain initiator at 475 K.	127
7.3	Enthalpy of reaction, ΔH _{rxn} , in kJ/mol for the different intermediates proposed in the diatomic reaction mechanisms for the first step of chain growth (mechanisms <i>B1</i> , <i>B2</i> and <i>B3</i>) and second step of chain growth (mechanisms <i>C1</i> , <i>C2</i> and <i>C3</i>) at 475 K.	129
A.1	Crystallite size distributions of calcined (<i>closed bars</i>) and reduced (<i>open bars</i>) alumina supported nano-sized crystallites as determined by means of TEM analysis.	156
A.2	Crystallite size distributions of reduced (<i>open bars</i>) and spent (<i>closed bars</i>) alumina supported nano-sized crystallites as determined by means of TEM analysis.	157
A.3	Example of typical chemisorption reading; sample: RM-2.	158
A.4	Number of exposed ruthenium atoms as function of crystallite size of ruthenium.	159
A.5	First derivative of weight vs. temperature profile from TGA analysis for the different organometallic complexes in 5 vol% hydrogen in argon.	163
A.6	First derivative of weight vs. temperature profile from TGA analysis for the different organometallic complexes in 5 vol% carbon monoxide in nitrogen.	164
B.1	A typical chromatogram obtained from GC-TCD analysis in FT synthesis (225°C/20 bar); catalyst sample RM-10 after 3 hours runtime.	165
B.2	A typical chromatogram obtained from GC-FID analysis in FT synthesis at 170°C/4 bar; catalyst sample RM-10 after 3 minutes runtime.	166
B.3	<i>top</i> : Changes in methane selectivities in volatile organic compounds in FT synthesis at 170°C/4 bar as function of time on stream for catalyst sample RM-2, with (●) and without (○) carbon monoxide pre-exposure after reduction prior to FT experiment.	
	<i>bottom</i> : Changes in molar contents of pentenes in C ₅ -fraction of linear hydrocarbons in FT synthesis as function of time on stream for catalyst sample RM-2, with (●) and without (○) carbon monoxide pre-exposure after reduction prior to FT experiments.	
	(T _{Reaction} = 170°C, P = 4 bar, GHSV = 7 ml(STP)/(min·g _{cat}), (H ₂ /CO) _{in} = 2:1)	177

B.4	<i>top:</i> Changes in chain growth probabilities in C ₄ -C ₇ hydrocarbons in FT synthesis at 170°C/4 bar for five selected supported nano-sized ruthenium crystallites.	
	<i>bottom:</i> Average chain growth probabilities (C ₄ -C ₇) in FT synthesis at 170°C/4 bar versus average ruthenium crystallite size of fresh (1-3 minutes runtime) or, respectively, spent (steady-state) model catalysts. (Note: Average crystallite sizes obtained from TEM micrographs of freshly reduced and spent catalysts.)	
	(T _{Reaction} = 170°C/225°C, P = 4 bar/20 bar, GHSV = 7 ml(STP)/(min·g _{cat}), (H ₂ /CO) _{in} = 2:1)	178
B.5	<i>top:</i> Changes in turnover frequencies of C ₁ -C ₄ hydrocarbons in FT synthesis at 170°C/4 bar as function of time on stream for the different alumina supported diatomic organometallic compounds.	
	<i>bottom:</i> Changes in turnover frequencies in FT synthesis at 170°C/4 bar as function of time on stream at extended runtimes for the alumina supported organometallic compounds Ru-3 and Ru-4. (T _{Reaction} = 170°C, P = 4 bar, GHSV = 7 ml(STP)/(min·g _{cat}), (H ₂ /CO) _{in} = 2:1)	180
B.6	<i>top:</i> Changes in turnover frequencies of C ₁ -C ₄ hydrocarbons in FT synthesis at 170°C/4 bar in hydrogen as function of time on stream for different alumina supported diatomic organometallic compounds.	
	<i>bottom:</i> Changes in turnover frequencies in FT synthesis at 170°C/4 bar in hydrogen as function of time on stream for selected alumina supported organometallic compounds. (T _{Reaction} = 170°C, P = 4 bar, GHSV = 7 ml(STP)/(min·g _{cat}))	181
C.1	Entropy of reaction, ΔS _{rxn} , in kJ/(mol·K) for the different intermediates proposed in the monoatomic reaction mechanisms A , B and C at 475 K.	187
C.2	Entropy of reaction, ΔS _{rxn} , in kJ/(mol·K) for the different intermediates proposed in the diatomic reaction mechanisms A , B and C leading to the generation of the chain initiator at 475 K.	188
C.3	Entropy of reaction, ΔS _{rxn} , in kJ/(mol·K) for the different intermediates proposed in the diatomic reaction mechanisms A , B and C leading to the first step of chain growth at 475 K.	188

List of Tables

2.1	Overview of common poisons classified by chemical structure (Bartholomew (2001)).	16
2.2	T_{melting} , $T_{\text{Hüttig}}$ and T_{Tamman} of metals and supports relevant for the FT synthesis.	18
4.1	Amounts of RuCl_3 , H_2O , PEGDE and n-hexane for preparation of different alumina supported nano-sized crystallites.	31
4.2	Conditions for gas chromatographic analysis using TCD detection.	46
4.3	Conditions for gas chromatographic analysis using FID and MS detection.	47
5.1	Viscosity (η) of microemulsion systems and respective volume fractions (Φ) of dispersed spheres.	52
5.2	TEM characterisation results of calcined and reduced supported nano-sized crystallites.	57
5.3	Dispersion (D) and average ruthenium crystallite sizes for reduced supported nano-sized crystallites ($\bar{d}_{\text{CO-Chem.}}$) by means of CO-chemisorption. Also listed are crystallite sizes from TEM analyses (see Table 5.2).	60
5.4	Characterisation data of calcined and reduced alumina supported nano-sized crystallites.	63
5.5	Decomposition temperatures (T_{decomp}) of organometallic clusters in different gas atmospheres determined by means of TGA analyses.	64
5.6	Summary of alumina supported organometallic compounds.	66
6.1	TEM characterisation results for reduced and spent alumina supported nano-sized crystallites.	70
6.2	Metal loadings of spent supported organometallic compounds observed from ICP analyses (loading of fresh samples: 3 wt%).	100
6.3	Chain growth probabilities, carbon number ranges C_1 to C_2 and C_3 to C_4 , obtained at 2 minutes runtime in FT tests on alumina supported organometallic compounds. ($T_{\text{Reaction}} = 170^\circ\text{C}$, $P = 4$ bar, $\text{GHSV} = 7$ ml(STP)/(min \cdot g $_{\text{cat}}$), $(\text{H}_2/\text{CO})_{\text{in}} = 2:1$)	102
6.4	Amount of carbon in hydrocarbons formed over five hours of testing the supported organometallic clusters in synthesis gas and in hydrogen relative to carbon present in ligands of the clusters (excluding carbon in cyclopentadiene and pentamethyl-cyclopentadiene ligands).	106
7.1	Calculated (DFT-BLYP) and literature data (experimental and calculated) of the known compounds for the proposed monoatomic FT reaction mechanism.	124

A.1	Chemicals used for model catalyst preparation.	154
B.1	Results of FT experiments in synthesis gas after 1-3 minutes runtime on different alumina supported nano-sized crystallites. ($T_{\text{Reaction}} = 170^{\circ}\text{C}$, $P = 4$ bar)	167
B.2	Results of FT experiments in synthesis gas after 10-20 minutes runtime on different alumina supported nano-sized crystallites. ($T_{\text{Reaction}} = 170^{\circ}\text{C}$, $P = 4$ bar)	167
B.3	Results of FT experiments in synthesis gas after 60 minutes runtime on different alumina supported nano-sized crystallites. ($T_{\text{Reaction}} = 170^{\circ}\text{C}$, $P = 4$ bar)	167
B.4	Results of FT experiments in synthesis gas at steady-state on different alumina supported nano-sized crystallites. ($T_{\text{Reaction}} = 170^{\circ}\text{C}$, $P = 4$ bar)	167
B.5	Steady-state results of FT synthesis at $225^{\circ}\text{C}/20$ bar for five selected alumina supported nano-sized crystallites. ($T_{\text{Reaction}} = 225^{\circ}\text{C}$, $P = 20$ bar, $\text{GHSV} = 7 \text{ ml(STP)}/(\text{min}\cdot\text{g}_{\text{cat}})$, $(\text{H}_2/\text{CO})_{\text{in}} = 2:1$)	172
B.6	Selected results of FT experiments in synthesis gas ($(\text{H}_2/\text{CO})_{\text{in}} = 2:1$) and in hydrogen after 1-3 minutes runtime on different supported organometallic compounds. ($T_{\text{Reaction}} = 170^{\circ}\text{C}$, $P = 4$ bar, $\text{GHSV} = 7 \text{ ml(STP)}/(\text{min}\cdot\text{g}_{\text{cat}})$)	173
B.7	Selected results of FT experiments in synthesis gas after 10-20 minutes runtime in synthesis gas ($(\text{H}_2/\text{CO})_{\text{in}} = 2:1$) and at maximal activities for performances in hydrogen (runtimes between 10-100 minutes) on different supported organometallic compounds. ($T_{\text{Reaction}} = 170^{\circ}\text{C}$, $P = 4$ bar, $\text{GHSV} = 7 \text{ ml(STP)}/(\text{min}\cdot\text{g}_{\text{cat}})$)	174
B.8	Selected results of FT experiments in synthesis gas after 300 minutes runtime on different supported organometallic compounds. ($T_{\text{Reaction}} = 170^{\circ}\text{C}$, $P = 4$ bar, $\text{GHSV} = 7 \text{ ml(STP)}/(\text{min}\cdot\text{g}_{\text{cat}})$, $(\text{H}_2/\text{CO})_{\text{in}} = 2:1$)	175
B.9	Metal loadings of spent supported organometallic compounds after FT testing in hydrogen observed by means of ICP analyses (loading of fresh samples: 3 wt%).	182

List of Schemes

1	Alkyl mechanism.	7
2	Alkenyl mechanism.	8
3	Enol mechanism.	8
4	CO-insertion mechanism.	9
5	Selective (<i>top</i>) and non-selective (<i>bottom</i>) poisoning in heterogeneous catalysis.	15
6	Different stages in the formation and growth from single atoms to three-dimensional particles on the support surface (Moulijn et al., 2001).	18
7	Formation of the volatile ruthenium-pentacarbonyl, Ru(CO) ₅ , via surface reaction of carbon monoxide with metallic ruthenium.	19
8	Schematic diagram of a “reverse micelle” system.	23
9	Schematic representation of the synthesis of nano-particles in microemulsions using two microemulsions.	25
10	Schematic representation of the preparation of ruthenium nano-particles by means of the reverse micelle technique.	30
11	Chemical structure of Ru ₄ (μ-H) ₄ (CO) ₁₂	35
12	Chemical structure of Ru ₅ C(CO) ₁₅	36
13	Chemical structure of Ru ₆ C(CO) ₁₇	36
14	Experimental set-up for FT synthesis. <i>Note:</i> P-1 to P-4: Pressure regulating valves; E-1 to E-4: Line filters; MFC-1, MFC-2 and MFC-4: Mass flow controllers; CV-1, CV-2 and CV-4: Check valves; V-1 to V-5: One-way valves; 4WV: 4-way valve; NV-1 to NV-3: Needle valves; AS: Ampoule sampler; CT: Cold-trap; FIC: Flow indicator and control; PI: Pressure indicator; PIC: Pressure indicator and control; R: Reactor; TI: Temperature indicator; TIC: Temperature indicator and control; W: Wax trap.	41
15	Modified experimental set-up for FT synthesis using labelled ¹³ C in CO. <i>Note:</i> P-2: Pressure regulating valve; E-1 and E-2: Line filters; MFC-1: Mass flow controller; CV-1: Check valve; V-1 to V-4: One-way valves; 3WV: 3-way valve; 4WV: 4-way valve; NV-1 to NV-3: Needle valves; AS: Ampoule sampler; CT: Cold-trap; FIC: Flow indicator and control; PI: Pressure indicator; PIC: Pressure indicator and control; R: Reactor; TI: Temperature indicator; TIC: Temperature indicator and control; W: Wax trap.	42
16	Schematic drawing of the heating-source and the reactor for FT experiments on supported nano-sized crystallites (<i>left</i>) and supported organometallic compounds (<i>right</i>), used as model catalysts.	44
17	Schematic drawing of the ampoule sampling device.	45
18	First steps of the proposed monoatomic FT reaction mechanisms.	117

19	Proposed monoatomic FT reaction mechanisms <i>A</i> , <i>B</i> and <i>C</i> divided in the generation of the chain starter and the first step of chain growth. . .	120
20	Generation of the chain starter for the proposed diatomic FT reaction mechanisms <i>A1</i> and <i>A2</i>	121
21	First part of the chain growth for the proposed diatomic FT reaction mechanisms <i>B1</i> , <i>B2</i> and <i>B3</i>	122
22	Second part of the chain growth expressed as the proposed diatomic FT reaction mechanisms <i>C1</i> , <i>C2</i> and <i>C3</i>	123
23	Description of the reverse micelle dimensions.	160

University of Cape Town

Nomenclature

Abbreviations

ASF	Anderson-Schulz-Flory
BLYP	Becke-Lee-Yang-Parr
DFT	Density Functional Theory
DNP	Double Numerical Basis Set with Polarization
ECP	Effective Core Potential
EXAFS	Extended X-ray Adsorption Fine Structure
FID	Flame Ionization Detector
FT	Fischer-Tropsch
FT-IR	Fourier-Transform Infrared
GC	Gas Chromatograph
GGA	General-Gradient Approximation
HTFT	High Temperature Fischer-Tropsch
ICP	Inductively Coupled Plasma
IR	Infrared
JCPDS	Joint Committee for Powder Diffraction Standards
LDA	Local Density Approximation
LTFT	Low Temperature Fischer-Tropsch
MS	Mass Spectrometry
NMR	Nuclear Magnetic Resonance
NTP	Normal Temperature Pressure (0°C; 1.01325 bar)
PMS	Polymethylene Synthesis
SCF	Self Consistent Field
SMDS	Shell Middle Distillate Synthesis
Sp	Surface Species
STP	Standard Temperature Pressure (25°C; 1.01325 bar)
TCD	Thermal Conductivity Detector
TEM	Transmission Electron Microscopy
TGA	Thermogravimetric Analysis
TPR	Temperature Programmed Reduction
VE	Valence Electron
VOC	Volatile Organic Compound
WGS	Water Gas Shift
XRD	X-Ray Diffraction Spectroscopy

Chemical abbreviations

Ag ₂ O	Silver oxide
AlCl ₃	Aluminium chloride
Al ₂ O ₃	Aluminium oxide ("Alumina")
AOT	Sodium bis-(2-ethylhexyl)-sulfosuccionate
BBr ₃	Boron tribromide
BHT	Butylated hydroxytoluene
CH ₄	Methane
CH _x	Cyclohexane
CH ₂ Cl ₂	Methylene dichloride
CH ₃ OH, MeOH	Methanol
CH ₂ O	Formaldehyde
CDCl ₃	Chloroform-d (deuterated)
C ₅ H ₆	Cyclopentadiene
C ₅ (CH ₃) ₅	Pentamethylcyclopentadiene
CO	Carbon monoxide
CO ₂	Carbon dioxide
COS	Carbonyl sulfide
CTAB	Cetyl trimethyl ammonium bromide
EtO ₂	Diethylether
Fe ₃ O ₄	Iron(II, III)-oxide ("Magnetite")
H ₂	Hydrogen
HF ₄	Tetrafluoroboric acid
HCl	Hydrochloric acid
HCN	Hydrogen cyanide
H ₂ O	Water (demineralised)
H ₂ S	Hydrogen sulfide
Ir ₄ (CO) ₁₂	Dodecacarbonyl-tetrairidium
KCl	Potassium chloride
KOH	Potassium hydroxide
MeLi	Methylithium
NaBH ₄	Sodium tetrahydridoborate
NaCl	Sodium chloride
NH ₃	Ammonia
(NH ₄) ₂ CO ₃	Ammonium carbonate
Ni(CO) ₄	Nickel-tetracarbonyl
NiO	Nickel oxide
NMP	N-methyl-pyrrolidone
NO	Nitrogen oxide
Os ₃ (CO) ₁₂	Dodecacarbonyl-triosmium
PEGDE	Penta-ethyleneglycol-dodecylether
Ru ₅ C(CO) ₁₅	μ ₅ -Carbido-pentadecacarbonyl-pentaruthenium
Ru ₆ C(CO) ₁₇	μ ₆ -Carbido-heptadecacarbonyl-hexaruthenium
RuCl ₃	Ruthenium chloride
Ru(CO) ₄	Ruthenium-tetracarbonyl
Ru(CO) ₅	Ruthenium-pentacarbonyl
Ru(CO) ₄ H ₂	Dihydrido-ruthenium-tetracarbonyl

$\text{Ru}_2(\text{CO})_4(\eta^5\text{-C}_5\text{H}_5)_2$	Tetracarbonylbis(η^5 -cyclopentadienyl)-diruthenium
$\text{Ru}_2(\text{CO})_4(\eta^5\text{-C}_5(\text{CH}_3)_5)_2$	Tetracarbonylbis(η^5 -pentamethyl-cyclopentadienyl)-diruthenium
$\text{Ru}_2(\text{CO})_2(\mu\text{-CO})(\mu\text{-CHCH}_3)(\eta^5\text{-C}_5\text{H}_5)_2$	μ -Carbonyl- μ -ethenylidene-bis[carbonyl-(η -cyclopentadienyl)ruthenium]
$\text{Ru}_2(\text{CO})_9$	Enneacarbonyl ruthenium
$\text{Ru}_3(\text{CO})_{12}$	Dodecacarbonyl-triruthenium
$\text{Ru}_4(\mu\text{-H})_4(\text{CO})_{12}$	Dodecacarbonyl-tetra(μ -hydrido)-tetraruthenium
RuO_2	Ruthenium dioxide
RuO_4	Ruthenium tetraoxide
SDS	Sodium dodecyl sulphate
SiC	Silicon carbide
SiO_2	Silicon oxide ("Silica")
THF	Tetrahydrofuran
TMS	Tetramethyl-silane
$\text{W}(\text{CO})_6$	Tungsten-hexacarbonyl

Notation

A	Area in chromatogram	-
a_m	Element specific lattice parameter	m^2
BDE	Bond dissociation energy	kJ/mol
c	Concentration	mol/l
d	Diameter	m
\bar{d}	Average diameter	m
D	Dispersion	%
E	Eigenvalue, Energy	eV
f	Response factor	-
G	Gibbs free energy	kJ/mol
GHSV	Gas Hourly Space Velocity (at STP conditions per gram of catalyst)	$\text{ml}/(\text{min}\cdot\text{g})$
H	Enthalpy	kJ/mol
H^0	Standard enthalpy (at 298 K and 1 bar)	J/mol
\hat{H}	Hamiltonian operator	-
\hbar	Planck's constant divided by 2π ; $1.054\cdot 10^{-34}$	J·s
j	Number of atoms on an equivalent edge	-
J	Coupling constant	Hz
k	Rate constant	$\text{m}^3/(\text{g}\cdot\text{min})$
l	Length	m
m	Mass	g
M	Molecular mass	g/mol
n	Mole	mol
N	Number	-
\dot{n}	Molar flow	mol/min
N_A	Avogadro's Number; $6.022\cdot 10^{23}$	mol^{-1}
p	Probability	-
P	Pressure	bar

r	Rate, Radius	mol/(min·g), m
R	General gas constant; 8.314	J/(mol·K)
S	Selectivity, Entropy	C%, kJ/(mol·K)
S ⁰	Standard entropy (at 298 K and 1 bar)	J/(mol·K)
S _{cryst}	Surface area of a single crystallite	m ²
S _{BET}	Specific surface area of support material	m ² /g
t	Thickness	m
T	Temperature	°C, K
T _p	Kinetic energy	eV
TOF	Turnover Frequency	s ⁻¹
TON	Turnover Number	s ⁻¹
U	Classical Coulomb interaction	eV
V	Volume	m ³
\dot{V}	Volumetric flow rate	ml/min
v _m	Element specific lattice parameter	m ³
V _m	Avogadro volume; 22.414	l/mol
V(r)	Potential energy	eV
W _N	Mass fraction of a product with N carbon atoms	wt%
x	Loading	wt%
X	Conversion	%
x _{chem.}	Chemisorption stoichiometry	-
Y	Yield	C%
z	Atomic loading	-
ZPVE	Zero point vibrational energy	kJ

Greek notations

δ	Chemical shift	Hz
Δ	Difference	-
η	Kinematic viscosity	cp
μ	Exchange-correlation potential	-
∇^2	Laplace operator	-
ν	Vibration frequency	s ⁻¹
ν_i	Stoichiometric factor of compound i	-
ω	Water-to-surfactant weight ratio	g/g
Φ	Volume fraction of suspended particles	-
ψ	Wave function	-
ρ	Density	g/cm ³
σ	Variance	m
Θ	Diffraction angle	°
ζ	Zetapotential	V

Subscripts Abbreviations

ag	Aggregation
atom	Single atom
bulk	Bulk atoms
c	Critical

C	Carbon
calc	Calcined sample
CH _x	Cyclohexane
chem	Chemisorbed gas required to form monolayer coverage
Chem.	Chemisorption
CO	Carbon monoxide
cryst	Crystallite
d	Desorption
decomp	Decomposition
elec	Electrons, Minimum electronic
exp	Exposed ruthenium atoms
FID	Flame ionisation detector
FT	Fischer-Tropsch
g	Chain growth
i	Compound/Sample
in	Inlet
int	Internal
lattice	Lattice of metallic ruthenium
ligands	Ligands
MS	Mass Spectrometry
out	Outlet
pore	Pore size
red	Reduced sample
ref	Reference
rel	Certain amount of surface atoms
rm	Reverse micelle
rot	Rotational
rxn	Reaction
s	Surfactant
Sp	Species
spent	Spent sample
sph	Spherical
TEM	Transmission electron microscopy
TCD	Thermal conductivity detector
total	Total
TPR	Temperature Programmed Reduction
trans	Translational
u	Unit cell
VE	Valence electron
vib	Vibrational
VOC	Volatile organic compound
w	Water
wp	Water-pool
wt	Weight
xc	Exchange correlation

Chapter 1

Introduction

The Fischer-Tropsch (FT) synthesis, named after the two German scientists Franz Fischer and Hans Tropsch, has been of industrial and academic interest ever since its first discovery in the 1920's (Fischer et al. (1923), Fischer and Tropsch (1923a), Fischer and Tropsch (1923b), Fischer et al. (1925), Fischer and Tropsch (1926)). A variety of catalyst systems has been tested, with cobalt and iron currently being the commercially used ones. Particularly in the years of oil crises FT synthesis proved to be a booming technology supplying the opportunity to generate petrol, diesel, waxes and chemicals from coal, natural gas and biomass.

This heterogeneous polymerisation reaction follows a complicated series of primary and secondary reactions, leading to a broad product spectrum ranging from methane to heavy waxes (Anderson (1956), Schulz and Claeys (1999a)). The product classes formed include predominantly linear paraffins, α -olefins and oxygenates.

Current research in the field of the FT synthesis focuses mainly on improving product selectivity and catalytic activity. It is understood that the metal crystallite size on support material can be very important to develop a catalyst, which meets the activity, stability and selectivity requirements of a particular catalytic process (Boudart and McDonald (1984), Lin et al. (1986), Abrevaya et al. (1990)). Whereas older perceptions suggested that an increase in catalyst surface area, generating more available active centres, leads to an increase in activity (on a mass basis), recent publications describe a different behaviour for very small crystallites of rhodium, iron and cobalt, which below a certain metal crystallite size were less reactive for FT synthesis than larger crystallites (Ojeda et al. (2004), Mabaso (2005), Barkhuizen et al. (2006), Bezemer et al. (2006), Mabaso et al. (2006)). This structure-sensitivity was ascribed to structural and electronical effects by Boudart (1969). In this structure-sensitive range, change in selectivity was also observed with increased methane selectivity (Mabaso (2005), Barkhuizen et al. (2006), Bezemer et al. (2006), Mabaso et al. (2006)) and increased paraffin to olefin ratios (Bezemer et al. (2006)) on catalysts with small crystallites. Tests to study such effects require supported, well-defined, nano-sized metal crystallites with narrow crystallite size distributions.

The preparation of such catalysts is not straight forward. Conventional impregnation and precipitation deposition techniques often lead to the formation of catalysts with very broad crystallite size distributions. Moreover, it is normally very difficult to vary the average crystallite size using these techniques. In recent years, studies to prepare narrow crystallite size distributions, like the novel "reverse micelle" technique were reported in

the literature (Abrevaya (1990), Eriksson et al. (2004)). The reverse micelle technique allows control of crystallite size over a wide nanometer range (2-18 nm (Mabaso (2005), Barkhuizen et al. (2006), Mabaso et al. (2006))). Crystallites smaller than 1-2 nm are generally difficult to prepare and characterise. The behaviour of very small crystallites, i.e. with a small number of ruthenium atoms, can however be studied using organometallic compounds of different nuclearity. These Ångström-sized compounds can be supported and then regarded as heterogenized homogeneous FT model catalyst systems.

Homogeneously catalysed reactions are known for their high selectivity towards specific products at mild reaction conditions, making them ideally suited for organic or medicinal chemistry applications. However, despite several attempts to develop a homogeneous FT catalyst (Bradley (1979), Dombek (1980), Keim et al. (1980)), stable homogeneously catalysed FT synthesis has not yet been reported as feasible, although recent work on FT synthesis using organometallic ruthenium compounds supported on silica suggests that FT products can be formed from such compounds if they contain at least two adjacent ruthenium atoms (Claeys et al. (2000a,b)).

The aim of this study is to compare/bridge findings obtained in FT tests on supported organometallic model compounds of varied nuclearity and ruthenium crystallites of different crystallite sizes. These tests should lead to a better understanding of the characteristics of the sites required for the reactions occurring in FT synthesis.

Chapter 2

Literature Review

2.1 Fischer-Tropsch Synthesis

It is widely understood that crude oil has a limited future of approximately 30 years, whereas hundreds of years of coal, tar sands, natural gas as well as biomass reserves are available around the globe at commonly projected energy and fuel needs. All of these hydrocarbon sources can serve for the generation of synthesis gas, a mixture of hydrogen and carbon monoxide, which is the feedstock for FT synthesis.

The importance of this process is underlined by a large number of recent journal and patent publications as well as strong research and development activities in most petrochemical producing countries which now have led to construction of new FT plants in Qatar (SASOL and Shell) and Nigeria (SASOL) in addition to existing plants in South Africa (SASOL and Petro SA) and Malaysia (Shell).

2.1.1 General - History and Development

The first hydrocarbon synthesis reaction, reported by Sabatier and Senderens (1902), was the methanation reaction of synthesis gas over nickel and cobalt catalysts. In the following years, various groups worked on this promising reaction. Several years later, for instance, the 'Badische Anilin und Soda Fabrik' (BASF) patented the preparation of hydrocarbon and oxygenate products by high pressure hydrogenation of carbon monoxide on oxide catalysts (BASF (1913, 1914, 1921)). The next breakthrough in this field was the synthesis of higher hydrocarbons under atmospheric pressure on cobalt, iron and nickel catalysts by Fischer et al. (1925). Fischer and Tropsch, both working at the "Kaiser-Wilhelm-Institut für Kohleforschung" in Mühlheim, developed their synthesis at low pressure conditions, because BASF had patent rights for the high pressure synthesis. From 1935 onwards the FT synthesis was operated commercially by the Ruhrchemie AG (Oberhausen) in Germany using cobalt catalysts. Starting at atmospheric pressure, catalyst performance and lifetime was increased by increasing to pressures of 5-20 bar (Dry, 1981). By 1938 nine FT plants were operating in Germany with a capacity of $600 \cdot 10^3$ tons per annum (Dry, 1996).

After World War II commercial FT operations were discontinued in Germany. However, in the 1940's and 50's the US Bureau of Mines revived interest in the FT technology by replacing the expensive cobalt catalysts with cheaper iron catalysts. First attempts with iron catalysts had already been done in Germany by the Fischer group in the mid 1930's (Fischer and Pichler (1937), Pichler (1952)). The usage of iron catalysts was

further improved in the United States of America (Storch et al., 1951). The next stage in FT history was the involvement of South Africa in the 1950's. The SASOL company (Sasolburg, South Africa) built a coal-based plant (Lurgi dry ash gasifiers) for synthesis gas generation, consisting of fixed-bed (Ruhrchemie/Lurgi) and circulating fluidized-bed (Kellogg) reactors for FT synthesis (Dry, 1996). The so-called "SASOL One" FT plant in Sasolburg had a capacity of $700 \cdot 10^3$ t/a.

Due to the oil crisis in the 1970's, SASOL developed the FT technology further and built SASOL II and SASOL III in the early 1980's. At present, SASOL uses two modes of FT operation with a combined capacity of $6000 \cdot 10^3$ t/a. The high-temperature (300-350°C) FT process (HTFT) with iron based catalysts is used mainly for the production of gasoline and linear, low molecular mass α -olefins, while the low-temperature (200-240°C) FT process (LTFT) with either cobalt or iron catalysts is used for the production of high molecular mass linear waxes (Dry, 2002), which can be processed further to maximize middle distillate yields of the overall process to up to 80 wt% (see below).

Petro SA (formerly Mossgas) in Mossel Bay, South Africa, commissioned FT technology based on natural gas in 1992 with a plant capacity of $900 \cdot 10^3$ t/a. The natural gas is transformed into synthesis gas via steam reforming, followed by HTFT synthesis for fuel production.

A further development in the field of FT synthesis aims at monetising "stranded natural gas reserves" which is converted into easily transportable fuels. High yields of middle distillate are achieved by hydrocracking and isomerisation of longchain products (wax). In 1993, such a process was commercialized as the "Shell Middle Distillate Synthesis" (SMDS) in Bintulu, Malaysia. Further such so-called "Gas-to-Liquid" plants are currently being commissioned and constructed at different places such as Quatar (SASOL and Shell) and Nigeria (SASOL) and the potential construction of more plants has been announced frequently, highlighting the important role FT technology will play in times of high oil prices and depleting oil reserves (van der Laan (1999), Steynberg (2004), Steynberg et al. (2004)).

2.1.2 Stoichiometry of the Fischer-Tropsch Reaction

The FT synthesis is the reaction of synthesis gas (H_2/CO), over a metallic catalyst, to give higher hydrocarbons. This highly exothermic reaction can be represented stoichiometrically as follows:



Water is a by-product of the FT synthesis. The stoichiometry of this polymerisation reaction usually implies a hydrogen to carbon monoxide ratio of 2:1. It is a polymerization reaction with a broad product distribution (see Section 2.1.3, p. 6). Linear α -olefins and paraffins are the main products. The product spectrum also contains minor quantities of oxygenates such as aldehydes and alcohols and branched products (predominantly "methyl-branched").

Depending on the catalyst, different side-reactions can occur. The water gas shift reaction (WGS)



is mainly catalysed by iron while cobalt or ruthenium catalysts have nearly no WGS activity.

Other side-reactions are methanation (equation 2.3) and the Boudouard reaction (equation 2.4). In particular, the Boudouard reaction (or carbon monoxide disproportionation reaction) can be problematic as it can lead to the formation of carbon on the surface of the catalyst, that can cause deactivation (see Section 2.2.2, p. 16).



Methane is the thermodynamically most stable FT product (Schulz and Cronjé (1977), Anderson (1984)). All other hydrocarbons are not thermodynamically preferred at typical FT conditions. The broad FT product spectrum with higher hydrocarbons therefore indicates that the FT reaction is kinetically and not thermodynamically controlled.

2.1.3 Fischer-Tropsch Products

2.1.3.1 Classification of Fischer-Tropsch Products

Since the early years of the FT synthesis, scientists have been investigating the different products obtained in this reaction. The FT synthesis includes the formation of paraffins and olefins as well as oxygenates such as alcohols, aldehydes, ketones and carboxylic acids (Anderson, 1984). The product spectrum is often affected by secondary reactions as olefins and oxygenates can readsorb on the catalyst surface and undergo secondary reactions such as hydrogenation or double bond shift (Schulz and Claeys, 1999b).

Already in the 1920's it was found that the main products using cobalt catalysts are linear **paraffins** and **olefins** (Tropsch and Koch (1929), Koch and Hilberath (1941)). In addition a small amount of non-linear products, consisting of predominantly mono-methyl branched compounds, was described. The olefin fraction typically mainly consists of α - and β -olefins. The large quantity of α -olefins in this fraction (>95 wt%) led to the conclusion that they are the primary products of the FT synthesis (Friedel and Anderson, 1950). Further work in this field by Pichler (Pichler et al. (1964, 1967)) reported an increase in α -olefin content in the product with increasing space velocity. At high residence times the primarily formed α -olefins are hydrogenated to paraffins in secondary reactions. Madon et al. (1995) concluded from their residence time studies that, in addition to n-paraffins and α -olefins, small amounts of cis-2-olefins are also primary FT products. Depending on reaction conditions more than 60 wt% olefins can be present

in the total FT synthesis product (Jager and Espinoza (1995), Dry (1999), Schulz and Claeys (1999b), Steynberg et al. (1999)). In the presence of severe secondary olefin hydrogenation, paraffins can become the dominant product.

Little is known about the formation of **oxygenates** (Kellner and Bell, 1981b). Up to around 10 wt% oxygenates can be found in the total product of commercial FT synthesis processes (Dry, 1999). Oxygenates formation is accounted for in different proposed mechanisms, namely in the enol (see Section 2.1.4, p. 8) and the CO-insertion mechanism (see Section 2.1.4, p. 9). They can be generated in primary and secondary reactions. Hydroformylation can, for example, lead to the formation of oxygenates from olefins during FT synthesis (Pichler and Roelen, 1957).

Branched compounds are also minor products of FT synthesis and can comprise up to 40 wt% of the HTFT process product (Jager, 1997). The majority of these products are mono-methyl branched compounds, mainly 2- and 3-methyl branched (Pichler et al., 1967). The formation of branched products can be explained by primary and secondary reactions (see Section 2.1.4, p. 7). The latter includes incorporation of primarily formed olefins such as propene (Pichler et al. (1967, 1968)).

In the HTFT process significant amounts of **aromatic** products are found (15 wt%, Steynberg et al. (1999)), but it is not known how these products are formed mechanistically.

2.1.3.2 Fischer-Tropsch Product Distributions

The FT reaction is a surface polymerization following the principles of Schulz-Flory kinetics (Schulz (1930), Flory (1936)) in FT synthesis commonly referred to as Anderson-Schulz-Flory (ASF) kinetics, which mathematically expresses the weight content of products of a certain carbon number as a function of carbon number (equation 2.5).

$$\lg \left(\frac{W_N}{N_C} \right) = N_C \cdot \lg(p_g) + \lg \left(\frac{(1 - p_g)}{p_g} \right) \quad (2.5)$$

The chain growth probability, p_g ,

$$p_g = \frac{r_g}{r_g + r_d} \quad (2.6)$$

can be extracted from the slope of the straight line obtained in semi-logarithmic plots of the molar product distribution, where r_g is the rate of chain growth and r_d is the rate of desorption.

However, this ideal case is often not observed in experimental FT data. The methane content, for instance, is often relatively high, particularly when using cobalt, nickel and ruthenium catalysts (Nie (1996), Claeys and van Steen (2002)). The molar C_2 -content can be relatively low, due to incorporation of the very reactive ethene in secondary FT reaction steps (Schulz and Claeys, 1999b). The chain growth probability, p_g , can show apparent chain length dependency, leading to a curved ASF distribution plot with preferred formation of long chain hydrocarbons. This trend has been explained by increased readsorption and incorporation of long chain olefins due to their increased carbon number dependent residence time which is a result of their increased solubility (Schulz and Claeys, 1999b) and/or decreased diffusivity (Iglesia et al., 1993).

Factors, such as synthesis gas ratio, temperature, pressure and residence time, can affect the FT product selectivity (Schulz and Cronjé (1977), Claeys and van Steen (2004)).

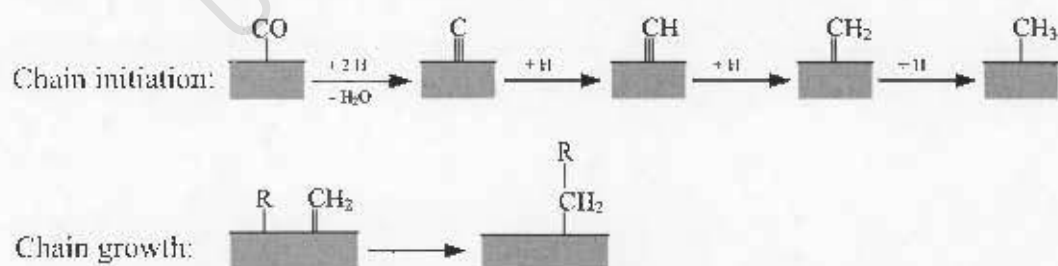
Methane selectivity and chain growth are generally oppositely affected. Methane selectivity increases at higher temperatures and with an increase of the hydrogen to carbon monoxide ratio and shorter residence times. Higher reaction temperatures also favour carbon deposition on the active catalyst. High pressure has a positive effect on chain growth and oxygenate selectivity and leads to smaller amounts of branched products.

2.1.4 Mechanisms in Fischer-Tropsch Synthesis

Different pathways have been suggested as reaction mechanisms for the FT synthesis. Key steps in all of these are a) the generation of the chain starter, b) the chain growth (propagation) and c) the chain growth termination (desorption) steps. The general perception is that not a single, but rather multiple parallel operating reaction pathways may exist in FT synthesis. The four most accepted reaction mechanisms are the "alkyl", the "alkenyl", the "enol" and the "CO-insertion" mechanism (Dry (1981), Anderson (1984), Claeys and van Steen (2004)).

2.1.4.1 Alkyl Mechanism

The alkyl mechanism (Scheme 1) is currently the most accepted one (Claeys and van Steen, 2004). It was developed from the so-called "carbide"-mechanism, which was the first proposed FT reaction mechanism (Fischer and Tropsch (1926), Craxford and Rideal (1939)). The chain initiation entails a dissociative CO-chemisorption to form carbon and oxygen atoms on the metal surface. The surface oxygen reacts either with adsorbed hydrogen to form water or with adsorbed carbon monoxide to form carbon dioxide. In a sequential reaction the surface carbon ("carbide") is hydrogenated to CH, CH₂ and CH₃ hydrocarbon species. The CH₂ species is considered the monomer and the CH₃ is regarded as chain initiator. Chain growth then takes place via incorporation of the monomer into surface alkyl species. The primary termination step includes either β -H elimination to form an olefin or H-addition to form a paraffin. Formation of oxygenates cannot be explained by the alkyl-mechanism, although, Johnson et al. (1991) suggested involvement of surface hydroxyl groups in their generation. The coupling of a surface hydroxyl group with an alkyl group may lead to the formation of alcohols.

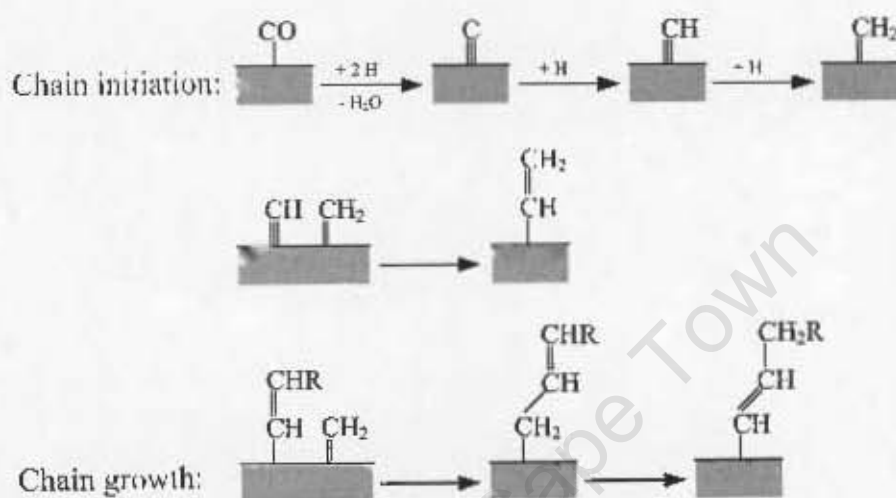


Scheme 1: Alkyl mechanism.

2.1.4.2 Alkenyl Mechanism

Maitlis and co-workers proposed the alkenyl mechanism (Maitlis (1989), Maitlis et al. (1996, 1999)), based on studies on organometallic model systems (see Scheme 2). The first step, the generation of a surface CH_x species, is the same as in the alkyl mechanism

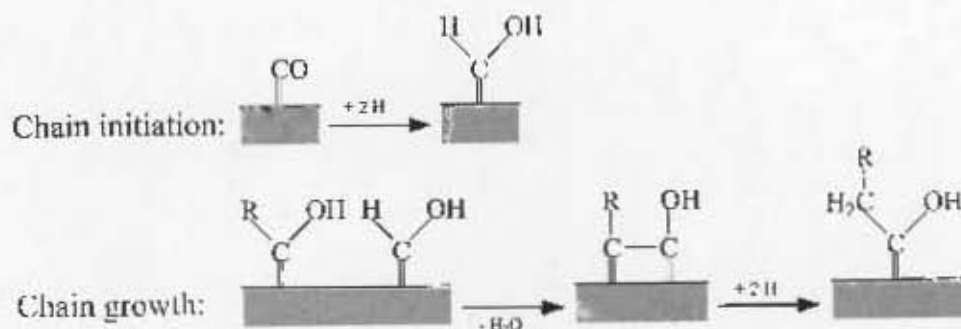
(see above). The surface CH_x species, viz. methyldene (CH) and methylene (CH_2) species, reacts in a first C-C carbon bond formation to form the chain initiator, which is believed to be a vinyl surface species ($\text{CH}=\text{CH}_2$). Chain propagation involves the addition of a methylene species to a surface vinyl species yielding a surface allyl species, followed by isomerisation to a surface alkenyl species. Addition of hydrogen then leads to desorption of the product as an α -olefin. Primary formation of paraffins is not explained by this reaction mechanism.



Scheme 2: Alkenyl mechanism.

2.1.4.3 Enol Mechanism

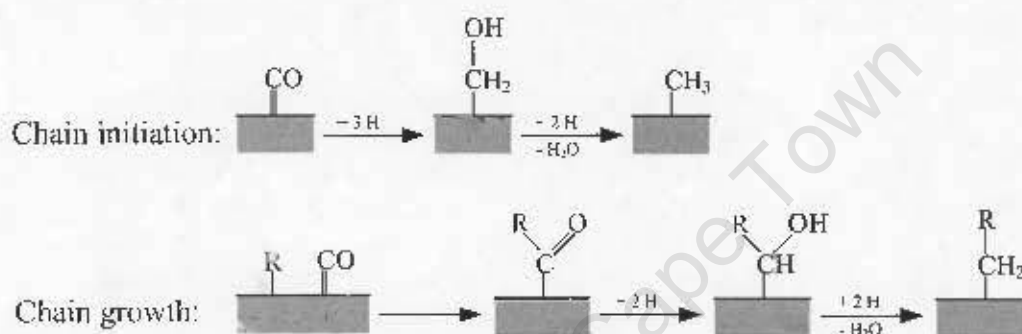
The enol mechanism, proposed by Storch et al. (1951), involves an enol species ($\text{M}=\text{CHOH}$) as the chain initiator. Its generation includes surface H-addition to chemisorbed carbon monoxide on the metal surface. Condensation reactions of two neighbouring enol species result in chain growth. Termination of those species can then yield oxygenates or α -olefins. The formation of *n*-paraffins is described as a secondary reaction by hydrogenation of primarily formed olefins. The primary formation of *n*-paraffins would require an alternative reaction pathway.



Scheme 3: Enol mechanism.

2.1.4.4 CO-Insertion Mechanism

The CO-insertion mechanism is often believed to be the main reaction pathway leading to the formation of oxygenates in FT synthesis (Anderson and Ekerdt (1985), Dry (1990), Hindermann et al. (1993)). It was originally formulated by Sternberg and Wender (1959) and Roginski (1965) and further refined by Pichler and Schulz (1970). In this mechanism chemisorbed carbon monoxide is considered the monomer. Reaction with activated hydrogen leads to the formation of the chain initiator, viz. a surface alkyl species. Chain growth takes place via CO-insertion in a methyl-alkyl bond leading to a surface acyl species. The C-O bond cleavage generates the longer chain surface alkyl species. Desorption of these species can either lead to the formation of α -olefins or n-paraffins, as already proposed in the alkyl-mechanism, or to the formation of aldehydes and alcohols from oxygen containing surface species.



Scheme 4: CO-insertion mechanism.

2.1.5 Different Catalysts for Fischer-Tropsch Synthesis

In principle, all transition metals have the ability to catalyse the FT synthesis; although the most studied ones are cobalt, iron, nickel and ruthenium.

Cobalt and **iron** are the commercially used FT catalysts. Only iron is used in HTFT synthesis whereas both metals are suitable for the LTFT process (see Section 2.1.1, p. 4). Potassium promotion is required in iron based FT to increase activity and improve selectivity. Cobalt does not require chemical promoters, but it is usually supported on a carrier to increase its dispersion and small quantities of noble metals are often added as reduction promoters. Although cobalt is more expensive than iron, it is probably the future FT catalyst of choice due to its "cleaner" performance in terms of its FT product spectrum (less side products) and its potentially longer catalyst lifetime (Schulz, 1999).

In the 1930's efforts were made to prepare commercially useful **nickel** catalysts. However, nickel forms volatile carbonyls, such as the toxic $\text{Ni}(\text{CO})_4$, at higher operating pressures (Shen et al., 1981). Nickel catalysts also often show a tendency for extensive methane formation (Mills and Steffgen, 1973).

Initial investigations using **ruthenium** as catalyst for FT synthesis were done by Pichler and Buffleb (1936). The reaction variables pressure and temperature strongly influenced the hydrocarbon chain length of the product. It was observed that low temperatures and high pressures led to the synthesis of very high molecular weight waxes ($M_{wt} > 100$

000 g/mol). This process is also known as polymethylene synthesis (PMS). At lower pressures ruthenium shows FT product distributions similar to those obtained on cobalt catalysts (Iglesia et al. (1991, 1992), Madon et al. (1993)), however it is often accompanied by a relatively high methane selectivity.

Ruthenium is not only active in water, but also in diluted acids, emphasizing its high activity and low tendency to oxidize (Fischer et al., 1939). Water added during FT synthesis can even decrease methane selectivity and improve chain growth, as reported by Claeys and van Steen (2002).

McKee (1967) and Shultz et al. (1967) showed that amongst the platinum group metals ruthenium is by far the most active catalyst for FT CO-hydrogenation. Several years later Vannice (1975a) showed the same trend for the group VIII metals, to which the commercially used iron and cobalt belong.

Ruthenium catalysts are active over a wide range of operating conditions: temperatures from 100 to 300°C and pressures from 1 to 2000 bar. In contrast to the other tested group VIII metals it can yield high average molecular weight products and the largest C₅₊-fraction (>75 wt%) even at atmospheric conditions (Anderson, 1984).

Ruthenium as a catalyst can be used as a pure metal, without any promoters, thus providing the "simplest catalytic system of FT synthesis" (Schulz, 1999). This means that mechanistic conclusions based on using ruthenium as catalyst should be the simplest. In fact, Okuhara et al. (1985) showed that potassium, a promoter often used in iron catalysed FT synthesis, lowers the reaction rate with this metal. Another advantage of ruthenium is that it does not form any carbides like iron does (Bahr and Jessen, 1933).

However, due to its high costs, when compared to iron or cobalt, ruthenium has never been used as a commercial catalyst in a FT process (Dry, 2002).

2.1.6 Effect of Crystallite Size in Fischer-Tropsch Synthesis

In structure-sensitive reactions catalyst activity and selectivity are dependent on the metal crystallite size of the catalyst. For instance, they can cause a decrease in activity for smaller crystallites.

Early systematic investigations on surface specific activity go back to the 1950's with work done by Boreskov and Karnaukhov (1952), who studied the adsorption of hydrogen and nitrogen on platinum surfaces in platinumized silica gels. Boudart et al. (1966) were the first to look into changes of specific activity with crystallite size for a platinum based hydrogenation of cyclopropene. Several years later this group stated that one must take note of possible effects of metal particle size and metal-support interactions in heterogeneous catalysis reactions (Boudart, 1969).

In ruthenium based FT synthesis, early studies on specific activity were done using Infrared (IR) studies of carbon monoxide chemisorbed on the active ruthenium metal (Blyholder (1964), Lynds (1964), McKee (1967), Kobayashi and Shirasaki (1973), Dalla Betta (1975), Brown and Gonzales (1976), Kellner and Bell (1981a), Fukushima et al. (1985)). Publications by Lynds (1964) stated an occurrence of linear and bridged CO-groups on the metal. This was followed by Kobayashi and Shirasaki (1973), who reported the formation of Ru(CO)₂ and Ru(CO)₃ groups on the metal surface. The first structure-dependency of CO-chemisorption was reported by Dalla Betta (1975). They found a single adsorption band for larger crystallites in IR spectra of ruthenium catalysts pretreated with carbon

monoxide, whereas smaller crystallites showed two different adsorption bands. They explained these findings by the different strengths of the C-O bond at different coordinating sites. On low-coordinating edge and corner sites the CO-adsorption is weaker than that on plane faces. In addition, multiple CO-adsorption occurs on these faces, producing species such as $\text{Ru}(\text{CO})_2$ on the surface. Brown and Gonzales (1976) explained these different adsorption bands with change in metal crystallite size by the incomplete reduction of the smaller crystallites under the operating conditions. Therefore, they proposed that this is not a crystallite size effect.

In the 1970's and 80's various groups worked on ruthenium based FT synthesis, aiming specifically to investigate a possible structure-sensitive behaviour of ruthenium. These studies led to different conclusions.

The first paper by Dalla Betta et al. (1974) described a structure-insensitive initial FT activity of ruthenium on alumina catalysts when varying the ruthenium particle size from <1 to 9 nm. No change in specific catalyst activity and methane selectivity, expressed as turnover numbers^a (TON), was found with different ruthenium crystallite sizes and the apparent activation energy for methanation remained constant with varying crystallite size. Merely a year later, the same group reported that the specific steady-state FT activity on the same catalysts increases with increase in metal crystallite size, thus displaying structure-sensitivity (Dalla Betta et al., 1975). Similar observations were reported by various other groups in the following years.

King (1978) studied the methanation and the C_{2+} -activity for ruthenium catalysts on several different supports. These catalysts were in the crystallite size range between 2.2 and 6.1 nm. They stated that support-interactions could influence the electronic structure of the metal. They also found a decrease in specific activity with smaller metal loadings and proposed that a more intimate contact of the metal on the support occurs in this case.

Kellner and Bell (1982) also reported an increase in FT activity with increasing ruthenium crystallite size supported on alumina. They measured the C_1 - C_{14} production for different carbon monoxide conversions at 1 and 10 bar. The specific activity for methane formation dropped drastically when ruthenium dispersions exceeded 70%, which corresponds to a crystallite size of 1.9 nm. The increase in activity with crystallite size for ruthenium dispersions less than 70% was ascribed to an increase in the number of planar sites on the ruthenium crystallites. The drastic change for ruthenium dispersions of more than 70% was ascribed to changes in the crystallites' electronic properties.

In a study on the FT activity of two highly dispersed alumina supported catalysts by Abrevaya et al. (1990) it was observed that smaller crystallites (2-4 nm) are less active than larger ones (4-6 nm). Due to the higher methane generation on the smaller crystallites, it was stated that smaller crystallites are less effective in promoting the CO-dissociation step, causing an enhancement of other reactions that do not require this step. One of these is the formation of $\text{Ru}(\text{CO})_x$ compounds, that lead to a loss of ruthenium during the reaction due to the formation of volatile ruthenium compounds.

Ragaini et al. (1996) investigated which atoms are most active in FT synthesis, following up on the theory by Boudart (1969) that metal atoms situated on the plane faces of the crystallites can be more active than those on edges and on corners. Their studies on a ruthenium on alumina catalyst (crystallite size range: 0.9-4.8 nm) suggested that

^aThe turnover number, TON, is defined as the number of moles per unit time of a compound converted per number of moles of surface metal atoms.

atoms with a higher number of nearest neighbours in flat faces and edges are more active than those on vertexes and edges at lower numbers of neighbouring atoms. Larger crystallites decompose carbon monoxide more easily than smaller ones, whereas formation of hydrocarbons does not strongly depend on the metal crystallite size. These authors concluded that FT synthesis is structure-sensitive for the initial step, though it is quite structure-insensitive when considered over the whole reaction time.

In contrast to this, Iglesia et al. (1992) described a structure-insensitive FT reaction at conditions that favour the formation of C_{5+} -hydrocarbons. The catalyst systems studied were cobalt and ruthenium on different supports with crystallite sizes ranging between 2.2 and 14.8 nm. They found the activity to be proportional to the number of exposed ruthenium surface atoms, and to be independent of crystallite size or support. This was ascribed to a possibility of a rate-limiting surface step that does not depend on local surface structures. Iglesia (1997a) further stated that cobalt crystallites smaller than 5-6 nm may become inactive for FT synthesis, as they might oxidize in the presence of the product water.

Despite such experimental findings, Baetzold (1973) and Boudart and McDonald (1984) gave mechanistical and quantum mechanical reasons why all group VIII metals are expected to be structure-sensitive in FT synthesis. The structure-sensitivity is based on changes in the atomic surface arrangement at crystallite sizes smaller than 5 nm (van Hardeveld and Hartog, 1969). This change is described as a combination of electronic and structural effects. According to various groups (Boudart and McDonald (1984), Freund et al. (2000), Ciobica and van Santen (2003), Ciobica et al. (2003), Zaera (2004), Mabaso (2005), Barkhuizen et al. (2006), Bezemer et al. (2006), Mabaso et al. (2006)) a minimum amount of adjacent surface metal atoms, defined as "ensembles" or "domains", is required for certain surface reaction steps. A decrease of crystallite size below a specific diameter leads to a significant decrease of these "ensembles" or, in other words, of the "active sites" of the catalyst. Schulz et al. (2002) proposed that the different reactions occurring during FT synthesis might take place on different sites, e.g. chain growth on peak sites and mountain sites of low coordination with several free valences for binding surface species and "ligands", CO-dissociation at hole and valley sites of high coordination, and CO-insertion steps on top sites with low coordination. These sites would start to form on the fresh catalyst during the initial stages of FT synthesis and the composition/distribution would be thermodynamically controlled and dependent on the gas environment (partial pressures of reactants and products).

For the investigation of crystallite size effects it is crucial that the metal crystallites are well-defined; most experimental data described above were generated on catalysts with relatively broad or unknown crystallite size distributions.

The crystallite-size dependency on well-defined rhodium, iron and cobalt model catalysts for FT synthesis was recently shown by Ojeda et al. (2004), Mabaso et al. (Mabaso (2005), Barkhuizen et al. (2006), Mabaso et al. (2006)) and Bezemer et al. (2006). Ojeda et al. (2004) explained this effect by a dependency of the CO-dissociation rate on the density of surface defects, which increases until a certain particle size is reached. This trend has been substantiated by molecular modelling work of van Santen and co-workers (De Koster and Van Santen (1991), Ciobica and van Santen (2003), Ciobica et al. (2003)). It has been proposed that on-top sites are preferred for CO-adsorption on Ru[0001] surfaces of which smaller crystallites have more (Michalk et al., 1983). However, some believe

that product desorption, and not CO-dissociation, is the rate-determining step in FT synthesis (van Steen and Schulz, 1999) and effects of CO-activation could therefore not account for the generally observed lower activity of smaller crystallites. Mabaso (2005) and Bezemer et al. (2006) explained their findings with the “ensemble theory” (see above) and, alternatively, with possible oxidative deactivation of small metal particles - an effect which has been substantiated by theoretical work on the thermodynamic stability of cobalt crystallites of different size in H₂/H₂O atmospheres (van Steen et al., 2005). In both studies selectivity aspects related to metal crystallite size have also been discussed. Smaller crystallites were found to generate more methane and a lower chain growth probability was observed in FT experiments. Furthermore, increased paraffin to olefin ratios were reported for smaller crystallites in the study by Bezemer et al. (2006).

No systematic study on the effect of well-defined and characterised ruthenium crystallites of different size (fresh and spent) on FT activity and selectivity has been reported in the literature yet. Such an investigation therefore forms part of the section of this work which deals with nanometer sized ruthenium crystallites. In addition, temporal changes in the performance of model catalysts during a FT experiment are reported.

2.1.7 Homogeneously Catalysed Fischer-Tropsch Synthesis

Homogeneously catalysed processes have a number of advantages over heterogeneously catalysed ones, including:

- adjustment of selectivity control by, for example, changing ligands
- relatively easy removal of the reaction heat
- sulfur tolerance of homogeneous catalysts^b
- relatively simple reactor construction

A possible disadvantage is the difficulty of separating the catalyst from the products (Anderson (1984)).

Several attempts have been made to develop homogeneously catalysed FT synthesis.

Muetterties (1975) suggested the use of multinuclear metal clusters as catalysts. They stated that these cluster systems are defined as multinuclear approximations of metal surfaces. On these metal cluster systems more carbon monoxide could be coordinated than on metal surfaces. Carbon and oxygen in carbon monoxide could even adsorb on two different adjacent metal atoms, weakening this bond. Hydrogen transfer is then favoured and chain growth can take place. Different ruthenium-carbonyls have been used in homogeneous FT synthesis studies. Generally, homogeneous FT reactions are believed to require severe pressure conditions, usually more severe than those of heterogeneous FT synthesis or the methanol synthesis (Anderson (1984)).

Bradley (1979) tested different organometallic ruthenium complexes, viz. Ru₃(CO)₁₂, H₄Ru₄(CO)₁₂, H₃Ru₄(CO)₁₂⁻ and Ru₆C(CO)₁₆²⁻, dissolved in tetrahydrofuran (THF)

^bSulfur as FT poison is described in Section 2.2.1, p. 15.

at temperatures between 225 and 275°C, and high pressures of 1300 bar. Only the formation of the C₁-oxygenates methanol and methylformiate was detected in this study. By using a more polar solvent, such as acetic acid and N-methyl-pyrrolidone (NMP), additional formation of 1,2-ethylene-glycol was found, principally indicating the ability of these complexes to promote a C-C coupling reaction, but no C-O bond dissociation (Dombek (1980), Keim et al. (1980)). In addition Keim et al. (1980) tested various group VIII metals in an attempt, to develop an activity profile similar to that described in previous work by Vannice (1975b) for heterogeneous FT catalysts (Section 2.1.6, p. 10). They found that rhodium is more active than ruthenium, followed by iridium and cobalt in the polar solvent NMP, whereas cobalt seemed to be the most active catalyst followed by ruthenium and rhodium when using the less polar solvent THF. Following the same trends, oxygenates and glycols were the only products obtained in homogeneously catalysed reactions on other organometallic complexes with other metals (such as iridium, iron, manganese, nickel and osmium) tested at similar reaction conditions (T = 200-225°C, P = 200-3000 bar) (Feder and Rathke (1978), Daroda et al. (1980), Fahey (1981)). The absence of hydrocarbon product species indicates that a C-O bond cleavage might not be preferred upon product desorption on such organometallic clusters. The authors continue to propose that methanol and ethylene glycol are primary products that can form acetic acid, ethanol and higher alcohols and acids in secondary reactions which may include a one-step homologation reaction in which formaldehyde may play a crucial role in analogy to CO-insertion in the well-known "Oxo-synthesis" which was discovered by Roelen (Friedrich et al., 1939).

Hydrocarbons as main products were found in studies by the group of Muetterties in which a Lewis acid was added as co-catalyst to organometallic complexes in CO-hydrogenation at 180°C and 1 bar. The co-catalyst reacted with the catalyst generating reactive intermediates, enhancing C-C bond formation. CO-hydrogenation on Ir₄(CO)₁₂, dissolved in a NaCl-AlCl₃ melt, showed formation of C₁-C₄ linear hydrocarbons as well as the branched products isobutane, neo- and isopentane, C₅ and C₆ methylcycloalkanes, trimethylbutane and dimethylcyclohexane (Wang et al., 1981). Similar products were obtained in CO-hydrogenation on Os₃(CO)₁₂ and BBr₃ (Choi and Muetterties, 1981) at similar reaction conditions (T = 170-180°C, P = 1 bar). Henrici Olivé and Olivé (1979) even reported the formation of alkyl benzenes when using W(CO)₆ and AlCl₃ as catalysts tested at 200°C and 120 bar.

Recent work in this field was focused on immobilization of the organometallic cluster on a support and testing the possible FT activity and selectivity of these model catalysts. Claeys et al. studied different organometallic ruthenium complexes on silica support at 2 bar and 170°C as model catalysts (Claeys et al. (2000a,b)). They found that only ruthenium complexes with a nuclearity of two or higher produced products that have more than one carbon atom. No FT activity was observed on a monoatomic ruthenium-dendrimer, whereas the two different diatomic ruthenium complexes tetracarbonylbis-(5-cyclopentadienyl)-diruthenium and tetracarbonylbis-(pentamethyl-5-cyclopentadienyl)-diruthenium and the triatomic dodecacarbonyl-triruthenium showed FT activity and the formation of C₁-C₅ hydrocarbons. This activity, which was based on the exposed ruthenium atoms, was much lower than that of a conventional heterogeneous FT catalyst and was restricted to the very initial phases of the experiments, indicating the complexes to be relatively unstable. It was uncertain whether the carbon found in the products originated from the synthesis gas or the CO-ligands in the original complexes, in other

words it was uncertain whether a catalytic process indeed took place. It can, however, be assumed that modification of the ligands or clusters of high nuclearity may show improved performance in CO-hydrogenation and such studies may aid to understand the site requirements for different reactions occurring during FT synthesis.

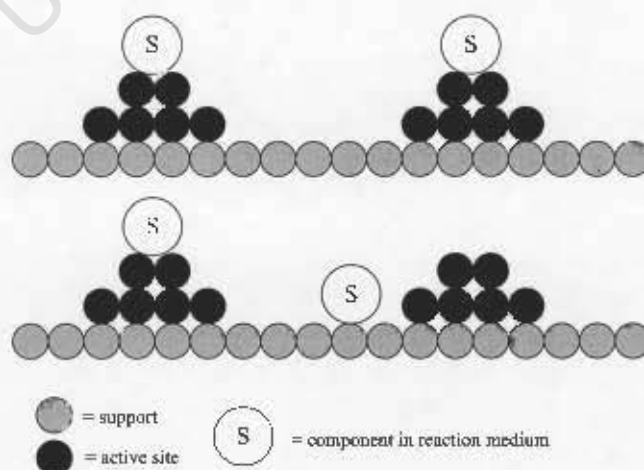
2.2 Catalyst Deactivation

One of the major problems in catalysed reactions is the “deactivation” of the catalyst, which is defined as a loss in catalyst activity as the reaction progresses. Recently, three overview articles regarding deactivation have been published, highlighting the importance of this topic (Forzatti and Lietti (1999), Bartholomew (2001), Moulijn et al. (2001)). There are several mechanisms of catalyst deactivation, which can be classified into five different types:

- poisoning
- fouling
- thermal degradation (sintering, evaporation)
- vapour compound formation accompanied by transport
- vapour-solid and/or solid-solid reactions

2.2.1 Poisoning

Poisoning is defined as deactivation by strong adsorption of, usually, impurities in the feed (Moulijn et al., 2001). Whereas inhibitors are generally weakly and reversibly adsorbed on the catalyst surface, poisons are substances whose interactions with the active sites are very strong and irreversible (Forzatti and Lietti, 1999). There are two different kinds of poisoning, namely selective and non-selective poisoning - as schematically shown in Scheme 5 (Moulijn et al. (2001)). Common poisons and their specific type of metal interactions are listed in Table 2.1.



Scheme 5: Selective (*top*) and non-selective (*bottom*) poisoning in heterogeneous catalysis.

Table 2.1: Overview of common poisons classified by chemical structure (Bartholomew (2001)).

Chemical type	Examples	Type of interaction with metals
Groups 15 and 16	N, P, As, Sb, O, S, Se, Te	Through s- and p-orbitals; shielded structures are less toxic
Group 17	F, Cl, Br, I	Through s- and p-orbitals; formation of volatile halides
Toxic heavy metals and ions	As, Pb, Hg, Bi, Sn, Zn, Cd, Cu, Fe	Occupy d-orbitals; may form alloys
Molecules which adsorb with multiple bonds	CO, NO, HCN, benzene, acetylene, other unsaturated hydrocarbons	Chemisorption through multiple bonds and back bonding

Organic bases and ammonia are typical poisons for acidic catalysts, such as zeolites used in cracking reactions, while ammonia as well as sulfur- and arsenic-containing compounds are typical poisons for metals in hydrogenation, dehydrogenation and steam reforming. Metal containing organic compounds are poisons in catalytic cracking and hydrocracking. Typical FT catalyst poisons are H_2S , COS , NH_3 and metal carbonyls of which sulfur poisoning in particular is the most challenging problem (Bartholomew, 2001). In FT synthesis coal is often the starting compound for the synthesis gas production and, being an organic material, it contains a significant amount of sulfur. Due to this, sulfur poisoning is one of the biggest issues in commercial FT synthesis. Sulfur as FT poison has already been described by Fischer and Tropsch (1926) in the early years of this process. Studies by several groups indicate that sulfur concentrations in the parts per billion range can cause a significant loss in activity and lifetime of the catalyst (Shultz et al. (1962), Dry (1981), Anderson (1984), Bromfield and Coville (1999), Duvenhage and Coville (2006)). Chlorine in the form of $RuCl_3$, used during the synthesis of the catalyst, can also act as FT poison if it is not completely removed in the calcination and reduction steps (Iyagba et al., 1990).

2.2.2 Fouling

Fouling is the physical or mechanical deposition of species from the fluid phase onto the catalyst surface, resulting in a loss of activity due to blockage of sites and/or pores (Bartholomew, 2001).

An important example of fouling is **coking**. Coking, the formation of carbonaceous residue overlayers on the active catalyst surface, is a typical deactivation mechanism for catalytic reactions involving hydrocarbons such as the FT process. Coke deposits may amount to 15 or even 20% of the catalyst surface and therefore the catalyst might also deactivate due to blocking of the catalyst pores (Forzatti and Lietti, 1999). Various mechanisms of coke formation on metal catalysts from carbon monoxide and hydrocarbons are

known. The first step is the formation of a C_α carbon, which is defined as adsorbed atomic carbon. This can react further to a polymeric carbon C_β . The most stable and most difficult to remove form of carbon is graphitic carbon generated from polymeric carbon (Bartholomew, 2001).

2.2.3 Thermal Degradation

Thermal degradation is a physical process leading to catalyst deactivation because of a) loss of catalytic surface area due to crystallite growth of the catalytic phase, b) loss of support area due to support collapse and/or c) loss of catalytic surface area due to pore collapse in crystallites of the active phase.

Sintering is a form of thermal degradation. It is defined as a loss of catalytically active surface due to crystallite growth of either the support material or the active phase (Moulijn et al., 2001). Initially, the atoms may be present as small clusters of atoms or as small metal crystallites. In a sequential process, surface diffusion of the atoms firstly leads to two-dimensional clusters, and at a later stage to three-dimensional particles. These particles can grow into larger ones through several mechanisms. Particles might move and coalesce or atoms may move from one particle to another, either by volatilisation or by surface migration, also known as Ostwald ripening (Datye et al., 2006). The typical sintering mechanisms are schematically shown in Scheme 6 (adapted from Moulijn et al. (2001)).

Sintering processes are strongly temperature dependent (Moulijn et al., 2001). The temperature at which sintering occurs, defined as the Hüttig or Tamman temperatures, is directly related to the melting point of the metal. Atoms located at defects in the crystal structure become more mobile at the Hüttig temperature and atoms from the bulk at the Tamman temperature while atom mobility will be so high at the melting point that liquid-phase behaviour is observed. Equations 2.7 and 2.8 are semi-empirical relations for the calculation of the Hüttig and Tamman temperatures respectively.

$$T_{\text{Hüttig}} = 0.3 \cdot T_{\text{melting}} \quad (2.7)$$

$$T_{\text{Tamman}} = 0.5 \cdot T_{\text{melting}} \quad (2.8)$$

Table 2.2 highlights the Hüttig, Tamman and melting temperatures for metals and support materials relevant to FT synthesis as published by Moulijn et al. (2001).

It must be mentioned that the temperature at which mobility occurs for small particles may be lower than that indicated by $T_{\text{Hüttig}}$ and T_{Tamman} (Moulijn et al., 2001). In contrast to this, small metal clusters are often stabilized on the support by anchoring them via chemical bonds that hinder their movement and therefore minimize effects of sintering.

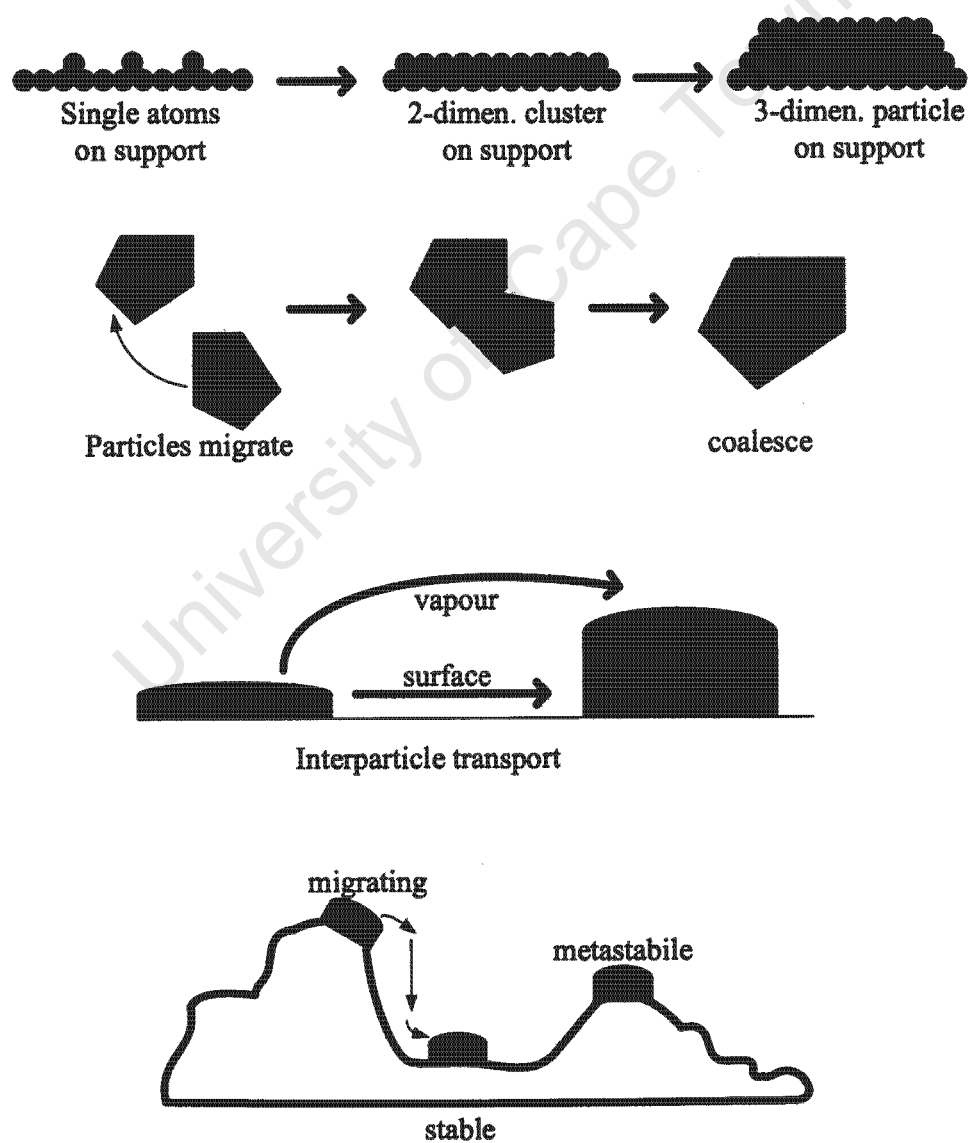
Another problem is that the melting point of some materials is not always well-defined. Some supports may decompose even before $T_{\text{Hüttig}}$ and T_{Tamman} are reached. The choice of support material is crucial as some support materials can start to sinter before the metal crystallites which are deposited on it. Supports which are suitable for typical heterogeneous reaction conditions are often referred to as thermostable supports. Wanke and Flynn (1975) stated that metals can also sinter relatively quickly under an oxidizing atmosphere, whereas the process is slower under reducing or diluted atmospheres.

Table 2.2: T_{melting} , $T_{\text{Hüttig}}$ and T_{Tamman} of metals and supports relevant for the FT synthesis.

Compound	T_{melting} in K	$T_{\text{Hüttig}}$ in K	T_{Tamman} in K
Ru	2723	817	1362
Fe	1808	542	904
Co	1753	526	877
Ni	1725	518	863
Al ₂ O ₃	2318	695	1159
SiO ₂ ^a	1986	596	993
SiO ₂ ^b	1883	565	942

^a Crystobalite

^b Quartz



Scheme 6: Different stages in the formation and growth from single atoms to three-dimensional particles on the support surface (Moulijn et al., 2001).

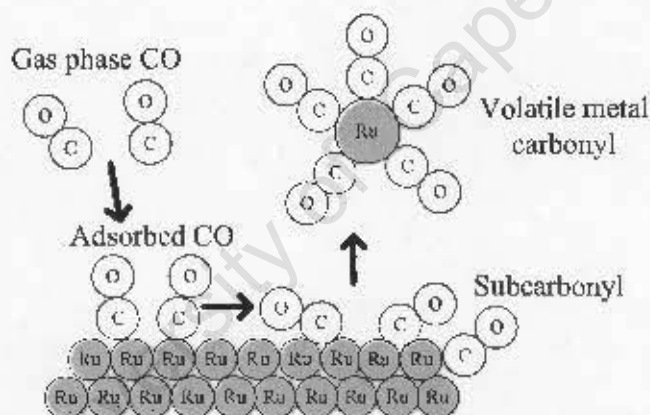
Dry (1981) pointed out that sintering is probably the main reason for FT catalyst deactivation and thus it is of special interest in this study.

2.2.4 Gas-solid and Solid-solid Reactions

In gas-solid and solid-solid reactions the catalyst deactivation can also be caused by a chemical reaction (Bartholomew, 2001).

Metal loss through **gas-solid reactions**, for example via the formation of volatile compounds, e.g. metal carbonyls, can be significant over a wide range of operating conditions, including relatively mild conditions (Bartholomew, 2001).

In ruthenium based FT synthesis there are some documented examples of a loss of the catalytically active metal as volatile compounds, due to reaction with carbon monoxide. Goodwin et al. (1986) reported metal loss of up to 40% due to the formation of volatile ruthenium carbonyls, such as $\text{Ru}(\text{CO})_5$. A schematic drawing of the formation of the volatile $\text{Ru}(\text{CO})_5$ is illustrated in Scheme 7. Similar losses of metal have been reported on nickel catalysts, where metallic nickel reacts to $\text{Ni}(\text{CO})_4$, a toxic, volatile compound (Shen et al., 1981).



Scheme 7: Formation of the volatile ruthenium-pentacarbonyl, $\text{Ru}(\text{CO})_5$, via surface reaction of carbon monoxide with metallic ruthenium.

Solid-solid reactions, including phase changes or reactions of the metal compound with the support, can also cause deactivation. In some cases this can also lead to an increase in catalytic activity. In iron based FT synthesis for instance, it is widely thought that some carbides such as $\text{Fe}_{2.2}\text{C}$, Fe_3C and Fe_7C_3 , which form as the FT reaction progresses, are FT active. Oxides, however, seem to be inactive for FT synthesis (Dry (1981), Anderson (1984)) and iron catalysts are known to deactivate through phase transformation from iron or iron carbide to inactive magnetite, Fe_3O_4 (at high conversions due to the high amount of the FT by-product water). The actual performance of an iron based FT catalyst is therefore often a result of catalyst pretreatment and process conditions. Similar effects may play a role when using cobalt as FT catalyst. Although a thermodynamic analysis on bulk cobalt shows that its oxidation is not feasible under FT conditions (Anderson, 1956), small crystallites of cobalt may be oxidized by the water by-product at FT conditions as proposed by Iglesia (1997b). Recently, a thermodynamic analysis on the oxidation of small cobalt clusters indeed confirmed that crystallites smaller than

4-5 nm may oxidize under typical FT conditions because the thermodynamics of the system is changed by their relatively more significant surface energies compared to the overall energies of the system (van Steen et al., 2005).

2.3 Preparation Methods for Heterogeneous Catalyst Systems

Industrially used metal catalysts consist of one or several active component(s) often deposited on a high surface area support. The main purpose of using a support is to achieve an optimal dispersion of the catalytically active component(s) and to stabilize it (them) (Che et al., 1997).

Commonly, during catalyst preparation immobilization of the metal compound on the support is followed by a calcination and an activation step.

2.3.1 Conventional Preparation Techniques

Apart from ion exchange, there are three major preparation methods for heterogeneous catalysts: impregnation, precipitation and deposition of organometallic compounds on a support material.

2.3.1.1 Impregnation Techniques

In impregnation techniques the catalytically active species are introduced into the pore space of a support material. The support material is chosen based on its desired specification, size and shape. There are two different known methods of impregnation, depending on whether the pore space of the support contains only air or gas at the start or whether it is already filled with the solvent of the impregnation solution. The first method is known as capillary impregnation and the second as diffusional impregnation.

The **capillary impregnation** technique is characterised by its exothermicity. Pressure is built-up inside the support pores resulting in a very fast preparation method. A special capillary impregnation technique is the "incipient wetness impregnation" (Adesina, 1996). This technique is used for supports with low adsorption capacity of the metal precursor (Huang and Schwarz (1987b), Calleja et al. (1991)). In this case, the amount of water used to dissolve the metal salt as catalyst precursor equals the amount of water needed to fill the support pores completely. The catalytically active compound is immediately transported onto the support via capillary-type forces or by diffusional effects.

The **diffusional impregnation** technique is neither exothermic nor fast (Che et al., 1997). In this technique, the pore space of the support is filled with the solvent used in the impregnation solution and it is therefore also known as "dipping" or "wet-soaking" impregnation (Adesina, 1996). The driving force is always the concentration gradient between the extra-granular solution and the advancement front of the soluble precursor in the intra-granular solution (Che et al., 1997). This technique is virtually never used for preparing catalysts where there is no appreciable interaction between the precursor and the support (as described by Huang and Schwarz (1987a)).

It is generally not easy to prepare catalysts with high metal loadings using impregnation techniques, and therefore multiple impregnation steps are often necessary. More impor-

2.3. PREPARATION METHODS FOR HETEROGENEOUS CATALYST SYSTEMS

tantly, the resulting crystallite size distributions on the support are often relatively wide and catalysts prepared in this manner are normally not well-suited as well-defined model catalysts or as catalysts with well-defined metal crystallites on the support surface (Dry (1981), Anderson (1984), Adesina (1996)).

2.3.1.2 Precipitation Techniques

In precipitation techniques, the precursors of the active metals are dissolved in a solvent such as water and then precipitated onto the support (Geus and van Dillen, 1997). This precipitation step can be forced by changing the pH value of the solution, causing the formation of less soluble salts from the precursor. The pH adjustment can either be done in the presence of a support material or the support material can be formed via co-precipitation. In the co-precipitation method, the support material is formed via a simultaneous precipitation with the corresponding precursor or metal salt. The advantage when compared to impregnation techniques is that the obtained composition on the support is much more homogeneous (Dry (1981), Anderson (1984)). Reuel and Bartholomew (1984), for instance, showed that cobalt catalysts prepared via precipitation can form much smaller metal crystallites on the support than in impregnation techniques. It is also possible to prepare catalysts with a high metal loading on the support in only one single preparation step. Crystallite size distributions obtained using precipitation techniques are typically much narrower than those obtained using impregnation. It is, however, not easy to adjust the average crystallite size, which is a crucial requirement for preparation of model type catalysts with varied average crystallite size as required in this work.

2.3.1.3 Synthesis from Organometallic Compounds

Literature suggests two different methods to synthesise supported organometallic compounds: a) the deposition of metal via decomposition of organometallic compounds in order to produce uniform metal crystallites and b) the deposition of organometallic complexes on the support and use their as such (Adesina, 1996).

To give examples, the deposition of metallic iron using iron carbonyl complexes and its use as model catalyst for CO-hydrogenation was reported by Johnston et al. (1999). The organometallic iron complexes were dissolved in THF and impregnated onto an alumina support, followed by reduction in hydrogen, generating well-defined metal crystallites on the alumina support. Similarly $\text{Ru}_3(\text{CO})_{12}$ and $\text{Ru}_6\text{C}(\text{CO})_{17}$ were used as catalyst precursors and the reduced catalysts were used for FT synthesis, creating well-dispersed model systems (Kuznetsov and Bell (1980), Kellner and Bell (1982), Okuhara et al. (1985)).

The preparation of unreduced organometallic ruthenium complexes on a silica support was studied by Claeys et al. (2000a,b). These model systems were tested for FT activity under moderate reaction conditions of 170°C and 2 bar in a fixed-bed reactor (results see above in Section 2.1.7 on p. 14). The interactions of adsorbed $\text{Ru}_3(\text{CO})_{12}$ on an alumina support was extensively studied by the Zeccina group (Guglielminotti and Zecchina (1982), Zecchina and Guglielminotti (1982)) They reported that, in the absence of oxygen, the surface hydroxyl groups act as oxidizing agents, leading to a variety of oxidized ruthenium species. The original triatomic framework of $\text{Ru}_3(\text{CO})_{12}$ remains, while true

bonds form between the ruthenium and the support. Asakura et al. (1985) identified these surface species by Extended X-ray Adsorption Fine Structure (EXAFS) analysis.

2.3.2 Microemulsion Technique

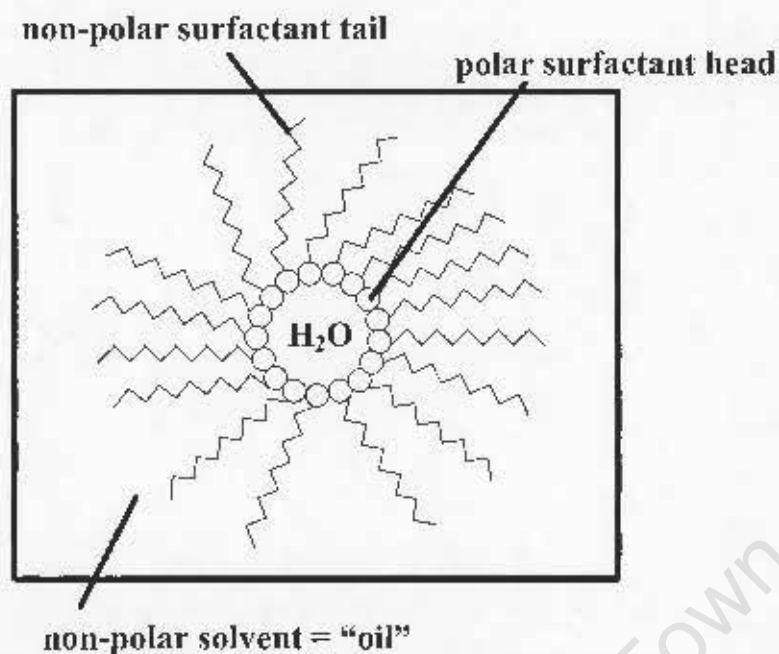
The term microemulsion was coined by Schulman and Friend (1949). Decades later the idea of using these microemulsion systems for catalyst preparation was suggested by Gault in collaboration with Friberg (Eriksson et al., 2004). Boutonnet et al. (1982) reported the preparation of metal nano-particles with this novel technique. In comparison to the conventional preparation methods, this technique allows the preparation of well-defined small metal nano-particles, due to the specific structure of the microemulsion (Boutonnet et al. (1982, 1987), Eriksson et al. (2004)). Importantly, the size of the resulting crystallites can be varied by changing the composition of the microemulsion and other preparation parameters.

2.3.2.1 Definition of a Microemulsion

Microemulsions are optically isotropic and thermodynamically stable systems consisting of a polar solvent, a non-polar solvent and an amphiphilic surfactant. The surfactants are molecules with a polar head and a non-polar tail. Three classes of surfactants are known, namely ionic, non-ionic and amphoteric. The polar head of the surfactant is hydrophilic and interacts with the water phase, whereas its non-polar tail is hydrophobic and it therefore interacts with the non-polar oil phase (see Scheme 8). The most commonly used surfactants in the microemulsion preparation are sodium bis-(2-ethylhexyl)-sulfosuccinate (AOT), sodium dodecyl sulphate (SDS) and cetyl trimethyl ammonium bromide (CTAB). These ionic surfactants contain sodium and sulfur, which, depending on its use, can have negative effects on the resulting catalyst. An alternative path with non-ionic surfactants, e.g. penta-ethyleneglycol-dodecylether (PEGDE), is thus often used instead. Sometimes co-surfactants, such as primary alcohols, are added to modify the rigidity of the micelle core, thus allowing for modification of transport processes through the core (Stenius et al. (1984), Boutonnet et al. (1987), Targos (1987), Pileni (1993)).

The stability of a "micelle" or reverse micelle is determined by the ratios of its constituents. At a high water concentration, the internal structure of the microemulsion consists of small oil droplets in a continuous water phase (see Figure 2.1). This system is called a "micelle" or "normal micelle". The oil core is stabilized with the non-polar tail of the surfactant in the oil phase. However, with increased oil concentration a bicontinuous phase without any clearly defined shape is formed. At high oil concentrations, this bicontinuous phase is transformed into a structure of small water droplets in a continuous oil phase. These systems are now called "reverse micelles". Here the water core is surrounded by the polar headed groups of the surfactant (see Scheme 8).

These systems are very sensitive with respect to temperature, particularly in the case of non-ionic surfactants. At higher temperatures the oil droplets will be destroyed, while the water droplets will be destroyed by a temperature decrease. Outside of the "micelle" and "reverse micelle" area, a two-phase system exists (Eriksson et al., 2004).



Scheme 8: Schematic diagram of a "reverse micelle" system.

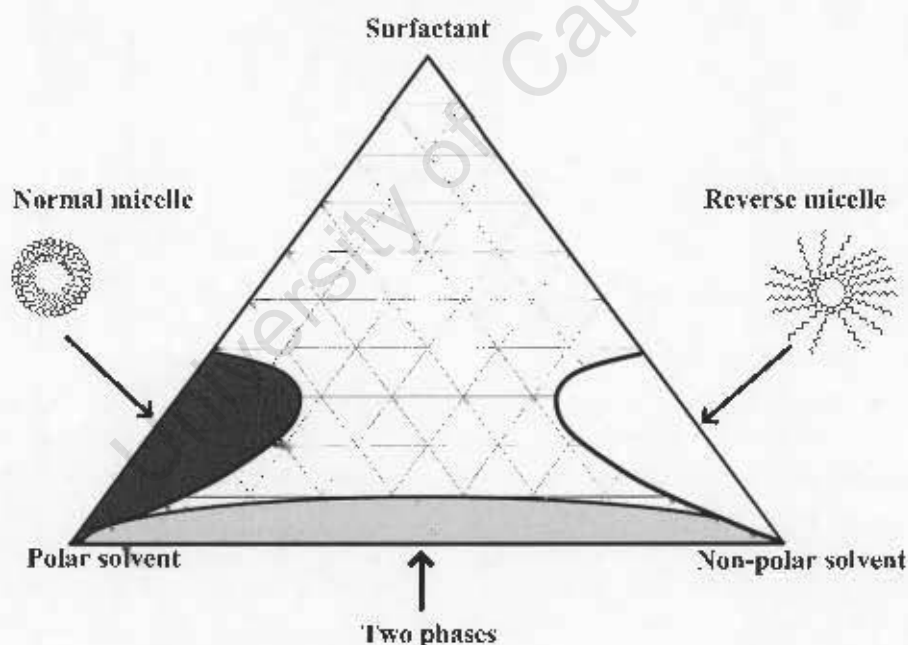


Figure 2.1: Schematic ternary-phase diagram of surfactant-oil-water system (Mahaso (2005)).

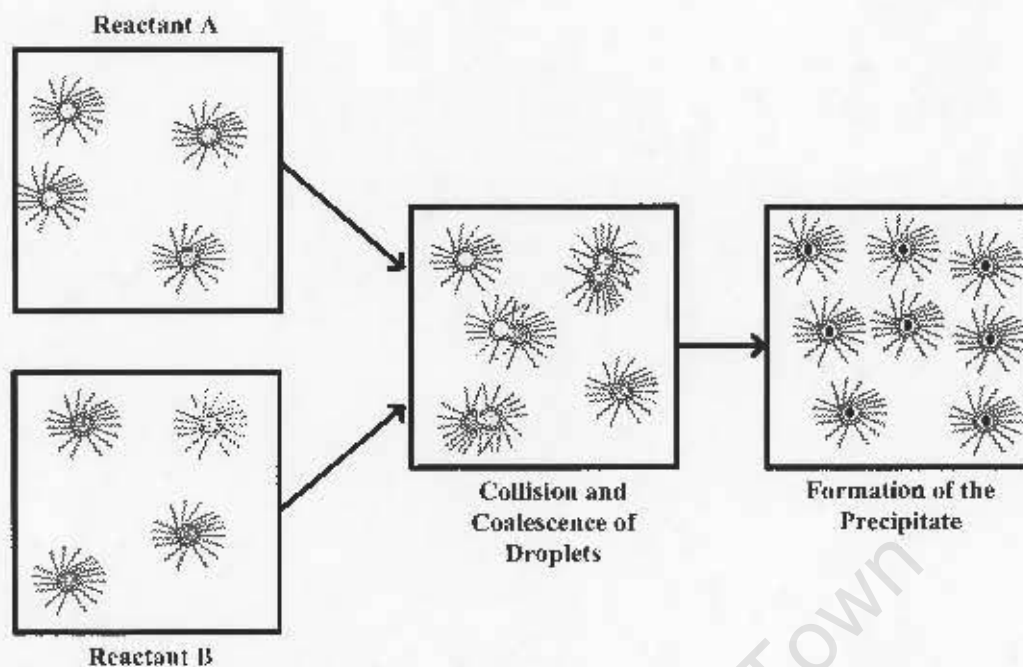
2.3.2.2 Preparation of Nano-particles

The dissolved reverse micelles have the uniform internal diameter of the nanometer sized water droplets. This makes them ideally suited for the preparation of well-defined and highly dispersed nano-particles. Water soluble metal salts can be incorporated into the aqueous phase of the reverse micelle, which is "dissolved" in the organic phase via the surfactant.

There are different ways in which the nano-particle preparation can occur inside the reverse micelles. The more common one is the precipitation of the precursor, often a metal salt, in the reverse micelles and the impregnation of it onto a support in a second step. This preparation of the nano-particle inside a reverse micelle can occur by mixing of two reverse micelle solutions with each other, one containing the precursor (Reactant A) and the other the precipitating agent (Reactant B). By adding and mixing these two microemulsions, the reactants A and B come in contact with each other, due to collision and coalescence of the droplets, and form the precipitate AB. This precipitate is confined to the interior of the microemulsion droplets and the size and shape of the particle formed reflects the interior of the droplet. This process is schematically shown in Scheme 9 (Pillai et al. (1995), Eriksson et al. (2004)). Another way is the direct addition of a precipitating or a reducing agent to the reverse micelle solution containing the metal precursor. Here the synthesis of nano-particles is based on the principle of confining the precipitation or reduction of the precursor to the water droplets of these reverse micelles (Pileni (1993), Pillai et al. (1995)). Common agents are hydrogen or weak bases such as hydrazine (Eriksson et al., 2004) or $(\text{NH}_4)_2\text{CO}_3$ (Mabaso, 2005).

In both methods the reverse micelles behave as microreactors. The size of the precipitated nano-particles is dependent on the size of the water droplet in the reverse micelles (Pileni (1993), Mabaso (2005)). By decreasing the water to surfactant ratio, for example, the generation of smaller reverse micelles is expected and *vice versa*. The homogeneous size of the reverse micelles in the oil phase at a certain mixing concentration will lead to the formation of well-defined nano-particles. The reverse micelle structure therefore provides a reaction template in the appropriate size range. The droplets are defined by the Brownian motion and collide continuously, leading to the formation of short-lived dimers and to the exchange of the aqueous contents in the micelles (see Scheme 9). The crystallite size can be influenced by different parameters, such as reaction time, chemical nature of the precursors and constituents of the micelle system. Also, similar to other preparation techniques, the drying or calcination temperature can play an important role (Boutonnet et al. (1982), Stenius et al. (1984), Boutonnet et al. (1987), Pileni (1993), Pillai et al. (1995), Song and Kang (2000)). At optimized conditions high purity nanosized crystallites can be produced.

Particularly in the field of catalysis, the use of the reverse micelle technique to prepare supported nano-particles is important. Kishida et al. (1996) and Hayashi et al. (2002) prepared supported nano-particles by *in-situ* formation of the support in the reverse micelle solution by precipitation of a support precursor. This can, however, lead to undesired encapsulation of metal crystallites by support material. Another possibility is combining the nano-particle precipitate and the support material while the reverse micelle systems are still intact followed by breakage of the reverse micelles, causing the nano-particles to settle onto the support. This technique was described by Mabaso (2005) for iron particles. However, a problem with this technique is that some of the nano-particles are not taken up by the support and the anticipated loadings is sometimes not achieved. The preparation of supported nano-particles without the precipitation of the metal salt is also possible. In this case the support is added to the metal precursor in the reverse micelle solution. By interionic interaction the support takes up the metal salt inside the reverse micelles followed up by micelle break up. This method has been described by various groups (Stenius et al. (1984), Abrevaya (1990), Abrevaya et al. (1990), Eriksson et al. (2004)).



Scheme 9: Schematic representation of the synthesis of nano-particles in microemulsions using two microemulsions.

Generally, little work has been done using reverse micelle derived model catalysts to study the effect of crystallite size in catalysis, particularly in FT synthesis. Ojeda et al. (2004) did work on rhodium catalysts and Mabaso (2005) on iron catalysts, both varying the metal crystallite sizes from 2 to 20 nm. With ruthenium as metal only the preparation and catalytic tests of crystallites with 4 and 6 nm has been reported in a patent by Abrevaya (1990).

University of Cape Town

Chapter 3

Scope of the Thesis

Although ruthenium is known to be the most active catalyst for FT synthesis it has never been used commercially due to its high costs compared to iron and cobalt. For optimum performance it is important to achieve maximum metal utilisation, particularly when expensive metals like ruthenium are used. In principal, the smaller the metal crystallites in a catalyst are, the more metal atoms are present on the surface and therefore available to catalyse the FT reaction. However, recent work published on well-defined model catalysts of supported cobalt, iron and rhodium (Ojeda et al. (2004), Mabaso (2005), Barkhuizen et al. (2006), Bezemer et al. (2006), Mabaso et al. (2006)), showed that crystallites smaller than a certain size in the nanometer range ("critical diameter") display lower metal surface area specific activity, expressed as turnover frequency, and inferior FT product selectivity with high methane selectivity. Similar studies are available for ruthenium based FT synthesis, but the catalysts used in these studies were generally poorly characterised and crystallite size distributions were not reported. These observed effects might be due to structure-sensitivity of the FT synthesis on these metals. There have also been several attempts to investigate the possibility to conduct a homogeneously catalysed FT synthesis using organometallic compounds. Such studies can be considered as extreme cases of metal dispersion with all metal atoms exposed to the reactants.

Experimental and theoretical methodologies are used in this work.

The experimental approach aims to compare/bridge the activities and selectivities obtained in FT tests on a series of supported organometallic ruthenium compounds with varied nuclearity (two to six) and supported ruthenium crystallites of different well-defined size. The challenges are the preparation, characterisation and FT application of these model-type well-defined catalysts.

The first task focuses on preparation of well-defined supported nano-sized crystallites referred to as "heterogeneous" catalyst systems. The preparation method chosen is the reverse micelle technique, as described by Abrevaya (1990), which has to be modified to increase the range of prepared crystallite sizes. All prepared samples, fresh and spent, will be fully characterised using standard catalyst characterisation methods such as Temperature Programmed Reduction (TPR), Transmission Electron Microscopy (TEM), X-ray Diffraction Spectroscopy (XRD) and CO-chemisorption. Organometallic clusters of different nuclearity are to be prepared and impregnated onto the same support material as to be used above. This approach will lead to model catalysts with metal frameworks in the Ångström range, referred to as "heterogenized homogeneous" catalyst systems.

FT performance of all model systems will be tested with particular emphasis on FT activity and selectivity as function of metal crystallite or cluster size respectively. Additional focus will be on temporal changes of product formation. The integrity of the model catalyst system has to be investigated by characterisation of the spent catalysts. As most of the above tests are to be conducted at relatively mild reaction conditions in order to avoid rapid decomposition of model clusters as well as to force back effects of crystallite sintering, some experiments with the "heterogeneous" catalyst systems are to be performed at more realistic FT conditions.

In addition to this experimental approach, theoretical work using molecular modelling calculations will be conducted to investigate the minimum number of adjacent ruthenium atoms which are theoretically required for the FT reaction to take place. These calculations should be done on intermediates proposed in the monoatomic and diatomic reaction mechanisms, including only elementary reaction steps with intermediates known from the literature.

The combination of the experimental and theoretical work will give important insight into the effect of ruthenium metal crystallite/cluster sizes in the FT reaction and possibly the site requirements for different reactions occurring during FT synthesis. The advantage of using ruthenium rather than iron or cobalt, apart from its high activity, is the relative stability of the organometallic complexes and the simplicity of the product spectra, making it easier to interpret the trends in activity and selectivity when varying the metal crystallite size or the cluster nuclearity.

Chapter 4

Experimental Methodology

4.1 Catalyst Preparation

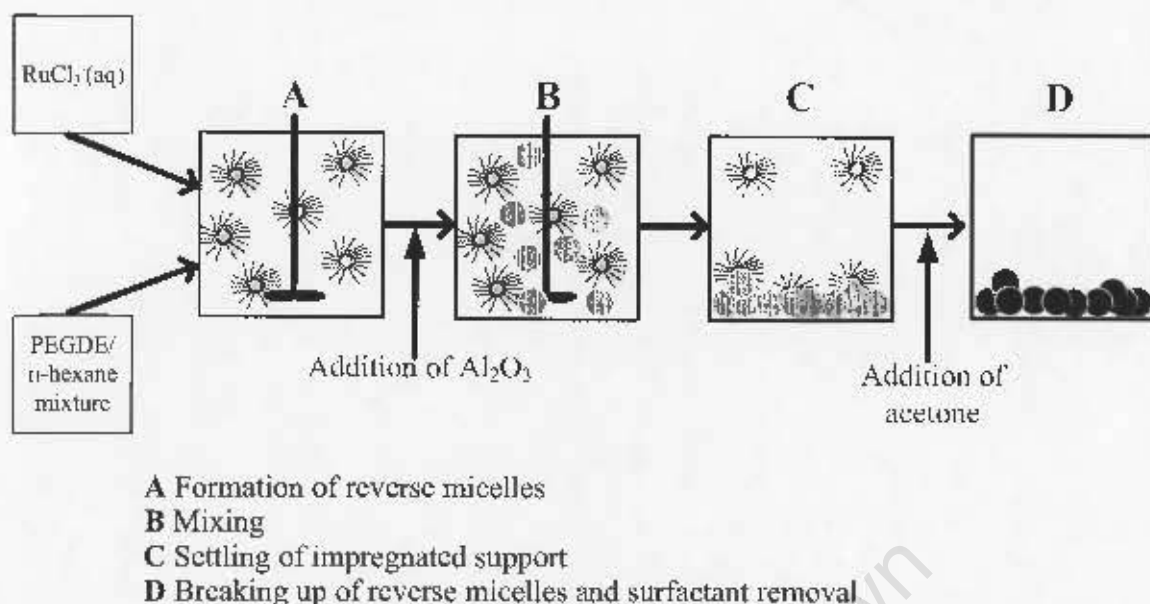
A broad spectrum of model catalysts with average ruthenium crystallite sizes in the nanometer range to ruthenium clusters in the Ångström range has been prepared as described below.

4.1.1 Supported Nano-sized Crystallites

Supported ruthenium on alumina model catalysts with narrow crystallite size distributions in the nanometer range were prepared by means of the reverse micelle technique (see Section 2.3.2, p. 23).

Penta-ethyleneglycol-dodecylether (PEGDE) was used as the surfactant in the reverse micelle system in this work and n-hexane as the organic phase. Both components were mixed in an Erlenmeyer flask and left overnight. The mixture was then filtered to remove any particulates or cloudiness that might be present and an aqueous ruthenium chloride solution was added, followed by stirring for two hours at room temperature. The mixture was then left overnight to generate and stabilize the reverse micelles. The alumina support (Puralox, see Appendix A.1, p. 154) was added while stirring the mixture (overhead stirrer: 800 rpm), resulting in an immediate uptake of the ruthenium salt onto the support surface, which was directly visible from a discolouration of the dark-brown micelle system. After 60 minutes the suspension was decanted and the solid was washed several times with acetone. In this step, any residual PEGDE was removed and the reverse micelle systems were broken up. The process of catalyst preparation using this method is schematically depicted in Scheme 10. The solid was dried in a rotary drier at 60°C and 300 mbar for an hour and at 50 mbar for an additional hour. Calcination in air in a fluidized-bed reactor (16 hrs, $T = 300^{\circ}\text{C}$, heating rate of $2^{\circ}\text{C}/\text{min}$, $\dot{V}(\text{Air}) = 30 \text{ ml}(\text{STP})/\text{min}$, $\text{GHSV}(\text{Air}) = 6 \text{ ml}(\text{STP})/(\text{min}\cdot\text{g})$) followed immediately. During calcination, the ruthenium salt on the alumina was transformed into ruthenium dioxide.

The stability region of the reverse micelle system used, as established by Targos (1987) and Mabaso (2005) via titration at room temperature, is shown in a ternary phase diagram in Figure 4.1. It shows the composition of the reverse micelle systems which were used in this work to prepare the different model catalysts. Table 4.1 lists compositions of the reverse micelle systems used as well as the ruthenium chloride concentrations in the aqueous



Scheme 10: Schematic representation of the preparation of ruthenium nano-particles by means of the reverse micelle technique.

phase. The catalysts were numbered according to their post-calcination crystallite sizes, i.e. the smallest crystallite size was numbered RM-1 and the largest RM-13. The sizes of the resulting supported crystallites were varied by changing preparation conditions such as the composition of the reverse micelle system and the ruthenium chloride concentration in the aqueous phase. In the preparation of model catalysts RM-5 to RM-10 and RM-12 and RM-13, the metal salt concentration in the aqueous phase was kept at a constant value of 0.34 g/g while the surfactant to n-hexane ratio was varied. In experiments RM-1 and RM-2, the metal salt to water ratio was changed, keeping the composition of the reverse micelle system constant. RM-11 and RM-12 also vary only in the metal salt concentration in the aqueous phase. The preparation of RM-10 and RM-13 included the same reverse micelle composition, but RM-13 was calcined at a higher temperature (400°C) than RM-10 to encourage sintering to larger crystallites.

4.1.2 Supported Organometallic Compounds

Organometallic complexes were used to generate model catalyst systems with Ångström-sized metal clusters as model systems for very small ruthenium crystallites. Organometallic complexes with different nuclearity varying from two to six ruthenium atoms were synthesised. A monoatomic compound was not included because it has been shown that these do not appear to be active for FT synthesis (Claeys et al., 2000a). The ligands only contained carbon, hydrogen and oxygen atoms with the CO-ligands dominating. Three diatomic complexes were prepared with different ligands in order to affect the catalyst stability and possible catalyst FT performance. Figure 4.2 depicts the structures of all the synthesised organometallic compounds. These organometallic clusters were deposited on an alumina support analogously to the nanometer sized crystallites (see below on p. 37).

The following Section describes the synthesis of the different organometallic compounds and their immobilization on the support material.

Table 4.1: Amounts of RuCl_3 , H_2O , PEGDE and n-hexane for preparation of different alumina supported nano-sized crystallites.

Sample code	m_{RuCl_3} in g	$m_{\text{H}_2\text{O}}$ in g	m_{PEGDE} in g	$m_{\text{n-hexane}}$ in g	$m_{\text{Al}_2\text{O}_3}$ in g
RM-1	0.3	3.8	42.7	497.8	5.0
RM-2	0.3	1.0	10.7	124.4	5.0
RM-3	0.3	7.1	17.8	124.4	5.0
RM-4	0.3	8.9	22.2	124.4	5.0
RM-5	0.3	1.0	10.0	48.0	5.0
RM-6	0.3	1.0	40.0	98.1	5.0
RM-7	0.3	1.0	10.7	48.0	5.0
RM-8	0.3	1.0	10.7	88.9	5.0
RM-9	0.3	1.0	9.2	48.0	5.0
RM-10	0.3	1.0	7.6	47.4	5.0
RM-11	0.4	1.0	11.1	48.0	6.3
RM-12	0.3	1.0	11.1	48.0	5.0
RM-13 ^a	0.3	1.0	7.6	47.4	5.0

^a calcination temperature: 400°C

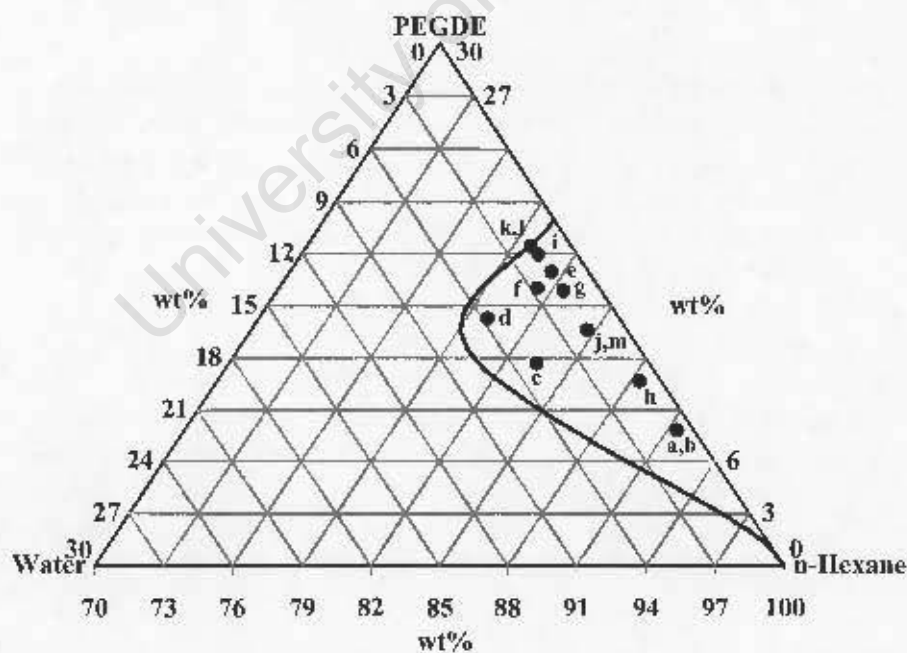


Figure 4.1: Ternary-phase diagram of water-PEGDE-n-hexane reverse micelle system indicating the stability region for the reverse micelles (as established by Mabaso (2005)) and the composition of the reverse micelle systems RM-1 to RM-13 used in this work. (Alphabetic codes correspond to the following catalysts: a: RM-1; b: RM-2; c: RM-3; d: RM-4; e: RM-5; f: RM-6; g: RM-7; h: RM-8; i: RM-9; j: RM-10; k: RM-11; l: RM-12; m: RM-13)

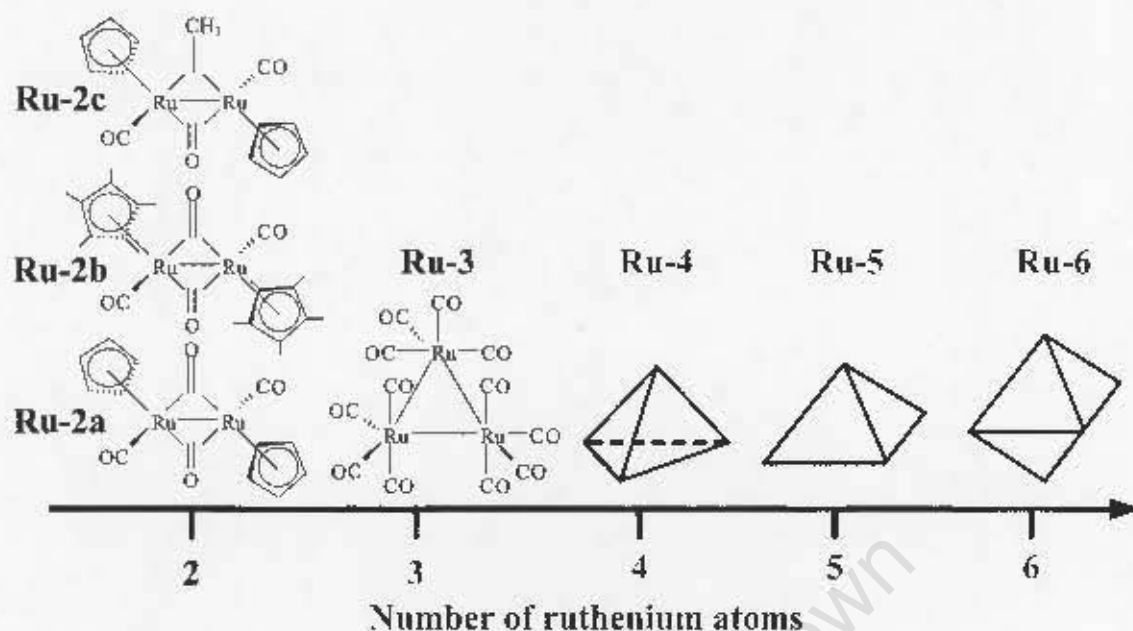
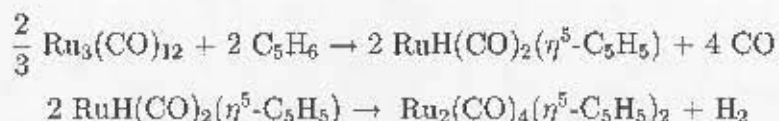


Figure 4.2: Structures of the different prepared organometallic compounds varying the number of ruthenium atoms from two to six. (Note: Chemical structures of Ru-4, Ru-5 and Ru-6 are shown below.)

4.1.2.1 Synthesis of Tetracarbonylbis(η^5 -cyclopentadienyl)-diruthenium $\text{Ru}_2(\text{CO})_4(\eta^5\text{-C}_5\text{H}_5)_2$

Firstly, dicyclopentadiene was cracked over iron filings in a nitrogen atmosphere at 140°C (Doherty et al., 1990). The cyclopentadiene fraction appeared as a colourless liquid at 43°C . A three neck flask with reflux condenser and magnetic stirring bar was filled with the liquid under a nitrogen atmosphere. Dry, deoxygenated n-heptane (175 ml) was added to a mixture of 8.75 g of the freshly distilled cyclopentadiene (132.5 mmol) and $\text{Ru}_3(\text{CO})_{12}$ (4.25 g, 6.5 mmol, for synthesis of $\text{Ru}_3(\text{CO})_{12}$ see below). The mixture was refluxed for one hour. Monitoring the reaction by *in-situ* Infrared^a (IR) showed the formation of $[\text{RuH}(\text{CO})_2(\eta^5\text{-C}_5\text{H}_5)]$. After complete disappearance of the $\text{Ru}_3(\text{CO})_{12}$ bands in the IR spectrum, the stopper was removed and the solvent volume was reduced to 25 ml. The brown-orange product started to precipitate. An additional 150 ml of n-heptane was added, the stopper put back in again and the solution refluxed for an additional 1.5 hours. The mixture was cooled down to room temperature and the product gradually precipitated. The solid was then filtered off, washed three times with n-hexane and dried *in vacuo* for several hours. The overall yield was 80% (Lit. 90-95% (Doherty et al., 1990)).



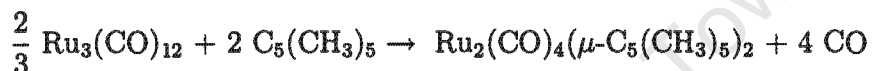
The IR spectrum in CH_2Cl_2 showed bands at 2001 (s), 1966 (s), 1933 (m), and 1769 (s) cm^{-1} ,

^aThis technique is described in Section 4.4.1, p. 37.

indicating the formation of tetracarbonylbis(η^5 -cyclopentadienyl)-diruthenium (Lit.: 2003 (s), 1966 (s), 1934 (m), 1771 (s) cm^{-1} (Doherty et al., 1990)) and Figure 4.2 shows its structure (Ru-2a).

4.1.2.2 Synthesis of Tetracarbonylbis(η^5 -pentamethyl-cyclopentadienyl)-diruthenium $\text{Ru}_2(\text{CO})_4(\eta^5\text{-C}_5(\text{CH}_3)_5)_2$

Following the method of King et al. (1979), nitrogen was bubbled through the solvent n-decane for 10 minutes. $\text{Ru}_3(\text{CO})_{12}$ (1.28 g, 2 mmol) and an excess of pentamethyl-cyclopentadiene was added to the deoxidized n-decane (40 ml) in a three neck flask with a reflux condenser. The mixture was stirred for 10 minutes before heating and refluxing for an additional three hours. During reflux, $\text{Ru}_3(\text{CO})_{12}$ dissolved gradually and red-orange crystals precipitated from the solution. The progress of the reaction was monitored with *in-situ* IR spectroscopy. The crystallites were isolated from the solution by filtration, washed with n-hexane and dried *in vacuo* for two hours, yielding 65% of the desired product (Lit. 70% (King et al., 1979)).



The IR spectrum in CH_2Cl_2 showed bands at 1926 (s) and 1746 (s) cm^{-1} , indicating the formation of $\text{Ru}(\text{CO})_4(\eta^5\text{-C}_5(\text{CH}_3)_5)_2$ (Lit.: 1925 (s), 1744 (s) cm^{-1} (King et al., 1979)). The structure of $\text{Ru}(\text{CO})_4(\eta^5\text{-C}_5(\text{CH}_3)_5)_2$ is depicted in Figure 4.2 (Ru-2b).

4.1.2.3 Synthesis of μ -Carbonyl- μ -ethenylidene-bis[carbonyl-(η -cyclopentadienyl)ruthenium] $\text{Ru}_2(\text{CO})_2(\mu\text{-CO})(\mu\text{-CHCH}_3)(\eta^5\text{-C}_5\text{H}_5)_2$

Tetracarbonylbis(η^5 -cyclopentadienyl)-diruthenium (1.00 g, 2.25 mmol) was added to 40 ml of dry, deoxygenated THF in a Schlenk flask with stopper, nitrogen by-pass and magnetic stirring bar (Doherty and Knox (1990)). After addition of 2.3 ml halide-free methyllithium in diethyl ether (1 M solution), the mixture was stirred for one hour at room temperature. The flask was cooled down to -78°C using a mixture of acetone and liquid nitrogen, and an excess of $\text{H}[\text{BF}_4] \cdot \text{OEt}_2$ was added and stirred for 30 minutes at this temperature. An excess of $\text{Na}[\text{BH}_4]$ was added and the mixture was warmed up to room temperature over a period of 30 minutes. Solvent evaporation in a rotary drier followed. The residue was dissolved in a 100 ml of CH_2Cl_2 and extracted over an alumina column. Thin layer chromatography in a 1:1 mixture of CH_2Cl_2 and n-hexane showed the product fraction as a single yellow band. The yield was 80% (Lit. 89% (Doherty and Knox, 1990)).



The IR spectrum in CH_2Cl_2 showed bands at 1973 (s), 1933 (m) and 1776 (m) cm^{-1} (Lit.:

1974 (s), 1933 (m), 1776 (m) cm^{-1} (Doherty and Knox, 1990)). The $^1\text{H-NMR}$ spectrum^b in CDCl_3 showed a mixture of the trans- and cis-isomer. The resonances for the trans-isomer were at $\delta = 3.16$ (d, $J = 7$ Hz, $\mu\text{-CHMe}$), 5.18 (s, C_5H_5), 5.24 (s, C_5H_5) and 10.14 (q, $J = 7$ Hz, $\mu\text{-CHMe}$) and for the cis-isomer at $\delta = 3.04$ (d, $J = 7$ Hz, $\mu\text{-CHMe}$), 5.18 (s, $2\text{C}_5\text{H}_5$) and 10.94 (q, $J = 7$ Hz, $\mu\text{-CHMe}$), which are in good agreement with literature data (Doherty and Knox, 1990).

The chemical structure of this compound with its bridging CO and CHCH_3 ligands is shown in Figure 4.2 (Ru-2c).

4.1.2.4 Synthesis of Dodecacarbonyltriruthenium $\text{Ru}_3(\text{CO})_{12}$

RuCl_3 of 2 g (9.64 mmol) was added to 100 ml freshly, over sodium dried methanol in a 200 ml autoclave (Bruce et al., 1990). The autoclave (Parr) was pressurized with carbon monoxide to 50 bar, followed by gradual heating to 125°C , causing a pressure increase in the autoclave to 70 bar. After keeping the autoclave at 125°C and under continual stirring for eight hours, it was slowly cooled to room temperature overnight. Orange $\text{Ru}_3(\text{CO})_{12}$ crystals then formed. They were filtered off using a Büchner funnel and washed repeatedly with dried methanol. Recrystallization in toluene followed as a purification step. The crystals were dried *in vacuo* for two hours. The reaction solvent was used as mother liquor in a three reaction sequence to increase the yield (Exp. 75%; Lit. 70-85% (Bruce et al., 1990)).



Note that the stoichiometry of this reaction equation is not understood yet. The IR spectrum in CH_2Cl_2 showed bands at 2061 (vs), 2030 (s) and 2011 (m) cm^{-1} , which are in good agreement with literature values for the desired compound, dodecacarbonyltriruthenium (Lit. 2061 (vs), 2031 (s), 2011 (m) cm^{-1} (Bruce et al., 1990)).

The chemical structure of dodecacarbonyltriruthenium is shown in Figure 4.2 (Ru-3).

4.1.2.5 Synthesis of Dodecacarbonyl-tetra(μ -hydrido)-tetraruthenium $\text{Ru}_4(\mu\text{-H})_4(\text{CO})_{12}$

A mixture of 1.2 g $\text{Ru}_3(\text{CO})_{12}$ (1.78 mmol) and 70 ml freshly dried n-heptane was poured into a 200 ml autoclave (Bruce and Williams, 1990). The autoclave was pressurised to 75 bar with hydrogen at room temperature and then heated-up to 150°C . After four hours the autoclave was gently cooled down over a period of several hours. Yellow crystals had been formed. They were filtered off using a Büchner funnel, washed several times with n-heptane and dried *in vacuo* for several hours. The obtained yield was 85% (Lit. 90% (Bruce and Williams, 1990)).

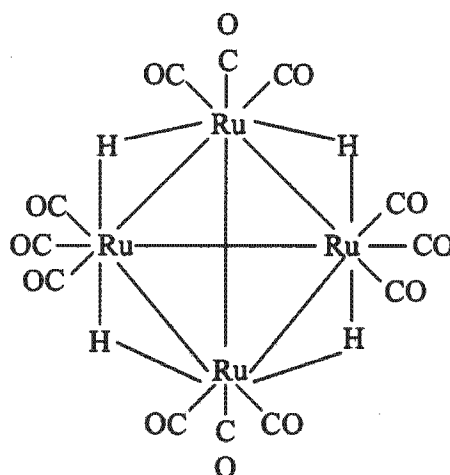


IR spectroscopy in n-hexane showed bands at 2080 (s), 2068 (vs), 2030 (m), 2024 (s) and 2007 (w) cm^{-1} (Lit.: 2081 (s), 2067 (vs), 2030 (m), 2024 (s), 2009 (w) cm^{-1} (Bruce and Williams, 1990)).

Figure 4.2 shows its three-dimensional metal cluster framework, referred to as Ru-4 in this work, and Scheme 11 depicts the chemical structure of $\text{Ru}_4(\mu\text{-H})_4(\text{CO})_{12}$ with its

^bA more detailed description of this technique can be found in Section 4.4.2, p. 38.

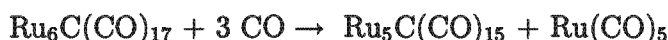
bridging hydride and terminal CO-ligands.



Scheme 11: Chemical structure of $\text{Ru}_4(\mu\text{-H})_4(\text{CO})_{12}$.

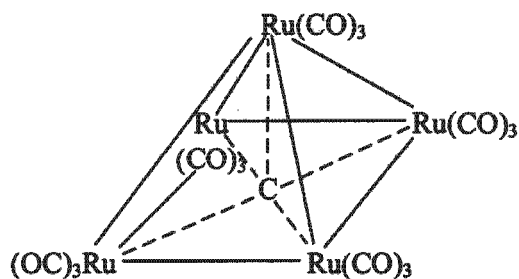
4.1.2.6 Synthesis of μ_5 -Carbido-pentadecacarbonyl-pentaruthenium $\text{Ru}_5\text{C}(\text{CO})_{15}$

$\text{Ru}_6\text{C}(\text{CO})_{17}$ of 250 mg (0.266 mmol) were added to 50 ml dried n-heptane in a 200 ml autoclave (Nicholls et al., 1990). The synthesis of $\text{Ru}_6\text{C}(\text{CO})_{17}$ is described below. To remove air from the system the autoclave was pressurized twice with carbon monoxide to 30 bar, stirred for a few minutes and vented to atmospheric pressure. Repressurization to 80 bar followed. The autoclave was heated to 90°C over a period of 30 minutes. It was kept at this temperature under strong stirring for an additional 3.7 hours. The autoclave was cooled down to room temperature overnight and repressurized in a fume hood to avoid carbon monoxide intoxication. After opening, the red solution was transferred into a 100 ml round-bottom flask covered with aluminium foil. Inside the autoclave red crystals had formed. They were washed three times with n-heptane. The red solution was evaporatively dried on a vacuum Schlenk line at room temperature. The evaporated reaction solvent, containing the volatile, toxic by-product $\text{Ru}(\text{CO})_5$ and the solvent n-heptane, was removed in the cold trap. The remaining red solid in the flask was dissolved with 50 ml of boiling n-hexane. Crystallization of the product was achieved by keeping the solution in a freezer overnight. The red crystals were collected by filtration. The overall yield was 75% (Lit. 93% (Nicholls et al., 1990)).



The dissolved red crystals in n-hexane showed IR adsorption bands at 2068 (s), 2036 (m) and 2017 (w) cm^{-1} (Lit.: 2067 (s), 2034 (m), 2015 (w) cm^{-1} (Nicholls et al., 1990)).

The metallic framework of this pentameric cluster, referred to as Ru-5 in this work, is shown in Figure 4.2. The chemical structure with its central C-atom and the terminal CO-ligands is schematically represented in Scheme 12.

Scheme 12: Chemical structure of $\text{Ru}_5\text{C}(\text{CO})_{15}$.

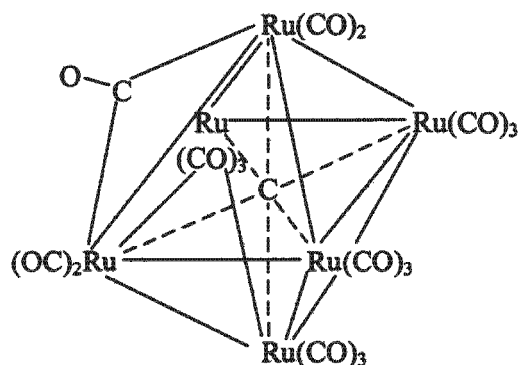
4.1.2.7 Synthesis of μ_6 -Carbido-heptadecacarbonyl-hexaruthenium $\text{Ru}_6\text{C}(\text{CO})_{17}$

Following the method of Nicholls et al. (1990) 400 mg of $\text{Ru}_3(\text{CO})_{12}$ (0.623 mmol) was added to 50 ml of freshly dried n-heptane in a 200 ml autoclave. The autoclave was pressurized twice with ethylene to 20 bar and vented to atmospheric pressure. This was to remove air from the autoclave system. Afterwards, the autoclave was pressurized with ethylene to 30 bar and heated to 165°C for two hours under strong stirring conditions to completely dissolve the $\text{Ru}_3(\text{CO})_{12}$. The autoclave was kept at 165°C for two hours, before gently cooling it down to room temperature overnight. The pressure was then released. The orange-red solution was removed immediately. Dark-purple crystals had formed inside the autoclave. These were washed three times with 10 ml of dry n-pentane. No further purification was necessary (Yield: Exp. 55%, Lit. 62% (Nicholls et al., 1990)).



The IR spectrum of the purple crystals in CH_2Cl_2 showed bands at 2067 (s) and 2045 (s, br) cm^{-1} , which is in agreement with literature IR data of the product $\text{Ru}_6\text{C}(\text{CO})_{17}$ (Lit.: 2066 (s), 2045 (s, br) cm^{-1} (Nicholls et al., 1990)).

Figure 4.2 and Scheme 13 show the structure of the metal framework in $\text{Ru}_6\text{C}(\text{CO})_{17}$ and the chemical structure of this hexameric cluster (Ru-6). The molecule consists of a central C-atom, one bridging and 13 terminal CO-ligands.

Scheme 13: Chemical structure of $\text{Ru}_6\text{C}(\text{CO})_{17}$.

4.1.2.8 Impregnation onto Alumina Support

Immobilization of the organometallic compounds was achieved by depositing them onto support material. To achieve this, the organometallic compounds were dissolved in acetone under reflux. After their complete dissolution, the alumina support was added. The anticipated ruthenium loading was 3 wt% in all cases. A sequence of two drying steps followed. The first step served to remove the solvent with a rotary drier at 60°C and 300 mbar, followed by a second step consisting of drying *in vacuo* at room temperature for several hours to ensure the complete removal of the solvent acetone from the support pores. All freshly prepared model catalysts had an orange-yellow colour. Their stability, judged from their visual appearance, could be lengthened by keeping them in a fridge under an argon atmosphere.

4.2 Characterisation of Water-in-Oil Microemulsions

An estimation of the sizes of reverse micelles consisting of water-PEGDE-*n*-hexane mixtures was conducted based on viscosity of the microemulsion solution. Viscosity measurements were done on all the different microemulsions using a Lauda viscosimeter (Lauda, Germany) connected with a S00 spindle at 25°C under a constant stirring speed of 100 rpm for 5 minutes. Obtained values were expressed as kinematic viscosities (η).

4.3 Characterisation of Support Material

Alumina (Puralox (Batch 9574), SCCa 5-150, Sasol Germany, $S_{\text{BET}} = 162 \text{ m}^2/\text{g}$, $V_{\text{pore}} = 0.47 \text{ cm}^3/\text{g}$, $\bar{d}_{\text{pore}} = 11.5 \text{ nm}$, particle size: 150-200 μm) was used as support material for all the prepared model catalysts.

The zetapotential of the alumina support was investigated using a Malvern Zeta 4 Instrument (Malvern, Micron Scientific, South Africa). The zetapotential, ζ , (or Coulomb potential) is an electrokinetic potential, which indicates the total surface charge. The surface charge of the support was measured at different pH values. The starting point was the pH value of 0.1 g of very finely ground support in 100 ml 0.1 M KCl solution. By adding drops of 10^{-3} M KOH and 10^{-3} M HCl solutions, a range of different pH values was screened and the ζ values versus pH recorded, to obtain the isoelectronic point of the support.

4.4 Characterisation of Organometallic Compounds

4.4.1 Infrared Spectroscopy (IR)

Infrared spectroscopy (IR) is a method which is often used to characterise organometallic compounds. The FT-IR technique (Fourier-Transform Infrared Technique) records the interaction of IR radiation with the sample by measuring the frequencies at which the sample absorbs the radiation and the intensity of this absorption. Photon absorption can combine the vibrations of CO-ligands in molecules for them to get excited. The C-O stretch vibrations vary from bridging (C-O triple bond) to terminal (C-O double bond) CO-ligands. IR measurements were done on a Perkin-Elmer 1000 FT-IR spec-

trometer (Perkin-Elmer, USA) in solution cells with NaCl windows. The solvents used were CH_2Cl_2 , n-heptane and n-hexane, depending on the complex which was studied.

4.4.2 Nuclear Magnetic Resonance Spectroscopy (NMR)

Liquid phase Nuclear Magnetic Resonance spectroscopy (NMR) is a tool to identify the three-dimensional molecular structure of organic and organometallic compounds. It is based on the magnetic property of a nucleus in an atom. Atoms with an uneven number of nuclei display a resulting magnetic moment. This magnetic moment creates a chemical shift, δ , which is characteristic of certain groups. ^1H and ^{13}C -NMR spectroscopy analyses were done on an Avance 500 (Bruker, Germany) at 500 MHz frequency for the ^1H and at 125 MHz for the ^{13}C measurements. The solvent used was deuterated chloroform (CDCl_3) and the calibration was done on tetramethyl-silane (TMS).

4.4.3 Thermogravimetric Analysis (TGA)

In order to determine a suitable reaction temperature for the FT experiments, the thermal stability of the ruthenium compounds was investigated by thermogravimetric analysis (TGA). This technique records weight changes in materials as a function of temperature. The measurements were done on a Mettler Toledo Star⁹ Thermal Analysis System (Mettler Toledo GmbH, Switzerland). Different gases were used to study the effect of different gas environments on the thermal and chemical stability of the ruthenium compounds. These included nitrogen, 5 vol% hydrogen in argon and 5 vol% carbon monoxide in nitrogen. The organometallic compounds ($m_i = 0.01$ g) were heated from 30 to 500°C at a heating rate of 5°C/min and a gas flow rate of 20 ml(NTP)/min.

4.5 Characterisation of Supported Model Catalysts

4.5.1 Inductively Coupled Plasma Spectrometry (ICP)

The ruthenium metal loadings of the spent supported organometallic compounds were determined by means of Inductively Coupled Plasma spectrometry (ICP). This is an analytical technique which can be used for the quantitative detection of trace amounts of metals. The samples were analysed by ICP optical emission spectroscopy using a Varian Vista-Pro instrument (Varian, USA) with radial torch configuration and scandium as internal standard.

4.5.2 Transmission Electron Microscopy (TEM)

Crystallite size distributions of the calcined, reduced and spent supported nano-sized crystallites and of the spent supported organometallic compounds, used as model catalysts, were determined using a transmission electron microscope (TEM). Two different TEM instruments were used. The model catalysts by means of the reverse micelle method were analysed with a LEO 912 (Leo, now Zeiss, Germany) operated at 120 kV. A JEM200CX (JEOL, Japan) TEM operating at 200 kV was used for the characterisation of the supported organometallic model catalysts.

Sample preparation was done using the so-called "resin" method, where very fine slices of the sample are made for better visibility under the microscope. Plastic sample holders

containing minimal amounts of sample were filled with resin. After solidification at 60°C for two days, the hard resin was cut in an Ultramicrotome LEICA Ultracut S (Leica, Austria) cutting machine to 0.1 μm thick sample disks. These were transferred onto Cu-grids before they were put in the microscope. Digital photos of the model catalysts were taken and later studied using the freely available software IMAGE J for crystallite size analysis.

To obtain statistically relevant information of crystallite size distribution and average crystallite size, a minimum of 300 crystallites was measured per sample.

4.5.3 CO-Chemisorption

Chemisorption is used to analyse the metal dispersion of supported crystallites, by measuring the gas-uptake at a specific temperature. Usually a monolayer-formation of the chemisorbed gas is assumed. The chemisorption stoichiometry is the average number of surface metal atoms associated with adsorption of each gas molecule at a monolayer coverage. The dispersion (D) can then be directly obtained from the following equation:

$$D = \frac{V_{\text{chem}} \cdot x_{\text{Chem.}} \cdot M_{\text{Ru}}}{22414 \cdot m_i} \quad (4.1)$$

with the parameters:

D = Dispersion of the metal atoms

V_{chem} = Volume of the chemisorbed gas required to form monolayer coverage

$x_{\text{Chem.}}$ = chemisorption stoichiometry

M_{Ru} = Molecular mass of Ru (= 101.91 g/mol)

m_i = mass of ruthenium in sample

The dispersion is related to the average crystallite size ($\bar{d}_{\text{red-Chem.}}$) as described in the following equation:

$$\bar{d}_{\text{red-Chem.}} = \frac{6 \cdot \left(\frac{v_m}{a_m}\right)}{D} \quad (4.2)$$

The variables a_m and v_m are element specific lattice parameter constants^c.

The measurements were done on an ASAP2020 Micromeritics Analyser (Micromeritics Instrument Corp., USA) using carbon monoxide as chemisorption gas. The chemisorption was conducted at 50°C and a stoichiometry of 1:1 carbon monoxide per exposed surface ruthenium atom was assumed. The catalyst was reduced *in-situ* at 300°C for five hours with a heating rate of 2°C/min. An example of a chemisorption reading is shown in Appendix A.3, p. 158, Figure A.3.

4.5.4 X-Ray Diffraction Spectroscopy (XRD)

The reduced and spent supported nano-sized crystallites as well as the spent supported organometallic compounds were examined using X-ray diffraction spectroscopy (XRD). XRD is a common method to investigate crystallinity, phase composition, and average crystallite size. The measurements were performed on a Phillips X-ray diffractometer (Phillips PW 1390, USA) with Cu-K_α radiation with a wavelength of 1.540 Å at 40 kV

^c $a_{m,\text{Ru}} = 13.65 \text{ \AA}^2$; $v_{m,\text{Ru}} = 6.35 \text{ \AA}^3$

and 25 mA. The scan range was between 20 and 80°. The diffraction peaks of crystalline phases were compared with those of standard compounds reported in the JCPDS^d data files.

4.5.5 Temperature Programmed Reduction (TPR)

Temperature programmed reduction (TPR) was used to study the reduction behaviour of the supported nano-sized crystallites. It was also used to determine the metal loading of these model catalyst samples. The calcined sample ($m_i = 1.0$ g) was placed in a quartz reactor of a Micromeritics AutoChem 2910 (Micromeritics Instrument Corp., USA). 5 wt% hydrogen in argon was the reducing gas ($\dot{V}(\text{H}_2/\text{Ar}) = 50$ ml(NTP)/min). After drying in argon at 120°C for 30 minutes, the sample was heated in the reducing gas to 1000°C at a linear temperature ramp of 10°C/min. The hydrogen consumption was measured with a thermal conductivity detector (TCD) with the assumption that two moles of hydrogen are needed to reduce one mol of ruthenium dioxide, RuO_2 , to metallic ruthenium and water. The ruthenium amount in the sample could be calculated from the hydrogen consumed. The instrument was calibrated at regular intervals using standards of pure NiO and Ag_2O .

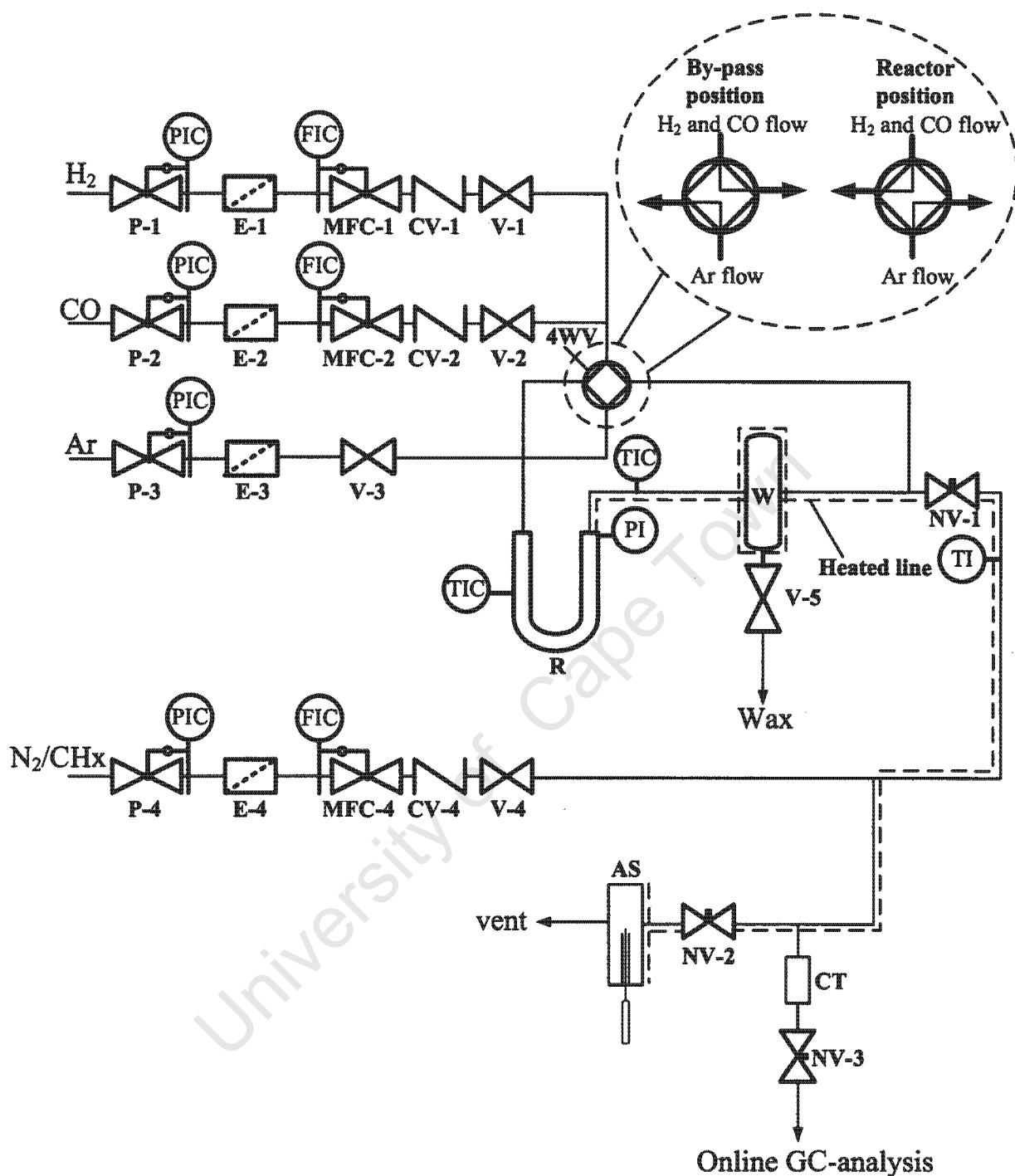
4.6 Fischer-Tropsch Synthesis Experiments

4.6.1 Reactor Set-up

The experimental set-up for the FT tests is shown schematically in Scheme 14. Scheme 15 illustrates the modified reactor set-up which was used in experiments in which ^{13}C labelled carbon monoxide was used. The catalyst was placed in the isothermal zone ($V_{\text{isothermal}} = 1.5$ cm³) of a U-tube fixed-bed reactor (1/4").

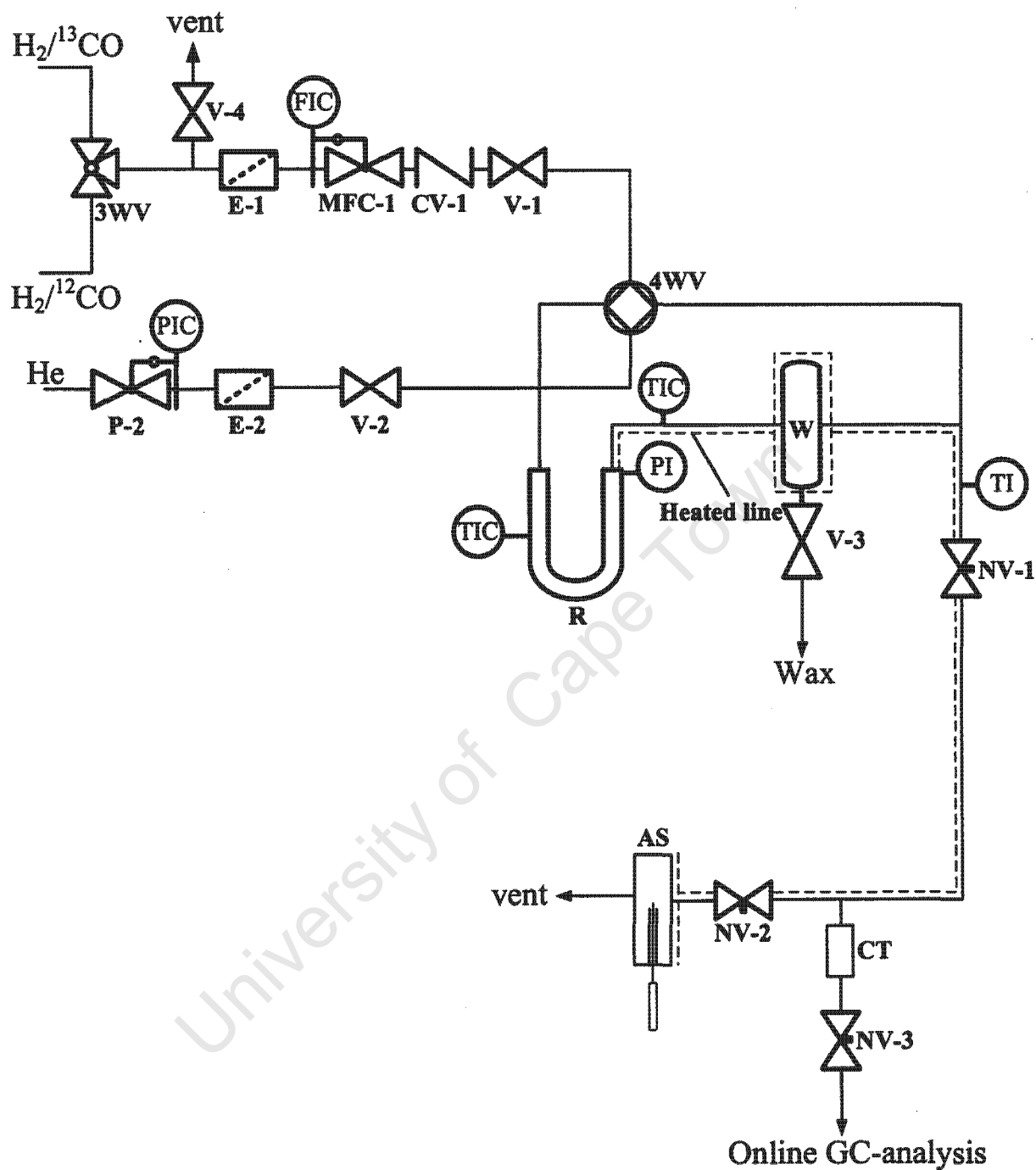
In normal operation, hydrogen, carbon monoxide and the reference gas were fed via mass flow controllers (Brooks 5850S, Brooks Instruments, The Netherlands) into the system. The reference gas, containing 0.15 vol% cyclohexane, CH_x , in nitrogen, was added to the product stream. It served as internal standard of samples in the gas chromatographic product analyses. A pressure controlled argon stream was fed before a needle valve (NV-1) for regulation and control of pressure in the reactor. The argon flow was pressure controlled and was used to build-up the pressure in the reactor system. The 4-way valve (4WV) could be set on by-pass position or on reactor position (see Scheme 14). On the by-pass position, argon flow went through the reactor, while hydrogen and carbon monoxide by-passed it. This position was used to set the synthesis gas ratio before the start of the reaction. It was then switched to the reactor position, with hydrogen and carbon monoxide passing over the catalyst bed in the reactor to start a FT experiment. A wax trap (W) after the reactor collected products which are liquid at reaction conditions ("wax"). After pressure release, the product stream was split into an online GC sampling end and an ampoule sampler (AS), used for offline sampling (see Scheme 17). The whole experimental structure was designed to monitor very rapid changes of catalyst activity and selectivity, which often particularly occur in the first minutes of an experiment. The

^dJoint Committee for Powder Diffraction Standards



Scheme 14: Experimental set-up for FT synthesis. *Note:* P-1 to P-4: Pressure regulating valves; E-1 to E-4: Line filters; MFC-1, MFC-2 and MFC-4: Mass flow controllers; CV-1, CV-2 and CV-4: Check valves; V-1 to V-5: One-way valves; 4WV: 4-way valve; NV-1 to NV-3: Needle valves; AS: Ampoule sampler; CT: Cold-trap; FIC: Flow indicator and control; PIC: Pressure indicator and control; R: Reactor; TI: Temperature indicator; TIC: Temperature indicator and control; W: Wax trap.

lag time from the reactor to the ampoule sampler using the reaction conditions applied was around 30 seconds.



Scheme 15: Modified experimental set-up for FT synthesis using labelled ^{13}C in CO. *Note:* P-2: Pressure regulating valve; E-1 and E-2: Line filters; MFC-1: Mass flow controller; CV-1: Check valve; V-1 to V-4: One-way valves; 3WV: 3-way valve; 4WV: 4-way valve; NV-1 to NV-3: Needle valves; AS: Ampoule sampler; CT: Cold-trap; FIC: Flow indicator and control; PI: Pressure indicator; PIC: Pressure indicator and control; R: Reactor; TI: Temperature indicator; TIC: Temperature indicator and control; W: Wax trap.

All lines after the reactor were heated to 150°C to avoid product condensation. The reactor was either heated with an insulated aluminium jacket in which heating cartridges had been placed or via a silicon oil bath. The aluminium jacket was used in experiments with the supported nano-sized crystallites, which were prereduced following use of a temperature programme. The supported organometallic complexes were not pretreated and - due to their limited stability - they were heated-up rapidly by dipping the loaded U-tube reactor into a preheated oil bath (see Scheme 16 in following Section).

In the study with ¹³C labelled carbon monoxide, premixed synthesis gases (H₂/CO = 2) were used (see Scheme 15). A 3-way valve (3WV) in the gas feeding system allowed for an instantaneous switch-over from one gas mixture to the other one. Helium was used as a pressure control gas in these experiments, and no reference gas was fed to the product stream as this was a qualitative study only. This was done in order to increase concentration levels in the product samples and therefore improve quality of product analysis in these experiments.

4.6.2 Operation of the Fixed-Bed Reactor Set-up and Reaction Conditions

The reactor was a U-tube fixed-bed reactor made from stainless steel (1/4", d_{int} = 4.4 mm^e). The isothermal section of the reactor (i.e. typical variance in the reaction temperature ±1°C) was filled with 1.26 g of catalyst. Due to the low ruthenium loadings no further catalyst dilution was necessary as is often needed in experimental FT studies to avoid hot spots and temperature run away. The reactor inlet side was filled with silicon carbide SiC (mesh size = 200-250 μm) in order to provide preheating for the reaction gases before they reached the catalyst bed. Tightly packed glass wool was placed in the outlet side of the reactor to prevent the catalyst from moving during the reaction (see Scheme 16).

The supported nano-sized crystallites were reduced at 300°C in pure hydrogen for five hours (V(H₂) = 30 ml(STP)/min) before an FT experiment. To avoid sintering of the small crystallites, the heating rate was set very low (2°C/min). After reduction, the catalyst bed was cooled down to the reaction temperature.

With the 4-way valve (4WV) in the by-pass position, the reactor pressure, 4 bar, was set with the pressure controlled argon stream and the flow was adjusted with the needle valve NV-1 to 12 ml(STP)/min, while hydrogen and carbon monoxide flows were set via the massflow controllers to 6 and 3 ml(STP)/min respectively; the reference gas flow rate was 3 ml(STP)/min. The corresponding "Gas Hourly Space Velocity" (GHSV^f) is 7 ml(STP)/(min·g_{cat}).

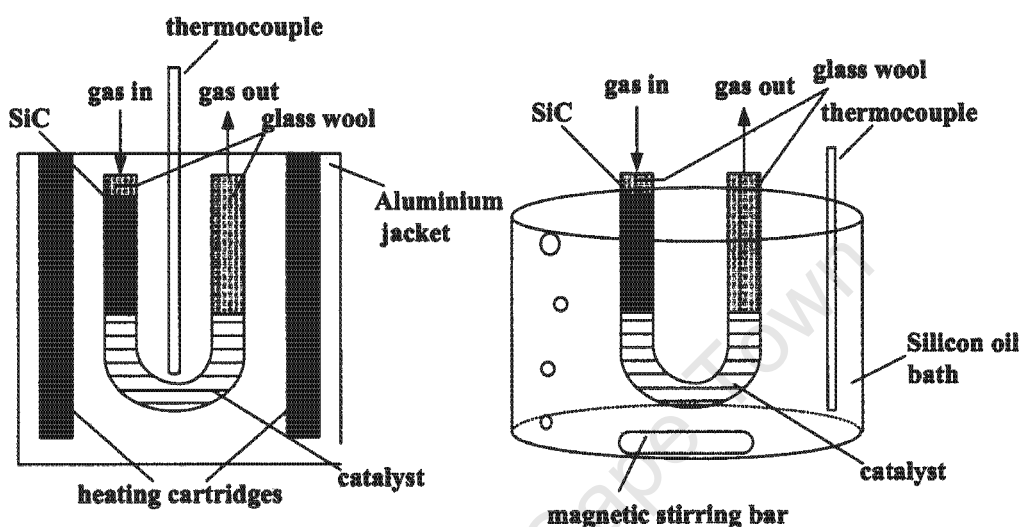
The same procedure was used for the supported organometallic compounds, but here no reduction step was applied. Additional tests were done on these complexes where only hydrogen (6 ml(STP)/min) was used to study their decomposition.

For the test in which ¹³C labelled carbon monoxide was used in the synthesis gas, helium was used as pressure control gas (pressure: 4 bar). Helium was also used as the carrier gas for the GC/MS analyses (see Section 4.7.3, p. 46) and therefore does not interfere with other compounds in these samples which would be the case if argon had been used. The flow of helium was again set to 12 ml(STP)/min, with the 4-way valve (4WV) in

^ed_{int} = internal diameter

^fThe GHSV equals the volumetric flow of the synthesis gas per minute divided by the mass of the catalyst.

the by-pass position. After this the flow of the synthesis gas was set to 9 ml(STP)/min. During the first 15 minutes on stream the synthesis gas containing labelled ^{13}C O was fed into the reactor, afterwards it was switched to the non-labelled gas mixture. After 280 minutes on stream it was switched back to the labelled ^{13}C O for the remaining 20 minutes until the shut-down of the reaction. In this way the initial behaviour and the steady-state behaviour of the reactions occurring on the complexes could be studied.



Scheme 16: Schematic drawing of the heating-source and the reactor for FT experiments on supported nano-sized crystallites (*left*) and supported organometallic compounds (*right*), used as model catalysts.

In the experiments with the supported nano-sized crystallites, heating was affected using an aluminium heating jacket (see Scheme 16 left). The reaction temperature in the experiments on the nano-sized crystallites and the organometallic complexes was 170°C . This was determined/limited by the thermal and chemical stability of the complexes (see Section 5.3.1, p. 64). Some of the nano-sized supported crystallites were also tested at an elevated temperature of 225°C to test their performance at more realistic FT conditions and higher conversion levels. The temperature was controlled with a thermocouple placed between the limbs of the reactor tube (see Scheme 16 left). The aluminium jacket was insulated with glass wool. In the case of the supported organometallic compounds, a silicon oil bath was used and the temperature was controlled via a thermocouple located in the silicon oil (see Scheme 16 right). The silicon oil bath was preheated to the reaction temperature, 170°C , before the loaded reactor was dipped into it. In this way the sample was heated up very rapidly ($>200^{\circ}\text{C}/\text{min}$) to the reaction temperature, a crucial requirement in the tests with these thermally unstable compounds.

After reaching the reaction temperature, the 4-way valve (4WV) was switched to the reactor position, followed by immediate product sampling. It was kept at this position throughout the reaction. To shut-down the reaction, the hydrogen and carbon monoxide flows were stopped and the catalyst bed was flushed with argon for several hours, to remove any volatile matter from the catalysts. After this the sample was passivated in carbon dioxide at room temperature for several hours, before the spent catalyst was finally removed from the reactor. The duration of a run with the nano-sized crystallites was typically five days, whereas the organometallic complexes were normally only tested for five hours.

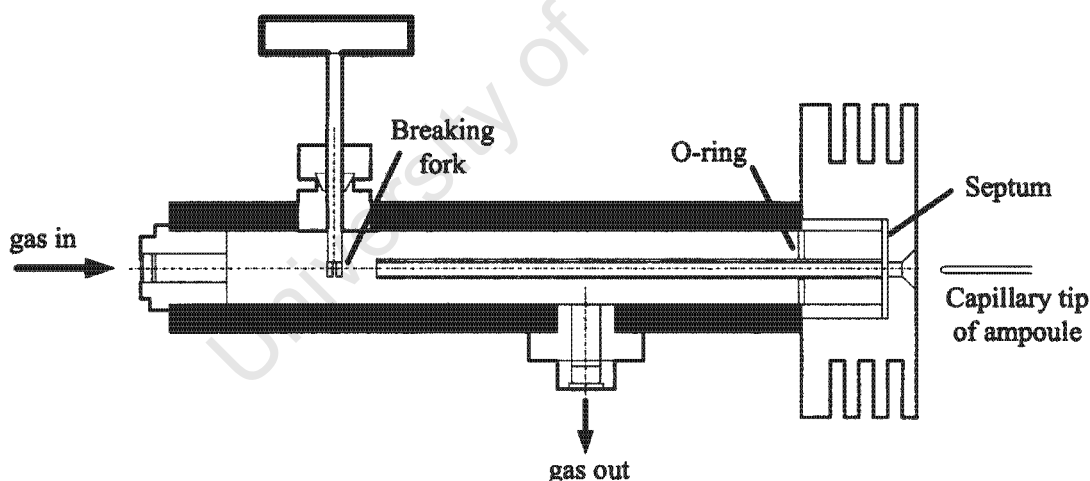
4.7 Analytical Procedures

4.7.1 Sampling Techniques

The ampoule sampling technique developed by Schulz et al. (1984) was used for off-line product sampling. Glass ampoules, prepared from commercially available Pasteur pipettes, were prepared as sampling devices. These ampoules were formed with capillaries of a length of 120 mm and around 1.5 mm in diameter. The internal volume of the evacuated ampoules was approximately 2 ml. During sampling the capillary end was inserted through an airtight septum into a heated sampling device, shown schematically in Scheme 17. By breaking the end of the capillary, the volatile compounds were sucked into the evacuated ampoule in less than 1/10 of a second and the capillary was sealed immediately afterwards with a butane flame. These samples can be stored and then analysed using a special ampoule breaking device connected to a gas chromatography (GC) system (Claeys, 1997).

The advantage of this technique, apart from the separation of sampling and analysis, is the possibility of rapid sampling at a frequency of less than 10 seconds, which provides a unique tool to investigate fast activity and selectivity changes, particularly at the beginning of the FT reaction. In addition to this offline method, larger samples of the product stream were taken in the test with ^{13}C labelled synthesis gas using gas tight syringes.

The experimental set-up was also connected to a GC system for analysis of inorganic gases and methane for online sampling (see next Section).



Scheme 17: Schematic drawing of the ampoule sampling device.

4.7.2 Analysis of Inorganic Compounds and Methane

A Thermal Conductivity Detector (TCD) in a Varian 3700 gas chromatograph was used to analyse the reagents hydrogen and carbon monoxide, the reference compound nitrogen, as well as the products methane and carbon dioxide.

The GC was connected directly to the outlet flow of the reactor, providing online analysis via injection by switching a six way valve to introduce the content collected in a gas sample loop. This technique allows monitoring of the change in hydrogen and carbon monoxide

Table 4.2: Conditions for gas chromatographic analysis using TCD detection.

Gas chromatograph	Varian 3700
Detector	four filament thermal conductivity detector (TCD) $T_{\text{detector}} = 200^{\circ}\text{C}$ $T_{\text{filament}} = 250^{\circ}\text{C}$
Column	packed, stainless steel $l = 3 \text{ m}$ $d_{\text{int}} = 2.1 \text{ mm}$ stationary phase: Carbosieve II, 80-100 mesh (Supelco)
Carrier gas	argon
Flow rate	30 ml(STP)/min
Analyses temperature	170°C (isothermal)
Analyses time	10 min

conversion during an experiment. For gas chromatographic conditions see Table 4.2; a typical TCD chromatogram is shown in Appendix B.1, Figure B.1, p. 165.

4.7.3 Analysis of Volatile Organic Compounds (VOC's)

Ampoule samples of the compounds which are volatile at reaction conditions (VOC's) were either analysed on a Varian 3400 GC or on an Agilent 6890N equipped with flame ionization detectors (FID). The gas chromatographic conditions of these analyses are shown in Table 4.2 and examples of typical FID chromatograms are illustrated in Section 6.2.1 (Figure 6.17, p. 94 and Figure 6.26, p. 107) and in Appendix B.1 (Figure B.2, p. 166).

For an analysis the ampoule sample was put into a specially designed ampoule breaking device (see Mabaso (2005)), in which it was crushed under nitrogen and introduced into the injector of the gas chromatograph. One minute after this introduction the nitrogen was replaced by hydrogen as a carrier in which the separation of the organic products, including the organic standard, cyclohexane (CH_x), was conducted on 60 m OV-1 type capillary columns.

Additional analysis of the organic products was done using a gas chromatograph (Agilent 6890N) coupled with a mass spectrometer (MS, Hewlett Packard 5973N) and an FID. These analyses were mainly conducted on samples of the experiments dealing with the supported organometallic compounds. Both ampoule samples and samples taken with gas tight syringes collected after the ampoule sampler, were analysed on this system. The injected gas sample was split into two identical columns: one connected to the MS and the other to the FID. The chromatographic conditions were identical to the ones used above (see Table 4.3) except that here helium was used as carrier and sample introduction gas. The mass spectrometer was operated in scan mode ($m/z = 2$ to $m/z = 100$) and the data was processed using the program MSDChem and the NIST library (Version 2.0).

Table 4.3: Conditions for gas chromatographic analysis using FID and MS detection.

Gas chromatograph	Varian 3400 ^a , Agilent 6890N ^a Hewlett Packard 5973N ^b
Detector	flame ionization detector (FID) mass spectrometer (MS) T _{FID} = 250°C T _{MS} = 280°C
Column	RTx-1 (Restek) fused silica capillary column, l = 60 m, d _{int} = 0.25 mm stationary phase: 0.5 μm dimethyl siloxane (crosslinked)
Introduction gas	nitrogen (FID) helium (MS)
Carrier gas	hydrogen (FID) helium (MS)
Column head pressure	2.9 bar (absolute)
Injector	split injector, T = 250°C split ratio: splitless to 1:200 (depending on amount of hydrocarbons in sample)
Temperature programme FID	-60°C, 3 min, isothermal at 15°C/min to -35°C, 0 min, isothermal at 10°C/min to -5°C, 2 min, isothermal at 2.5°C/min to 25°C, 0 min, isothermal at 5°C/min to 250°C, 10 min, isothermal
Temperature programme MS	-60°C, 5 min, isothermal at 10°C/min to 280°C, 0 min, isothermal 280°C, 5 min, isothermal
Temperature of ampoule breaking device	250°C

^a GC^b GC/MS

4.8 Data Work-up

The quantitative analysis of the GC measurements relied on the reference compounds, nitrogen and cyclohexane (0.15 vol%), which were fed to the exit stream after the reactor in known amounts.

Nitrogen was used as internal standard for TCD analysis to quantify the rates of the inorganic compounds and methane. The molar standards of compound i in the obtained TCD chromatogram were calculated as follows:

$$\dot{n}_i = f_{\text{TCD},i} \cdot \left(\frac{A_i}{A_{\text{N}_2}} \right) \cdot \dot{n}_{\text{N}_2} \quad (4.3)$$

with

\dot{n}_i = Molar flow rate of compound i

$f_{\text{TCD},i}$ = Response factor for the inorganic compound i

A_i = Area of compound i in chromatogram

A_{N_2} = Area of N_2 (reference gas) in chromatogram

\dot{n}_{N_2} = Molar flow rate of N_2 (reference gas)

The response factors relative to nitrogen for the different compounds i were determined at regular intervals (i.e. weekly) using a calibration gas mixture of known composition containing hydrogen, carbon monoxide, methane, carbon dioxide and nitrogen^g.

Cyclohexane, CH_x , which is not a FT product, was added as reference compound for the quantification of the formation rates of the volatile organic compounds (VOC's) from FID analyses. The molar flow rate of the reference compound cyclohexane, \dot{n}_{CH_x} , equals:

$$\dot{n}_{\text{CH}_x, \text{ref}} = \frac{c_{\text{CH}_x, \text{ref}} \cdot \dot{V}_{\text{ref}}}{V_m} \quad (4.4)$$

with the following parameters:

$c_{\text{CH}_x, \text{ref}}$ = Concentration of cyclohexane in the reference gas

\dot{V}_{ref} = Volumetric reference gas flow rate at STP

V_m = Avogadro volume ($22.414 \frac{\text{l}}{\text{mol}}$)

The molar flow rate of the product i on a carbon basis, $\dot{n}_{i, \text{C}}$, can be expressed as:

$$\dot{n}_{i, \text{C}} = \left(\frac{\dot{n}_{i, \text{C}}}{\dot{n}_{\text{N}_2}} \right) \cdot \dot{n}_{\text{N}_2} = \frac{N_{\text{CH}_x, \text{C}}}{N_{i, \text{C}}} \cdot \frac{f_i \cdot A_i}{f_{\text{CH}_x} \cdot A_{\text{CH}_x}} \cdot \dot{n}_{\text{CH}_x} \quad (4.5)$$

with the following parameters:

$N_{\text{CH}_x, \text{C}}$ = Number of carbon atoms in cyclohexane (= 6)

$N_{i, \text{C}}$ = Number of carbon atoms in product i

f_i = Compound specific response factors^h

^gtypical factors: $f_{\text{TCD}, \text{H}_2} = 0.083$; $f_{\text{TCD}, \text{CO}} = 1.0058$; $f_{\text{TCD}, \text{CH}_4} = 0.290$; $f_{\text{TCD}, \text{CO}_2} = 0.969$

^hThis equals 1 for hydrocarbons. For oxygenates theoretical incremented response factors (Kaiser, 1969) were used to ensure that the response for all carbon atoms which are not bonded to an oxygen atom is 1, that the response of carbon atoms with a single bond to an oxygen atom is 0.55 and that those carbon atoms with C=O double bonds give no response;

$$f_i = \frac{N_{\text{C}, i}}{N_{\text{C}(\text{no O})} + 0.55 \cdot N_{\text{C}(\text{CO})}} \quad (4.6)$$

A_{CH_x} = Area of cyclohexane in the GC chromatogram

The molar flow of nitrogen in the reference gas (\dot{n}_{N_2}) is:

$$\dot{n}_{\text{N}_2} = \frac{c_{\text{N}_2, \text{ref}} \cdot \dot{V}_{\text{ref}}}{V_m} \quad (4.7)$$

with $c_{\text{N}_2, \text{ref}}$ being the nitrogen concentration in the reference gas.

4.8.1 Conversion, Yield and Selectivity

The conversion of a reactant i is generally defined as:

$$X_i = \frac{\dot{n}_{i, \text{in}} - \dot{n}_{i, \text{out}}}{\dot{n}_{i, \text{in}}} \quad (4.8)$$

The yield ($Y_{i, \text{C}}$) and the selectivity ($S_{i, \text{C}}$) of a product i on a carbon basis are expressed as:

$$Y_{i, \text{C}} = \frac{\dot{n}_{i, \text{out}}}{\dot{n}_{\text{CO}, \text{in}}} \quad (4.9)$$

$$S_{i, \text{C}} = \frac{Y_{i, \text{C}}}{X_{\text{CO}}} \quad (4.10)$$

Alternatively a selectivity/carbon content within the fraction of volatile products can be defined:

$$S_{i, \text{VOC}, \text{C}} = \frac{\dot{n}_{i, \text{C}}}{\sum_i \dot{n}_{i, \text{VOC}, \text{C}}} \quad (4.11)$$

4.8.2 Turnover Frequency

The catalyst activity of the different model catalysts was compared using turnover frequencies which express the rate of carbon monoxide disappearance per exposed ruthenium atom on the crystallite surface ($N_{\text{exp}, \text{total}}$) multiplied by Avodagro's number (N_A):

$$\text{TOF} = \frac{\dot{n}_{\text{CO}, \text{in}} - \dot{n}_{\text{CO}, \text{out}}}{N_{\text{exp}, \text{total}}} \cdot N_A \quad (4.12)$$

In the case of the organometallic clusters it was assumed that all ruthenium atoms were on the surface, i.e. accessible to synthesis gas.

In this work, turnover frequencies, reflecting formation rates of a defined carbon number ranging from C_i to C_{ii} for volatile organic compounds, were also used to express catalyst activities per number of exposed surface atoms. The turnover frequency can be expressed as:

$$\text{TOF}(C_i - C_{ii}) = \frac{\sum \dot{n}_{i, \text{C}, \text{VOC}}}{N_{\text{exp}, \text{total}}} \cdot N_A \quad (4.13)$$

The total number of exposed surface atoms in the tested catalysts equals the product of exposed surface atoms per crystallite of average size, $N_{\text{exp}, \text{cryst}}$ (size determined for

example by TEM measurement) and the number of crystallites (N_{cryst}) on a catalyst:

$$N_{\text{exp, total}} = N_{\text{exp, cryst}} \cdot N_{\text{cryst}} \quad (4.14)$$

The number of exposed surface atoms on a crystallite was estimated using a method described by van Hardeveld and Hartog (1969) (see Appendix A.4, p. 158).

The number of ruthenium crystallites on a catalyst, N_{cryst} , can be calculated as follows:

$$N_{\text{cryst}} = \frac{V_{\text{cryst, total}}}{V_{\text{cryst}}} \quad (4.15)$$

with V_{cryst} , the volume of a single ruthenium crystallite:

$$V_{\text{cryst}} = \frac{1}{6} \cdot \pi \cdot \bar{d}_{\text{cryst}}^3 \quad (4.16)$$

and $V_{\text{cryst, total}}$, the volume of all crystallites in the catalyst loaded:

$$V_{\text{cryst, total}} = \frac{m_{\text{Ru, total}}}{\rho_{\text{Ru}}} \quad (4.17)$$

with $m_{\text{Ru, total}}$, being the total ruthenium mass on the catalyst (taking actual loading into account) and ρ_{Ru} , the density of ruthenium.

Chapter 5

Characterisation Results

5.1 Characterisation of the Reverse Micelle System and the Catalyst Support

For the reverse micelle systems in this study, stable and optically transparent water-in-oil microemulsions can only be synthesized in the highlighted region shown in Figure 4.1, p. 31 (see Mabaso (2005)). Phase separation or cloudy solutions were noticeable outside these limits.

5.1.1 Viscosity Measurements and Water-pool Size

All microemulsions prepared for this study were characterised by means of their viscosities. Table 5.1 lists viscosities of different microemulsions and calculated volume fractions, Φ (i.e. the formation of spherical micelles, comprising water-pool plus surfactant, in the ternary-phase system) based on the viscosity relation developed by Cheng and Schachmann (Kinugasa et al. (2002); see equation A.6 in Appendix A.5, p. 160).

An almost linear relationship was obtained between water-pool sizes (d_{wp}), calculated from volume fractions (Φ), and the water-to-surfactant weight ratios (ω_{wt}) (see Figure 5.1). It can be noted that an increase in the water-to-surfactant weight ratio from 0.02 to 0.4, results in only a five times larger water-pool size in the reverse micelle.

This dependency of micelle size with water-to-surfactant weight ratio had earlier also been reported by others for various microemulsion systems (Nagy et al. (1983), Stenius et al. (1984), Hall et al. (1998), Mabaso (2005)). Figure 5.1 also shows water-pool sizes using an idealistical equation derived by Mabaso (2005) (for derivation see Appendix A.5, pp. 160) which does not include inter-particle interactions and which is independent of viscosity:

$$d_{wp} = \frac{2 \cdot t_s}{\left(\frac{\rho_w + \omega_{wt} \cdot \rho_s}{\omega_{wt} \cdot \rho_s} \right)^{1/3} - 1} \quad (5.1)$$

where ρ_w is the density of water, ρ_s is the density of the surfactant and t_s is the effective length of the surfactant molecule ($t_s(\text{\AA}) = 1.5 + 1.265 N$ (Tanford, 1972)) with N being the number of carbon atoms in the chain.

Table 5.1: Viscosity (η) of microemulsion systems and respective volume fractions (Φ) of dispersed spheres.

Sample code	ω_{wt} in g/g	η in cp	Φ -
RM-1	0.089	0.721	0.0578
RM-2	0.089	0.596	0.0619
RM-3	0.400	0.721	0.1131
RM-4	0.095	0.786	0.1351
RM-5	0.125	0.891	0.1351
RM-6	0.023	1.109	0.2220
RM-7	0.089	0.828	0.1286
RM-8	0.089	0.636	0.0801
RM-9	0.103	0.756	0.1253
RM-10	0.125	0.714	0.1108
RM-11	-	-	-
RM-12	0.085	0.834	0.1502
RM-13	-	-	-

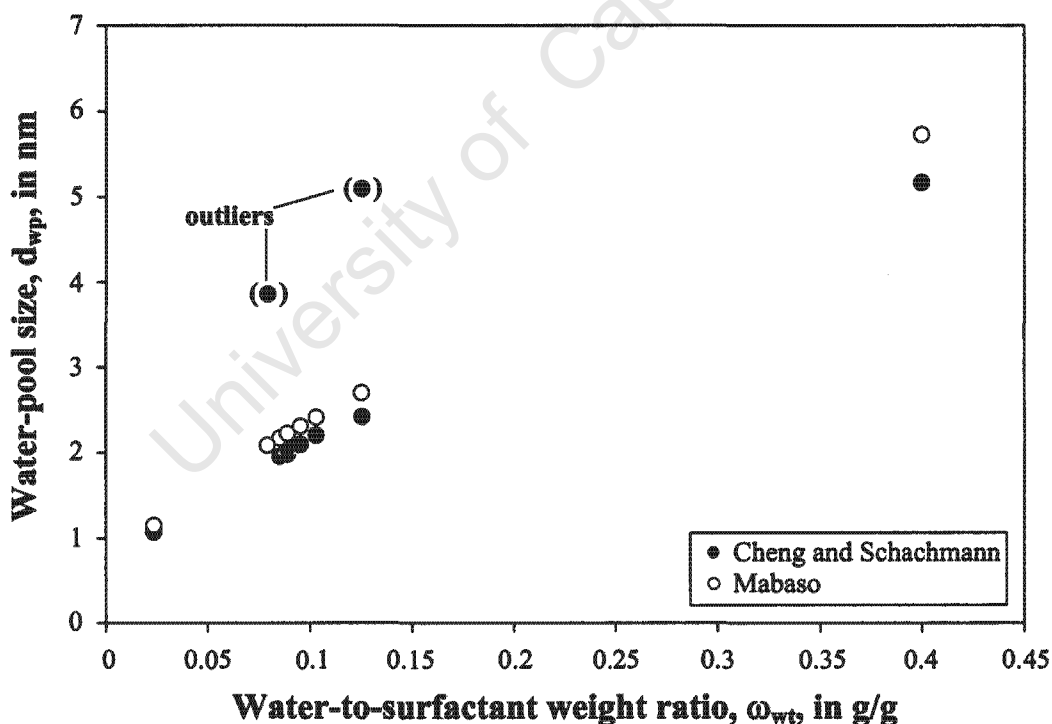


Figure 5.1: Water-pool size, d_{wp} , as estimated by viscosity correlation equation by Cheng and Schachmann, and calculated using equation by Mabaso.

This observed effect might be caused by the fact that, for a fixed amount of surfactant, the interfacial area, stabilized by the surfactant, is fixed and new water-pools cannot be formed if the water-to-surfactant weight ratio is increased. Therefore, water-pools must swell to accommodate extra water added to the system (Hall et al., 1998). At the same

metal salt concentration a decrease in water droplet size also causes the number of metal ions per droplet to decrease, which might affect sizes of the resulting metal crystallites on the catalyst support (see Section 5.2.1, p. 54).

5.1.2 Zetapotential of Support

Using zetapotential measurements, the isoelectronic point of the alumina support material was determined as being 9.0 (see Figure 5.2) indicating a very positively charged support surface during the preparation procedure as the used 0.15 molar RuCl_3 -solution is highly acidic ($\text{pH} = 1.87$) - for preparation details see Section 4.1.1, p. 29. It can thus be assumed that the ion exchange between O-H bonds on the support surface and the positively charged Ru^{3+} -ions provide the driving force for the immediate uptake of the ruthenium salt onto the support surfaces evidenced visually by fast discolouration of the reverse micelle system upon addition of the support material.

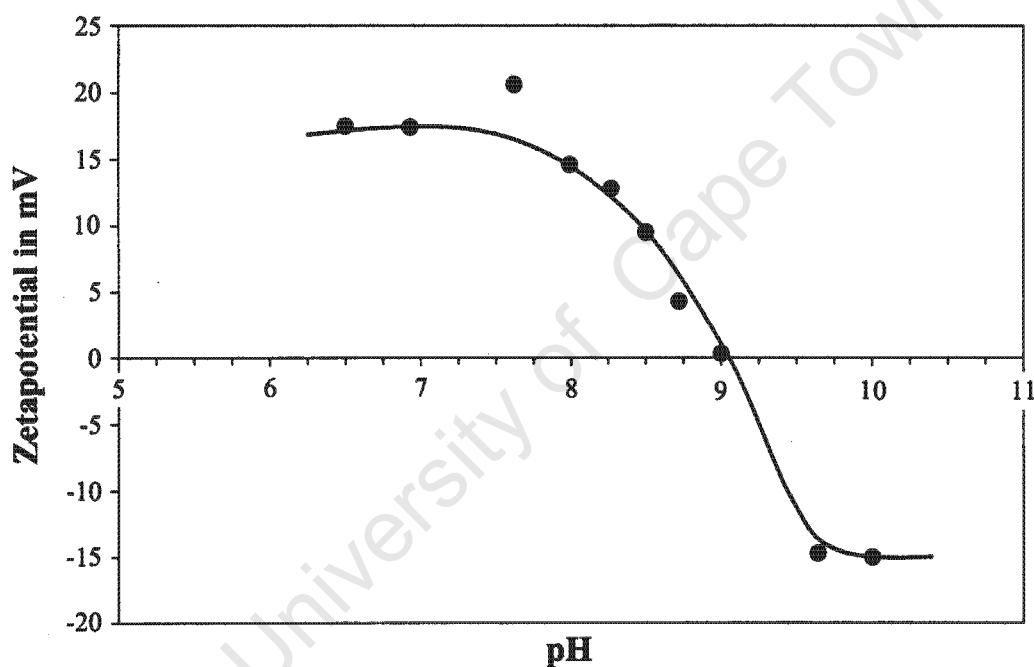


Figure 5.2: Zetapotential of alumina support as function of pH value.

5.2 Supported Nano-sized Crystallites

The alpha-numeric sample codes for the supported nano-sized crystallites (for details on the preparation see Section 4.1.1, p. 29) comprise the preparation method identifier RM, viz. Reverse Micelle, and a numerical indicator increasing towards larger crystallite sizes in the calcined catalyst.

Calcined catalyst refers to a catalyst in its oxidized state, as obtained after catalyst preparation and calcination.

Reduced catalysts refer to calcined catalysts that have undergone reductive pretreatment in flowing hydrogen at 300°C for five hours, a heating rate of 2°C/min and a space velocity of 24 ml(NTP)/(min·g_{cat}). In experimental FT runs this pretreatment was conducted prior to the run *in-situ* in the fixed-bed reactor. For characterisation purposes the catalysts were also reduced externally at the same conditions in an external glass tube fluidized-bed reactor. To allow handling of these samples in air they were subsequently exposed to flowing carbon dioxide at room temperature for one hour. This commonly used passivation process is believed to form a thin protective oxide layer around the reduced crystallites without affecting the crystallite morphology or size (Mabaso, 2005). Characterisations of reduced catalysts are crucial to ascertain the phases present after catalyst pretreatment, to determine the exact metal crystallite size just prior to catalytic test experiments, and to check for possible hydrogen pretreatment induced changes in catalyst crystallite size.

5.2.1 TEM Analysis of Supported Nano-sized Crystallites

Transmission electron micrographs of four selected calcined and reduced model catalysts are shown in Figure 5.3. Crystallites of ruthenium are clearly visible as dark spots on the alumina support. These crystallites are fairly well distributed over the support indicating the suitability of this method for preparation of model catalysts. Only little tendency for cluster formation was observable, mainly in the samples with larger crystallites. The corresponding histograms in Figure 5.4 depict size distributions based on size evaluation of a minimum of 300 crystallites from such micrographs (see Appendix A.2, Figure A.1, p. 155 for samples not shown in Figure 5.4).

Based on these results crystallite sizes in the catalysts ranging between 2 to 10 nm were synthesized by adjusting the composition of the microemulsions (see Section 4.1.1, p. 29). The crystallite size distributions were typically narrow with relative standard deviations^a between 15 and 35% for the calcined samples and 16 to 27% for the reduced samples (see Table 5.2). Negligible changes in crystallite sizes and distributions indicated the absence of severe sintering upon reductive treatment. Ideally, reduced catalysts were expected to be smaller than those in calcined catalysts due to the lower density of ruthenium dioxide ($\rho(\text{RuO}_2) = 6.5 \text{ g/cm}^3$) when compared to metallic ruthenium ($\rho(\text{Ru}) = 12.7 \text{ g/cm}^3$). Slightly larger obtained sizes may possibly be explained by sintering of smaller crystallites to thermodynamically more stable sizes.

^aStandard deviations were calculated as follows:

$$\sigma = \sqrt{\frac{1}{N} \sum_{i=1}^N (d_i - \bar{d})^2} \quad (5.2)$$

with N the number of crystallites, d_i the diameter of a single crystallite i and \bar{d} the average diameter of N crystallites.

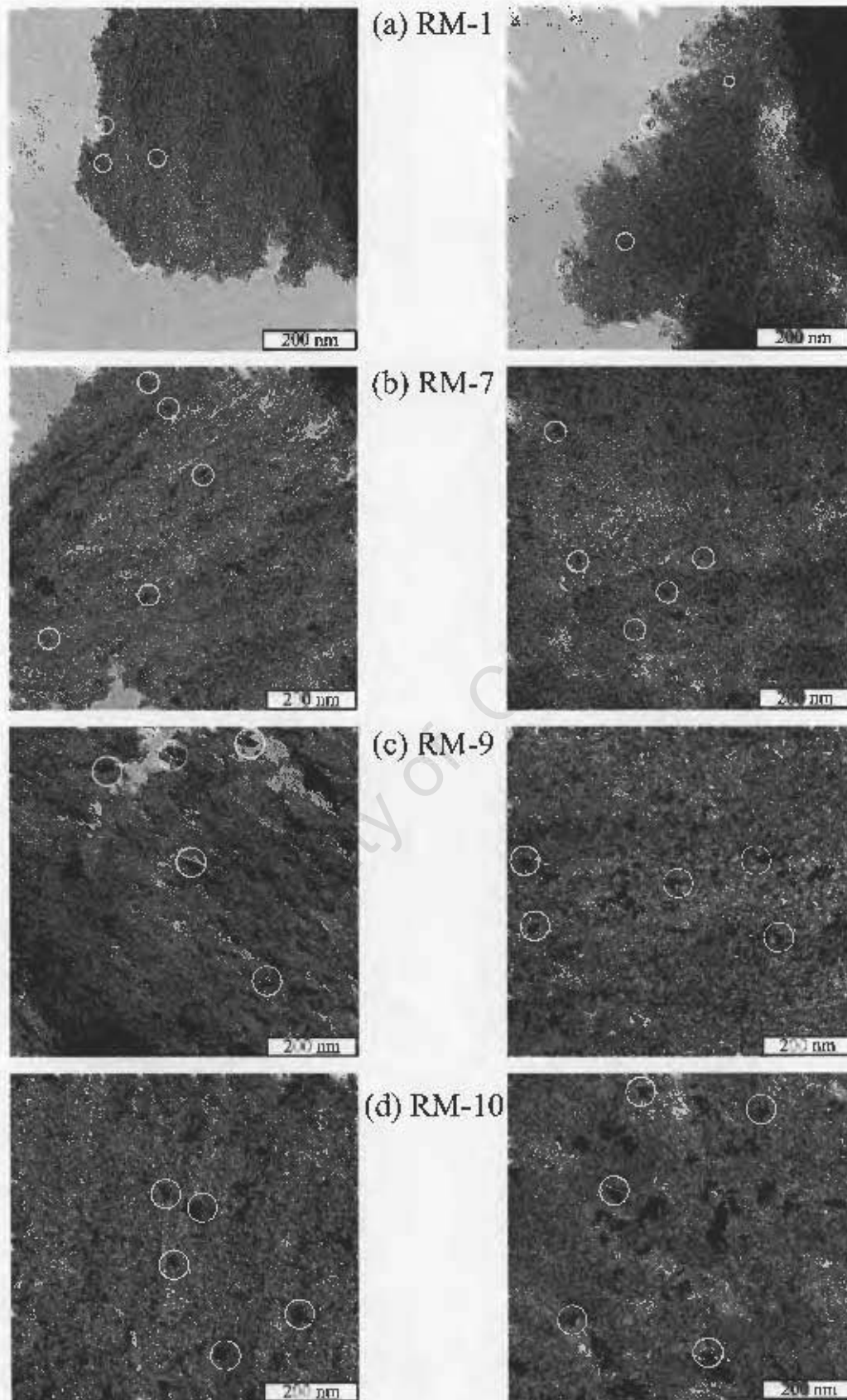


Figure 5.3: TEM micrographs of four selected alumina supported nano-sized crystallites; *left*: after calcination, *right*: after reduction and passivation.

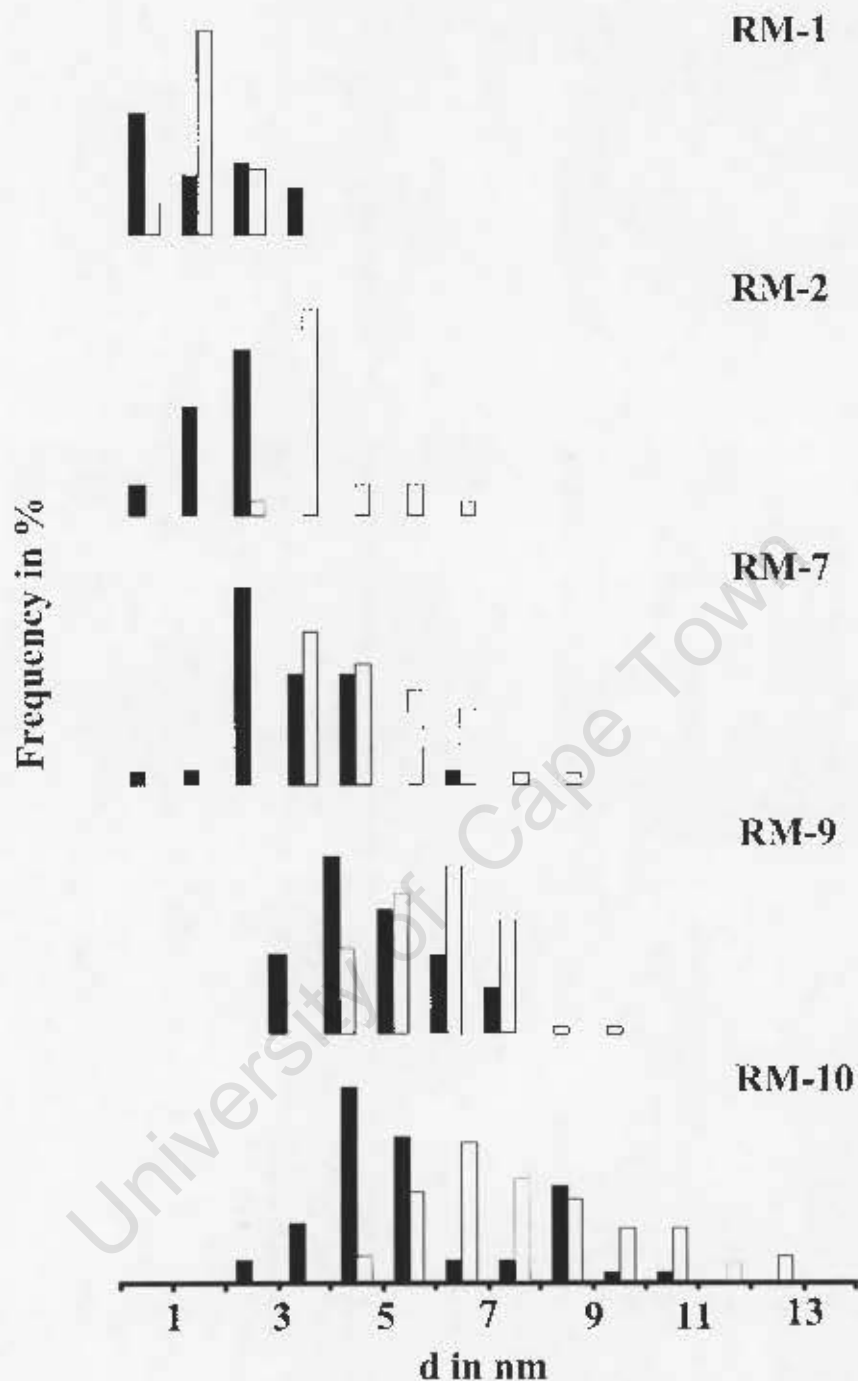


Figure 5.4: Crystallite size distributions of five selected calcined (*closed bars*) and reduced (*open bars*) alumina supported nano-sized crystallites as determined by means of TEM analysis. (For crystallite size distributions of remaining supported nano-sized crystallites see Appendix A.2, Figure A.1, p. 155.)

It must be noted, though, that the Hüttig temperature^b, which indicates the probability of surface atom mobility, was not exceeded during reduction.

^bThe Hüttig temperature of ruthenium ($T_{\text{Hüttig}}$) is 544°C (Moulijn et al., 2001).

Table 5.2: TEM characterisation results of calcined and reduced supported nano-sized crystallites.

Sample code ^c	$\bar{d}_{\text{calc-TEM}} \pm \sigma^a$ in nm	$\bar{d}_{\text{red-TEM}} \pm \sigma^b$ in nm	$N_{\text{exp-calc}}^c$	$N_{\text{exp-red}}^d$
RM-1	1.7±0.6	1.5±0.3	570	510
RM-2	2.8±0.7	3.9±0.9	1870	3680
RM-3	3.0±0.8	4.1±1.1	2190	3690
RM-4	3.4±0.7	3.8±0.9	2600	3550
RM-5	3.5±1.0	4.1±1.0	2890	3680
RM-6	4.8±0.8	4.7±0.9	5250	5050
RM-7	5.3±0.9	4.9±1.1	6600	5600
RM-8	5.4±1.6	6.3±1.0	7200	9700
RM-9	5.5±1.1	6.7±1.1	7250	10500
RM-10	8.2±1.2	8.3±1.8	16000	16500
RM-11	8.6±1.9	7.9±1.3	17750	15000
RM-12	9.6±2.0	7.7±1.3	23000	14300
RM-13	10.5±2.6	9.6±2.2	27000	22000

^a average crystallite sizes and relative standard deviations of the calcined catalysts obtained from TEM analyses

^b average crystallite sizes and relative standard deviations of the reduced catalysts obtained from TEM analyses

^c number of exposed ruthenium surface atoms per crystallite of average size in calcined catalysts

^d number of exposed ruthenium surface atoms per crystallite of average size in reduced catalysts

Previous work by Mabaso (2005), in which crystallites of iron oxide were prepared from the same reverse micelle system as used in this work, showed an almost linear increase of the prepared crystallites with increasing water-to-surfactant weight ratio and water-pool size respectively. When plotting the average crystallite sizes of the calcined catalysts produced in this work over the water-to-surfactant weight ratio no such correlation can be found (see Figure 5.5).

The two studies, however, differ in their approach in that in Mabaso's work the crystallite precursors were obtained by precipitation via combining two reverse micelle solutions (iron salt solution plus precipitant solution) before support addition, whereas in this work the ruthenium salt containing reverse micelle solution was contacted directly with the alumina support. It is evident that the size of the reverse micelle is not, or at least not the only, determining factor. While in Mabaso's work precipitate or crystallites respectively form within the confined space of the reverse micelle, the crystallite formation in this work only takes place during drying and calcining. From visual observation during catalyst synthesis of a fast discolouration of the micelle solution upon support addition, it appears that either the micelles or the aqueous ruthenium chloride solution may have been taken up by the support.

It should be noted, though, that although the micelles (including the surfactant) should be small enough to enter the pore system of the support material, which has an average pore size of 11.5 nm, the pore volume of the support (0.47 cm³/g) would not be able to accommodate the 4 to 20 times larger combined volume of the water and the surfactant phase in the preparation. It is therefore more likely that the polar water phase directly enters the pore system of the support material when the ruthenium gets deposited. (Note that except in preparations of RM-1, RM-3 and RM-4, where low concentrations of

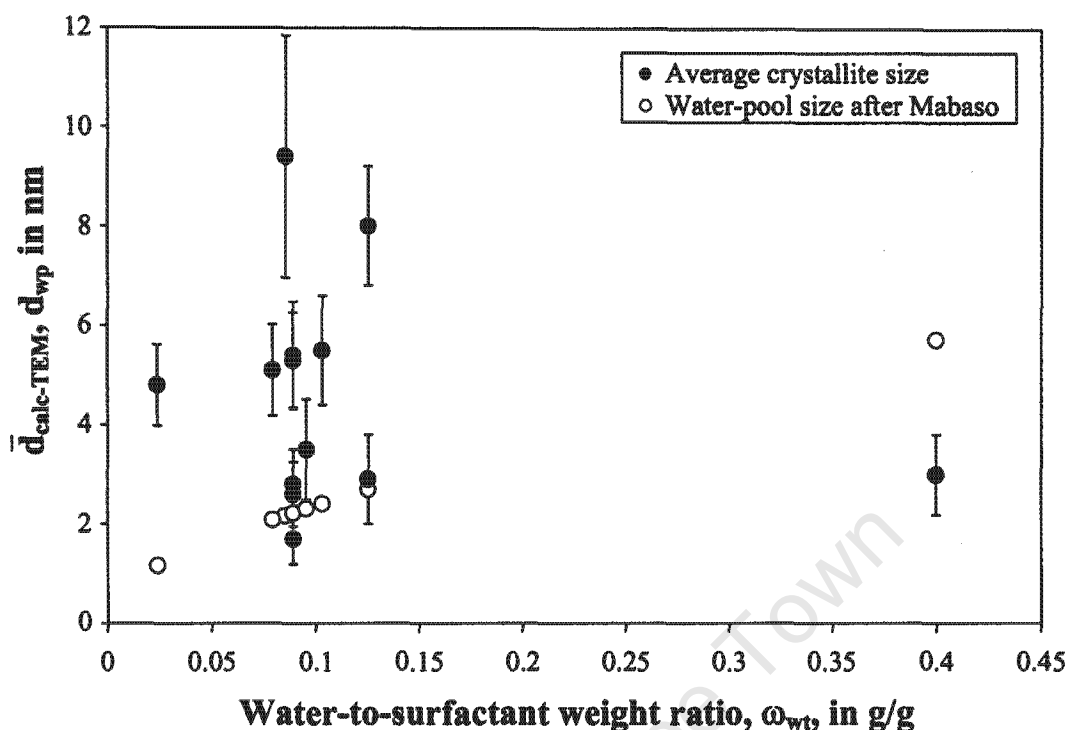


Figure 5.5: Average crystallite size of calcined catalyst and the corresponding water-pool size in the corresponding reverse micelle solution they were prepared from, as function of water-to-surfactant weight ratio; y-bars indicate width of distribution expressed as standard deviation.

ruthenium salt were used, the water phase amounts to only half of the pore volume of the support added.) This might then coincide with a collapse of the reverse micelle system and coalescence of water-pools and the ruthenium ions therein. A combination of ruthenium atoms from several water-pools is also necessary to account for the formation of crystallites of the observed size, as, for example, the ruthenium atoms in the largest water-pool (10 nm) obtained in this study should only generate crystallites sized below 0.8 nm. Although it is not clear how the ruthenium crystallites form and how the composition of the reverse micelle system impacts on the size of the crystallites formed, a number of distinctly different model catalysts could be prepared with this method. No obvious design parameters could be identified as yet, but it appears that among the wide range of reverse micelle systems prepared the ones towards the confine of the stability region of the reverse micelle systems result in larger crystallites (see Figure 5.6).

It may further be noted that the ruthenium salt concentration seems to have no obvious effect on the resulting ruthenium crystallite size (see samples RM-1 and RM-2, where increasing the ruthenium concentration by a factor of four only led to a size increase from 1.7 to 2.8 nm, while a 30% increase in this concentration between samples RM-11 and RM-12 led to a slight decrease in crystallite size). Samples RM-10 and RM-13 were prepared from reverse micelle solutions with a composition which lies on the border of the reverse micelle stability region. Here much larger crystallites were formed than expected from the described trend. The samples also show the least homogeneous crystallite size population with almost bimodal distributions as determined by means of TEM analyses (see Figure 5.4 and Figure A.1 in Appendix A.2, p. 155). It may be speculated that no homogeneous and stable reverse micelle system was present in these preparations,

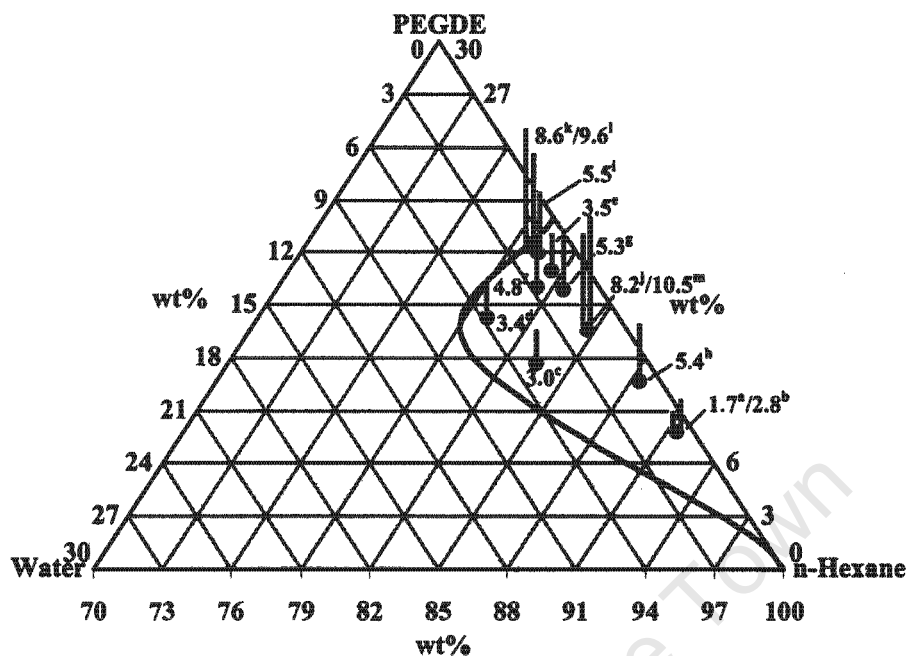


Figure 5.6: Ternary-phase diagram of water-PEGDE-n-hexane reverse micelle system indicating the stability region for the reverse micelles (as established by Mabaso (2005)), the composition of the reverse micelle systems RM-1 to RM-13 used in this work and the resulting average crystallite sizes of the calcined catalysts (in nm). (Alphabetic codes correspond to the following catalysts: a: RM-1; b: RM-2; c: RM-3; d: RM-4; e: RM-5; f: RM-6; g: RM-7; h: RM-8; i: RM-9; j: RM-10; k: RM-11; l: RM-12; m: RM-13)

possibly leading to regions of water-pool regions not fully stabilized by surfactant, which would impact on the mechanism of ruthenium deposition and crystallite formation.

5.2.2 Chemisorption Analysis of Supported Nano-sized Crystallites

Average ruthenium crystallite sizes on reduced samples were also obtained from CO-chemisorption analyses (see Table 5.3), assuming spherical crystallite shapes (for calculation see Section 4.5.3, p. 39). Prior to these analyses the samples were reduced *in-situ* in hydrogen at conditions identical to reductions before the start of FT experiments.

Trends obtained were in qualitative agreement with TEM analyses (see Section above). However, average sizes obtained for smaller crystallites in particular tend to exceed sizes found by means of TEM evaluation. This may be because the assumed 1:1 stoichiometry (see Section 4.5.3, p. 39) of carbon monoxide on metallic ruthenium does not hold for smaller crystallites, where larger numbers of corner and edge metal atoms could adsorb larger amounts of carbon monoxide than on a plane face (see e.g. Dalla Betta et al. (1974)).

Table 5.3: Dispersion (D) and average ruthenium crystallite sizes for reduced supported nano-sized crystallites ($\bar{d}_{\text{CO-Chem.}}$) by means of CO-chemisorption. Also listed are crystallite sizes from TEM analyses (see Table 5.2).

Sample code	D in %	$\bar{d}_{\text{red-Chem.}}$ in nm	$\bar{d}_{\text{red-TEM}} \pm \sigma$ in nm
RM-1	33.3	4.0	1.5±0.3
RM-2	35.5	3.8	3.9±0.9
RM-3	28.2	4.7	4.1±1.1
RM-4	26.4	5.1	3.8±0.9
RM-5	34.5	3.9	4.1±1.0
RM-6	29.4	4.5	4.7±0.9
RM-7	29.4	4.5	4.9±1.1
RM-8	11.1	12.1	6.3±1.0
RM-9	17.3	7.7	6.7±1.1
RM-10	11.5	11.6	8.3±1.8
RM-11	8.9	15.0	7.9±1.3
RM-12	16.6	8.0	7.7±1.3
RM-13	n/a	n/a	9.6±2.2

5.2.3 TPR Analysis of Supported Nano-sized Crystallites

The reduction behaviour of model catalysts was characterised by means of TPR analyses. The recorded hydrogen consumption as function of temperature for all 13 samples is plotted in Figure 5.7.

All curves show a single narrow reduction peak between 150 and 250°C, indicative of the one-step reduction of ruthenium dioxide to metallic ruthenium ($\text{RuO}_2 + 2 \text{H}_2 \rightarrow \text{Ru} + 2 \text{H}_2\text{O}$). The narrowness of the peak suggests this transformation to be a fast process (Koopman et al., 1981). It is evident from the TPR spectra that complete reduction was obtained in all samples and that the pretreatment in hydrogen at 300°C before the reaction is sufficient for complete catalyst reduction. There was a slight shift of the reduction peak towards higher reduction temperatures for the smallest crystallite sizes, possibly indicating metal-support interactions (King, 1978).

Ruthenium loadings of the catalysts were determined from TPR analyses. 1.4 to 3.2 wt% metal loadings were obtained at an anticipated 3 wt% metal loading. This indicates a loss of ruthenium during preparation of some of the samples (see Table 5.4 for analysis results). This loss was particularly pronounced in samples RM-3 and RM-4 where low ruthenium salt concentrations and large amounts of water were used.

5.2.4 Further Characterisation of Supported Nano-sized Crystallites

Attempts to measure average crystallite sizes in calcined and reduced samples by means of XRD analyses were unsuccessful as no ruthenium dioxide or ruthenium diffraction peaks could be detected (see Figure 5.8 as example of an XRD pattern of calcined sample RM-10 and the pure support material). The ruthenium loading on the samples is probably

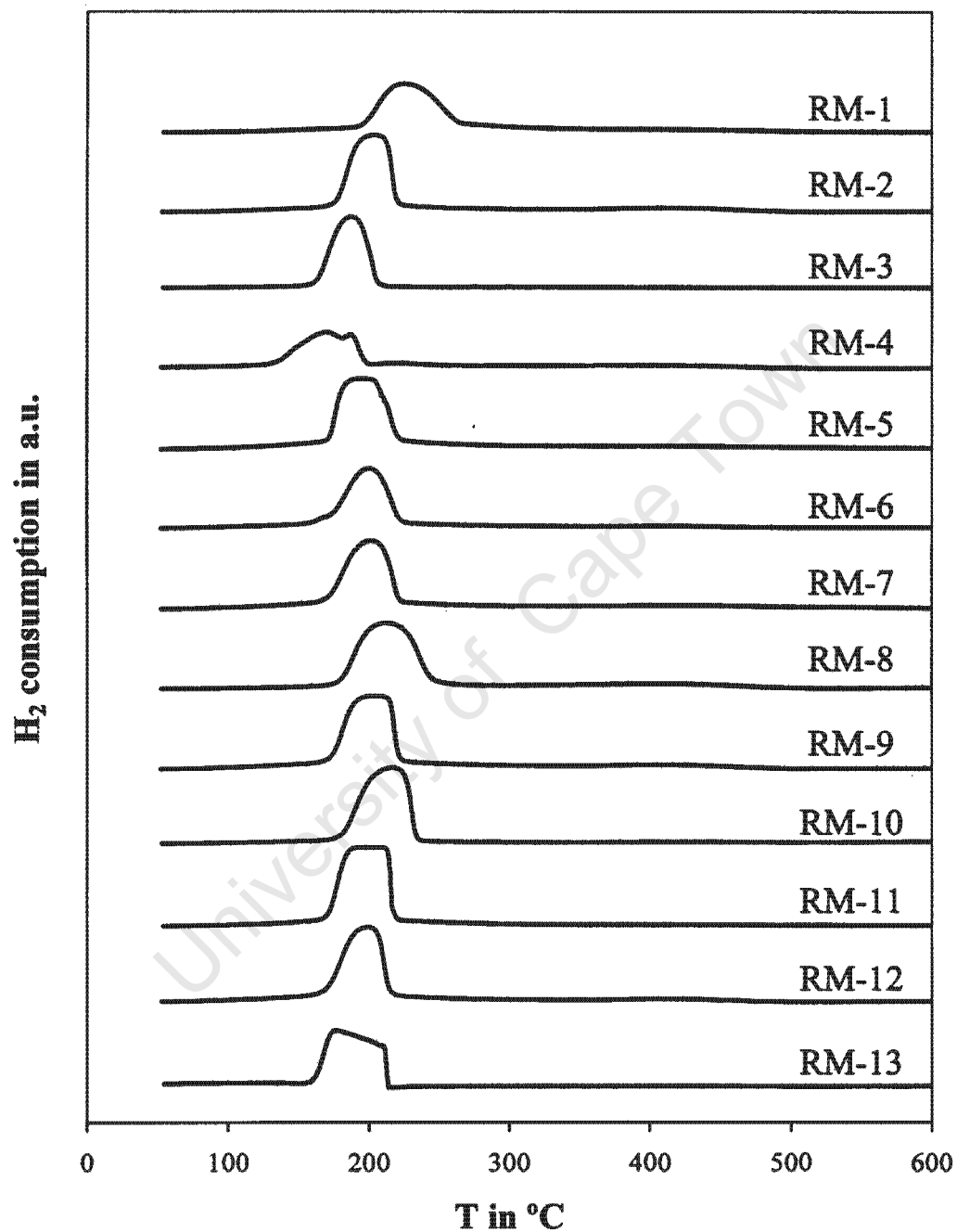


Figure 5.7: TPR patterns of the different alumina supported nano-sized crystallites.

too low to allow for reliable XRD characterisation.

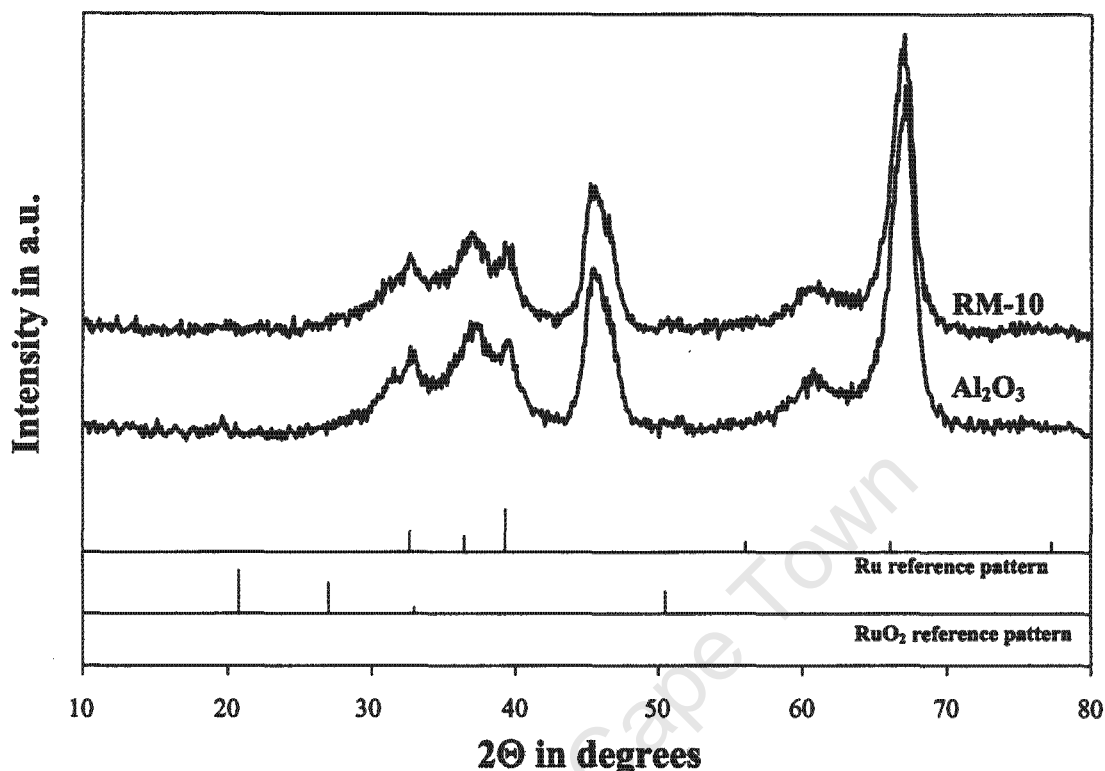


Figure 5.8: XRD patterns of calcined sample RM-10 and pure alumina support, including reference patterns for metallic ruthenium and ruthenium dioxide.

The catalysts were also analysed for the possible presence of any residual organic matter (e.g. the surfactant) which might still be present on the samples after catalyst preparation. The effective removal of the surfactant from the catalyst before FT experiments is crucial as it might hinder access to active catalytic sites, thus impacting on measured catalyst activities. Washing steps of the uncalcined samples in acetone (for catalyst preparation see Section 4.1.1, p. 29) may not be effective for complete surfactant removal (as shown by Mabaso (2005)). Therefore, ampoule samples of the “product” gas were taken and analysed during reductive pretreatment of the catalysts in the reactor before commencement of FT testing. Indeed, trace amounts of unidentified organic products were found during initial stages of the 300°C reduction, probably due to hydrogenolytic break up of larger molecules, catalysed by metallic ruthenium, which is known to be a very effective catalyst for this reaction (Carter and Sinfelt, 1978). However, after five hours reductive pretreatment at this temperature no products could be detected and it was thus assumed that the reduced catalysts were free of any carbonaceous material.

5.2.5 Summary of Characterisation Results of Alumina Supported Nano-sized Crystallites

In conclusion, model catalysts with narrow crystallite size distributions and average crystallite sizes ranging between 2 and 10 nm were successfully prepared using the reverse micelle technique (see Table 5.4). Their model character remained mainly unaffected

throughout the reductive pretreatment, resulting in ideally suited catalyst systems for the anticipated experiments. Table 5.4 summarizes data obtained by means of different characterisation techniques. It also includes the number of exposed ruthenium metal atoms per average sized ruthenium crystallite as determined by TEM analyses. These values were used for interpretations of possible size effects obtained at initial stages of FT experiments.

Table 5.4: Characterisation data of calcined and reduced alumina supported nano-sized crystallites.

Sample code	TPR	TEM		$N_{\text{exp-red}}^b$	Chemis.
	$x_{\text{Ru-TPR}}^a$ in wt%	$\bar{d}_{\text{calc-TEM}} \pm \sigma$ in nm	$\bar{d}_{\text{red-TEM}} \pm \sigma$ in nm		$\bar{d}_{\text{red-Chem.}}$ in nm
RM-1	2.8	1.7±0.6	1.5±0.3	510	4.0
RM-2	2.8	2.8±0.7	3.9±0.9	3680	3.8
RM-3	1.7	3.0±0.8	4.1±1.1	3690	4.7
RM-4	1.4	3.4±0.7	3.8±0.9	3550	5.1
RM-5	2.2	3.5±1.0	4.1±1.0	3680	3.9
RM-6	2.1	4.8±0.8	4.7±0.9	5050	4.5
RM-7	2.8	5.3±0.9	4.9±1.1	5600	4.5
RM-8	3.1	5.4±1.6	6.3±1.0	9700	12.1
RM-9	3.0	5.5±1.1	6.7±1.1	10500	7.7
RM-10	3.2	8.2±1.2	8.3±1.8	16500	11.6
RM-11	2.7	8.6±1.9	7.9±1.3	15000	15.0
RM-12	2.5	9.6±2.0	7.7±1.3	14300	8.0
RM-13	1.8	10.5±2.6	9.6±2.2	22000	n/a

^a ruthenium loading obtained from TPR analyses

^b number of exposed ruthenium surface atoms per crystallite of average size in reduced catalysts

5.3 Organometallic Model Catalysts

Characterisation of unsupported and supported organometallic ruthenium compounds is described in the following Section. Alpha-numerical sample codes for unsupported and supported clusters contain "Ru" for Ruthenium, followed by the number of metal atoms in the cluster framework. Sample codes for the three different diatomic ruthenium complexes additionally include a letter code, a, b or c^d. *Fresh catalysts* refer to clusters immobilized on the support (see Section 4.1.2, p. 37).

5.3.1 Thermal Stability of Unsupported Organometallic Clusters in Different Gases

The thermal stability of the unsupported organometallic clusters was characterised by means of TGA analysis in nitrogen. The stability increases for larger cluster frameworks (see Figure 5.9) probably caused by an increasing metallic character in the framework of larger clusters. The high stability of the diatomic ruthenium compounds can be explained by their stabilising cyclopentadiene ligands, generating a positive inductive effect (+I-effect). This enhanced +I-effect increases the electron density on the electron poor metal atoms thus increasing thermal stability of these complexes.

TGA analyses on the compounds were also done using hydrogen and carbon monoxide containing gases to study their thermal and chemical stability in these components of FT synthesis gas. For reasons of instrumental limitations these gases were only used in dilute form, i.e. 5 vol% hydrogen in argon and 5 vol% carbon monoxide in nitrogen. The corresponding results of these analyses are shown in Figures A.5 and A.6 in Appendix A.6, pp. 163 and the observed decomposition temperatures of all TGA analyses are listed in Table 5.5.

Table 5.5: Decomposition temperatures (T_{decomp}) of organometallic clusters in different gas atmospheres determined by means of TGA analyses.

Sample code	Compound	T_{decomp} (°C)		
		in N ₂	in H ₂ /Ar	in CO/N ₂
Ru-2a	Ru ₂ (CO) ₄ (η^5 -C ₅ H ₅) ₂	235	250	251
Ru-2b	Ru ₂ (CO) ₄ (η^5 -C ₅ (CH ₃) ₅) ₂	295	>280	259
Ru-2c	Ru ₂ (CO) ₂ (μ -CO)(μ -CHMe)(η^5 -C ₅ H ₅) ₂	232	263	263
Ru-3	Ru ₃ (CO) ₁₂	172	179	185
Ru-4	Ru ₄ (μ -H) ₄ (CO) ₁₂	198	202	223
Ru-5	Ru ₅ C(CO) ₁₅	205	227	234
Ru-6	Ru ₆ C(CO) ₁₇	244	224	232

The gas environment appeared to have only a small effect on the stabilities of organometallic compounds. Based on decomposition temperature of the least stable compound, Ru-3, the reaction temperature for the FT experiments using these compounds was set to 170°C.

^da = Ru₂(CO)₄(η^5 -C₅H₅)₂; b = Ru₂(CO)₄(η^5 -C₅(CH₃)₅)₂; c = Ru₂(CO)₂(μ -CO)(μ -CHCH₃)(η^5 -C₅H₅)₂

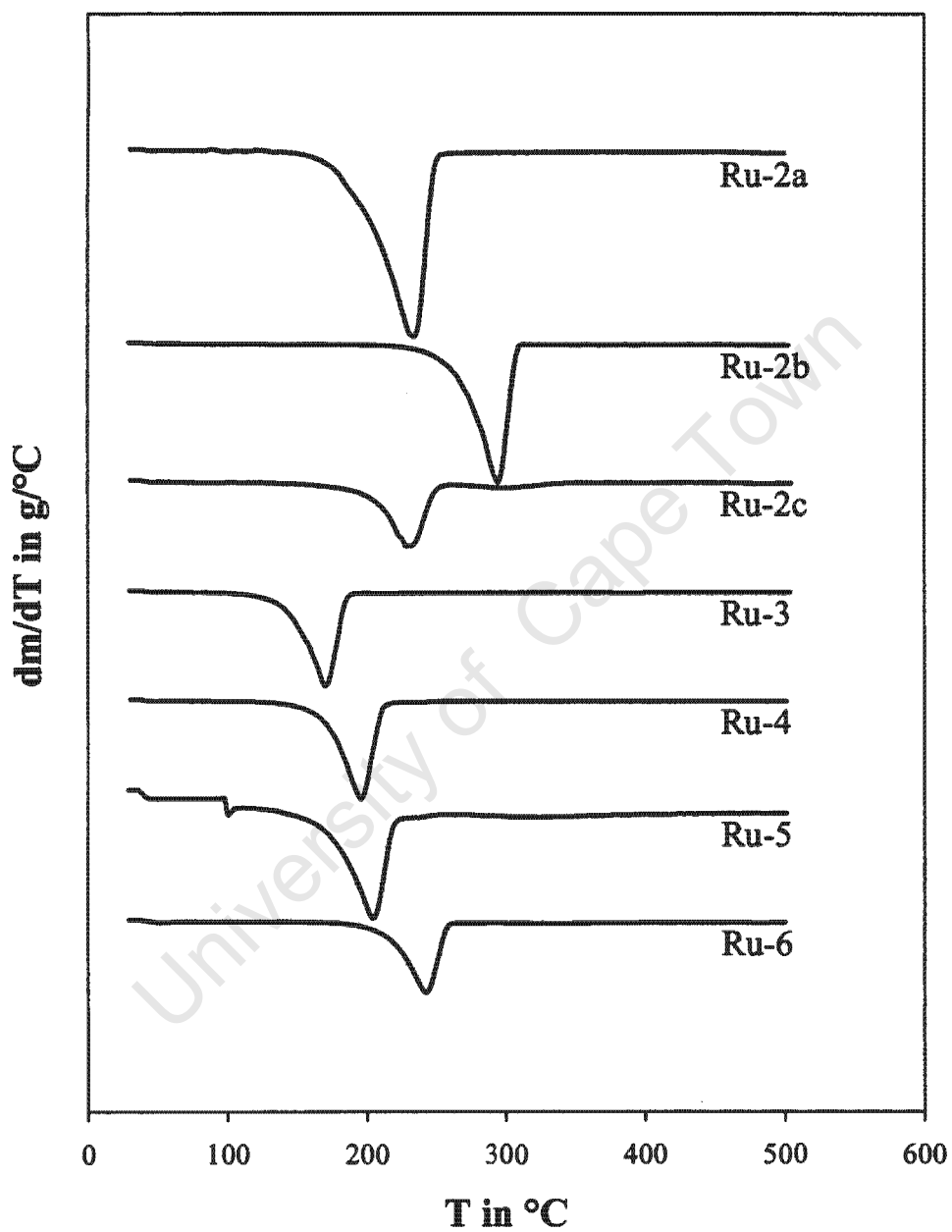


Figure 5.9: First derivative of weight vs. temperature profile from TGA analysis for the different organometallic complexes in nitrogen.

5.3.2 Characterisation of Alumina Supported Organometallic Clusters

After impregnation of the organometallic clusters onto the alumina support material, the model catalysts were investigated by means of TEM analyses. The absence of larger cluster agglomerates suggested preservation of the cluster framework during immobilization on the support. No loss of compounds was assumed to occur during the impregnation onto the support, i.e. no further chemical analyses was conducted. Ruthenium loading was therefore assumed to be 3 wt% in all samples. It was further assumed that all ruthenium atoms in a cluster are "exposed" and therefore available for possible reaction with synthesis gas in the FT experiments.

Table 5.6 summarizes characteristics of the supported organometallic compounds indicating the assumed number of exposed ruthenium atoms per gram of supported model catalyst.

Table 5.6: Summary of alumina supported organometallic compounds.

Sample code	Compound ^a	x_{Ru} ^b in wt%	N_{exp} ^c
Ru-2a	$\text{Ru}_2(\text{CO})_4(\eta^5\text{-C}_5\text{H}_5)_2$	3	2
Ru-2b	$\text{Ru}_2(\text{CO})_4(\eta^5\text{-C}_5(\text{CH}_3)_5)_2$	3	2
Ru-2c	$\text{Ru}_2(\text{CO})_2(\mu\text{-CO})(\mu\text{-CHMe})(\eta^5\text{-C}_5\text{H}_5)_2$	3	2
Ru-3	$\text{Ru}_3(\text{CO})_{12}$	3	3
Ru-4	$\text{Ru}_4(\mu\text{-H})_4(\text{CO})_{12}$	3	4
Ru-5	$\text{Ru}_5\text{C}(\text{CO})_{15}$	3	5
Ru-6	$\text{Ru}_6\text{C}(\text{CO})_{17}$	3	6

^a supported on alumina

^b metal loading of freshly prepared catalysts

^c number of ruthenium metal atoms in organometallic compounds

Chapter 6

Fischer-Tropsch Testing of Model Catalysts

6.1 Supported Nano-sized Crystallites

Catalytic performances of supported nano-sized crystallites were tested in a fixed-bed reactor with 1.26 g of catalyst loaded. *In-situ* reduction of the calcined catalyst was done in pure hydrogen prior to the start of each FT experiment (at 300°C for 5 hrs, heating rate of 2°C/min). All catalysts were tested at a reaction temperature of 170°C, a total pressure of 4 bar and a constant synthesis gas flow rate with a hydrogen to carbon monoxide ratio of 2. In addition, five selected catalysts (RM-2, RM-3, RM-7, RM-9 and RM-10) were tested at elevated temperatures and pressures (225°C, 20 bar). All experiments were run over a five day period. In the low temperature/pressure experiments, temporal changes were monitored from the start to the steady-state of an experiment, whereas only steady-state data are reported for the elevated temperature/pressure experiments. Data reported for initial catalysts behaviour refer to crystallite sizes of the freshly reduced catalysts, whereas at steady-state crystallite sizes of the spent catalysts were used. For clarity some of the Figures below only show data of selected runs. Relevant reaction data of all the runs conducted are listed in Tables B.1-B.5, Appendix B.2, pp. 167.

6.1.1 Fischer-Tropsch Activity

FT activity was expressed in terms of turnover frequencies in order to investigate specific effects of crystallite size on it. The turnover frequencies were based on product formation rates per number of metal surface atoms present after pretreatment in hydrogen, while taking actual metal loadings into account. Note that conversion levels in the low temperature/pressure experiments were below 1% and therefore activity had to be determined from product formation rates obtained from analyses of organic products using the internal standard (see Section 4.8, p. 48). The carbon monoxide conversion levels in the elevated temperature/pressure experiments ranged between 25 and 45% and could be measured directly via the online GC with TCD detection. No carbon dioxide formation was detected via TCD analysis, indicating that carbon dioxide selectivities were below 1 C%. Traces of carbon dioxide could be found using offline GC/MS analysis, but these have not been quantified. Turnover frequencies of the volatile organic compounds (C₁-C₉ hydrocarbons) were obtained from FID analyses only.

Catalyst activities of the low temperature/pressure runs as function of time on stream

are shown in Figure 6.1 (top). Generally, severe catalyst deactivation was observed over the first 10-15 minutes. Larger crystallites displayed higher specific activities (TOF), which appear to peak at earlier stages of the reaction (1-3 minutes) when compared to activities obtained on the smaller crystallites (maximal specific activities at 2-3 minutes). Steady-state was reached after ca. 1000 minutes and product spectra showed formation of C_1 to C_{9+} hydrocarbons (see typical chromatogram in Appendix B.1, Figure B.2, p. 166).

Figure 6.1 (bottom) plots the crystallite size dependency of turnover frequencies of the volatile organic products (VOC's, C_1 - C_9 hydrocarbon-fraction) obtained with all catalyst samples at maximum initial activity, i.e. after 1-3 minutes time on stream, and at steady-state after more than 1000 minutes runtime. Steady-state turnover frequencies for the VOC's (C_1 - C_9) obtained in the tests at elevated temperature/pressure are included in the bottom of Figure 6.1. All data shown for early runtimes refer to crystallite sizes of the freshly reduced catalysts while steady-state data take crystallite sizes of the "spent catalysts"^a into account.

Although exhibiting relatively large scatter at, particularly, the initial stages (mainly believed to be due to the difficulties in capturing the maximum activity) smaller crystallites generally appeared to be less active than larger ones at all reaction periods and conditions, although apparently less pronounced at elevated temperature and pressure. Similar steady-state behaviour in ruthenium based FT synthesis has been described on catalysts with broad or unknown crystallite size distributions (King (1978), Kellner and Bell (1982), Abrevaya et al. (1990), Ragaini et al. (1996)) and for FT synthesis on well-defined iron, cobalt and rhodium catalysts (Ojeda et al. (2004), Mabaso (2005), Barkhuizen et al. (2006), Bezemer et al. (2006), Mabaso et al. (2006)).

In two of these studies clear indications were observed that turnover frequencies levelled off above certain crystallite sizes, namely around 5-6 nm for cobalt (Bezemer et al., 2006) and 7-8 nm for iron catalyst (Mabaso (2005), Barkhuizen et al. (2006), Mabaso et al. (2006)). This was not found in the present work. All studies listed above report catalyst performances at steady-state conversion, and refer to crystallite sizes or metal surface areas of the freshly reduced catalyst as determined by means of chemisorption or TEM analyses. Strictly this is only applicable in experiments in which no severe effects of crystallite sintering are observed. This study therefore puts large emphasis on monitoring temporal changes of catalyst performance as well as size characterisation of freshly reduced and spent catalysts.

Figure 6.2 depicts TEM micrographs of four selected samples of spent catalysts with different ruthenium crystallite sizes tested at 170°C and 4 bar and two selected ones tested at 225°C and 20 bar. These micrographs are clearly similar to the corresponding micrographs of the freshly reduced samples (see Figure 5.3, p. 55) that show largely well dispersed crystallites and some clusters of crystallites present in the samples with larger crystallites. The crystallite size distributions remained largely unaffected during runtime, pronounced sintering was only obtained for the small ruthenium crystallites that were tested (see Figure 6.3 and Figure A.2, p. 157 in Appendix A.2). Similarly, no significant changes in crystallite sizes were observed in the catalysts tested at elevated temperature and pressure (see Table 6.1). The catalyst deactivation shown in Figure 6.1, which was observed for all samples to a similar extent (i.e. a factor 5-10, see

^a"Spent catalysts" refer to catalyst samples evaluated after FT testing, overnight subjection to argon flow and one hour subjection to carbon dioxide flow at room temperature.

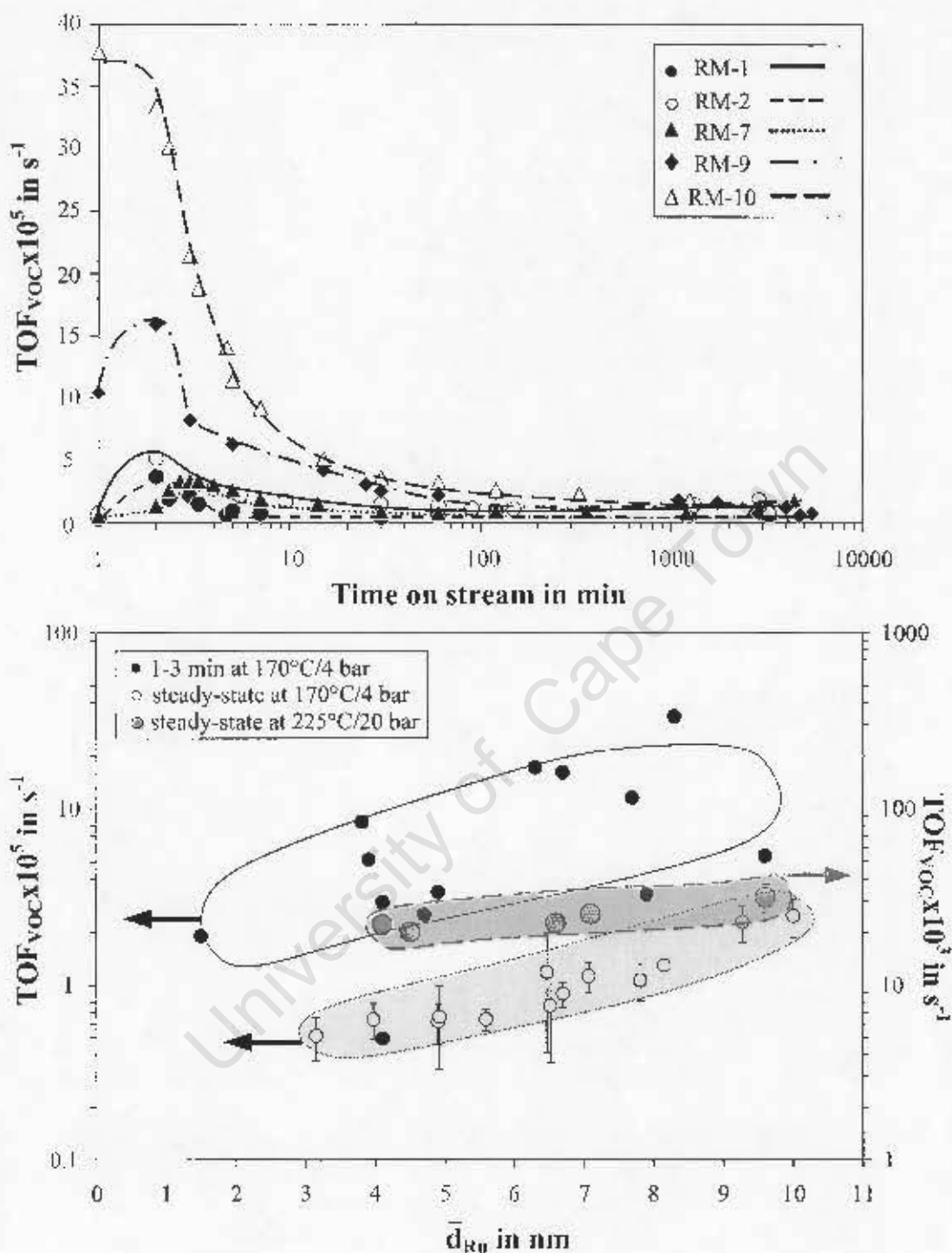


Figure 6.1: *top:* Changes in turnover frequencies of volatile organic compounds in FT synthesis at 170°C/4 bar as function of time on stream for five selected alumina supported nano-sized ruthenium crystallites.

bottom: Maximal initial and average steady-state turnover frequencies of volatile organic compounds in FT synthesis versus average ruthenium crystallite size of fresh (1-3 minutes runtime) or, respectively, spent (steady-state) catalysts.

(Note: Average crystallite sizes obtained from TEM micrographs of freshly reduced and spent catalysts.)

($T_{\text{Reaction}} = 170^\circ\text{C}/225^\circ\text{C}$, $P = 4 \text{ bar}/20 \text{ bar}$, $\text{GHSV} = 7 \text{ ml(STP)}/(\text{min}\cdot\text{g}_{\text{cat}})$, $(\text{H}_2/\text{CO})_{\text{In}} = 2:1$)

Figure 6.1 (bottom)), therefore appears not to be specific to crystallites of a certain size range, but rather to be an effect which impacts equally on the performance of all samples.

Table 6.1: TEM characterisation results for reduced and spent alumina supported nano-sized crystallites.

Sample code	$\bar{d}_{\text{red-TEM}} \pm \sigma$ in nm	$\bar{d}_{\text{spent-TEM}} \pm \sigma$ in nm	$N_{\text{exp-red}}^a$	$N_{\text{exp-spent}}^b$
catalysts tested at 170°C/4 bar				
RM-1	1.5±0.3	4.0±1.1	510	3700
RM-2	3.9±0.9	5.6±0.9	3680	7300
RM-3	4.1±1.1	4.9±0.9	3690	5600
RM-4	3.8±0.9	3.2±1.1	3550	2250
RM-5	4.1±1.0	4.9±0.6	3695	5500
RM-6	4.7±0.9	6.7±1.2	5050	10500
RM-7	4.9±1.1	6.5±1.1	5600	10200
RM-8	6.3±1.0	7.1±1.3	9700	11200
RM-9	6.7±1.1	6.7±1.2	10500	11100
RM-10	8.3±1.8	9.3±1.6	16500	20670
RM-11	7.9±1.3	7.9±1.3	15000	15500
RM-12	7.7±1.3	7.8±1.1	14300	14500
RM-13	9.6±2.2	9.8±1.2	22000	23500
catalysts tested at 225°C/20 bar				
RM-2	3.9±0.9	4.1±1.3	3680	4110
RM-3	4.1±1.1	4.5±1.4	3690	4950
RM-7	4.9±1.1	6.6±1.2	5600	10445
RM-9	6.7±1.1	7.1±1.3	10500	12000
RM-10	8.3±1.8	9.6±1.5	16500	22700

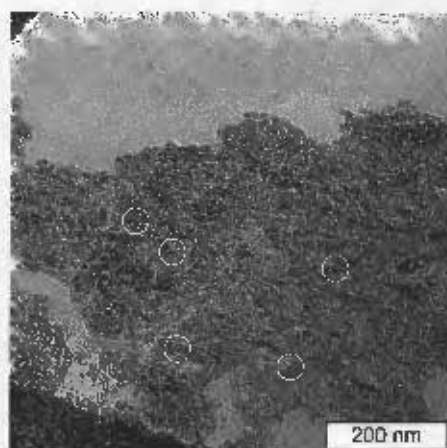
^a number of exposed ruthenium surface atoms per crystallite of average size in reduced catalysts

^b number of exposed ruthenium surface atoms per crystallite of average size in spent catalysts

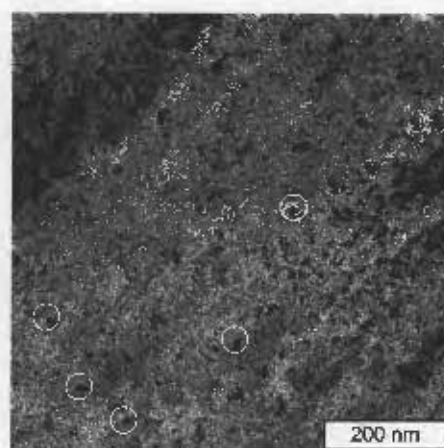
In an attempt to explore the possible origin of this deactivation a sample of the reduced catalyst RM-2 was exposed to pure carbon monoxide for 60 minutes at reaction temperature and 1 bar (carbon monoxide flow-rate identical to FT test condition) and then tested for its FT performance. In this experiment low initial FT activities at levels close to the steady-state activity were obtained (see Figure 6.4). It is therefore possible that initial deactivation, which was obtained for all runs in the first 10 minutes time on stream, is due to inhibition of the FT reaction by initially adsorbing carbon monoxide, or due to effects of reconstruction of the metal surface caused by carbon monoxide. The latter effects, for example, have been evidenced using spectroscopic methods by Geerlings et al. (1991) and Bczemer et al. (2006) and are believed to account for activity and selectivity changes which can occur at initial stages of FT experiments (Schulz et al., 2002).

Lower steady-state FT activity of small crystallites of cobalt (Iglesia (1997a), van Steen et al. (2005)) and iron (Mabaso (2005), Barkhuizen et al. (2006), Mabaso et al. (2006)) had earlier been suspected to be due to the thermodynamically preferred possibility of their oxidation by product water due to effects of surface energy. Metal oxides are generally considered to be inactive, or at least, much less active for FT synthesis (Mansker

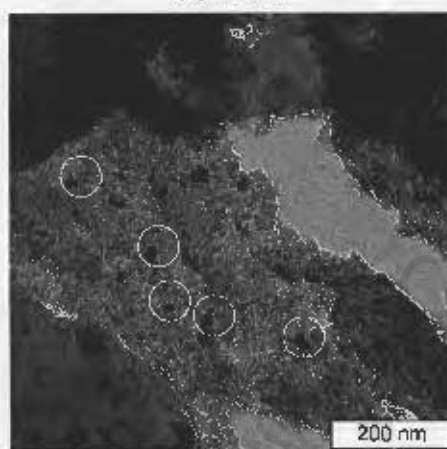
after 5 days
at 170°C/4 bar



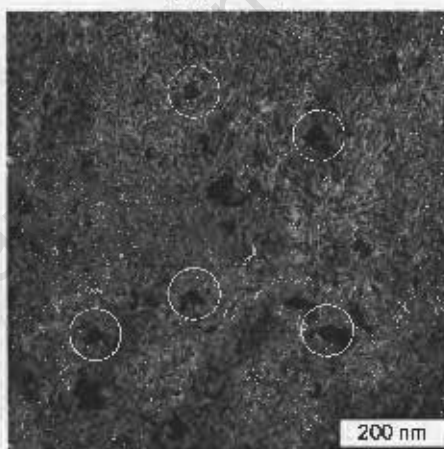
(a) RM-1



(b) RM-7

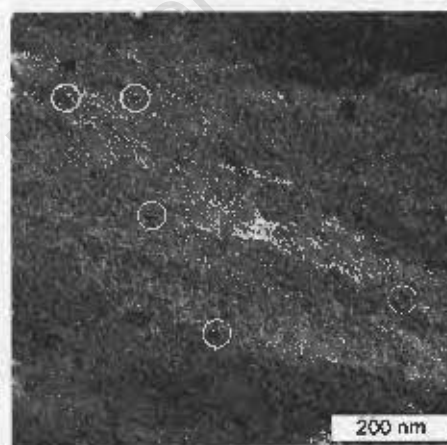


(c) RM-9

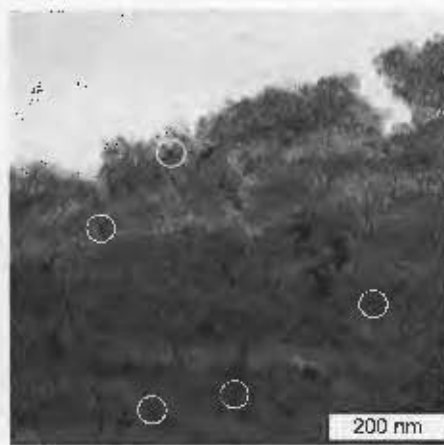


(d) RM-10

after 5 days
at 225°C/20 bar



(e) RM-2



(f) RM-3

Figure 6.2: TEM micrographs of four selected spent alumina supported nano-sized ruthenium crystallites after FT testing for five days at 170°C/4 bar (a to d) and, respectively, two selected spent catalysts after FT testing for five days at 225°C/20 bar (e and f).

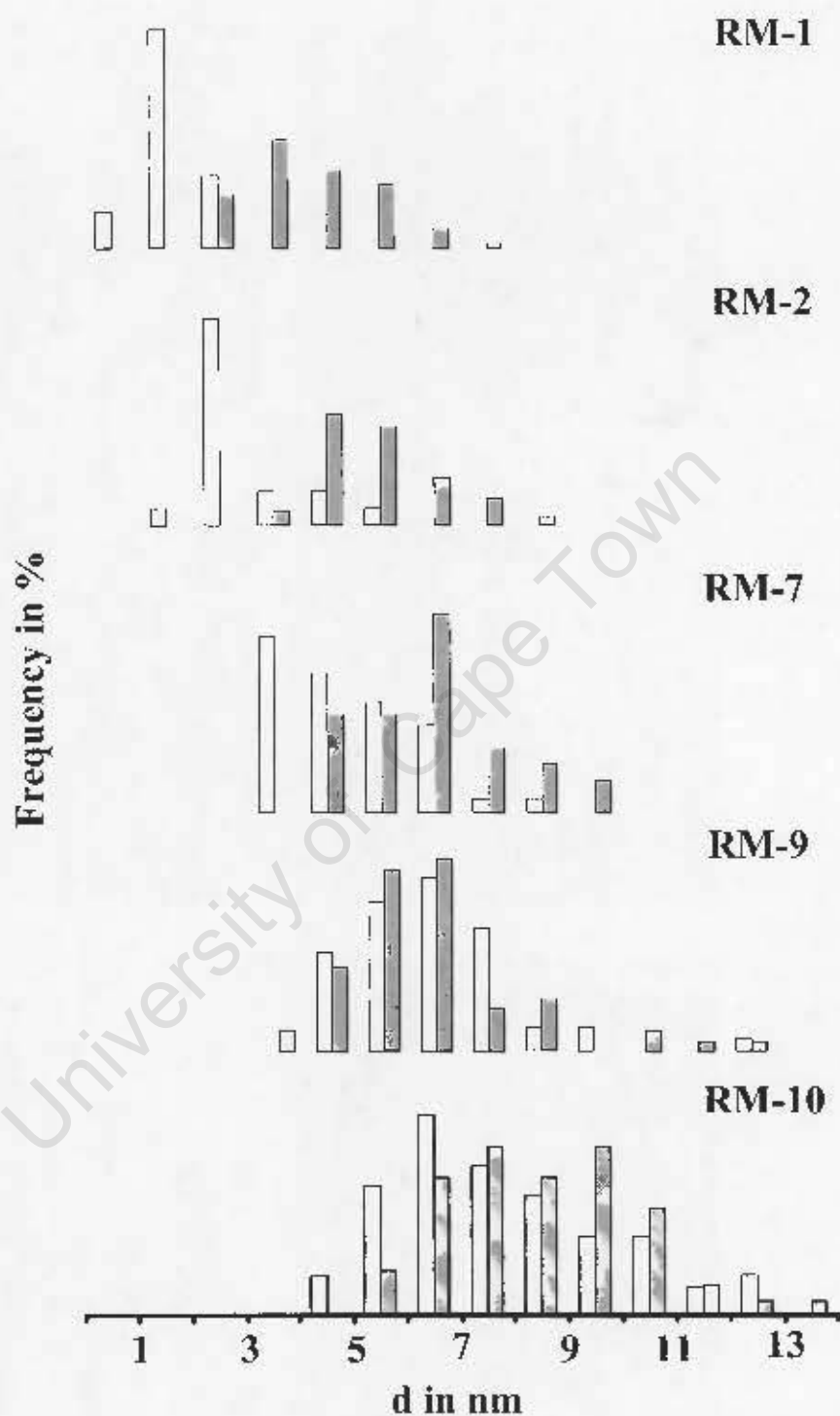


Figure 6.3: Crystalline size distributions of five selected reduced (*open bars*) and spent (*closed bars*) alumina supported nano-sized crystallites after FT testing for five days at 170°C and 4 bar as determined by means of TEM analysis. (For crystallite size distributions of other model catalysts see Appendix A.2, Figure A.2, p. 157.)

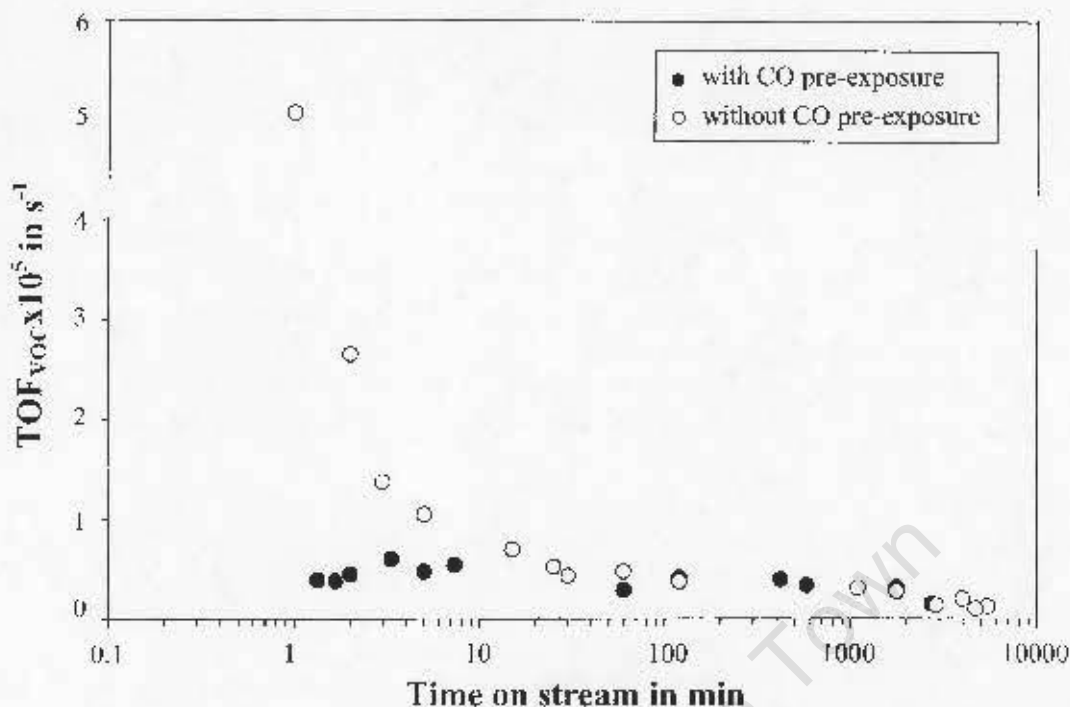
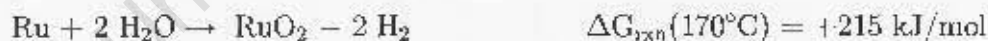


Figure 6.4: Changes in turnover frequencies of volatile organic compounds in FT synthesis at 170°C/4 bar as function of time on stream for catalyst sample RM-2, with (●) and without (○) carbon monoxide pre-exposure after reduction prior to FT experiment. ($T_{\text{Reaction}} = 170^{\circ}\text{C}$, $P = 4$ bar, $\text{GHSV} = 7$ ml(STP)/(min·g_{cat}), $(\text{H}_2/\text{CO})_{\text{in}} = 2:1$)

et al. (1999), Bian et al. (2002), Li et al. (2002)). Thermodynamically, reactions of bulk ruthenium and FT products such as water, carbon monoxide and carbon dioxide are not likely as these reactions have highly positive Gibbs free energies (thermodynamic data from Knacke et al. (1991)):



Oxidation of ruthenium should be less likely than that of other FT active metals. This can also be concluded from the stable activity that was obtained when testing it with pure water or even acids as solvents in FT tests (Fischer et al., 1939). Furthermore,

water partial pressure in the present work was extremely low, at least in the low temperature tests (conversion below 1%), compared to conditions of more than 60% conversion where oxidation of cobalt crystallites smaller than 5 nm might occur (Iglesia (1997a), van Steen et al. (2005)). One may assume that small crystallites of ruthenium may also be more prone to the formation of oxides or carbonyls (see also Abrevaya (1990)). Both ruthenium oxides and ruthenium carbonyls are volatile at reaction conditions, but none of these compounds could be detected in the exit stream during the experiments using GC/MS analysis techniques (see Section 4.7.3, p. 46). This and the observation that the crystallites of different sizes are almost equally affected by catalyst deactivation, i.e. no preferred deactivation of catalysts with smaller crystallites, probably indicate that a different effect causes the observed crystallite size dependent activity that was obtained when testing the catalyst samples at different temperatures and pressures.

Studies on CO-adsorption showed preferential carbon build-up on smaller palladium crystallites because of the higher susceptibilities of low coordination edge/defect sites (present in high concentration on small crystallites) to carbon poisoning (Rainer et al., 1996). This effect can cause formation of different carbon overlayers, of which different types are known for ruthenium (Duncan et al. (1985), Winslow and Bell (1985), Zhou and Gulari (1987)). However, it is not clear whether this observation is applicable to a hydrogen rich atmosphere such as in FT synthesis. Moreover this effect - unless it is very rapid - should cause preferred deactivation of very small crystallites, which was not observed in this study.

It has been suggested that the rate of CO-dissociation might depend on crystallite structure or size and that CO-dissociation would preferably take place on two well separated sites to accommodate separated carbon and oxygen atoms (De Koster and Van Santen (1991), Ciobica and van Santen (2003), Ciobica et al. (2003), Ojeda et al. (2004), Phala (2004)). On-top sites are proposed to be preferred for CO-adsorption on Ru[0001] surfaces of which smaller crystallites have more of them (Michalk et al., 1983). However, product desorption and not CO-dissociation has been considered as the rate-limiting step of the FT reaction by van Steen and Schulz (1999) as otherwise the FT product composition, which is strictly ruled by kinetics, might approach the equilibrium composition of the FT product, which exceeds 95 C% methane (Anderson, 1984).

It has been reported that certain catalytic reactions may require sites which contain a minimum number of neighbouring metal atoms, that may also have to be present in certain configurations, defined as "ensembles" or "domains" (Boudart and McDonald (1984), Freund et al. (2000), Ciobica and van Santen (2003), Ciobica et al. (2003), Zaera (2004), Mabaso (2005), Barkhuizen et al. (2006), Bezemer et al. (2006), Mabaso et al. (2006)). It is likely that particularly complex reactions such as FT synthesis, in which a number of reaction steps is involved (activation of hydrogen and CO-hydrogenation, C-C bond formation and product desorption), occur on such ensembles rather than on single surface metal atoms. It may be speculated that such sites are present in higher relative densities on larger crystallites and that crystallites smaller than a certain critical size may display no FT activity at all, an effect which was, for example, observed for very small ruthenium crystallites (<2 nm) tested for ammonia synthesis (Honkala et al., 2005). This explanation would account for the crystallite size dependent activity observed in this work and similar FT experiments done by others (Mabaso (2005), Barkhuizen et al. (2006),

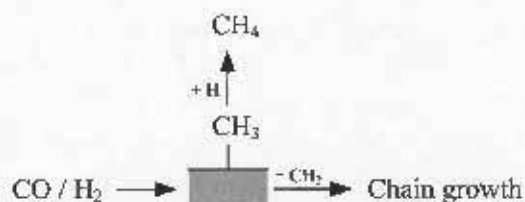
Bezemer et al. (2006), Mabaso et al. (2006)). It does however raise questions as to the use of expressing catalyst activity in terms of “turnover frequency” as this definition implies reactions to occur on single surface metal atoms as determined by means of chemisorption or TEM analysis, while turnover frequency should strictly relate to the number of surface ensembles (Schulz, 2006).

6.1.2 Product Formation

Spectra of the organic products in the runs conducted at 170°C and 4 bar were recorded with a high temporal resolution by using the ampoule sampling technique and FID analysis. Due to the low conversion levels in the experiments of these runs, only very low yields of organic products were detected and a quantification of side products such as branched compounds and oxygenates was not possible. The formation of these products is therefore only discussed for the tests done at elevated temperature and pressure. Detailed selectivity results of both series are tabulated in Appendix B.2, pp. 167. Reported methane and C₅₊-selectivities are product contents (in C%) in the compounds which are volatile at reaction conditions, i.e. C₁ to C₉, (VOC's) as obtained from FID analyses only (see Section 4.7.3, p. 46). Note that here the selectivities overemphasise methane formation and underestimate C₅₊-selectivity as long chain products could not be taken into account. Methane and C₅₊-selectivities in the total hydrocarbon-fraction were also obtained by either extrapolation of FID results to carbon numbers of 100 by assuming ideal Anderson-Schulz-Flory (ASF) kinetics at the measured chain growth probabilities determined in each experiment for the low temperature/pressure experiments or from combining FID analyses and online carbon monoxide conversions obtained from TCD analyses for tests conducted at 225°C and 20 bar. Due to the very low product yields in the low temperature/pressure series of experiments, the scatter of these data is relatively large, but general trends are still clearly observable^b.

6.1.2.1 Methane Formation and Chain Growth

Methane is thermodynamically the most stable product of FT synthesis (Schulz and Cronjé (1977), Anderson (1984)). It is formed via associative desorption of a methyl species and activated surface hydrogen. Alternatively, the methyl species can act as chain starter.



Methane selectivities in the volatile organic compounds (S(CH₄)_{VOC}) obtained in experiments conducted at 170°C and 4 bar on five selected model catalysts are plotted as function of time on stream in Figure 6.5 (top). High methane selectivities of 80 to 90 C% were observed during initial stages of the experiments followed by a sharp decrease to virtually constant values of 40-70 C% after 10 minutes time on stream. Generally, higher

^bNote, that values reported here are averaged selectivities measured between 1 to 3 minutes or three to five days respectively (obvious outliers have been omitted).

steady-state methane selectivities in the volatile organic compounds were obtained on the smaller crystallites (see Figure 6.5 (bottom)). Due to the scatter of the data recorded at 1-3 minutes time on stream it is not clear whether this trend is present during this stage of the reaction as well. A strong decline from 70 to around 50 C% was also detected with increasing crystallite size in the tests done at 225°C and 20 bar.

These observations on methane selectivity are mirrored by selectivities of C_{5+} -products ($S(C_{5+})_{VOC}$) in the volatile organic compounds which may serve as a measure to characterise chain growth or the formation of valuable long chain products (see Figure 6.6). These selectivities are initially very low and increase with reaction time to constant values after approximately 10 minutes time on stream (see Figure 6.6 (top)). Again, a strong crystallite size dependency could be observed (see Figure 6.6 (bottom)), with steady-state C_{5+} -selectivities strongly increasing from below 10 C% to approximately 30 C% with an increase in ruthenium crystallite size (spent catalyst) for both series. The same trends were observed in methane and C_{5+} -selectivities in the total formed product for both series (see Figure 6.7). Due to high chain growth probabilities of 70 to 90% (as shown below), significantly lower methane selectivities, ranging from 50 to 30 C% for the low temperature/pressure series and from 50 to 15 C% at elevated conditions, were obtained in the total product (C_{3+} -selectivities: 50-70 C% at 170°C/ 4 bar and 40-80 C% at 225°C/ 20 bar).

Higher initial methane selectivities and correspondingly lower selectivities for long chain products have been reported previously for FT synthesis using cobalt (Nie (1996), Schulz et al. (2002)), nickel (Nie, 1996) and iron catalysts (Claeys (1997), van Steen and Schulz (1999), Schulz et al. (1999), Claeys and Schulz (2004)). This observation was attributed to an inhibition of methane formation while the kinetic FT regime establishes due to effects of inhibition by carbon monoxide and effects of catalyst reconstruction. Apparently these processes are completed after approximately 10 minutes runtime. It may be noted that the model catalyst RM-2, which had been pre-exposed to carbon monoxide prior to the FT test, showed no temporal changes in methane selectivity, i.e. low initial methane selectivity (see Appendix B.3, Figure B.3 (top), p. 177). This might indicate that the catalyst formation is due mainly to interactions with carbon monoxide.

An increase of methane selectivity and a corresponding decrease of chain growth with decreasing crystallite size were also reported in FT synthesis on cobalt, iron and rhodium (Ojeda et al. (2004), Mabaso (2005), Barkhuizen et al. (2006), Bezemer et al. (2006), Mabaso et al. (2006)) and this was attributed to effects of structure-sensitivity as in small crystallites the relative number of "ensembles" needed for chain growth would be lower than in large crystallites (Mabaso, 2005). In other words, the requirements for an "ensemble", which allows chain growth might be such that it is less likely to occur on the surface of smaller crystallites which have more corner atoms and less plane surfaces and terraces. It may be speculated that the formation of methane, which should be less demanding, would still be possible on simple "ensembles" which can still form on small crystallites, therefore accounting for the shift towards lighter products during FT synthesis on small crystallites. It has indeed been proposed in the literature that methane formation sites might be present which are different from FT sites on which chain growth can occur (Schulz et al. (1995), Zaera (2004)). The fact that the chain growth probabilities of 70 to 90% obtained from ASF product distributions (carbon number range from C_4 to C_9) for the two series of this work do not seem to be affected much by crystallite size (see Appendix B.3, Figure B.4, p. 178) while methane selectivity increased pronouncely with

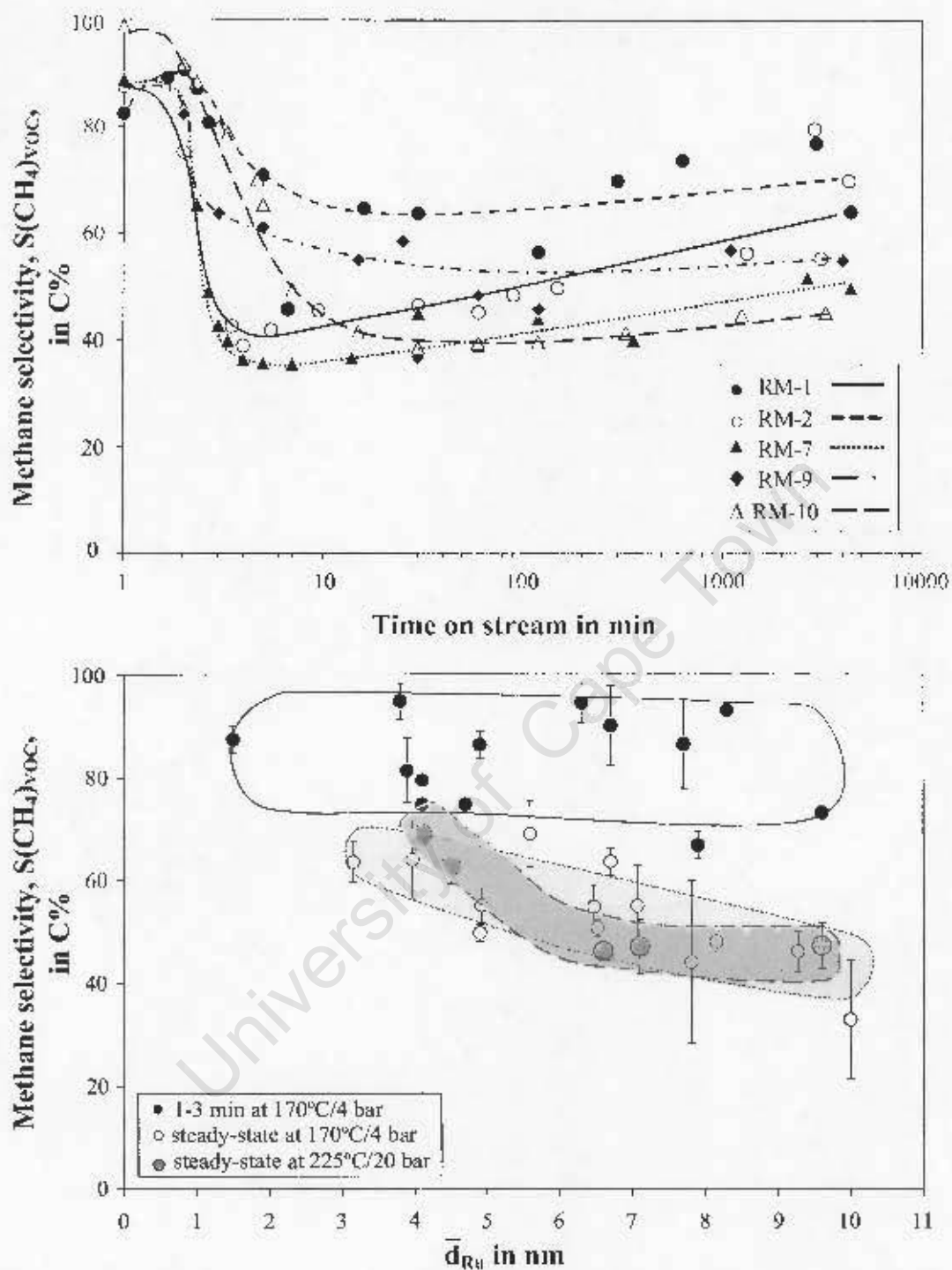


Figure 6.5: *top*: Changes in methane selectivities in volatile organic compounds in FT synthesis at 170°C/4 bar as function of time on stream for five selected alumina supported nano-sized ruthenium crystallites.

bottom: Average methane selectivities in volatile organic compounds in FT synthesis versus average ruthenium crystallite size of fresh (1-3 minutes runtime) or, respectively, spent (steady-state) model catalysts.

(Note: Average crystallite sizes obtained from TEM micrographs of freshly reduced and spent catalysts.)

($T_{\text{Reaction}} = 170^{\circ}\text{C}/225^{\circ}\text{C}$, $P = 4 \text{ bar}/20 \text{ bar}$, $\text{GHSV} = 7 \text{ ml(STP)}/(\text{min}\cdot\text{g}_{\text{cat}})$, $(\text{H}_2/\text{CO})_{\text{in}} = 2:1$)

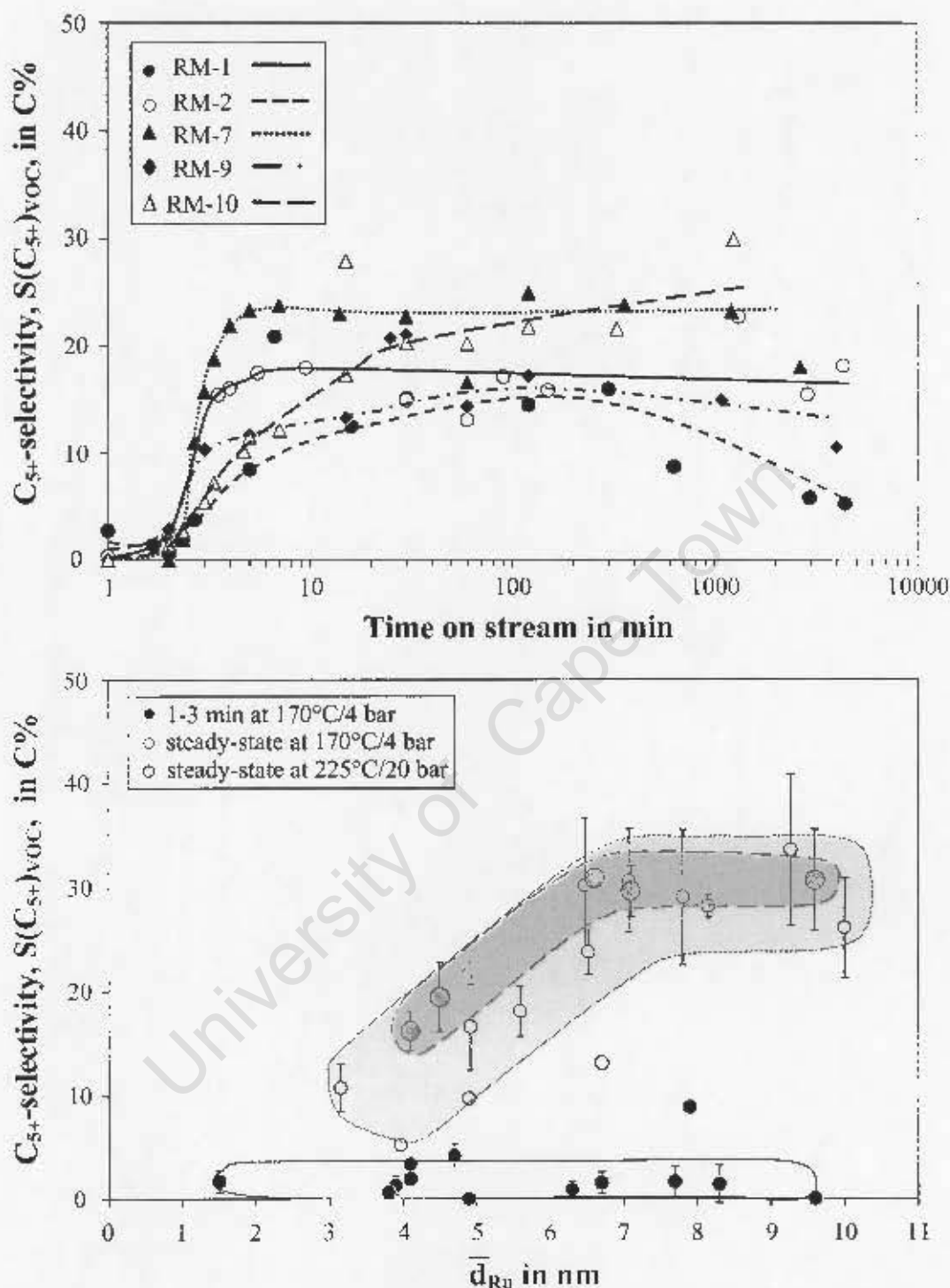


Figure 6.6: *top*: Changes in C₅₊-selectivities in volatile organic compounds in FT synthesis at 170°C/4 bar as function of time on stream for five selected supported nano-sized ruthenium crystallites.

bottom: Average C₅₊-selectivities in volatile organic compounds in FT synthesis versus average ruthenium crystallite size of fresh (1-3 minutes runtime) or, respectively, spent (steady-state) model catalysts.

(Note: Average crystallite sizes obtained from TEM micrographs of freshly reduced and spent catalysts.)

(T_{Reaction} = 170°C/225°C, P = 4 bar/20 bar, GHSV = 7 ml(STP)/(min-g_{cat}), (H₂/CO)_{in} = 2:1)

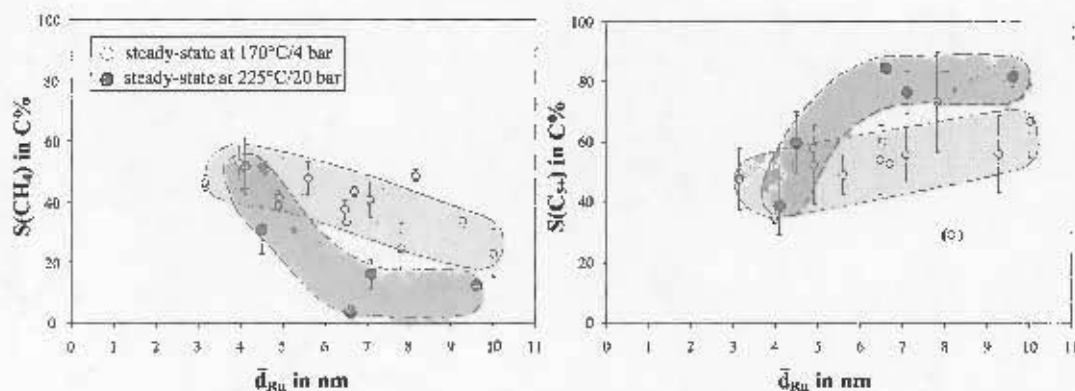


Figure 6.7: *left:* Average steady-state methane selectivities in the total formed product in FT synthesis versus average crystallite size of spent (steady-state) model catalysts. *right:* Average steady-state C_{3+} -selectivities in the total formed product in FT synthesis versus average ruthenium crystallite size of spent (steady-state) model catalysts. (Note: Average crystallite sizes obtained from TEM micrographs of freshly reduced and spent catalysts.)
 $(T_{\text{Reaction}} = 170^{\circ}\text{C}/225^{\circ}\text{C}, P = 4 \text{ bar}/20 \text{ bar}, \text{GHSV} = 7 \text{ ml(STP)}/(\text{min}\cdot\text{g}_{\text{cat}}), (\text{H}_2/\text{CO})_{\text{in}} = 2:1)$

decreasing crystallite size, in particular in the series conducted at elevated temperature and pressure, might substantiate that methane formation sites are more prevalent in comparison to FT chain growth sites on smaller crystallites^c.

Turnover frequencies of the volatile organic compounds shown in Figure 6.1 (bottom) can therefore be strongly affected by such additional methane formation, in particular for small crystallite sizes.

In order to eliminate this effect, the turnover frequencies of C_{2+} -products in the volatile organic compounds obtained for the differently sized crystallites of the two series, are shown in Figure 6.8. The trends observed here, which show a more pronounced increase with crystallite size, can now be interpreted as a true reflection of crystallite size effects on FT activity.

From an economic point of view methane selectivity in a gas-to-liquid or coal-to-liquid process is to be kept as low as possible and, correspondingly, C_{3+} -selectivities as high as possible. Although the methane selectivities in this study are relatively high and although, due to its high costs, ruthenium is not a catalyst of commercial choice for FT synthesis, the findings reported here appear to be in-line with those observed by others using cobalt (Bezemer et al., 2006), iron (Mabaso (2005), Barkhuizen et al. (2006), Mabaso et al. (2006)) and rhodium (Ojeda et al., 2004), and are of high fundamental importance to understand optimisation of FT catalysts.

6.1.2.2 Olefin Formation

Olefins, predominantly α -olefins, are the main primary organic products of FT synthesis (Iglesia et al. (1991), Schulz et al. (1999)).

^cNote, that in absence of additional methane formation, the expected methane selectivity according to ideal ASF kinetics at chain growth probabilities above 80%, lies below 10 C%, in contrast to e.g. 50 C% obtained for the smallest crystallite of the series conducted at 225°C and 20 bar.

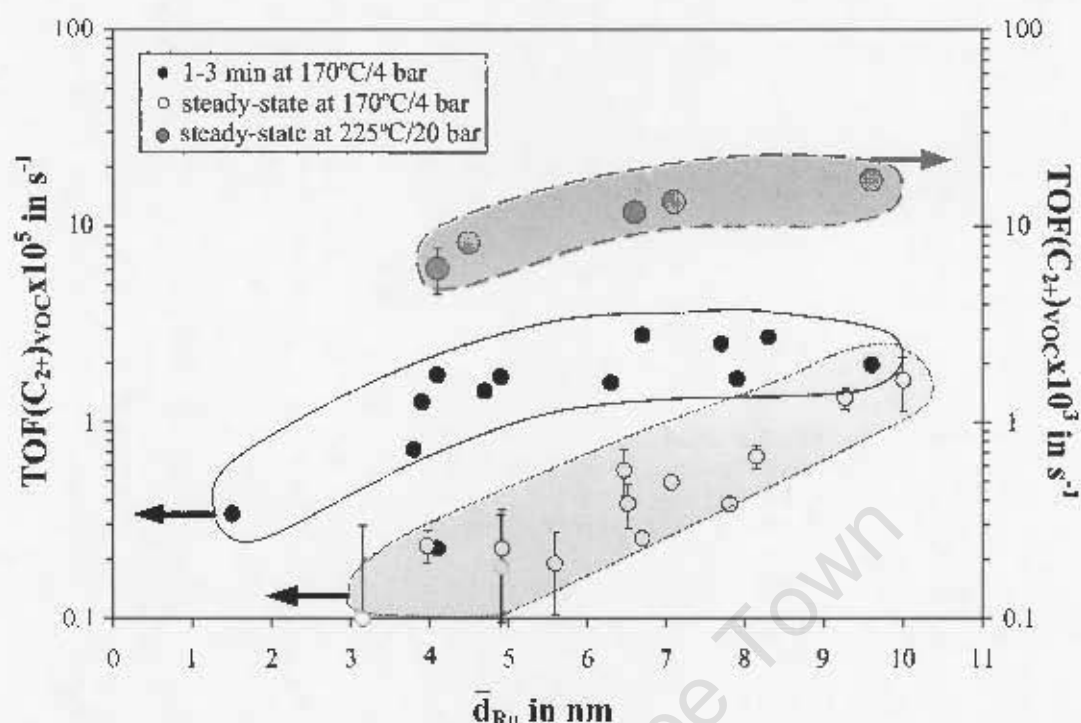
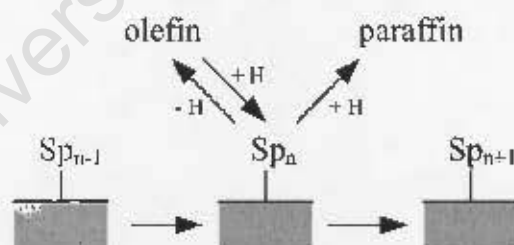


Figure 6.8: Maximal initial and average steady-state turnover frequencies of C_{2+} hydrocarbons in the volatile organic compounds (C_2-C_9) in FT synthesis versus average ruthenium crystallite size of fresh (1-3 minutes runtime) or, respectively, spent (steady-state) catalysts. (Note: Average crystallite sizes obtained from TEM micrographs of freshly reduced and spent catalysts.)
 ($T_{\text{Reaction}} = 170^\circ\text{C}/225^\circ\text{C}$, $P = 4 \text{ bar}/20 \text{ bar}$, $\text{GHSV} = 7 \text{ ml(STP)}/(\text{min}\cdot\text{g}_{\text{cat}})$,
 $(\text{H}_2/\text{CO})_{\text{in}} = 2:1$)



Olefins are thought to form via dissociative β -H elimination from an alkyl surface species. Alternatively, associative desorption of the alkyl species with H-addition can yield paraffins. The step of olefin desorption is reversible as olefins can readsorb and undergo secondary reactions, such as hydrogenation, to corresponding paraffins or incorporation to grow chains - the former reaction usually dominating (Schulz and Claeys, 1999a). Paraffin desorption is, however, irreversible. In the absence of such reactions primary carbon number independent olefin contents of 70-80 mol% are expected (Schulz and Cronjé (1977), Schulz and Claeys (1999b)). These contents may even be somewhat lower (i.e. around 60 mol%) in ruthenium catalysed FT synthesis (Claeys and van Steen, 2002). Values significantly lower than this can supply valuable information regarding the extent of secondary olefin consumption.

The C_2 , C_3 and C_5 -fractions were chosen as representative of other carbon number frac-

tions to ascertain olefin formation and the extent of secondary hydrogenation and incorporation. Figures 6.9, 6.10 and 6.11 (top) show the molar amount of ethene, propene or pentenes respectively in the corresponding linear hydrocarbon-fractions obtained in low temperature/pressure runs with five selected catalysts as function of time on stream. Typically, very low initial olefin contents were obtained, which increased with time. The steady-state C_2 and C_3 -fractions were crystallite size dependent with values ranging between 40 and 70 mol% with an increase towards larger crystallites (see Figures 6.9 and 6.10 (bottom)). The C_5 -fraction, however, reached crystallite size independent values of approximately 60 mol% (see Figure 6.11 (bottom)). All values are typically found for primary olefin selectivity in ruthenium based FT synthesis. It can further be noted that with reaction time the increase in olefin content depends on the crystallite size of the catalyst. Generally, it occurs that larger crystallites reach steady-state faster than smaller ones.

Low initial olefin contents, which are indicative of pronounced secondary olefin hydrogenation (and incorporation), have previously also been reported for FT synthesis using cobalt (Nie (1996), Schulz et al. (2002)), nickel (Nie, 1996), and iron catalysts (Claeys (1997), Schulz et al. (1999), van Steen and Schulz (1999), Claeys and Schulz (2004)) and have been attributed to a more facile readsorption of olefins on the initially less "populated" and hydrogen richer metal surface. In addition to the build-up of chemisorbate and the formation of reaction intermediates, the establishment of the FT regime coincides with structural changes on the metal surface.

It is interesting to note that, whereas turnover frequency and methane selectivity reach steady-state after 10-20 minutes in all experiments of this series, the olefin content reaches steady-state at different stages of the experiments depending on crystallite size, i.e. much later for smaller crystallites than for larger ones. It may therefore be speculated that secondary olefin hydrogenation to an extent occurs on sites differently affected than those of FT chain growth.

Indeed it has been proposed by Schulz et al. (Schulz and Claeys (1999a,b), Schulz et al. (2002)) that olefin hydrogenation and also double bond shift isomerisation might take place on sites which do not allow for chain growth. (Effects of double bond shift isomerisation are discussed in the Section following this one.) The catalyst RM-2, which had been pre-exposed to carbon monoxide before the FT experiment showed slightly higher initial olefin contents than those observed in the run with the corresponding catalyst RM-2 which was not pretreated in carbon monoxide (see Appendix B.3, Figure B.3 (bottom), p. 177), while the final olefin content remained unchanged. This indicates that although carbon monoxide pre-exposure causes some inhibition of this secondary reaction and may have caused some surface reconstruction, ultimately the sites on FT catalysts only develop under the influence of synthesis gas. With the exception of the C_5 -fraction, in this series of experiments a decrease of molar olefin contents was observed for smaller crystallites at steady-state (see Figures 6.9, 6.10 and 6.11 (bottom)). This effect, with lower olefin contents on smaller crystallites, was found when testing some of these catalysts at higher conversion conditions at higher temperatures and pressures (see Figures 6.9 and 6.10 and 6.11 (bottom)). Due to the higher product yields the scatter of data in this series is much less, and an evaluation of other carbon number fractions was also possible. Figure 6.12 depicts the steady-state olefin contents in the corresponding linear hydrocarbon-fractions as function of carbon number for differently sized supported ruthenium crystallites obtained in the series conducted at 225°C and 20 bar.

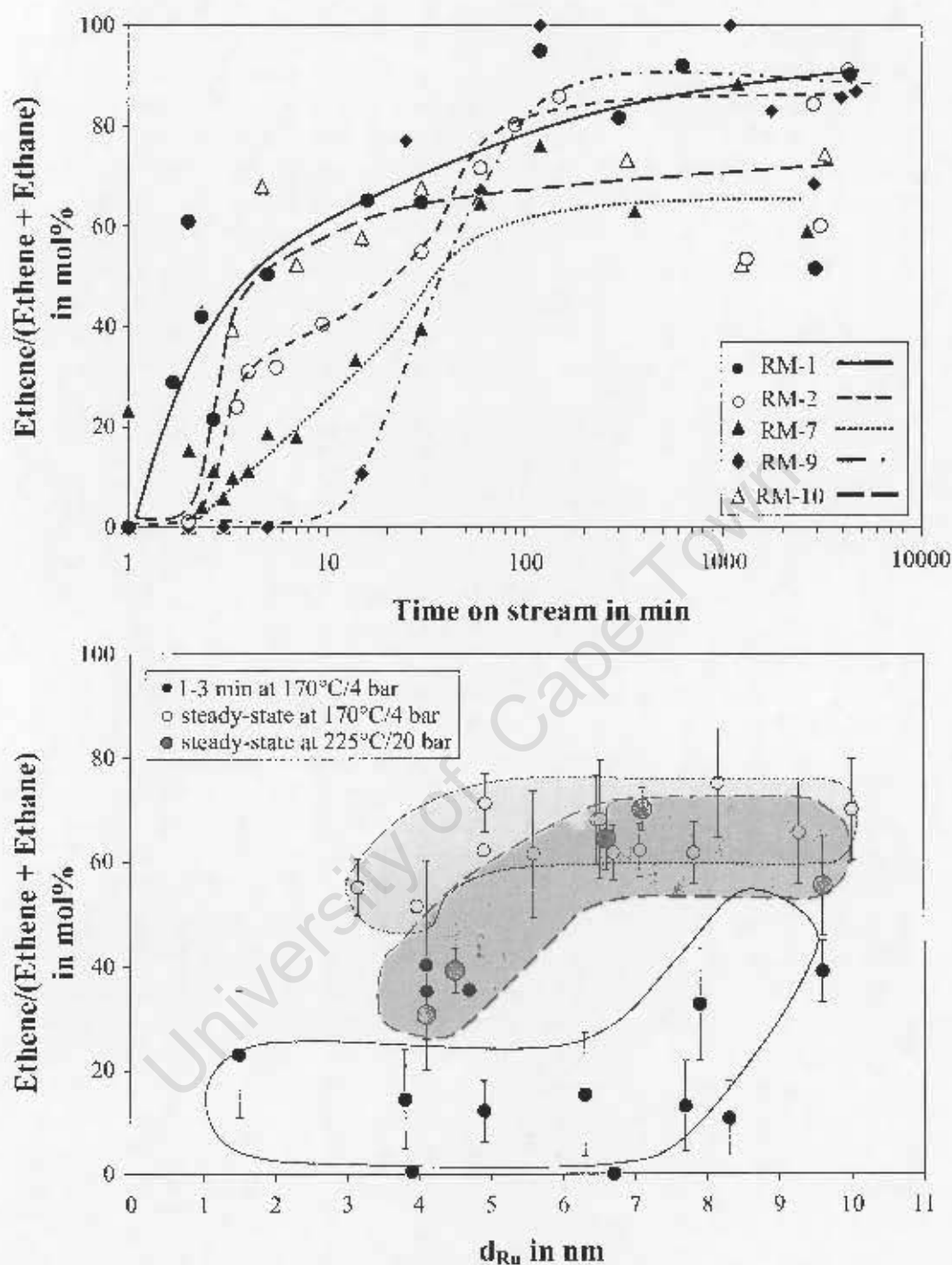


Figure 6.9: top: Changes in molar content of ethene in C_2 hydrocarbon-fraction in FT synthesis at $170^\circ\text{C}/4$ bar as function of time on stream for five selected alumina supported nano-sized ruthenium crystallites.

bottom: Average molar contents of ethene in C_2 hydrocarbon-fraction in FT synthesis as function of crystallite size of fresh (1-3 minutes runtime) or, respectively, spent model catalysts (steady-state).

(Note: Average crystallite sizes obtained from TEM micrographs of freshly reduced and spent catalysts.)

($T_{\text{reaction}} = 170^\circ\text{C}/225^\circ\text{C}$, $P = 4$ bar/20 bar, $\text{GHSV} = 7$ ml(STP)/(min-g_{cat}), $(\text{H}_2/\text{CO})_{\text{in}} = 2:1$)

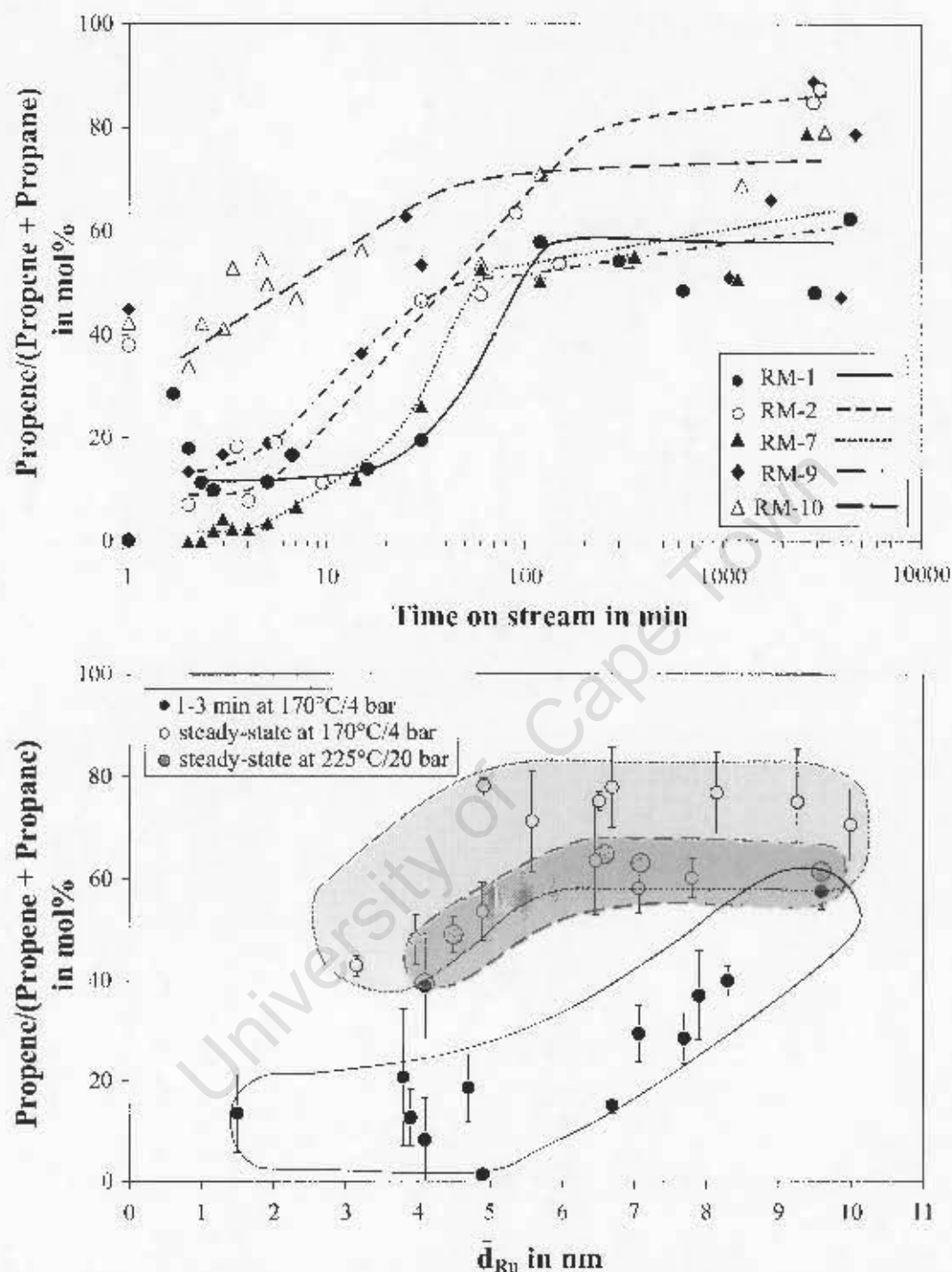


Figure 6.10: *top*: Changes in molar content of propene in C_3 hydrocarbon-fraction in FT synthesis at $170^\circ\text{C}/4$ bar as function of time on stream for five selected alumina supported nano-sized ruthenium crystallites.

bottom: Average molar contents of propene in C_3 hydrocarbon-fraction in FT synthesis as function of crystallite size of fresh (1-3 minutes runtime) or, respectively, spent model catalysts (steady-state).

(Note: Average crystallite sizes obtained from TEM micrographs of freshly reduced and spent catalysts.)

($T_{\text{Reaction}} = 170^\circ\text{C}/225^\circ\text{C}$, $P = 4$ bar/20 bar, $\text{GHSV} = 7$ ml(STP)/(min \cdot g $_{\text{cat}}$), $(\text{H}_2/\text{CO})_{\text{in}} = 2:1$)

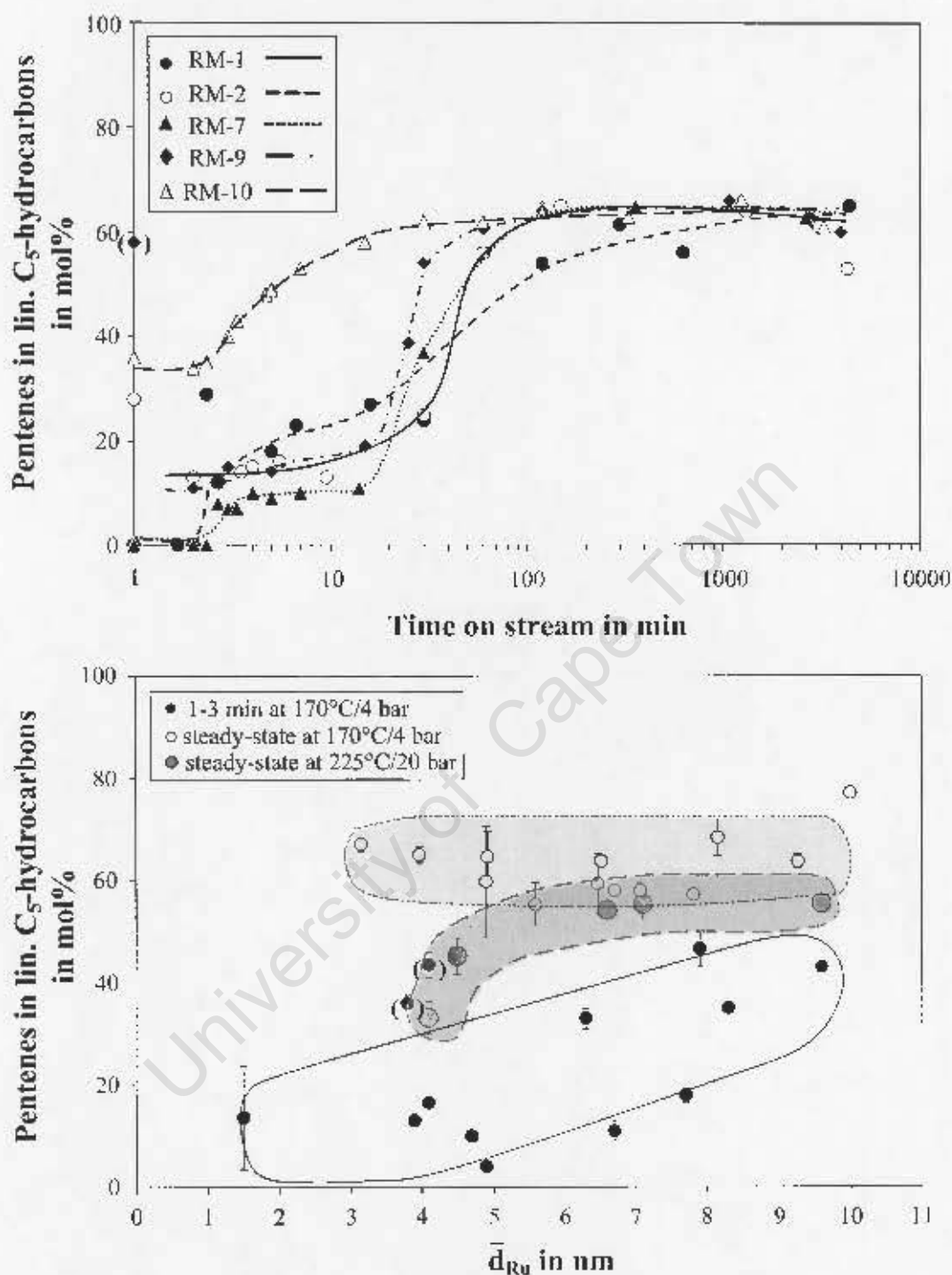


Figure 6.11: *top*: Changes in molar contents of pentenes in C₅-fraction of linear hydrocarbons in FT synthesis at 170°C/4 bar as function of time on stream for five selected alumina supported nano-sized ruthenium crystallites.

bottom: Average molar contents of pentenes in C₅-fraction of linear hydrocarbons in FT synthesis as function of crystallite size of fresh (1-3 minutes runtime) or, respectively, spent model catalysts (steady-state).

(Note: Average crystallite sizes obtained from TEM micrographs of freshly reduced and spent catalysts.)

($T_{\text{Reaction}} = 170^{\circ}\text{C}/225^{\circ}\text{C}$, $P = 4 \text{ bar}/20 \text{ bar}$, $\text{GHSV} = 7 \text{ ml(STP)}/(\text{min}\cdot\text{g}_{\text{cat}})$, $(\text{H}_2/\text{CO})_{\text{in}} = 2:1$)

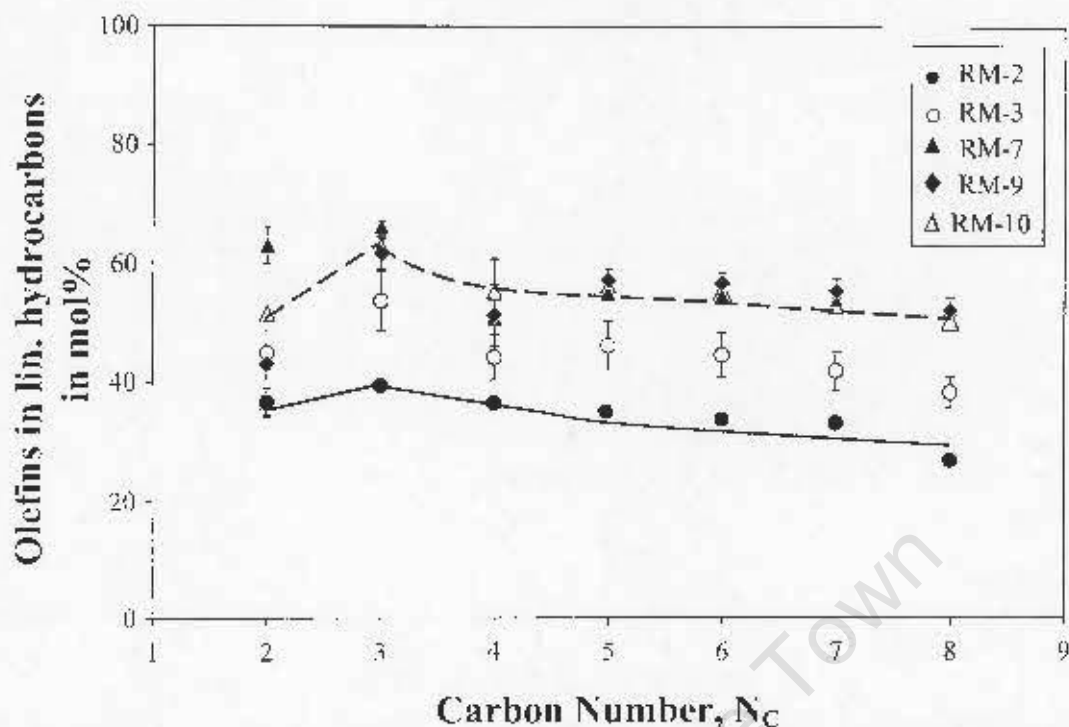


Figure 6.12: Average molar contents of olefins in linear hydrocarbons in FT synthesis at 225°C/20 bar (steady-state) as function of carbon number on alumina supported nano-sized ruthenium crystallites.

($T_{\text{Reaction}} = 225^\circ\text{C}$, $P = 20$ bar, $\text{GHSV} = 7 \text{ ml(STP)}/(\text{min} \cdot \text{g}_{\text{cat}})$, $(\text{H}_2/\text{CO})_{\text{in}} = 2:1$)

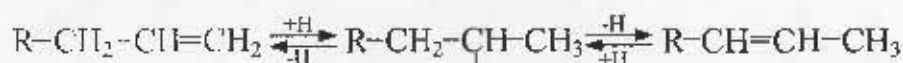
In the presence of pronounced secondary olefin hydrogenation (and incorporation) these curves often show relatively low olefin contents in C_2 (see C_2 olefins in low temperature/pressure runs in Tables B.1-B.5 in Appendix B.2, pp. 167), reflecting the high reactivity of ethene compared to longer chain olefins, and a decrease of olefin content from carbon number C_3 onwards, which is believed to be due to effects of carbon number dependent diffusion rates (Iglesia et al., 1993) and/or carbon number dependent solubility (Schulz and Claeys, 1999b) leading to higher residence times in the liquid filled pores of the catalyst and therefore increased readsorption probabilities. Slight deviations from carbon number independent olefin contents were indeed found, indicating some secondary olefin consumption. Overall the extent of secondary hydrogenation (and incorporation) appears to be larger on the small crystallites as here the molar olefin contents are lower. It can be noted, however, that the deviations from carbon number independent trends are not very pronounced, and that the shift towards lower olefin contents observed on the small crystallites may also be due to a shift of primary olefin selectivity.

Generally, the formation of olefins versus paraffins and secondary olefin consumption can be associated with the availability of hydrogen on the catalyst surface and effects of decreased specific carbon monoxide. It may be speculated that this availability, which must be seen in relation to availability of carbon monoxide, which is known to specifically inhibit secondary olefin hydrogenation (Schulz et al., 1995), is indeed higher on the small crystallites. Further, it has been reported that alkyl species and olefin readsorption are more likely to occur on sites of low coordination (Schulz et al., 2002), as present on edges and corners of small crystallites, although, in the absence of carbon monoxide, reactions of

olefin hydrogenation on Pt/SiO₂ did not show structure-sensitivity (Dorling et al. (1969), Klabunde et al. (1995)).

Similarly, increased paraffin to olefin ratios were observed during FT synthesis on cobalt crystallites smaller than 5 nm by Bezemer et al. (2006), while no effects were found on supported iron crystallites of different sizes (Mabaso (2005), Barkhuizen et al. (2006), Mabaso et al. (2006)). It may therefore be speculated that these crystallite size effects are not only influenced by reaction conditions, as seen in this study, but also by the metal used.

α -olefins can also readsorb non-terminally to the catalyst surface and upon desorption form olefins with internal double bonds:



This reaction is known to occur readily on metal surfaces in the presence of hydrogen (Germain, 1969). Alternatively, double bond shift isomerisation can also occur on acidic sites which may be present on support material. It is believed that α -olefins as primary products are formed almost exclusively among olefins in each carbon number fraction, i.e. 95 to 100 mol% (Schulz and Gökcebay (1984), Schulz and Claeys (1999a)). The contents of α -olefins in the carbon number olefin fraction therefore gives an indication to what extent this secondary reaction had occurred. Figure 6.13 shows the temporal changes of the 1-pentene content in the linear C₅-olefins observed with model catalysts of different crystallite sizes in the FT experiment conducted at 170°C and 4 bar.

Initially very low 1-olefin contents (10 to 40 mol%) which were found in all experiments increased to steady-state values between 80 and 100 mol%. Pronounced double bond shift isomerisation in initial stages in FT experiments were also obtained on cobalt (Nic (1996), Schulz et al. (2002)), nickel (Nic, 1996) and iron (Claeys (1997), Schulz et al. (1999), van Steen and Schulz (1999), Claeys and Schulz (2004)) catalysts.

This reaction is believed to be more facile on the freshly reduced catalyst surface, before it is filled with surface species and then inhibited upon catalyst reconstruction and the formation of the FT regime.

Slightly lower olefin contents might be present on the smallest crystallites, as shown in Figure 6.13 (bottom). A similar observation is obtained in Figure 6.14, which depicts the steady-state α -olefin contents in the corresponding fraction of linear olefins as function of the carbon number of the series measured at 225°C and 20 bar. The lower α -olefin contents obtained on the small crystallites might, in agreement with the findings described with respect to olefin hydrogenation (see above), indicate that olefin readsorption and secondary olefin reactions are more likely to occur on small crystallites.

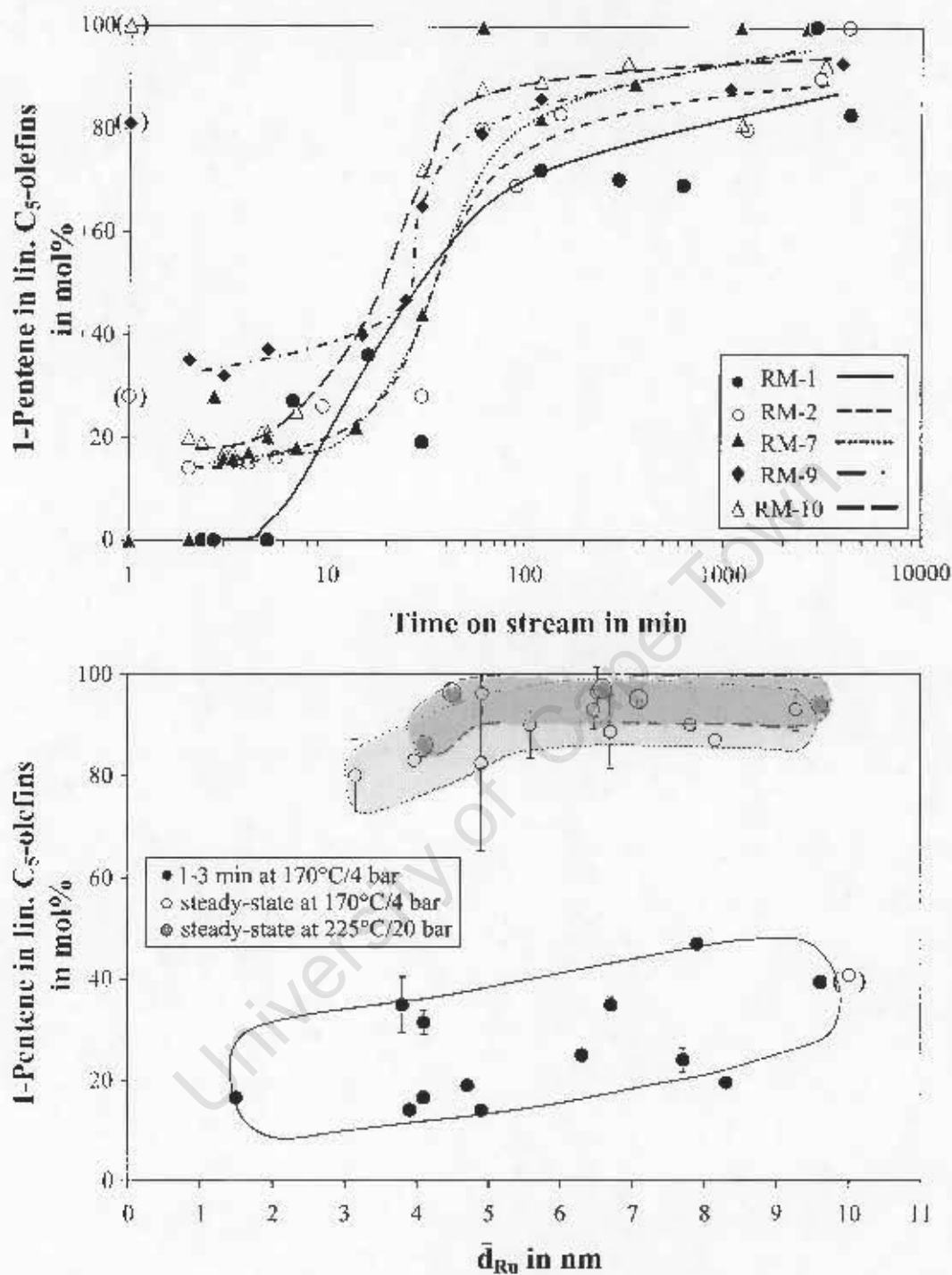


Figure 6.13: *top:* Changes in molar contents of 1-pentene in linear C₅-olefins in FT synthesis at 170°C/4 bar as function of time on stream for five selected alumina supported nano-sized crystallites.

bottom: Average molar contents of 1-pentene in linear C₅-olefins in FT synthesis as function of crystallite size of fresh (1-3 minutes runtime) or, respectively, spent model catalysts (steady-state).

(Note: Average crystallite sizes obtained from TEM micrographs of freshly reduced and spent catalysts.)

(T_{Reaction} = 170°C/225°C, P = 4 bar/20 bar, GHSV = 7 ml(STP)/(min·g_{cat}), (H₂/CO)_{in} = 2:1)

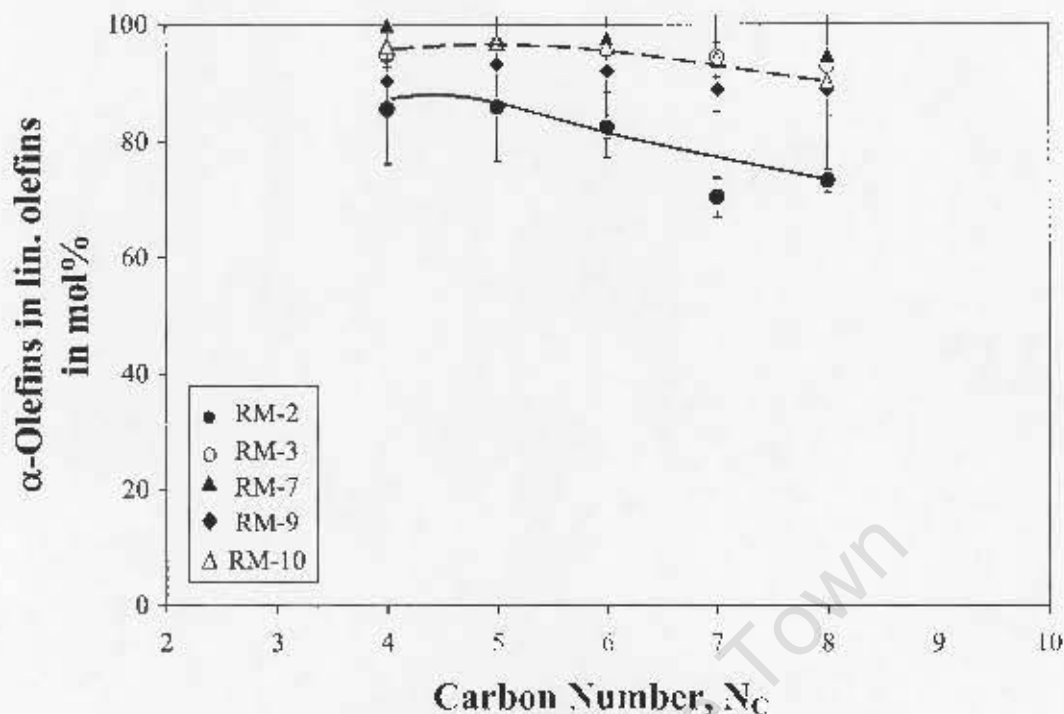
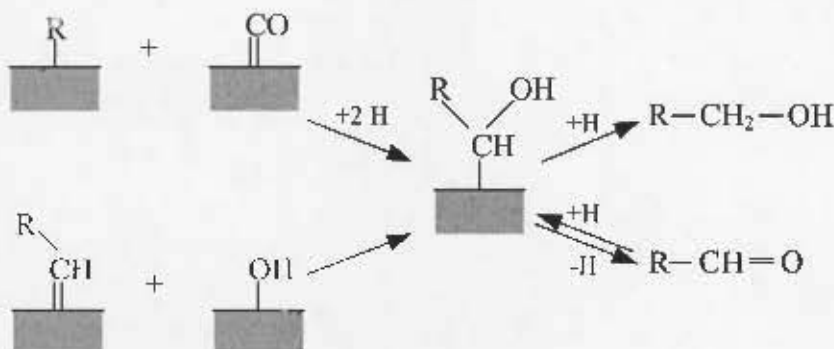


Figure 6.14: Average steady-state molar contents of α -olefins in the corresponding fraction of linear olefins in FT synthesis at 225°C/20 bar at steady-state as function of carbon number for supported nano-sized ruthenium crystallites.

($T_{\text{Reaction}} = 225^\circ\text{C}$, $P = 20$ bar, $\text{GHSV} = 7 \text{ ml(STP)}/(\text{min}\cdot\text{g}_{\text{cat}})$, $(\text{H}_2/\text{CO})_{\text{in}} = 2:1$)

6.1.2.3 Formation of Oxygenates

Oxygenates, mainly aldehydes and alcohols, are minor products of FT synthesis and little is known about their formation routes. Pichler and Schulz (1970) postulated that an oxygen containing surface species can be formed via CO-insertion to a surface alkyl group. Johnson and Joyner (1993) proposed that the same species could be formed by addition of hydroxyl groups to an alkylidene species. Desorption of this species then leads to formation of alcohols or aldehydes respectively.



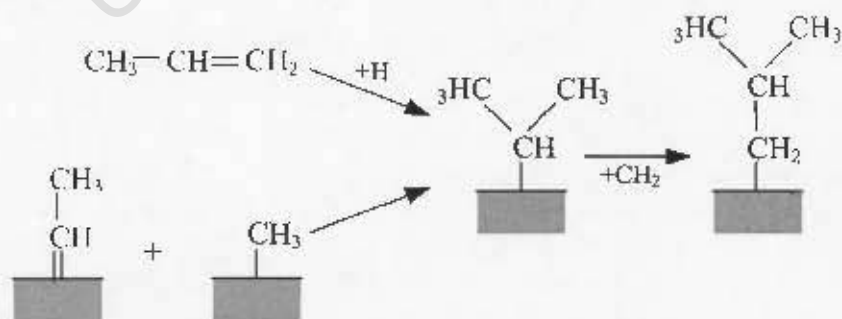
Generally, small amounts of oxygenates were found and these could only be quantified in the product spectra of the elevated temperature/pressure series runs (see Figure 6.15). At steady-state, increasing amounts of the oxygenates pentanol and pentanal were found

in the fraction of linear C₅-products as the crystallite size increased. It has been speculated that reactions of CO-insertion might preferably occur on metal sites with low coordination (Schulz et al. (2002), Schulz (2003)), i.e. on atoms with small numbers of neighbours which should preferably be found on corners and edges of small crystallites. Indeed enhanced oxygenate selectivity has been reported in FT synthesis studies on small crystallites with rhodium (Ojeda et al., 2004), cobalt (Bezemer et al., 2006) and iron (Mabaso, 2005). Unless the reversed trends observed in this study are a reflection of increased primary oxygenates selectivity, e.g. via the mechanism proposed by Johnson and Joyner (1993), the decreasing content of oxygenates towards smaller crystallites may be an indication that primary formed oxygenates are consumed in secondary reactions including their hydrogenation and/or incorporation into growing chains. These consecutive reactions are known to occur in FT synthesis as evidenced by e.g. Tau et al. (1988) via co-feeding experiments and this observation would be in-line with the enhanced secondary conversion of olefins on small crystallites as discussed above. Preferred formation of alcohols versus aldehydes was obtained for small crystallites in this series (see Figure 6.15).

Alddehydes are believed to be formed primarily at larger quantities than the corresponding alcohols, but it can easily be converted to the alcohol via consecutive hydrogenation (Dector and Bell (1986a,b)). Analogously to the observations made with respect to olefins an increased relative hydrogen availability on small crystallites might not only account for preferred secondary oxygenates conversion, but also for a shift of their primary selectivity with decreased relative formation of oxygen containing surface species or their rapid hydrogenation to the corresponding alkyl surface species and a shift towards the hydrogen-rich oxygenate, the alcohol, upon desorption of oxygen containing surface species (see Scheme above).

6.1.2.4 Formation of Branched Products

In addition to linear products, small amounts of branched products were detected. Formation of branched hydrocarbons is believed to occur in primary and secondary reaction pathways (Schulz et al., 1988), namely via a) combination of an alkylidene and a methyl surface species or b) secondary incorporation of α -olefins.



The formation of branched species is thought to be more spatially demanding than linear chain growth. It has therefore been suggested to be ideally suited as a probe reaction to trace back spatial constraints on different reaction pathways in FT synthesis (Schulz et al., 1994). Representative of other carbon number fractions the ratio of branched and linear products in the C₅-fraction as observed at steady-state for the model catalysts of

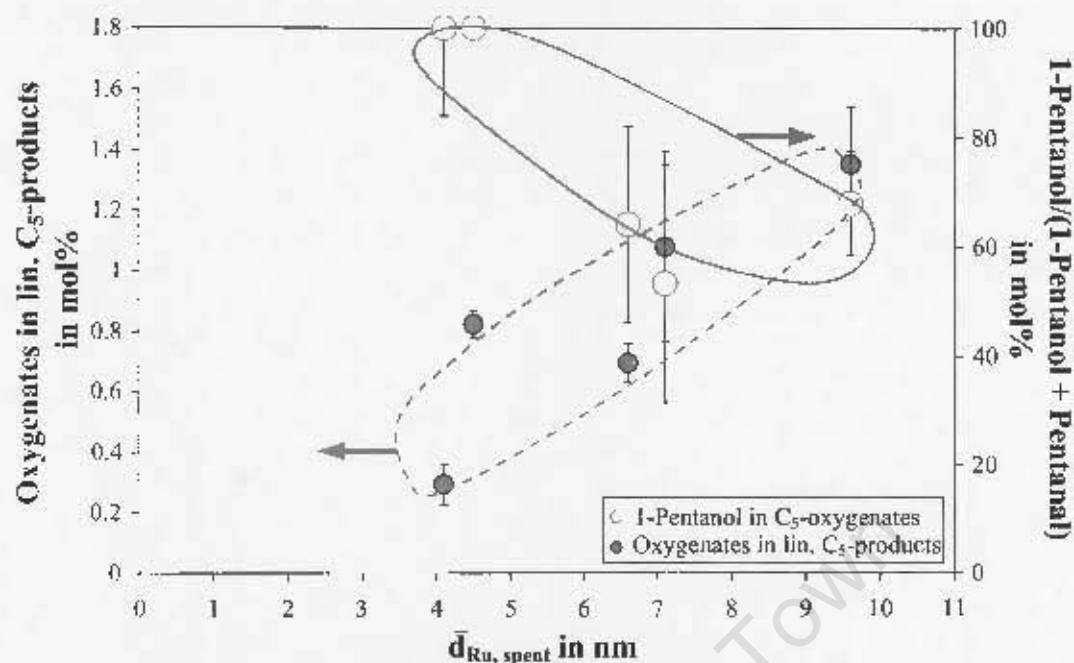


Figure 6.15: Average steady-state molar contents of oxygenates in the linear C_5 -products (left y -axis) and average steady-state molar contents of 1-pentanol in C_5 -oxygenates (right y -axis) in FT synthesis at $225^\circ\text{C}/20$ bar versus average ruthenium crystallite size of spent (steady-state) catalysts.

(Note: Average crystallite sizes were obtained from TEM micrographs of spent catalysts.)
 $(T_{\text{Reaction}} = 225^\circ\text{C}, P = 20 \text{ bar}, \text{GHSV} = 7 \text{ ml(STP)}/(\text{min} \cdot \text{g}_{\text{cat}}), (\text{H}_2/\text{CO})_{\text{in}} = 2:1)$

the series conducted at 225°C and 20 bar are plotted against ruthenium crystallite size in Figure 6.16.

Increased branching was found in the product obtained with the small crystallites, which most likely indicates that, again, secondary reactions, such as incorporation of primarily formed olefins, occur preferentially on smaller crystallites and thus leading to the higher branching probabilities.

6.1.3 Conclusions of Findings of Fischer-Tropsch Experiments on Supported Nano-sized Crystallites

The results of the studies conducted on the FT performance of the supported nano-sized crystallites show that activity and product selectivity can be affected strongly by ruthenium crystallite size in the tested range between 2-10 nm. This influence of crystallite size does, however, vary depending on the stage of an experimental run (initial versus steady-state) and the reaction conditions (temperature and pressure).

An increase of catalyst activity was observed with increasing crystallite size at initial stages of the experiment and at steady-state conversion at the two different applied temperature/pressure conditions. Catalyst deactivation was obtained in all runs. Its extent did not depend on crystallite size, was not caused by crystallite sintering and most probably not caused by oxidation of the metal crystallites. At steady-state, generally positive effects obtained are decreased methane selectivity, increased C_{5+} -product selectivity and, at elevated temperature and pressure, increased contents of olefins (in particular α -olefins) and oxygenates for larger crystallites. Some of these trends were previously reported for

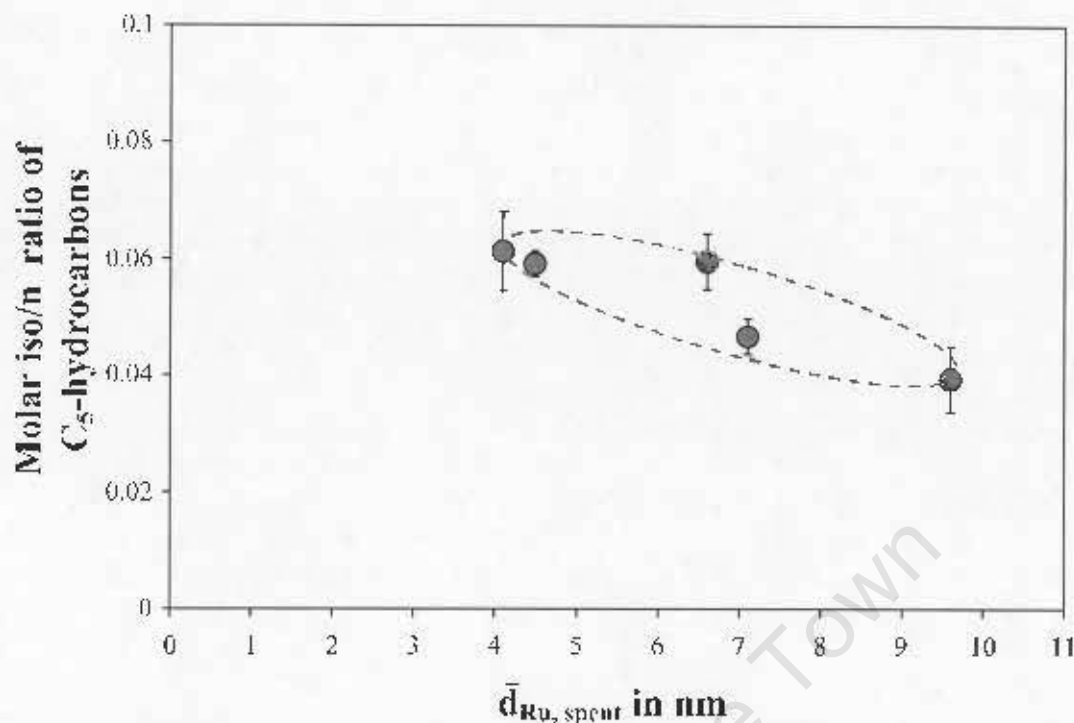


Figure 6.16: Average steady-state molar ratios of branched to linear (iso/n) C₅ hydrocarbons in FT synthesis at 225°C/20 bar versus average ruthenium crystallite size of spent (steady-state) model catalysts.

(Note: Average crystallite sizes were obtained from TEM micrographs of spent catalysts.)
(T_{Reaction} = 225°C, P = 20 bar, GHSV = 7 ml(STP)/(min·g_{cat}), (H₂/CO)_{in} = 2:1)

CO-hydrogenation on other model catalyst systems including cobalt (Bezemer et al., 2006), iron (Mabaso (2005), Barkhuizen et al. (2006), Mabaso et al. (2006)) and rhodium (Ojeda et al., 2004), and were ascribed to effects of structure-sensitivity as only certain “ensembles/domains” of surface atoms would catalyse certain reactions occurring during FT synthesis (Bezemer et al. (2006), Mabaso (2005)).

These different reactions during FT synthesis include *inter alia*, complex steps of CO-dissociation, chain growth and formation of different products (e.g. methane versus chain growth) and it can be expected that the number of sites on which the rate determining step occurs, will ultimately determine the overall product formation rate, while the product selectivity will depend on the relative abundance of such sites on metal crystallites of different sizes. On small crystallites, a disproportional increase of methane selectivity at largely unaffected chain growth probability suggests an increased ratio of sites of methane formation relative to those on which FT chain growth can occur. It can be assumed that sites or “ensembles” required for chain growth are more complex than those for methane formation and that the ratio of chain growth versus methane formation sites decreases with decreasing crystallite size. In addition to preferred methane formation, the product obtained on small crystallites was richer in hydrogen with enhanced paraffin to olefin ratios and increased alcohol to aldehyde ratios. This may be an indication of increased relative hydrogen availability on the surface of small crystallites, which can either cause a shift to primary relative formation of different product classes (e.g. paraffins versus olefins) and/or affect secondary conversion of reactive products such as olefins and oxy-

genates.

Readsorption of these compounds might be more facile on metal surface atoms of low coordination as more prevalent on the edges and corners of small crystallites, therefore also implying structure-sensitivity of secondary reactions during FT synthesis.

Such effects of crystallite size were not observed at initial stage in the experimental runs where secondary reactions dominate, possibly indicating that structure-sensitivity effects on selectivity only develop with crystallite reconstruction under the influence of synthesis gas and the development of the kinetic FT regime. Although some analogy to results obtained in work on cobalt and iron could be drawn, it was noted that, no constant level of specific catalyst activity was obtained for larger ruthenium crystallites, in contrast to cobalt and iron where catalyst activity per number of surface atoms did reach constant values from diameters of 5-6 nm (cobalt) and 7-8 nm (iron) onwards. Assuming a metal independent "ensemble" size accounts for FT activity, it can indeed be expected that for ruthenium, with its relatively large atoms, this threshold crystallite diameter is indeed much larger than for cobalt and iron. This diameter, however, is likely to depend on the testing conditions as well.

6.2 Supported Organometallic Compounds

In an attempt to study the requirements of specific sites/“ensembles” that might play a role in FT synthesis the supported organometallic compounds of different nuclearity were tested in a modified reactor system, which allowed for instantaneous heating of the complexes to avoid their decomposition prior to a run. No reduction step was applied before the start of the FT reaction. The reactions were again performed at a reaction temperature of 170°C, a pressure of 4 bar and a constant synthesis gas flow of 7 ml(STP)/(min·g_{cat}) (H₂:CO = 2). All tests were done over a five hour period and two selected model catalysts were tested for extended reaction times of five days. Due to the limited stability of the organometallic compounds in particular, the initial behaviour of the compounds is of interest as only at this stage of the testing the cluster framework was still largely intact. Some of the data reported for specific reaction times can be found listed in Appendix B.2, Tables B.6-B.8, pp. 173. The chemical structures of the compounds are described in Section 4.1.2, pp. 30. For quick reference the compounds are again listed below:

Ru-2a	$\text{Ru}_2(\text{CO})_4(\eta^5\text{-C}_5\text{H}_5)_2$
Ru-2b	$\text{Ru}_2(\text{CO})_4(\eta^5\text{-C}_5(\text{CH}_3)_5)_2$
Ru-2c	$\text{Ru}_2(\text{CO})_2(\mu\text{-CO})(\mu\text{-CHCH}_3)(\eta^5\text{-C}_5\text{H}_5)_2$
Ru-3	$\text{Ru}_3(\text{CO})_{12}$
Ru-4	$\text{Ru}_4(\mu\text{-H})_4(\text{CO})_{12}$
Ru-5	$\text{Ru}_5\text{C}(\text{CO})_{15}$
Ru-6	$\text{Ru}_6\text{C}(\text{CO})_{17}$

6.2.1 Fischer-Tropsch Activity

Formation of typical FT products, namely linear hydrocarbons ranging from C₁ to C₄, could be detected in all experiments (see an example chromatogram in Figure 6.17) and at longer runtimes hydrocarbons up to C_{7, 8} could be detected. Formation of the non-FT synthesis products cyclopentadiene and cyclopentane was also observed in the spectra of the runs with the diatomic samples. Their presence indicates loss of ligands from these compounds and they were not included in the reported catalyst activities.

The catalyst activities were reported in terms of turnover frequencies based on the formation rates of C₁-C₄ hydrocarbons and the number of ruthenium atoms in the cluster at a metal loading of 3 wt%. It is therefore assumed that all metal atoms in the cluster frameworks are accessible to a degree comparable to surface atoms in a nano-sized crystallite. The monitored activities of all compounds went through a maximum between 1-3 minutes, followed by rapid deactivation (see Figure 6.18 (top)). For clarity, only the results of the model compound Ru-2a are shown here as representative for the diatomic compounds. The corresponding diagrams for Ru-2b and Ru-2c are shown in Appendix B.3.2, Figure B.5 (top), p. 180. Some model compounds showed an increase in product formation rates, namely after 10 minutes for Ru-6, after 60 minutes for Ru-5, after 300 minutes for Ru-2c, Ru-3 and Ru-4 (see Figure 6.18 (top)). This effect is more pronounced for FT synthesis on Ru-5 and Ru-6 where activity at longer reaction times exceeded the initially produced formation rates.

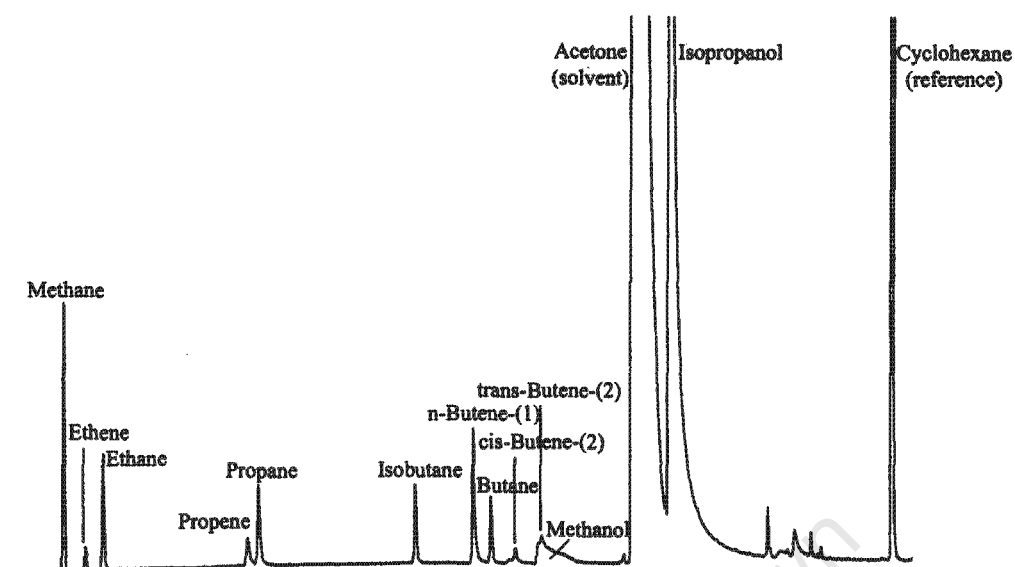


Figure 6.17: Gas chromatogram of product obtained after 2 minutes of testing compound Ru-6 in synthesis gas.
 ($T_{\text{Reaction}} = 170^{\circ}\text{C}$, $P = 4$ bar, $\text{GHSV} = 7 \text{ ml(STP)}/(\text{min} \cdot g_{\text{cat}})$, $(\text{H}_2/\text{CO})_{\text{in}} = 2:1$)

In order to compare the activity of the different model systems the initial maximum turnover frequencies observed for the different clusters of varied nuclearity are shown in Figure 6.18 (bottom). At this reaction time the frameworks of the clusters, which are known to be of limited stability at reaction conditions as shown via TGA characterisation (see Section 5.3.1, p. 64), are believed to still be largely intact. An increase in activity with increase in cluster size was found for the runs Ru-3 to Ru-6, while the activity of the diatomic compounds varied over a wide range. It can be speculated that this different behaviour might be related to their different ligand systems, which already showed marked effect on the relative thermal stabilities of these clusters (see Section 5.3.1, p. 64). The clusters Ru-3 to Ru-6 contain only CO-ligands, and the observed increase may therefore be directly related to the number of metal atoms in the cluster.

Due to the limited thermal and chemical stability of the compounds and the fact that some of the organic ligands seemed to appear in the product it can be assumed that the organometallic compounds decomposed to some degree. It can be expected that decomposition of the compounds may result in formation of larger ruthenium clusters or crystallites. Furthermore, some ruthenium might be lost via formation of volatile ruthenium-organic compounds. In order to assess these effects the spent catalysts were characterised by means of TEM analyses to check for crystallite formation and ICP analyses to determine the ruthenium content after an experiment. It was also attempted to redissolve the compounds after an experiment and characterise them by means of IR analysis. Volatile ruthenium compounds were searched for in the product stream using GC/MS analysis.

TEM analyses conducted on samples that had been exposed for five hours indeed indicated formation of some nano-sized crystallites with diameters in the range of 2 to 3 nm (see

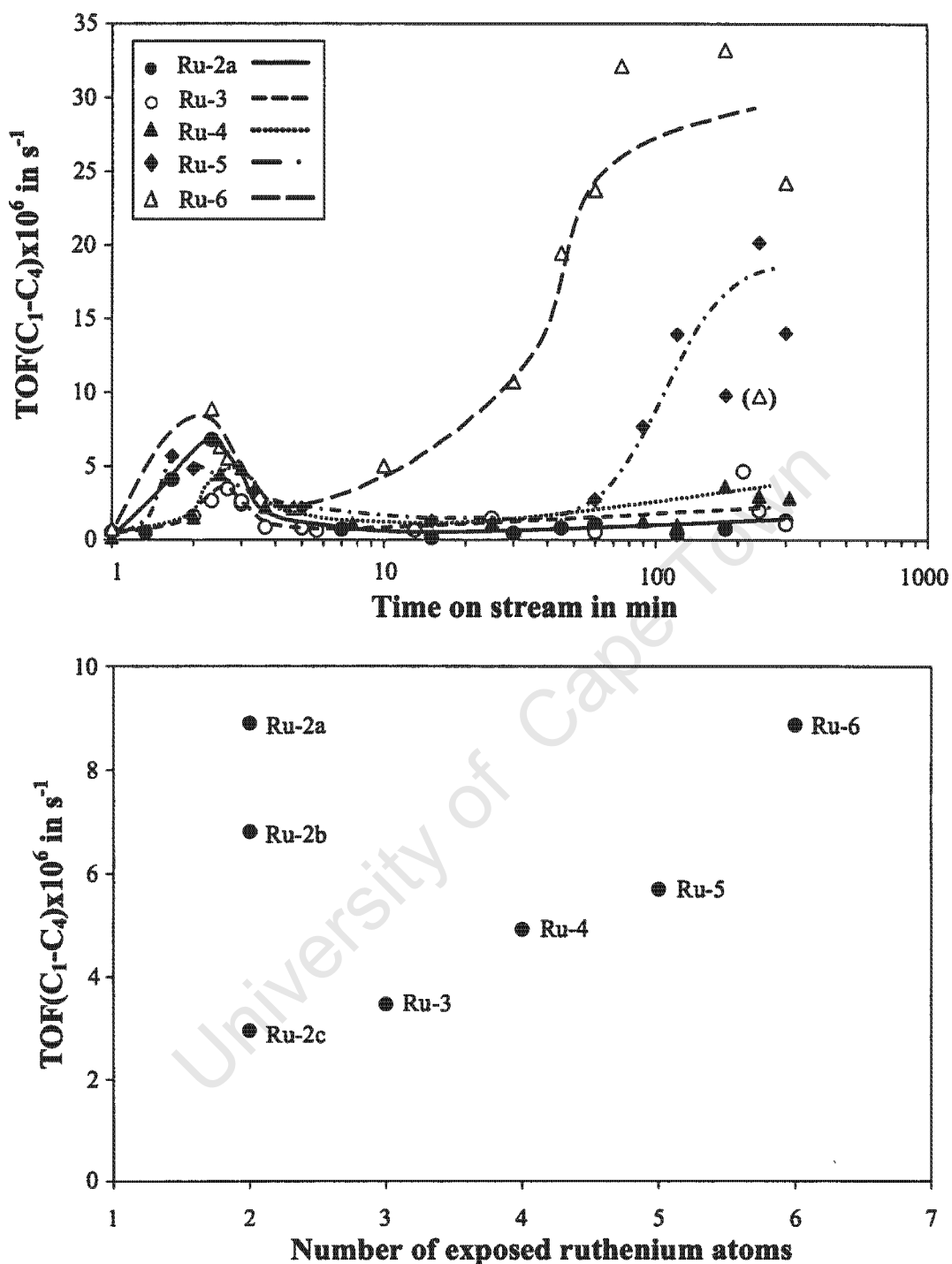


Figure 6.18: *top:* Changes in turnover frequencies of C₁-C₄ hydrocarbons in FT synthesis as function of time on stream for five selected alumina supported organometallic compounds. *bottom:* Maximal initial turnover frequencies of C₁-C₄ hydrocarbons in FT synthesis versus initial number of exposed metal atoms on alumina supported organometallic compounds.

(Note: TOF was calculated from the initial cluster size.)

(T_{Reaction} = 170°C, P = 4 bar, GHSV = 7 ml(STP)/(min·g_{cat}), (H₂/CO)_{in} = 2:1)

Figure 6.19 (top)). Judging from an apparent increase of their density, the formation of these crystallites formed preferably with increasing size of the original cluster and in samples Ru-3 and Ru-4 which were tested in extended runs (see Figure 6.19 (bottom)). The increase in activity with reaction progress and the onset of this increase might therefore be related to the stability of the initial cluster structure and the formation of crystallites which display higher activity than the starting compounds. It can be noted that the sizes of the crystallites in these spent samples were in the same range as the smallest crystallites of the model catalyst prepared via the microemulsion technique. On some of the samples, Ru-5 and Ru-6, the activity after five hours was only ca. 20% lower than the activity of the model catalysts with these crystallite sizes, suggesting that similar catalysts were present at this stage of testing.

The tendency of crystallite formation on support materials from metallic cluster carbonyls is a known phenomenon (Kuznetsov and Bell (1980), Okuhara et al. (1985)) and has frequently been utilized to prepare highly dispersed model catalysts (e.g. ruthenium (Kellner and Bell, 1982) and iron (Johnston et al., 1999)).

Apart from the formation of some larger crystallites, there is indirect evidence that the spent catalysts still contain organometallic frameworks, since all spent samples maintained the yellow-orange colours of the original samples. In addition, organometallic compounds from spent samples of Ru-2c and Ru-3 were partially redissolved in methylene dichloride and analysed using IR and MS spectroscopy. Figure 6.20 (top) shows that IR spectra of the redissolved compound from spent sample Ru-2c and that of the initial organometallic compound $\text{Ru}_2(\text{CO})_2(\mu\text{-CO})(\mu\text{-CHCH}_3)(\eta^5\text{-C}_5\text{H}_5)_2$ are identical. This finding was substantiated by MS analyses (data not shown). The fact that the dimer Ru-2c could be extracted may suggest that it was not the catalyst, it may however also mean that it has at least partially reacted in the initial stages of the reaction and only the remaining fraction which not reacted is still present, even after five hours of testing. The IR spectrum for the redissolved material from spent sample Ru-3, which was tested for five hours, however, varied from the original compound $\text{Ru}_3(\text{CO})_{12}$ (see Figure 6.20 (bottom)). It shows three major adsorption bands at 2080, 2065, and 2021 cm^{-1} , which coincide with the main bands that were obtained for the freshly prepared compound $\text{Ru}_4(\mu\text{-H})_4(\text{CO})_{12}$ (the precursor for model catalyst Ru-4), and which are listed in literature (Bruce and Williams (1990); see also Chapter 4). It must be noted that the synthesis of $\text{Ru}_4(\mu\text{-H})_4(\text{CO})_{12}$ is generally done starting from $\text{Ru}_3(\text{CO})_{12}$ at high hydrogen pressure (Bruce and Williams, 1990).

MS analyses of the compound(s) redissolved from the spent sample Ru-3 (after removal of the solvent) indicated the presence of a tetrameric and a trimeric ruthenium structure, which have not been characterised in detail. The formation of the tetrameric compound from the trimeric compound in the presence of hydrogen is to be expected, in analogy to the preparation of the tetrameric compound. It is not clear whether the trimeric structure observed in this analysis was present in the sample or formed upon fragmentation in the MS. Attempts to redissolve other organometallic compounds after their use as model catalysts were unsuccessful. IR characterisation of the supported samples, which can be used to identify the status of such clusters, has been reported to show evidence that such clusters can interact with support materials to varied extents and even form ruthenium aluminates depending on the strength of this interaction and the reaction environment (Kuznetsov and Bell (1980), Guglielminotti and Zecchina (1982), Zecchina and Guglielminotti (1982)). It was, however, reported that in the presence of carbon

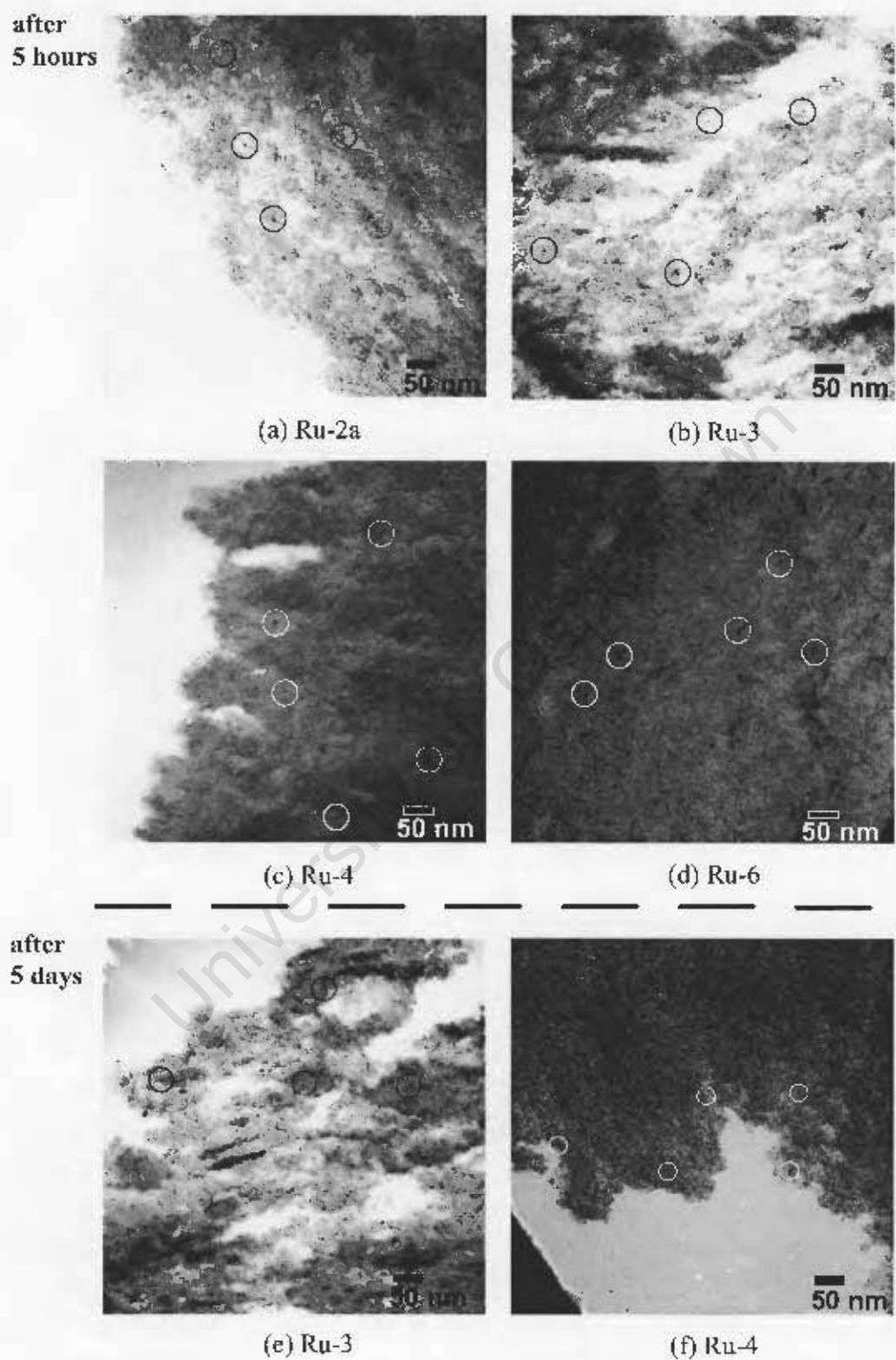


Figure 6.19: TEM micrographs of spent supported organometallic compounds after FT synthesis for five hours (a to d), and respectively five days (e and f).

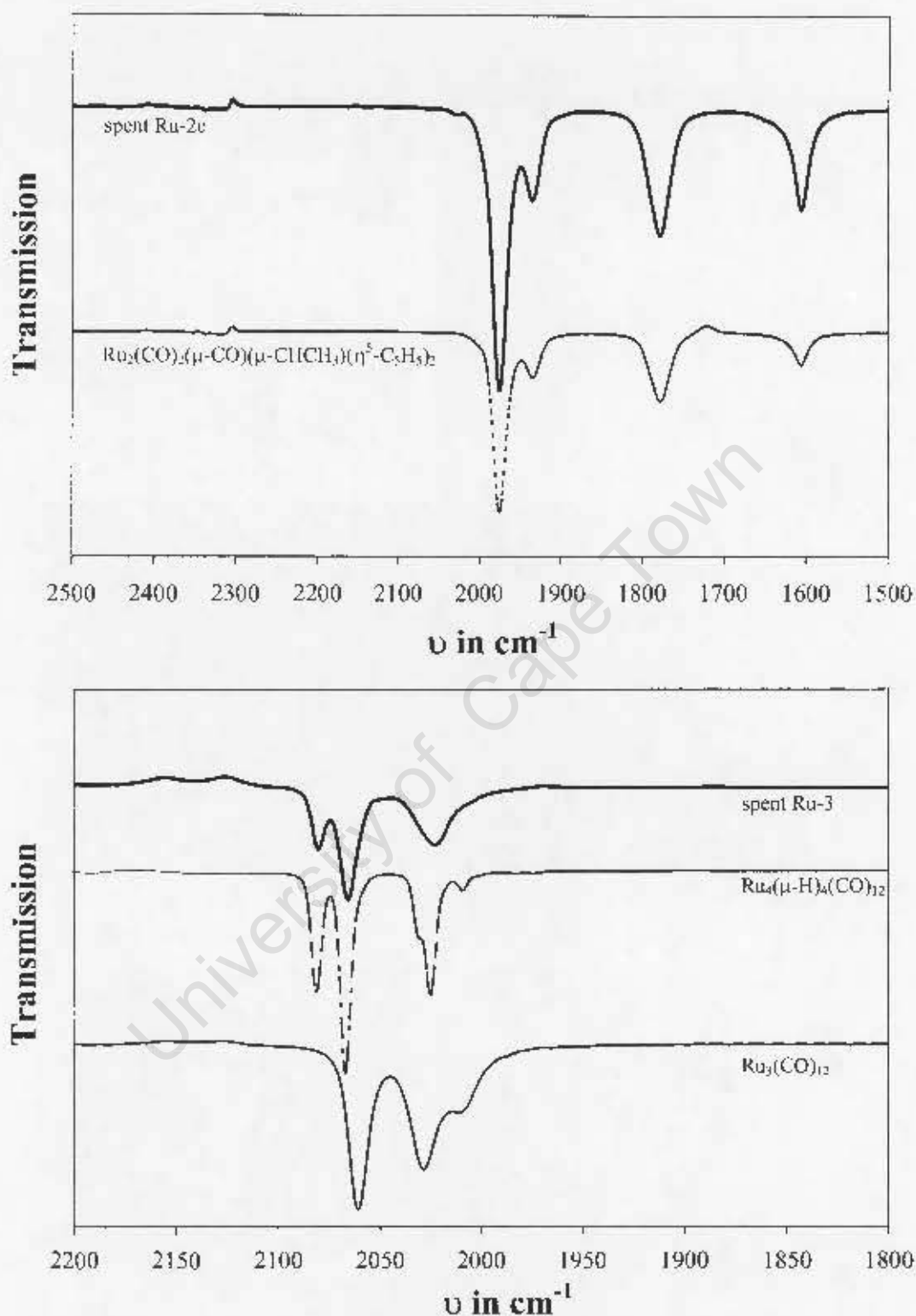


Figure 6.20: *top*: IR spectra for spent (after FT performance for 5 hrs) redissolved Ru-2c and fresh $\text{Ru}_2(\text{CO})_2(\mu\text{-CO})(\mu\text{-Cl})\text{CH}_3(\eta^5\text{-C}_5\text{H}_5)_2$ dissolved in methylene chloride.

bottom: IR spectra for spent (after FT performance for 5 hrs) redissolved Ru-3 and fresh $\text{Ru}_4(\mu\text{-H})_4(\text{CO})_{12}$ and $\text{Ru}_3(\text{CO})_{12}$ dissolved in methylene chloride.

monoxide the initial structures of $\text{Ru}_3(\text{CO})_{12}$, $\text{Ru}_4(\mu\text{-H})_4(\text{CO})_{12}$ and $\text{Ru}_6\text{C}(\text{CO})_{17}$ could

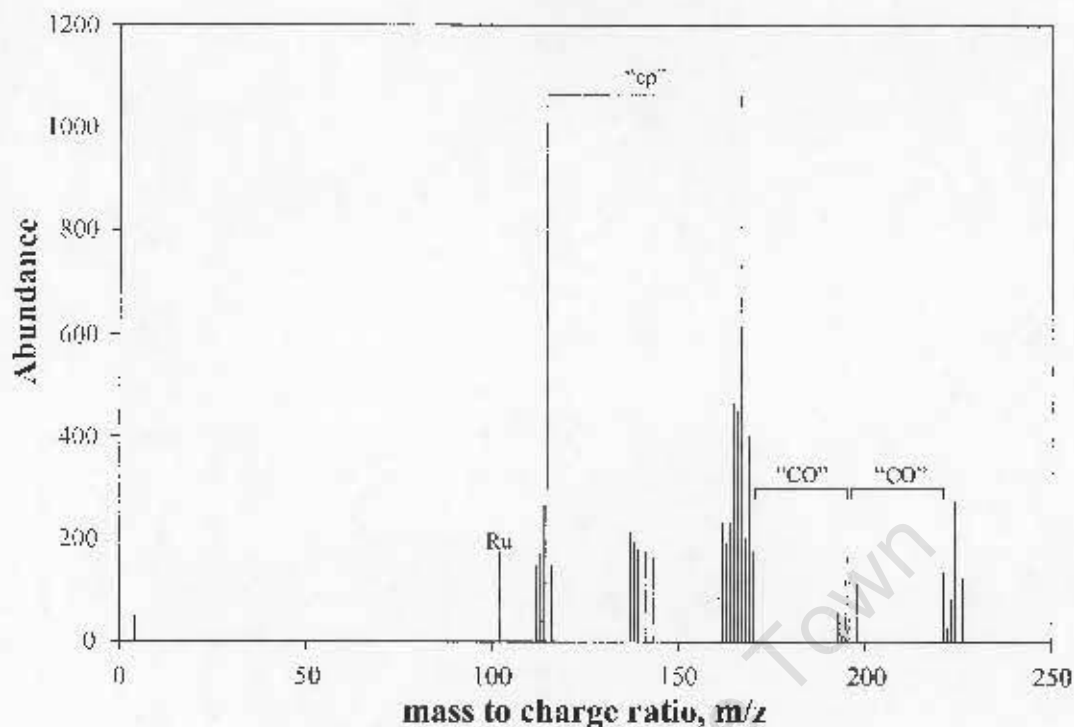


Figure 6.21: MS histogram of organometallic compound found in the outlet flow of FT performance of Ru-2a. (Note: Spectrum indicates formation of monoatomic ruthenium complex containing a cyclopentadiene group and two CO-ligands.)

be regained (Kuznetsov and Bell, 1980).

Although some decomposition of the complexes at reaction conditions is to be anticipated, the observations described above provide some evidence that the organometallic complexes did not undergo complete transformation via such interaction with the support and/or metallic crystallites, and it can therefore be concluded that they were, in principle, still available for synthesis gas conversion even after five hours of testing.

Formation of volatile ruthenium compounds (e.g. $\text{Ru}(\text{CO})_5$ and $\text{Ru}(\text{CO})_4$), which may form at reaction conditions, can account for loss of ruthenium and loss of activity. Therefore, product streams were analysed using GC/MS analyses^d (see Section 4.7.3, p. 46) and metal loadings of spent catalysts were determined using ICP analyses.

Only the analysis of the initial products of the tests on Ru-2b showed formation of an additional peak in the GC/MS chromatogram, which had characteristics of a ruthenium compound containing a cyclopentadiene group and two CO-ligands of volatile ruthenium compounds identified by means of GC/MS analyses (see Figure 6.21). ICP analysis of the spent Ru-2b substantiate the finding that ruthenium loss occurred during this experiment as only 0.92 wt% ruthenium was found in this sample in comparison to the 3.0 wt% initial loading. Although no volatile ruthenium compounds could be detected in product streams of the other compounds, ICP analyses on corresponding spent samples showed ruthenium loadings between 0.45 to 2.75 wt%, therefore lower than the initial ones, indicating losses of up to 85% (see Table 6.2).

^dRu has a unique isotope spectrum with isotopes at 95.91, 96.41, 97.91, 98.91, 99.90, 100.91, 101.90, 102.41 and 103.91 g/mol (major peaks in MS histogram: $m/z = 102$; Perry and Green).

Table 6.2: Metal loadings of spent supported organometallic compounds observed from ICP analyses (loading of fresh samples: 3 wt%).

Sample code	x_{Ru} (spent) in wt%
Ru-2a	0.92
Ru-2b ^a	0.45
Ru-2c	1.99
Ru-3	2.64
Ru-4	2.75
Ru-5	1.17
Ru-6	1.95

^a volatile ruthenium containing compounds found in the outlet flow

In conclusion, the different alumina supported organometallic compounds tested in this work all showed formation of C_{2+} hydrocarbons. The formation of these FT-typical products from di- and tri-nuclear ruthenium compounds supported on silica has previously been reported by Claeys et al. (2000b), while FT product formation from tetra-, penta- and hexameric structures additionally observed in this work has not been reported before. Frameworks of the model compounds at the final stages of the tests were not well-defined anymore and spent catalysts might contain a mixture of original organometallic compounds, medium-sized cluster systems and nano-sized crystallites. The product formation at the initial stages of the experiments is believed to be due to the starting compound, therefore indicating the ability of compounds with a minimum of two ruthenium atoms to promote C-C bond formation. A dendritic monoatomic ruthenium cluster had been reported to display no activity for FT product formation (Claeys et al., 2000a), and theoretical DFT calculations seem to confirm that indeed more than one ruthenium atom is required (see Chapter 8 in this work). The nuclearity and the nature of the ligands seem to have an effect on the initial specific activity of the compounds, but they also impact on the stability of the clusters at reaction conditions. Their effect on the product selectivity is discussed in the following Section.

6.2.2 Product Formation

Product spectra showed mainly the formation of hydrocarbons (C_1 - C_4). Oxygenates were formed as by-products at negligible amounts and have not been taken into account. Cyclopentadiene and cyclopentane formation was detected in the experiments with the diatomic compounds Ru-2a, Ru-2b and Ru-2c, and these are believed to originate from the cluster ligands. Initially acetone and isopropanol were monitored in GC-FID analyses. It was assumed that these compounds were not direct products, as acetone was used as solvent during immobilization of organometallic compounds on the support (see preparation in Section 4.1.2, p. 37). Products were analysed using offline GC-FID analysis. The product yields after the initial maximum (see Figure 6.18 (bottom)) were too low for reliable determination of selectivity data. The results presented in the following Section therefore only focus on the selectivity of the products observed during the first 3 minutes of testing. At this early stage the structures of the compounds are believed to be mainly intact and the observed results should therefore be directly due to the starting structure.

Detailed selected activity and selectivity results can be found listed in Appendix B.2, Tables B.6-B.8, pp. 173. In addition to formation of hydrocarbons, carbon dioxide was detected at initial stages of the tests using GC/MS analyses.

6.2.2.1 Methane Formation and Chain Growth

The average methane contents obtained in the C₁ to C₄-fraction between 1 and 3 minutes runtime, for the different ruthenium compounds, are shown in Figure 6.22. Generally, fairly high methane selectivities were found for all compounds, the diatomic complexes Ru-2a and Ru-2b apparently displaying higher methane formation than the larger clusters.

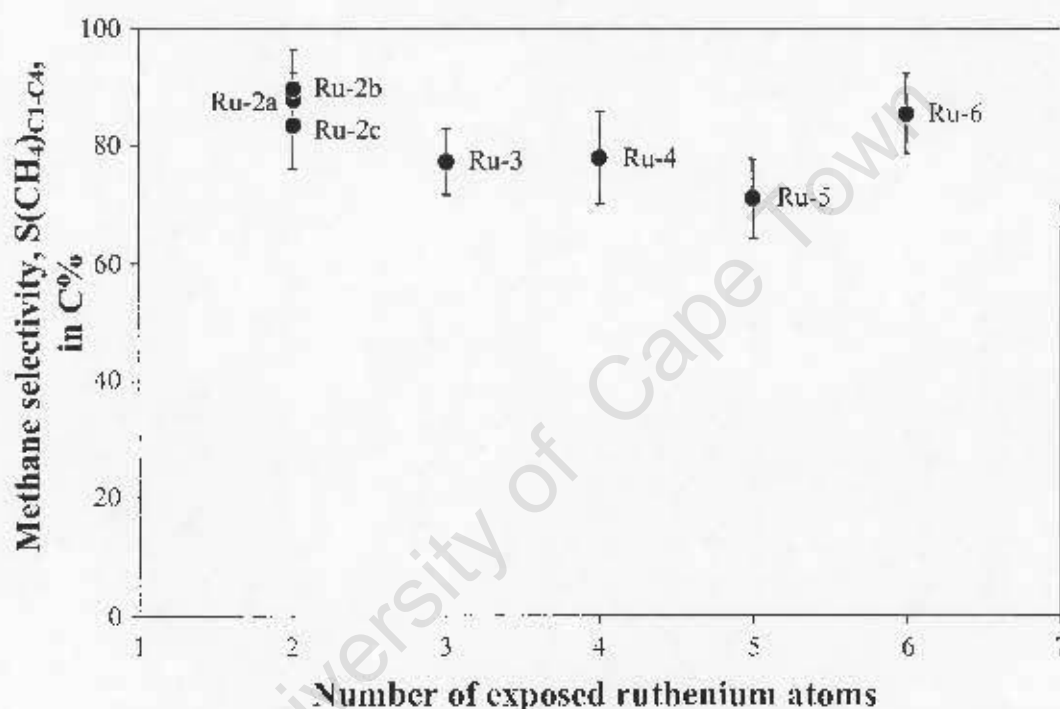


Figure 6.22: Average initial methane selectivities in the C₁-C₄ hydrocarbons between 1-3 minutes runtime in FT synthesis versus initial number of exposed metal atoms on alumina supported organometallic compounds.

(T_{Reaction} = 170°C, P = 4 bar, GHSV = 7 ml(STP)/(min-g_{cat}), (H₂/CO)_{in} = 2:1)

Nonetheless, formation of C₂ up to C₄ hydrocarbons was obtained on all the clusters. In order to characterise their formation, the molar contents of all hydrocarbons detected in the experiments obtained between 1 and 3 minutes of testing are plotted logarithmically against carbon number in Figure 6.23. Straight lines in these Anderson-Schulz-Flory-type plots indicate ideal chain growth and the chain growth probability can be derived directly from their slopes (see equation 2.5, p. 6). Remarkably, approximately straight lines were obtained for some of the compounds, namely Ru-2b and Ru-6, whereas non-ideal behaviour was found for the other compounds. Some deviations with relatively high methane contents and relatively low C₂ contents are commonly observed in FT-product distributions, and are generally attributed to effects of additional methane formation and secondary ethene incorporation (Iglesia (1997b), Schulz and Claeys (1999a)). The latter effect normally coincides with olefin contents in the C₂-fraction lower than those in the

C_3 -fraction. This was, however, not observed for the clusters Ru-2a, Ru-3 and Ru-4, which all show a relatively low C_2 formation in the ASF plots (for C_2 and C_3 olefin contents see Figure 6.25 (top and bottom) and Section below). It can also be noted that relatively large formation of C_2 and C_4 hydrocarbons was observed with the compound Ru-2c (see Figure 6.23 (left)), which is likely to originate from the bridging "CH-CH₃" ligand present in this cluster. The irregularities of chain growth obtained for the tested clusters may, to an extent, be due to non steady-state conditions and a rather random combination of different species that may form on the clusters under synthesis gas flow. Nonetheless, overall an FT-like product has been obtained and, albeit possibly not strictly applicable, chain growth probabilities have been derived from the slopes between C_1 to C_2 and C_3 to C_4 of the graphs in Figure 6.23, and are listed in Table 6.3. In qualitative accordance with the relatively high methane selectivities obtained in these runs, fairly low chain growth probabilities, mostly lower than 30%, were found.

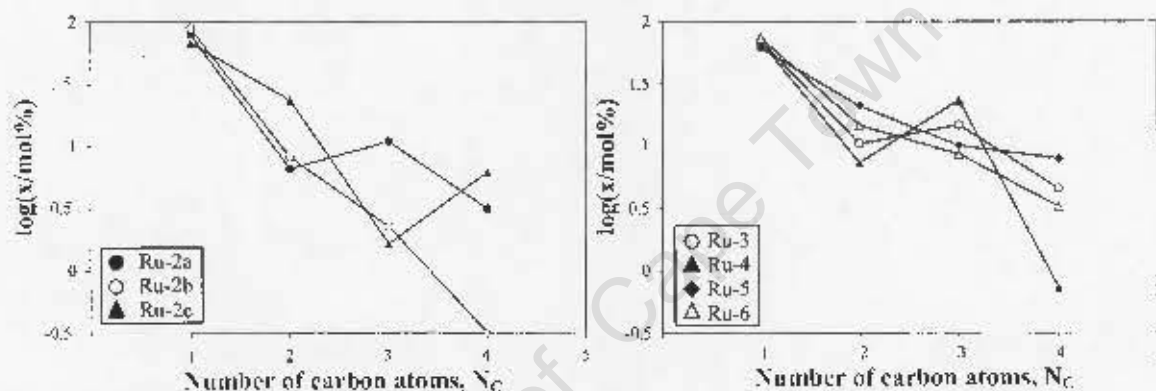


Figure 6.23: Molar product contents (C_1 to C_4) obtained at 2 minutes runtime in FT tests as function of carbon number on alumina supported organometallic compounds (left: Ru-2a, Ru-2b and Ru-2c; right: Ru-3, Ru-4, Ru-5 and Ru-6).

$(T_{\text{Reaction}} = 170^\circ\text{C}, P = 4 \text{ bar}, \text{GHSV} = 7 \text{ ml(STP)}/(\text{min}\cdot\text{g}_{\text{cat}}), (\text{H}_2/\text{CO})_{\text{in}} = 2:1)$

Table 6.3: Chain growth probabilities, carbon number ranges C_1 to C_2 and C_3 to C_4 , obtained at 2 minutes runtime in FT tests on alumina supported organometallic compounds.

$(T_{\text{Reaction}} = 170^\circ\text{C}, P = 4 \text{ bar}, \text{GHSV} = 7 \text{ ml(STP)}/(\text{min}\cdot\text{g}_{\text{cat}}), (\text{H}_2/\text{CO})_{\text{in}} = 2:1)$

Sample code	$P_{g,C1-C2}$	$P_{g,C3-C4}$
Ru-2a	0.09	0.28
Ru-2b	0.08	0.16
Ru-2c	0.39	(>1)
Ru-3	0.15	0.34
Ru-4	0.11	0.03
Ru-5	0.37	0.56
Ru-6	0.25	0.46

The specific formation rates of the detected hydrocarbons with two or more carbon atoms (i.e. $\text{TOF}(C_2-C_4)$) show an increase with increasing nuclearity of the clusters, suggesting

that the combination of surface species for chain formation is more facile on the larger clusters (see Figure 6.24).

The findings in this work confirm that two adjacent ruthenium atoms can promote C-C bond formation. Similar work on the clusters Ru-2a, Ru-2b and Ru-3 supported on silica already demonstrated the feasibility of C-C bond formation (Claeys et al. (2000a,b)), while tests on monoatomic ruthenium on a dendritic structure supported on silica only resulted in formation of methane, at rates much lower than those recorded with clusters of high nuclearity. Clusters with four or more ruthenium atoms were shown to display C-C bond formation activity for the first time in this work, but it appears that the methane selectivity is not affected much for clusters with more than three ruthenium atoms. It may be concluded that methane selectivity is enhanced on very small clusters, namely the diatomic ones, and largest, i.e. 100 C%, on monoatomic complexes. It should be borne in mind, though, that the findings reported here may be greatly affected by the ligands attached to the original clusters.

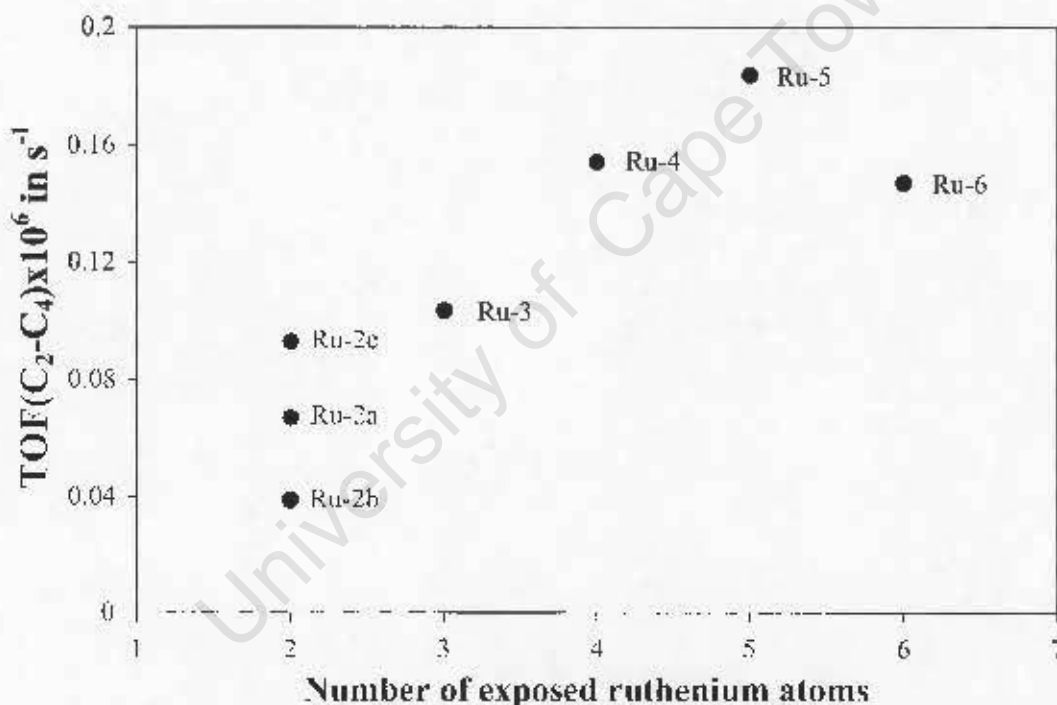


Figure 6.24: Maximal initial turnover frequencies of C₂-C₄ hydrocarbons in FT synthesis tests versus initial number of exposed metal atoms on alumina supported organometallic compounds. ($T_{\text{Reaction}} = 170^{\circ}\text{C}$, $P = 4$ bar, $\text{GHSV} = 7$ ml(STP)/(min \cdot g $_{\text{cat}}$), $(\text{H}_2/\text{CO})_{\text{in}} = 2:1$)

6.2.2.2 Olefin Formation

The C₂ and C₃-fractions were monitored to analyse effects of cluster size on olefin versus paraffin formation. The average olefin contents in these fractions obtained after 1-3 minutes of testing at FT-conditions are shown in Figure 6.25.

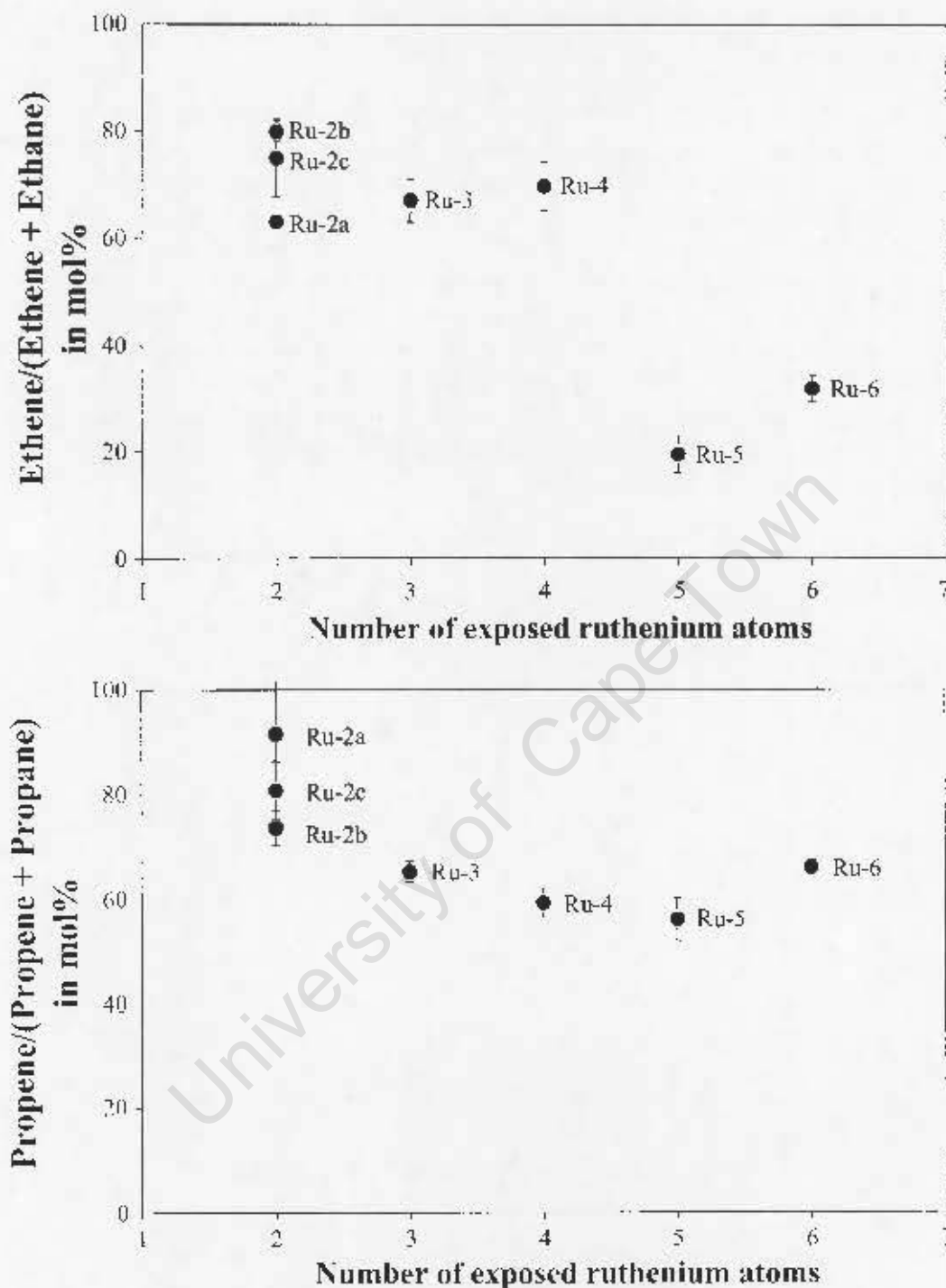


Figure 6.25: Average initial molar contents of ethene in C_2 hydrocarbons (*top*) and propene in C_3 hydrocarbons (*bottom*) between 1-3 minutes runtime in FT synthesis versus initial number of exposed metal atoms on alumina supported organometallic compounds. ($T_{\text{Reaction}} = 170^\circ\text{C}$, $P = 4$ bar, $\text{GHSV} = 7 \text{ ml(STP)}/(\text{min}\cdot\text{g}_{\text{cat}})$, $(\text{H}_2/\text{CO})_{\text{in}} = 2:1$)

Except for the ethene content in the C_2 -fraction on clusters Ru-5 and Ru-6, the olefin contents in both carbon number fractions on all clusters were between 60 and 80 mol%. These values are in the range of those typically regarded as for primary selectivity in

conventional FT synthesis (Iglesia (1997b), Schulz and Claeys (1999a)). It is not clear to what extent paraffins may have formed via secondary hydrogenation of the olefins. It was however noted that in all the runs acetone, which was used as a solvent during deposition of the clusters onto the support, was found in the chromatograms. In addition, with the clusters containing three or more ruthenium atoms, Ru-3 to Ru-6, iso-propanol was detected to amounts almost equalling that of acetone. No iso-propanol formation was detected in the test with the bimetallic clusters. Iso-propanol is believed to be formed via hydrogenation of acetone and the observations made may be interpreted as a probe reaction for the "hydrogenation activity" of the clusters. The absence of this activity for the diatomic compounds suggests that also no secondary olefin hydrogenation has occurred on these compounds, and the obtained olefin contents may therefore be a true reflection of primary olefin/paraffin selectivity.

The low olefin contents in the C₂-fraction obtained on the clusters Ru-5 and Ru-6 may be due to hydrogenation of ethene, which is known to be much more reactive than propene (Iglesia (1997b), Schulz and Claeys (1999a)). It might again be speculated that the ligands in the clusters, in this case the central carbon atom in the framework of clusters Ru-5 and Ru-6, impact on this reaction. It is surprising to note, though, that cluster Ru-4, which contains bridging hydrogen atoms and which should therefore potentially have the highest hydrogen availability, did not display enhanced formation of paraffins. Generally, the activation of hydrogen for formation of FT products, including chain growth and product desorption, seem to be fairly facile on all the clusters tested.

6.2.2.3 Does CO-activation take place on the supported organometallic compounds?

Although C-C formation was observed from initial stages of the tests with all the supported organometallic compounds, it is not clear whether the carbon in the hydrocarbon product originated from carbon monoxide in the synthesis gas or just from the carbon present in cluster frameworks. In order to investigate whether carbon monoxide was activated on the clusters, carbon balances were performed in which the sum of carbon in hydrocarbon products formed over the period of testing a compound, was compared to the carbon in the cluster (i.e. carbon in the form of CO-ligands, the CH-CH₃ group in complex Ru-2c and the central carbon atom in clusters Ru-5 and Ru-6; cyclopentadiene and pentamethyl-cyclopentadiene ligands have not been taken into account). These carbon balances are listed in Table 6.4.

The products formed over five hours of testing in synthesis gas only contained 2 to 26% of the carbon originally present in the cluster. Even after five days of testing the clusters Ru-3 and Ru-4 the cumulative amount of carbon in the products was lower than that in the clusters, although loss of carbon, including formation of volatile organometallic ruthenium complexes (see Section 6.2.1) and possibly desorption of carbon monoxide and formation of carbon dioxide (the latter was detected via GC/MS analyses, but not quantified), has not been taken into account. This evaluation does not allow for conclusions on the origin of carbon in the products. Table 6.4 also lists the relative amount of carbon found in hydrocarbon products in experiments where the clusters were exposed to hydrogen only. Although generally larger percentages of carbon were detected no full "recovery" of the ligand carbon was found.

In contrast to the runs conducted in synthesis gas, the spent catalysts of these runs had a black colour and redissolving of organometallic material from the supports was not suc-

Table 6.4: Amount of carbon in hydrocarbons formed over five hours of testing the supported organometallic clusters in synthesis gas and in hydrogen relative to carbon present in ligands of the clusters (excluding carbon in cyclopentadiene and pentamethyl-cyclopentadiene ligands).

Sample code	$m_{\text{C, HCN's}}/m_{\text{C, lig}}, \%$ tests in H_2/CO	$m_{\text{C, HCN's}}/m_{\text{C, lig}}, \%$ tests in H_2
Ru-2a	3.6	45.9
Ru-2b	2.2	2.4
Ru-2c	8.6	36.0
Ru-3	3.5 [30.3] ^a	20.4
Ru-4	4.9 [29.3] ^a	13.3
Ru-5	12.1	15.5
Ru-6	26.3	6.8

^a after five days testing

cessful. Furthermore, no formation of volatile organometallic ruthenium complexes could be detected and the ruthenium loading determined by means of ICP analyses showed that the loss of metal was much lower in these experiments (i.e. around 5 to 30%, see Table B.9 in Appendix B.4, p. 182) whereas in experiments, where carbon monoxide was present, up to 80% of ruthenium loss was recorded.

The products and product distributions observed in these experiments, however, resemble those obtained in the corresponding experiments in which synthesis gas was used, indicating that hydrocarbons do possibly originate from carbon in the ligands. The product obtained in these experiments was generally more paraffinic than that in the runs where carbon monoxide was present^e. An example chromatogram obtained at 3 minutes runtime with cluster Ru-6 is shown in Figure 6.26; selected results can be found listed in Tables B.6-B.7 in Appendix B.2, pp. 173. The clusters tested in hydrogen showed maximum product formation only at much later reaction times (between 10 to 100 minutes) compared to the experiments where synthesis gas was used (see Figure 6.27, for example Ru-3; for other clusters see Figure B.6 in Appendix B.3.2, p. 180). This delay may be an indication that carbon monoxide affects the stability of the clusters and plays some role in the activation of the clusters for product formation.

Experiments using ¹³C labelled carbon monoxide in the feed of the synthesis gas were done on clusters Ru-3 and Ru-6 in an attempt to throw more light on the origin of the hydrocarbons and the question of CO-activation on the clusters. In these runs the ¹³CO/H₂ mixture was flowed over the supported organometallic compounds for the first 15 minutes, and the feed then replaced with unlabelled synthesis gas. After five hours runtime labelled synthesis gas was again passed over the samples for 15 minutes. During these 15 minutes episodes product samples were taken and analysed by means of GC/MS analysis.

^eAll clusters have also been tested in argon at otherwise identical conditions, but no formation of hydrocarbons could be detected.

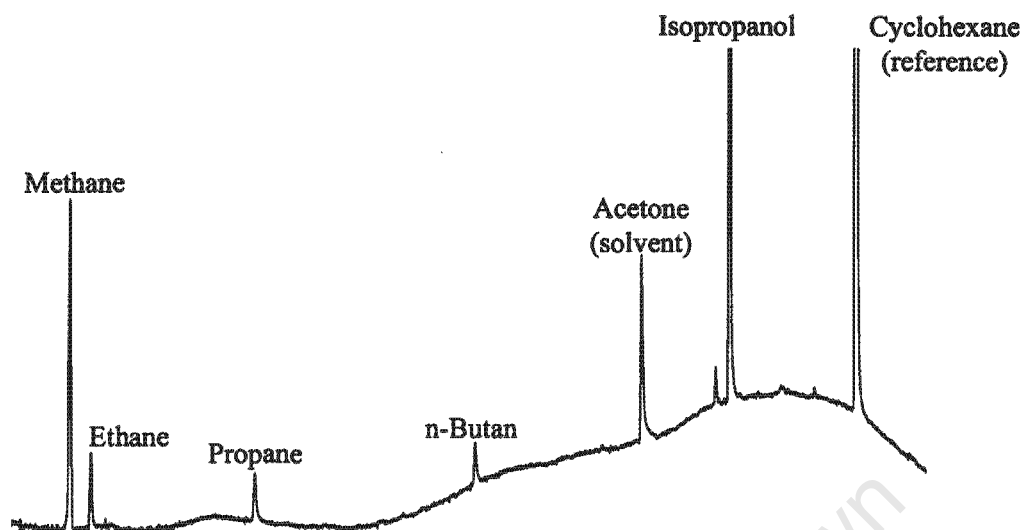


Figure 6.26: Gas chromatogram of product obtained after 3 minutes of testing compound Ru-6 in pure hydrogen.
 ($T_{\text{Reaction}} = 170^{\circ}\text{C}$, $P = 4$ bar, $\text{GHSV} = 7 \text{ ml(STP)}/(\text{min}\cdot\text{g}_{\text{cat}})$)

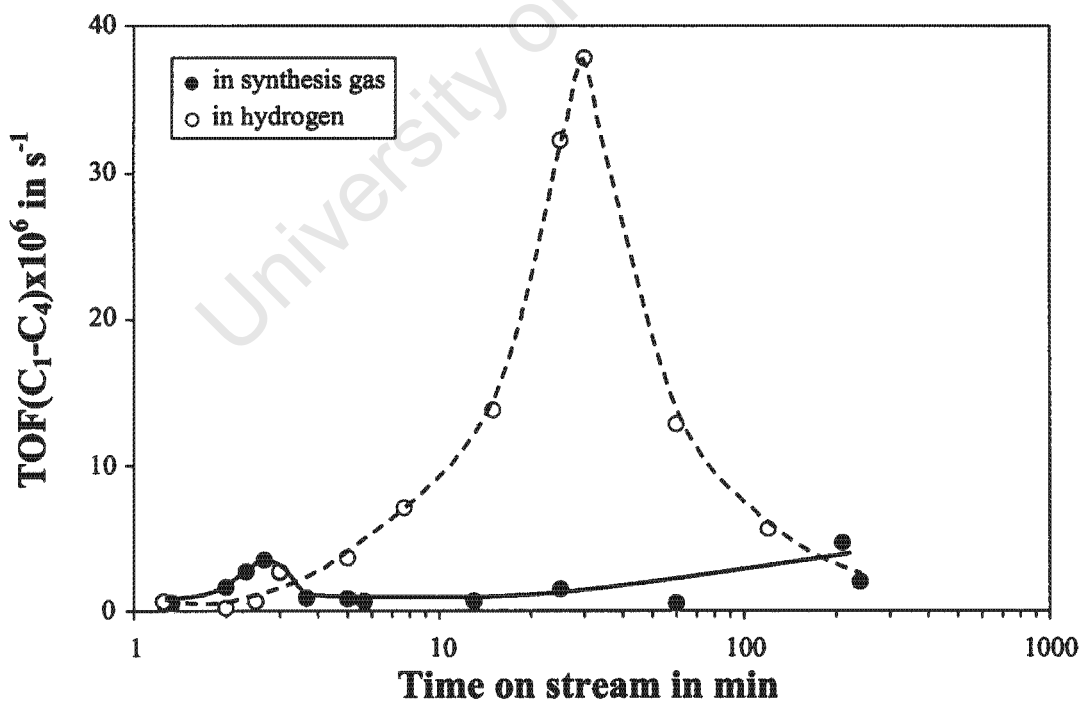


Figure 6.27: Changes in turnover frequencies of C₁-C₄ hydrocarbons in FT synthesis as function of time on stream for catalyst sample Ru-3, in synthesis gas (●) and in hydrogen (○).
 ($T_{\text{Reaction}} = 170^{\circ}\text{C}$, $P = 4$ bar, $\text{GHSV} = 7 \text{ ml(STP)}/(\text{min}\cdot\text{g}_{\text{cat}})$, $(\text{H}_2/\text{CO})_{\text{in}} = 2:1$)

No labelled carbon could be detected in the C₁ to C₃ hydrocarbons formed at the initial testing period, showing that, at least during the first 15 minutes, the carbon in these products must have originated from the ligands in the clusters. During this period, however, a marked increase of ¹³C was noticed in the carbon dioxide which was formed at this stage of the reaction, as evidenced by an increase in the 45 to 44 ion mass ratios. The gas phase carbon monoxide, therefore, seems to have interacted with the clusters resulting in formation of carbon dioxide. This would indicate that some activation of gas phase carbon monoxide did take place on the clusters, and this interaction may facilitate the product formation on the clusters, which showed enhanced initial product formation rates when tested in environments containing carbon monoxide. Removal of oxygen from the cluster CO-ligands would potentially result in formation of carbon species which, upon hydrogenation, could form CH_x species required for FT chain growth.

Surprisingly, also after monitoring of the products formed in synthesis gas for five hours runtime, no evidence of ¹³C was found in the hydrocarbon product. From TEM characterisation of spent catalysts it is known that, at this stage of testing, ruthenium crystallites sized between 2-3 nm are present, and regular FT CO-activation should thus occur. It is therefore suspected that the 15 minutes of monitoring were too short to investigate product formation representative of the actual reactant gas composition. This may also have affected the initial readings. It is therefore recommended to repeat such studies over extended testing times in future work before it can be concluded whether or not gas phase carbon monoxide can be incorporated into hydrocarbon products on the organometallic compounds tested in this work.

6.2.3 Conclusions of Findings of FT Experiments on Supported Organometallic Compounds

All the supported organometallic compounds tested in this series did display formation of typical FT products, viz. C₁ to C₄ hydrocarbons. Although some decomposition of the clusters with formation of volatile organic ruthenium complexes and growth of crystallites occurred over prolonged testing, product formation monitored in the very first minutes of testing is interpreted to be representative for reaction steps - which can occur on these structures. The following important observations and conclusions were reported:

- C-C bond formation on clusters of nuclearities with two to six ruthenium atoms is possible
- C-O bond cleavage must have occurred on all clusters
- there is no direct evidence that gas phase carbon monoxide has been activated on the clusters for FT product formation. Carbon monoxide does, however, seem to interact with the clusters and enhance initial product formation rates
- the activity of the clusters for product formation seems to depend on the nuclearity of the clusters and the chemical nature of the ligands
- the product selectivity obtained on these clusters generally shows very high methane contents (>80%), low chain growth probabilities (<30%) and olefin selectivities of 60-90% per carbon number, and it is not affected much by the cluster nuclearity, but possibly by the ligands on the cluster; diatomic clusters show enhanced methane

formation, and some secondary olefin hydrogenation may take place on clusters with five or more ruthenium atoms

Although it could not be conclusively shown that all steps required for stable FT synthesis are feasible on the model compounds tested, the observations with regard to product formation and selectivity may provide relevant information in order to understand site requirements on surfaces of larger agglomerates, i.e. crystallite surfaces. Variation of cluster structures, including their ligand systems and their size, is recommended for future work in order to understand the role of the "chemical environment" or the steps of product formation that will help to improve selectivity of desired products, e.g. olefins versus paraffins. Such studies may include a study of different support materials and/or support materials pretested in different ways in order to affect interaction of the cluster with the support. More efficient ways of linking the clusters to supports may also be investigated.

University of Cape Town

6.3 Nano- and Ångström-sized Crystallites/Clusters - Comparison and Discussion

This Section describes an attempt to compare/bridge the findings obtained in FT tests on the supported organometallic model compounds of varying nuclearity and the ruthenium crystallites of different crystallite sizes.

This comparison is made on the basis of the number of exposed ruthenium atoms, which in the case of the clusters equals the number of ruthenium atoms in their structure, whereas in the case of the crystallites the number of surface ruthenium atoms, as estimated from TEM characterisation of the fresh and spent catalysts, was taken into account. The performance of the organometallic compounds is believed to be best represented by the period of 1-3 minutes time of testing, when they show maximum activity and their original structure and nuclearity should still be largely preserved. For the ruthenium crystallites, both initial and steady-state data are shown. Only the results obtained at conditions identical to the ones applied with the clusters, i.e. 170°C reaction temperature and 4 bar total pressure, are taken into account here.

The turnover frequencies obtained with model catalysts of the two series is shown in Figure 6.28 (top). Generally, an increase of catalyst activity with an increase in number of exposed ruthenium atoms is observed. In addition to initial and steady-state turnover frequencies for formation of products which are volatile at reaction conditions, total turnover frequencies were calculated for steady-state conditions via extrapolation of formation rates to products up to a carbon number of 100 assuming ideal Anderson-Schulz Flory kinetics at the actual measured chain growth probability determined in each experiment (grey circles in Figure 6.28 (top)). These data points can be considered the closest possible reflection of the true turnover frequency which equals the surface atom specific rate of carbon monoxide disappearance that, could not be measured directly at the low conversion levels in these experiments. Such a correlation is not necessary or even not valid for data recorded at initial stages of the experiment where chain growth probabilities are low and long chain products should not have been formed yet. The data recorded at initial stages of both series of experiments is therefore a good representation of the crystallites or cluster activities for product formation. At early stages of an experiment the crystallites are deficient in carbon monoxide compared to the organometallic compounds which have CO-ligands attached to them. The performance of the crystallites at steady-state conversion, after possible reconstruction by carbon monoxide or synthesis gas, is therefore probably more suited for a comparison with the performance of the cluster, although this comparison should be done with much caution. It can be noted that the total turnover frequencies of the two series, i.e. the clusters at 1 to 3 minutes and the crystallites at steady-state (data point highlighted in grey areas), connect almost continuously, which possibly indicates that the steps of product formation on the largest clusters indeed simulate those occurring on crystallites.

A similar comparison of the specific formation rates of C_{2+} products (Figure 6.28 (bottom)), however, shows a relatively large gap with lower values of turnover frequencies ($TOF(C_{2+})$) for the organometallic compounds.

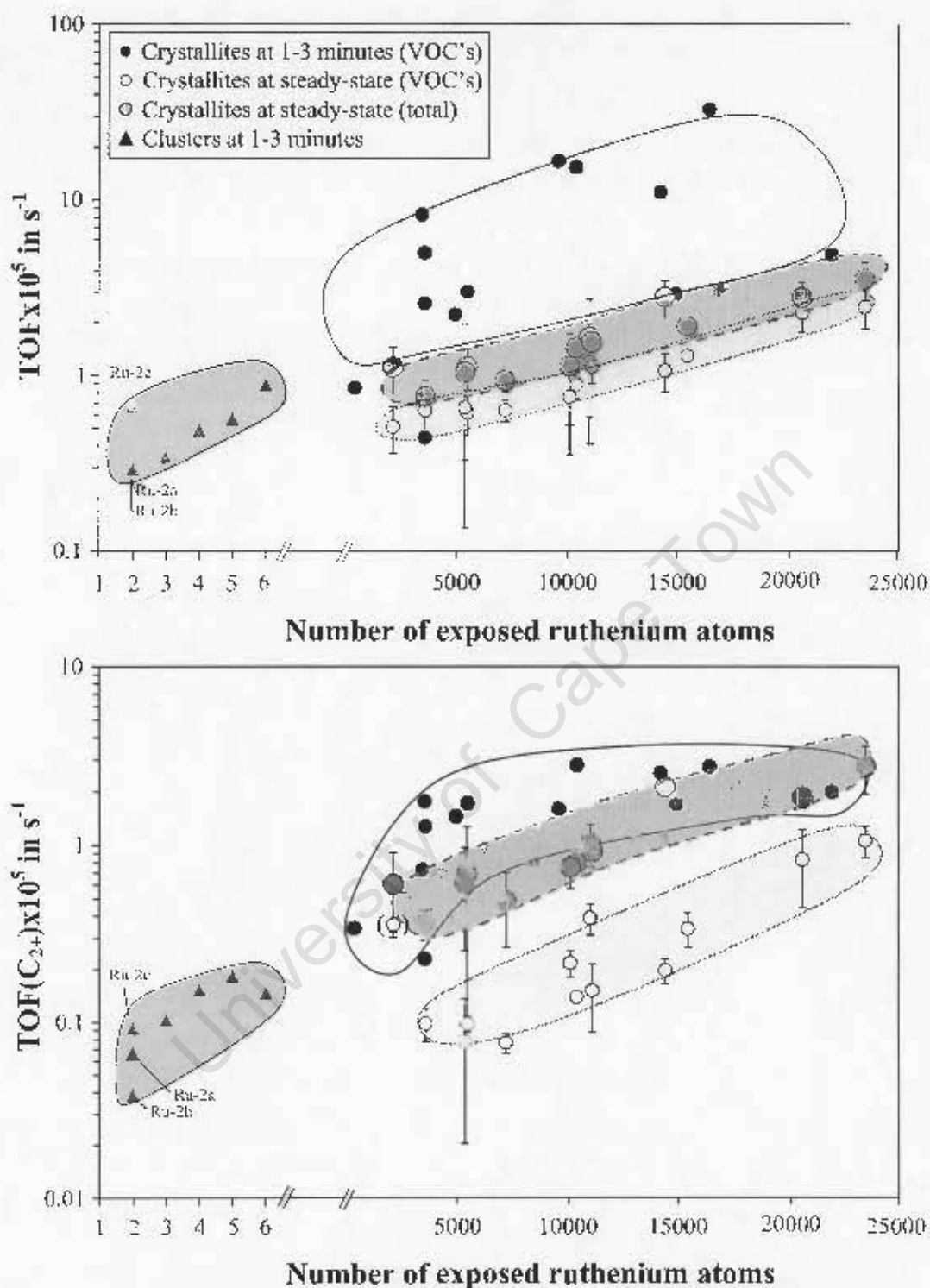


Figure 6.28: *top*: Maximal initial and average steady-state turnover frequencies in FT synthesis as function of number of exposed ruthenium atoms of fresh (1-3 minutes runtime) or, respectively, spent model catalysts (steady-state). *bottom*: Maximal initial and average steady-state turnover frequencies of C₂₊ hydrocarbons in FT synthesis as function of number of exposed ruthenium atoms of fresh (1-3 minutes runtime) or, respectively, spent model catalysts (steady-state). ($T_{\text{Reaction}} = 170^\circ\text{C}$, $P = 4 \text{ bar}$, $\text{GHSV} = 7 \text{ ml(STP)}/(\text{min} \cdot \text{g}_{\text{cat}})$, $(\text{H}_2/\text{CO})_{\text{inlet}} = 2:1$)

As chain growth probabilities obtained on these clusters were much lower than those obtained on crystallites (i.e. less than 30% compared to 75-90%), it may be speculated that the product formation observed on these clusters mainly represent formation of methane on sites which are atypical of FT chain growth sites. Such methane formation sites, "ensembles", may be present in relatively increased densities on smaller crystallites, where more ruthenium atoms of low coordination are present, and which can approximate the structures of the clusters.

Correspondingly, a strong increase in steady-state methane selectivity in the total product with decrease of crystallite size or the number of exposed ruthenium atoms, respectively, was obtained (see Figure 6.29). In addition, effects of decreased inhibition of carbon monoxide resulting in a hydrogen richer product may play a role on crystallites of smaller size.

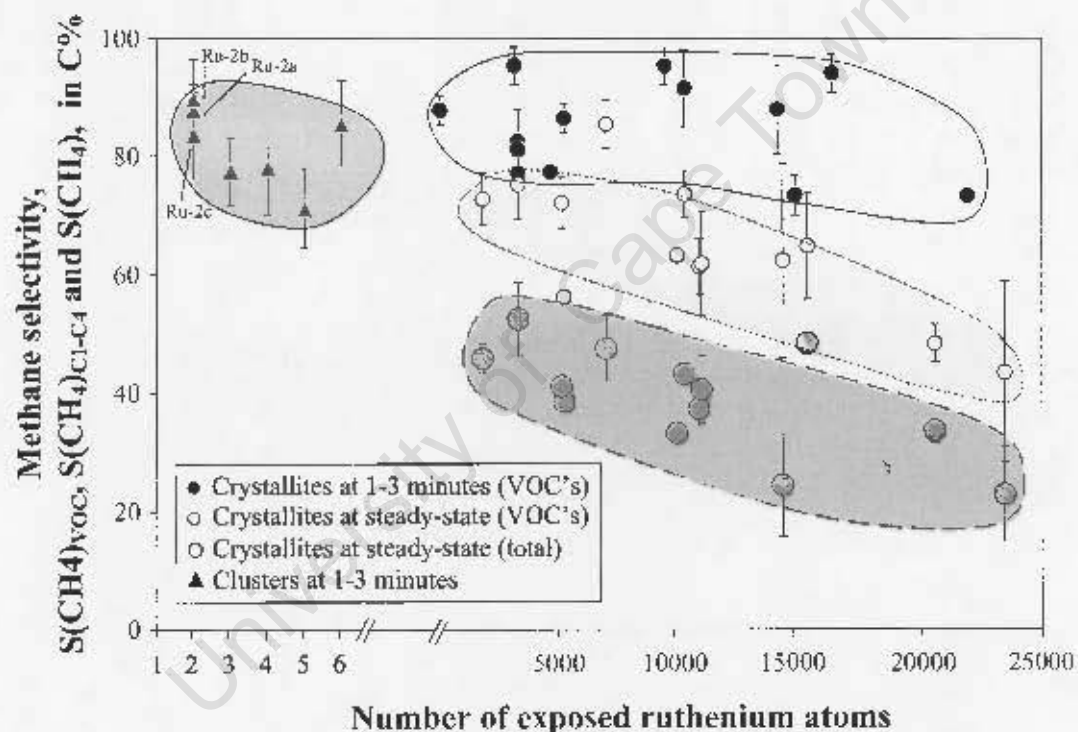


Figure 6.29: Average initial and steady-state methane contents in FT synthesis as function of number of exposed metal atoms of fresh (1-3 minutes runtime) or, respectively, spent model catalysts (steady-state).
($T_{\text{reaction}} = 170^{\circ}\text{C}$, $P = 4 \text{ bar}$, $\text{GHSV} \approx 7 \text{ ml(STP)}/(\text{min}\cdot\text{g}_{\text{cat}})$, $(\text{H}_2/\text{CO})_{\text{inlet}} = 2:1$)

The molar olefin contents in the C_2 and C_3 -fractions obtained with the organometallic compounds are in the same range as those obtained on the larger crystallites at steady-state conditions, i.e. approximately 60 to 80 mol%. This may be an indication that the steps of product desorption on the two model systems are indeed similar or even identical. On very small crystallites a decrease in olefin content was obtained at steady-state conditions, which was suggested to be either due to a shift of primary selectivity as a consequence of enhanced hydrogen availability or, respectively, decreased effects of CO-inhibition or enhanced secondary olefin readsorption on smaller crystallites. Effects of carbon monoxide deficiency should not play a role for the clusters. Very low ethene

contents obtained on the clusters Ru-5 and Ru-6, however, suggest that ethene hydrogenation has occurred on these structures.

In **conclusion** it can be stated that the experiments on the organometallic model compounds provide important clues on the site requirements for different reaction steps occurring during FT synthesis on nano-sized crystallites. Steps of gas phase CO-activation for product formation may not have occurred on the clusters. Steps of C-O bond cleavage and C-C bond formation, however, seem to be feasible on compounds with two ruthenium atoms although only at very low chain growth probabilities. The following Section presents attempts to investigate this feasibility on monoatomic versus diatomic model structures using a molecular modelling approach.

University of Cape Town

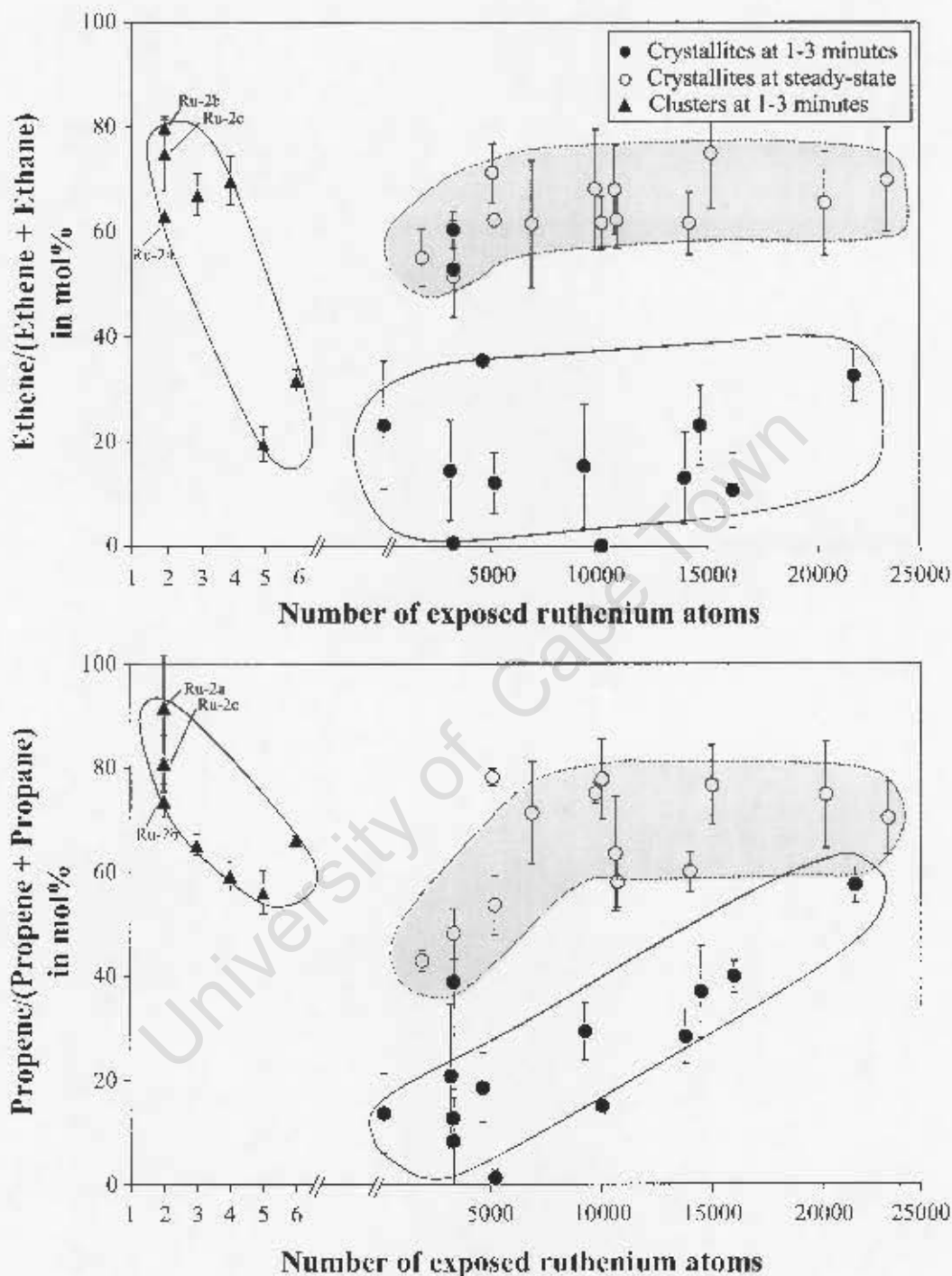


Figure 6.30: *top*: Average initial and steady-state molar contents of ethene in the C_2 -fraction in FT synthesis as function of number of exposed metal atoms of fresh (1-3 minutes runtime) or, respectively, spent model catalysts (steady-state).

bottom: Average initial and steady-state molar contents of propene in the C_3 -fraction in FT synthesis as function of number of exposed metal atoms of fresh (1-3 minutes runtime) or, respectively, spent model catalysts (steady-state).

($T_{\text{Reaction}} = 170^\circ\text{C}$, $P = 4$ bar, $\text{GHSV} = 7 \text{ ml(STP)}/(\text{min}\cdot\text{g}_{\text{cat}})$, $(\text{H}_2/\text{CO})_{\text{inlet}} = 2:1$)

Chapter 7

Theoretical Feasibility of CO-Activation and FT Chain Growth on Mono- and Diatomic Ruthenium Compounds

The theoretical feasibility of CO-activation and FT chain growth on a single metal centre and two adjacent metal atoms was investigated. These active centres containing one or two metal atoms are expressed as organometallic ruthenium complexes. FT reaction mechanisms based on experimental findings have been proposed, starting with known organometallic compounds.

7.1 Proposed Reaction Mechanisms

All possible reaction mechanisms for the mono- and diatomic model systems under consideration have been proposed based on commonly postulated pathways, viz. CO-insertion, carbide, enol, alkoxy and alkenyl mechanisms (Section 2.1.4, p. 7). As a starting point, the transformation of the ligands on the ruthenium centre is envisaged to take place in accordance with the empirical principles established in organometallic chemistry. The proposed intermediates have generally 18 valence electrons for the transition metal, hence reactive species have 16 valence electrons. The proposed mechanisms are divided into generation of the catalytically active species, generation of a chain starter and chain growth, as is common practice for polymerization reactions (see Section 2.1.4, p. 7). Additional limitations include a minimum number of six ligands on a ruthenium centre, one ligand for the Ru-Ru bond in the diatomic ruthenium complexes, and a number of carbon atoms equal to or exceeding the number of oxygen atoms. Carboxyl-ruthenium-compounds (Ru-OR) and hydroxyl-ruthenium-compounds (Ru-OH) were not considered.

7.1.1 Monoatomic Reaction Mechanism

$\text{Ru}(\text{CO})_5$ as the simplest monoatomic ruthenium complex was used as starting compound for the proposed monoatomic FT reaction mechanisms. Product desorption steps were included to allow comparison of theoretical selectivities with experimental observations done in a homogeneous environment.

A reaction scheme was developed to calculate the possible ruthenium complexes for a given hydrogen, carbon and oxygen atom number on a single ruthenium atom to verify that there are no additional reaction mechanisms possible. Plausible ligands consisting of carbon, hydrogen and oxygen atoms ($-H$; $\equiv C$; $\equiv CH$; $=CH_2$; $-CH_3$; $-CHO$; $-COOH$; $-CH_2CHO$; $-CH_2OH$; $=CHOH$; $-COCH_3$; $=CO$) were added to a ruthenium centre, with the restriction that the number of valence electrons (N_{VE}) equals 18 and 16 respectively, based on empirical organometallic chemistry rules (Cotton and Wilkinson, 1973). A set of numerical equations was solved for a given molecule $RuC_xO_yH_z$. In this equation set, the possible ligands were replaced with letters in alphabetical order^a. Each ligand was multiplied by the amount of donating electrons to the ruthenium centre. In equations 7.1, 7.2 and 7.3 the total number of hydrogen ($N(H)$), oxygen ($N(O)$) and carbon atoms ($N(C)$) was respectively calculated. The total amount of valence electrons on the ruthenium centre was calculated using equation 7.4, including 8 fixed valence electrons for the $4d^8$ ruthenium system. A valid solution was obtained when the different restrictions were verified. These restrictions stated that the number of oxygen atoms had to be equal to or smaller than the number of carbon atoms and that the maximal amount of ligands was restricted to six ($N(O) \leq N(C)$; $N_{ligands} \leq 6$).

$$N(H) = 1 \cdot a + 1 \cdot c + 2 \cdot d + 3 \cdot e + 1 \cdot f + 1 \cdot g + 3 \cdot h + 3 \cdot i + 2 \cdot j + 3 \cdot k \quad (7.1)$$

$$N(O) = 1 \cdot f + 2 \cdot g + 1 \cdot h + 1 \cdot i + 1 \cdot j + 1 \cdot k + 1 \cdot l \quad (7.2)$$

$$N(C) = 1 \cdot b + 1 \cdot d + 1 \cdot e + 1 \cdot f + 1 \cdot g + 2 \cdot h + 1 \cdot i + 1 \cdot j + 2 \cdot k + 1 \cdot l \quad (7.3)$$

$$N(Ru)_{elec} = 8 + 1 \cdot a + 3 \cdot b + 3 \cdot c + 2 \cdot d + 1 \cdot e + 1 \cdot f + 1 \cdot g + 1 \cdot h + 1 \cdot i + 2 \cdot j + 1 \cdot k + 2 \cdot l \quad (7.4)$$

The number of proposed monoatomic reaction mechanisms was equal to the maximum number of possible solutions for different combinations of carbon, oxygen and hydrogen atoms in different ligand systems for 18 and 16 valence electron species. Due to restrictions, it was not possible to calculate the maximum number of solutions for the diatomic systems.

Overall, three reaction mechanisms were proposed, viz. mechanism *A*, *B* and *C*.

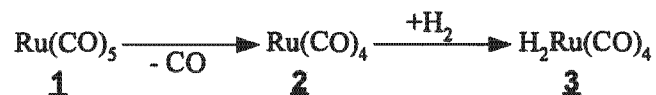
Generation of the Starter of the Catalytic Cycle

The first step is the transformation of the model catalyst $Ru(CO)_5$ (**1**) via CO-desorption into the 16 valence electron species $Ru(CO)_4$ (**2**). Hydrogenation of $Ru(CO)_4$ generates $H_2Ru(CO)_4$ (**3**), which is regarded as the starter of the catalytic cycle (see Scheme 18). These three species are all known and well characterised (Calderazzo and L'Eplattenier (1967), Huq et al. (1980), Ziegler et al. (1987), Huang et al. (1990), Ehlers and Frenking (1995), Decker and Klobukowski (1998), Wang et al. (2003)).

The catalytic cycle starts from $H_2Ru(CO)_4$ and involves the generation of the chain starter and then chain growth (see Scheme 19). Several possible desorption mechanisms have been included that lead to the formation of FT product compounds, such as methane

^aAlphabetical numbering system: H = a; C = b; CH = c; CH_2 = d; CH_3 = e; CHO = f; COOH = g; CH_2CHO = h; CH_2OH = i; CHOH = j; $COCH_3$ = k; CO = l

CH₄, methanol CH₃OH, and formaldehyde CH₂O.



Scheme 18: First steps of the proposed monoatomic FT reaction mechanisms.

Generation of the Chain Starter

The generation of the chain starter is based on the enol mechanism (Storch et al. (1951), Kolbel et al. (1966), Gupta et al. (1972)). CO-adsorption on H₂Ru(CO)₄ (**3**) with a simultaneous migration of ruthenium bonded hydrogen towards a CO-ligand generates a ruthenium-aldehyde species (**4**). The simultaneous action is required to keep the number of valence electrons constant. The aldehyde group undergoes a tautomerisation to the ruthenium-enol species (**5**). From here, three different mechanisms have been proposed for the generation of the chain starter including a C-O bond cleavage. HRu(CO)₄CH₃ (**7**) is regarded as the chain starter. Similar reduction mechanisms of M-CO via M-CHO into M-CH₃ are known in homogeneous environments (Sweet and Graham, 1979). Methyl surface species on bulk catalyst surfaces during FT synthesis are proposed in the alkyl mechanism (Yamasaki et al. (1981), Erley and McBreen (1983), Wang and Ekerdt (1984), Kaminsky et al. (1986)) and have been observed on surfaces involved in CO-hydrogenation (Wang and Ekerdt (1984)).

Mechanism A

In mechanism *A* water and carbon monoxide desorb from the ruthenium-enol species with simultaneous H-addition to form a ruthenium-methylidyne (Ru≡C) (**6a**¹), which is a typical intermediate in the carbide-mechanism (Fischer et al. (1925), Craxford and Rideal (1939), Claeys and van Steen (2004)). Methylidyne are known for ruthenium as well as various other transition metals such as e.g. rhodium (Herrmann et al. (1980)) and tungsten (Holmes et al. (1982)). It is unlikely that this is an elementary reaction, and may thus not be feasible on a monoatomic ruthenium complex. Hydrogenation of this 'carbide'-intermediate and simultaneous desorption of a CO-ligand leads to the ruthenium-methylene H₂Ru(CO)₃CH₂ (**6a**²), again a known compound for ruthenium (Carter and Goddard III (1986)). H-shift and CO-adsorption lead to the formation of the chain starter HRu(CO)₄CH₃ (**7**).

Mechanism B

In mechanism *B* H₂-adsorption and simultaneous CO-desorption yields H₂Ru(CO)₃(CHOH) (**6b**¹). CO-assisted desorption of this species may lead to the formation of formaldehyde and H₂Ru(CO)₄ or to the formation of methanol and Ru(CO)₄, which can be transformed into H₂Ru(CO)₄ by hydrogenation (not shown). Another H₂-addition was proposed to saturate the Ru=C bond, generating a ruthenium-alkoxy species (**6b**²), followed by water condensation on the alkoxy group to a ruthenium-methylene (**6b**³). H-shift from the ruthenium centre to the unsaturated methylene group generates the 16 valence electron transition state species **6b**⁴, and CO-addition forms the chain starter (**7**). All reaction steps in mechanism *B* are elementary and all intermediates have 18 valence electrons.

Mechanism C

The C-O bond cleavage in mechanism *C* yields another ruthenium-methylene intermediate (**6c²**). This species is formed via a ruthenium-methoxy (**6c¹**) involving H-shift and water elimination. Methylene groups as intermediates during FT synthesis are proposed in the alkyl and in the alkenyl mechanisms (Long et al. (1997), Claeys and van Steen (2004)). The ruthenium-methylene adsorbs another H₂-molecule to either generate the chain starter (**7**), or a ruthenium-aldehyde species (**7c¹**) and keeping the methylene group on the ruthenium. The second pathway by-passes the chain starter and goes directly via tautomerisation to **7c²** and finishes with another CO-insertion forming a C₂-keto ligand on the ruthenium (**8**).

7.1.2 Diatomic Reaction Mechanism

Ru₂(CO)₉ (**1**) was taken as the starting compound for the proposed diatomic FT reaction mechanisms. It was selected as model compound for FT synthesis and not the experimentally used ones, due to limited computer resources. These computer resources were drastically increased by simplifying the compound to CO-ligands.

The first step is H₂-activation and adsorption with simultaneous CO-desorption, generating compound **2** (see Scheme 20). Two different mechanisms (mechanism *A1* and *A2*) for the formation of the chain starter (**4**) were proposed. Three different mechanisms were proposed for the first and second part of the chain growth (mechanisms *B1/B2/B3* and *C1/C2/C3*; see Schemes 21 and 22). All proposed reaction steps are elementary and all intermediates have 18 valence electrons.

Mechanisms A1, B1 and C1

Mechanisms *A1*, *B1* and *C1* follow the same reaction sequence, where the C-O bond cleavage occurs on the bridging CO-ligands. Therefore, in mechanism *B1* and *C1*, the first step is the transformation of a terminal CO-ligand from compounds **4** and **6** into a bridging CO-ligand. H₂-addition on the bridging CO reduces it to a bridging ruthenium-methoxy (**3a¹**, **5a²**, **7a²**). The next step is water desorption with simultaneous H₂-addition in mechanisms *B1* and *C1* and, respectively, CO-adsorption with simultaneous water desorption in mechanism *A1* generating a bridging ruthenium-methylene (**3a²**, **5a³**, **7a³**). Bridging ruthenium-methylenes are known compounds (Davies et al., 1984). In mechanism *A1*, the bridging methylene-ligand transforms into a terminal methylidene-ligand, forcing a rearrangement of a terminal carboxyl into a bridging position (**3a³**). H₂-addition on the unsaturated Ru=CH₂ generates the chain starter Ru(CO)₄(CH₃)RuH(CO)₄ (**4**). In mechanisms *B2* and *C2* the bridging methylene-ligand shifts directly to a terminal position, generating the ruthenium-alkyl compounds with longer hydrocarbon chains (**6**, **8**).

Mechanisms A2, B2 and C2

The C-O bond cleavage in mechanisms *A2*, *B2* and *C2* is based on the enol mechanism (see Section 2.1.4, p. 8). In mechanism *A2* an additional step is included, where the ruthenium-enol (**3b²**) is formed over di-hydrido-octacarbonyl-diruthenium (**3b¹**) via H₂-addition. In mechanisms *B2* and *C2* the ruthenium-enol (**5b¹**, **7b¹**) is directly generated via hydrogenation of a CO-ligand from the ruthenium-alkyls **4**, **6**. H₂-addition reduces the ruthenium-enol to a ruthenium-methoxy (**3b³**, **5b²**, **7b²**). H-shift from a terminal

hydrogen to the unsaturated Ru=C of the ruthenium-methoxy with simultaneous water desorption, forms the ruthenium-methylenes **3b⁴**, **5b³** and **7c³**. In mechanism **A2**, a H-atom rearranges to the methylene with a simultaneous CO-adsorption, forming the chain starter **4**. The methylene-ligand inserts into the ruthenium-alkyl ligand of the adjacent ruthenium atom and CO adsorbs in mechanisms **B2** and **C2**, leading to the formation of the ruthenium-alkyl compounds **6** and **8**.

Mechanisms B3 and C3

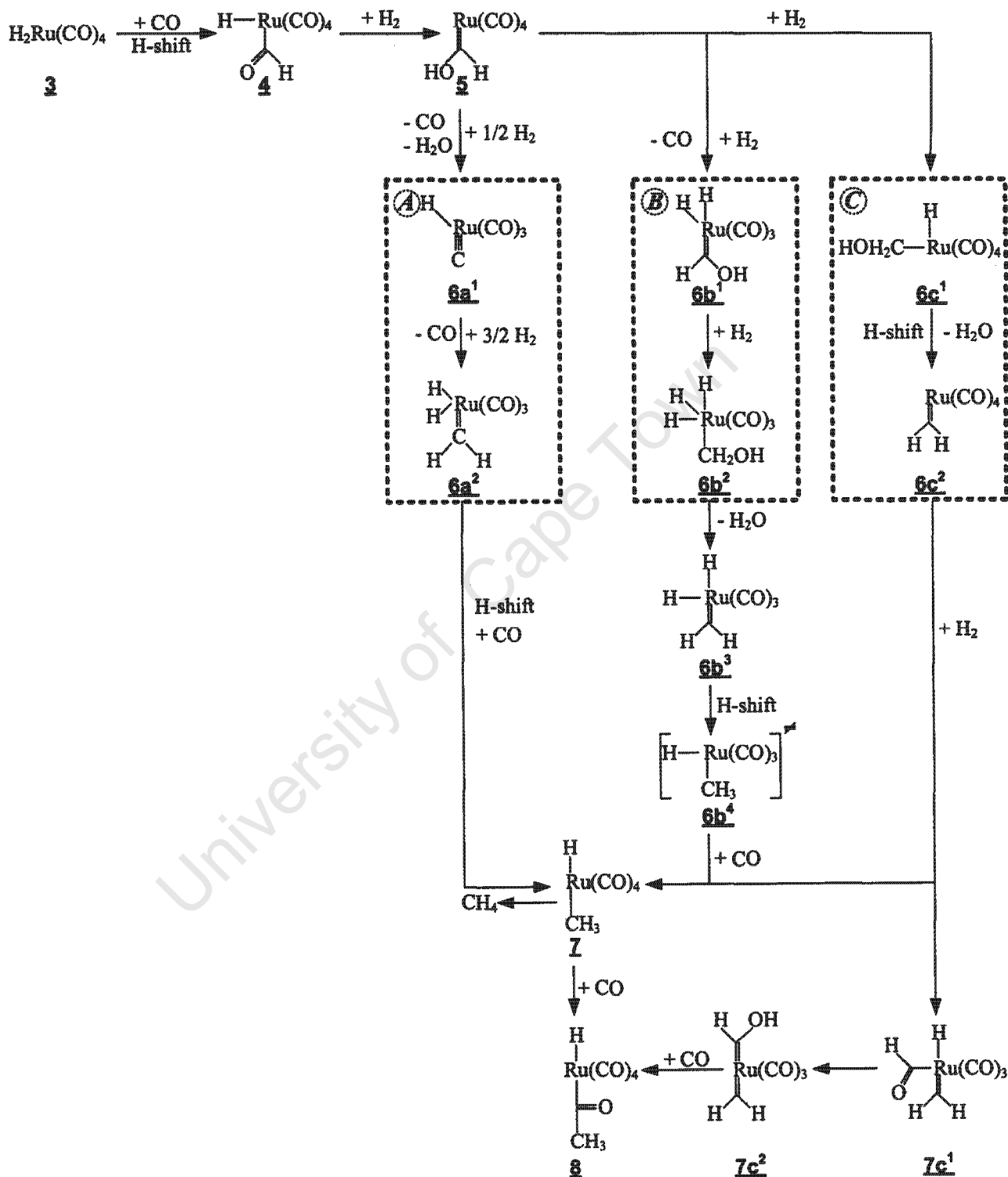
CO-insertion in the Ru-C bond of the ruthenium-alkyl ligand of the compounds **4** and **6** are proposed in mechanisms **B3** and **C3**. The generated ruthenium-keto (**5c¹**, **7c¹**) hydrogenates to a ruthenium-methoxy (**5c²**, **7c²**), water and CO desorb, H₂ adsorbs and a ruthenium-alkylidene (**5c³**, **7c³**) is generated. H-shift and CO-adsorption on the unsaturated hydrocarbon bond generates, based on the CO-insertion mechanism, the ruthenium-alkyl species with a hydrocarbon chain length of respectively two (**6**) and three (**8**).

7.2 Computational Details

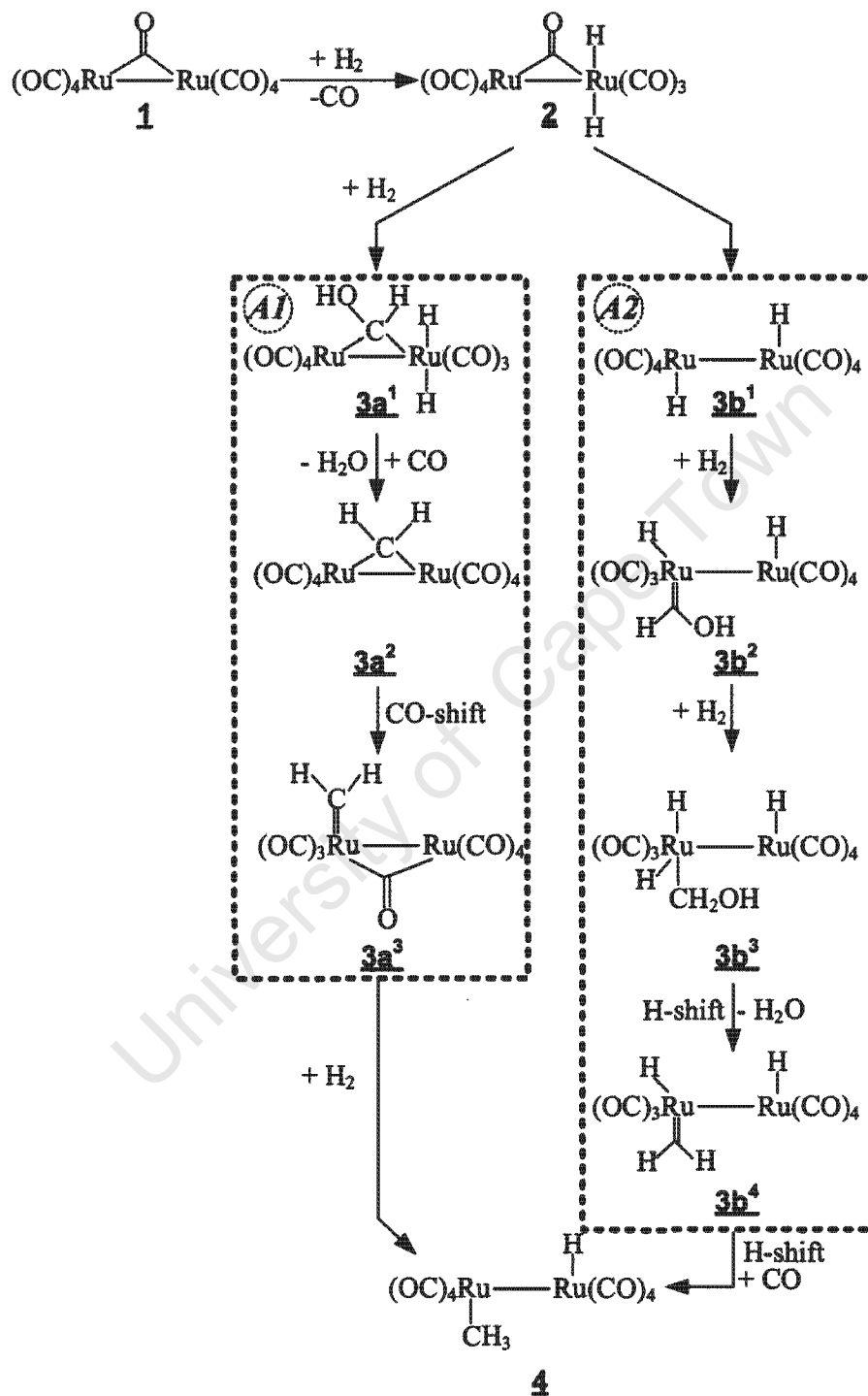
To investigate the feasibility of the proposed mechanisms, geometry optimization calculations based on the density functional theory (DFT) were performed on each intermediate. The calculations were done using Materials Studio, employing DFT-GGA (general-gradient approximation) as implemented in the DMol code (Delley (1989, 2000)). The ruthenium core, [Kr]5s², was treated using an effective core potential (ECP) (Dolg et al. (1987), Bergner et al. (1993)) and for the valence electrons, 5p¹4d⁵, a double numerical basis set with polarization (DNP) was used. For hydrogen, carbon and oxygen all electrons were included in the calculations^b. Geometry optimization calculations were done for different multiplicities to investigate the minimum electronic energy, E_{elec}. All calculations were performed in the gas phase using the BLYP functional. Stationary points were characterised as local minima by ensuring the absence of imaginary frequencies in the vibrational analysis, which also enabled correction of the electronic energies for zero-point vibrational energies. The energy convergence tolerance was 2.0 × 10⁻⁵ Ha, the basis set cut-off radius was 4.3 Å, the maximal force 0.004 Ha/Å, and the maximum displacement 0.005 Å. Electronic smearing was used in cases where the convergence was problematic.

The minimum electronic energies, E_{elec}, are static energies at 0 K. These results were used to calculate the enthalpy, H, and entropy, S, of each compound extrapolated to other temperatures (T = 25-1000 K) using standard thermo-chemical approximations. The energies reported are at a temperature of 475 K, which is a typical reaction temperature for ruthenium based FT synthesis. The amounts of hydrogen, carbon, oxygen and ruthenium atoms were kept constant for every reaction step and all the surrounding molecules were taken into account in the stability calculation.

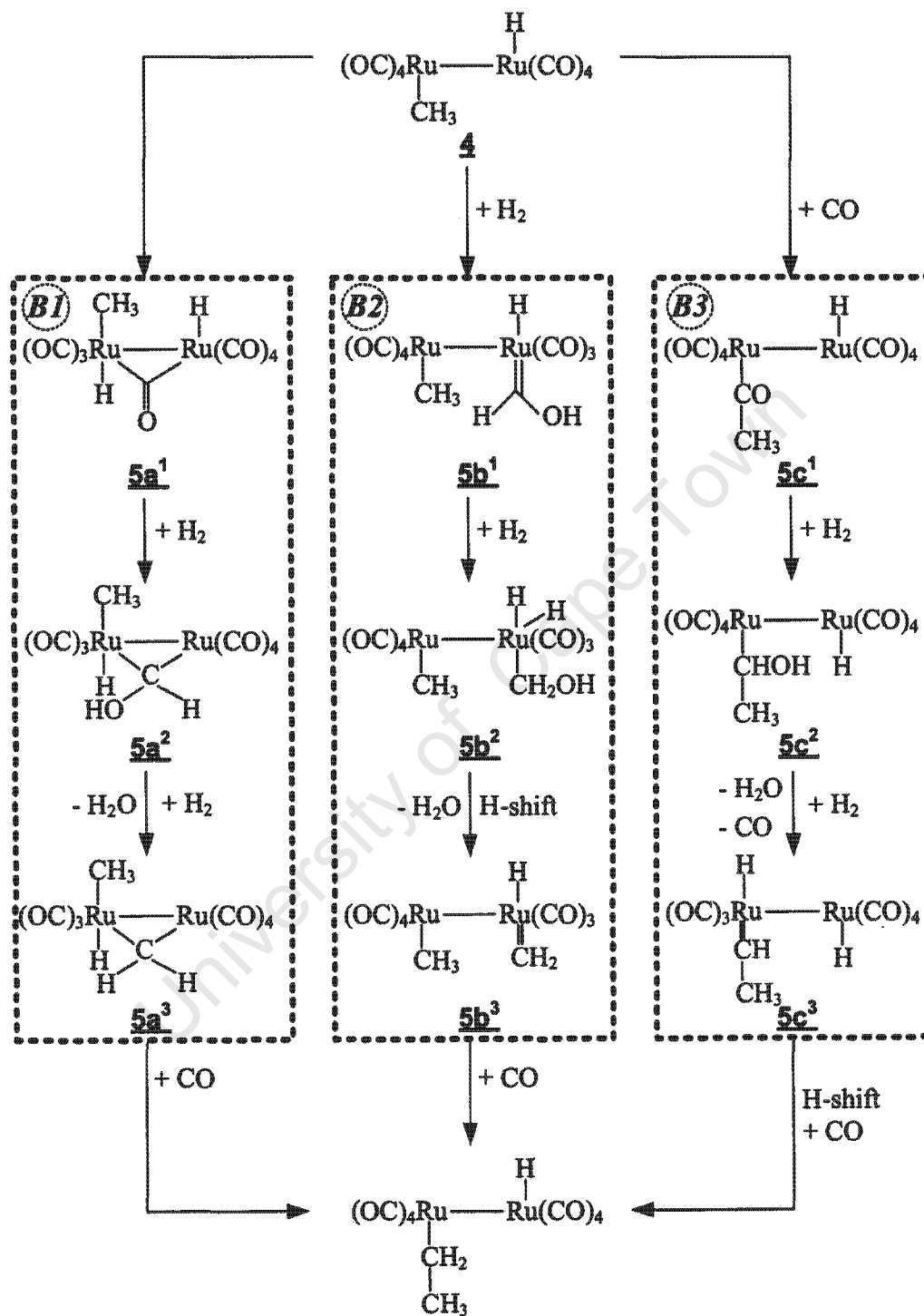
^bH 1s¹: 1 VE, C [He]2s²2p²: 4 VEs, O [He]2s²2p⁴: 6 VEs



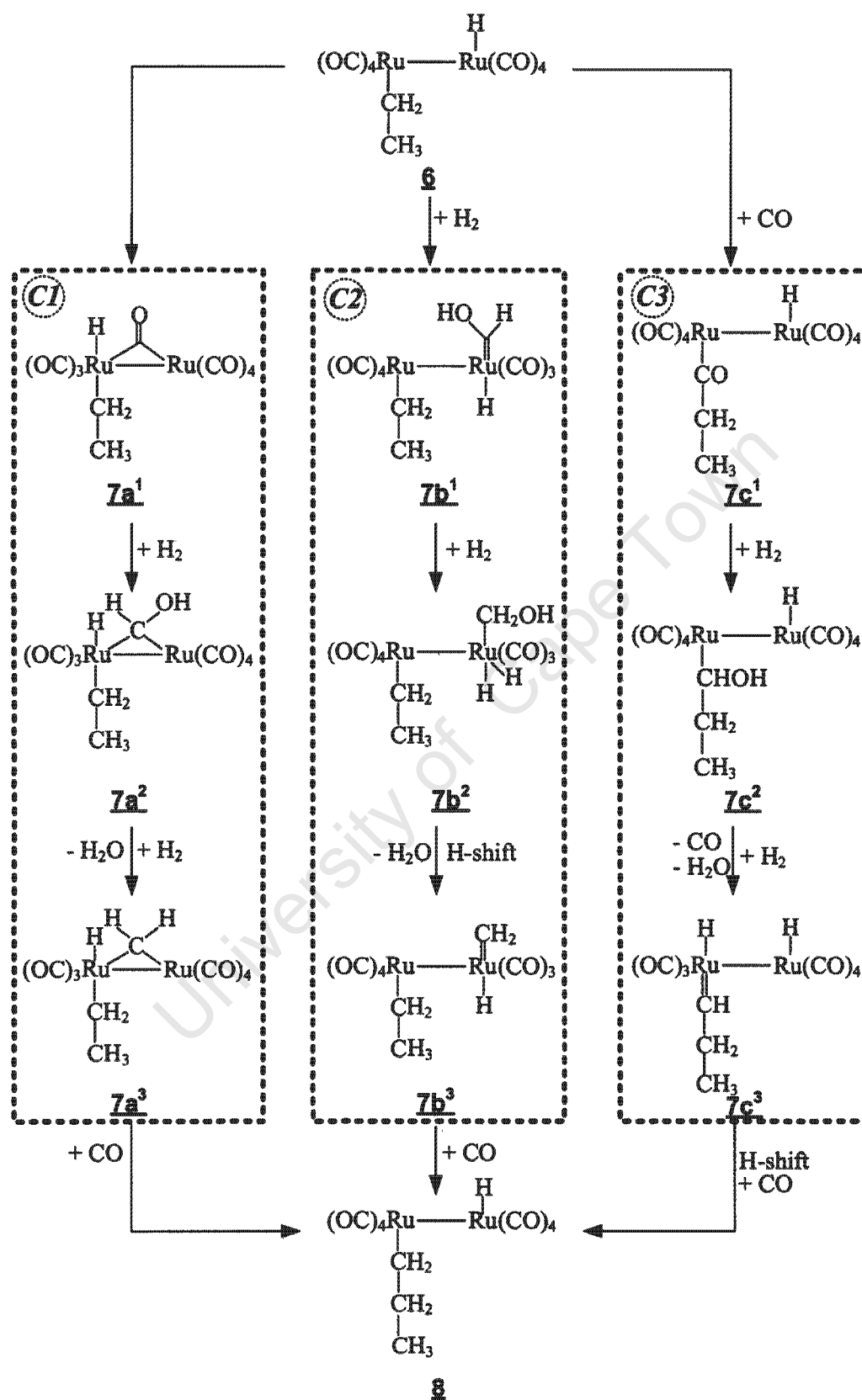
Scheme 19: Proposed monoatomic FT reaction mechanisms A, B and C divided in the generation of the chain starter and the first step of chain growth.



Scheme 20: Generation of the chain starter for the proposed diatomic FT reaction mechanisms A1 and A2.



Scheme 21: First part of the chain growth for the proposed diatomic FT reaction mechanisms *B1*, *B2* and *B3*.



Scheme 22: Second part of the chain growth expressed as the proposed diatomic FT reaction mechanisms *C1*, *C2* and *C3*.

7.3 Validity of the Theoretical Method

The minimum electronic energy, E_{elec} , was calculated for different multiplicities of different species to investigate ground state spin-states and possibilities of spin-crossing during the reaction. However, for all species the lowest spin-state was found to have the lowest energy.

The validation of the theoretical method was performed using the first three compounds of the proposed reaction mechanisms. Four different DFT functionals in the DMol³ code were tested: BLYP (LYP (Lee et al., 1988) and B88 NLDA (Becke, 1988)), BP (PW91 (Perdew and Wang, 1992) and B88 NLDA), PW91 and PBE (Perdew et al., 1996). The properties investigated were: Ru-C, C-O and Ru-H bond lengths for the known species, IR C-O frequencies for Ru(CO)₅ and the bond dissociation energy (BDE) for the first reaction step. BLYP and BP appeared to be the most appropriate functionals (see Table 7.1). The main calculations were therefore performed with the BLYP function.

Table 7.1: Calculated (DFT-BLYP) and literature data (experimental and calculated) of the known compounds for the proposed monoatomic FT reaction mechanism.

Compound	ν_{CO} in cm^{-1}	CO_{ax} in Å	CO_{eq} in Å	Ru-C^{ax} in Å	Ru-C^{eq} in Å	Ru-H in Å	BDE in kJ/mol
Ru(CO) ₅	2001.17/2017.8 1999/2035	1.154	1.159	1.978	1.977		118.72 ^a
							115.56 ^b
		1.142	1.147	1.950	1.969		^c
				1.95	1.96		^d
		1.162	1.165	1.943	1.952		^e
Ru(CO) ₄		1.160	1.159	1.996	1.957		^f
		1.161	1.171	1.951	1.904		^g
		1.160	1.164	1.987	1.971		^h
H ₂ (CO) ₄		1.152	1.151	1.965	1.998	1.652	^a
		1.149	1.150	1.950	1.988	1.651	^a

^a this study

^b Huq et al. (1980)

^c Huang et al. (1990)

^d Calderazzo and L'Eplattenier (1967)

^e Ziegler et al. (1987)

^f Ehlers and Frenking (1995)

^g Decker and Klobukowski (1998)

^h Wang et al. (2003)

A similar validation analysis was performed for the diatomic reaction mechanism (data not shown) based on literature data of the starting compound Ru₂(CO)₉. Bond lengths and angles were compared with each other, ensuring that the used basis set is also appropriate for this system.

7.4 Monoatomic Reaction Mechanism

Three different reaction pathways are proposed to yield the chain starter (**7**) (see Scheme 19). The numerical calculations have shown that the proposed mechanisms covers the entire range of possible reaction pathways. Figure 7.1 shows the change in the enthalpy

relative to the enthalpy of the starter of the catalytic chain, $\text{H}_2\text{Ru}(\text{CO})_4$ (**3**), and the change in the entropy of the three proposed reaction pathways is shown in Figure C.1, Appendix C.3.1, p. 187.

Formation of the Starter of the Catalytic Chain

The formation of the starter of the catalytic chain is thermodynamically not favoured. Especially the CO-dissociation from $\text{Ru}(\text{CO})_5$ to 16 valence electron species $\text{Ru}(\text{CO})_4$ is highly unfavoured (at 475 K: $\Delta H_{\text{rxn}} = 120$ kJ/mol; $\Delta G_{\text{rxn}} = 47$ kJ/mol). The postulated consecutive formation of the starter of the catalytic chain, $\text{H}_2\text{Ru}(\text{CO})_4$, from $\text{Ru}(\text{CO})_4$ is exothermic (at 475 K: $\Delta H_{\text{rxn}} = -85$ kJ/mol; $\Delta G_{\text{rxn}} = -18$ kJ/mol). However, the overall generation of the starter of the catalytic chain from $\text{Ru}(\text{CO})_5$ is not favoured.

Formation of the Chain Starter

All proposed reaction pathways require the formation of the ruthenium-enol species (**5**) from the starter of the catalytic cycle (**3**) over a ruthenium-aldehyde species (**4**) via tautomerisation. Both reactions are endothermic ($\Delta H_{\text{rxn}} = 63$ kJ/mol) and entropically demanding ($\Delta S_{\text{rxn}} = -135$ J/mol·K) making the reactions thermodynamically not favoured.

Mechanism A

The formation of an intermediate Ru-C species (**6a**¹) as postulated in mechanism **A** is highly endothermic. The transformation of the ruthenium-enol species (**5**) into the Ru-C species is not expected to be an elementary reaction step, due to the complexity of the reaction. Furthermore, the formation of this carbide analogue is highly endothermic ($\Delta H_{\text{rxn}} = 441$ kJ/mol) making this route highly unlikely. The hydrogenation of this 'carbide'-intermediate yielding $\text{H}_2\text{RuCH}_2(\text{CO})_3$ (**6a**²) is also endothermic. The consecutive formation of the chain starter $\text{HRu}(\text{CO})_4\text{CH}_3$ (**7**) is highly exothermic.

Mechanism B

In mechanism **B** the ruthenium-enol species (**5**) is converted in an endothermic reaction ($\Delta H_{\text{rxn}} = 256$ kJ/mol) into $\text{H}_2\text{Ru}(\text{CO})_3(\text{CHOH})$ (**6b**¹), followed by a slightly less endothermic H_2 -addition ($\Delta H_{\text{rxn}} = 227$ kJ/mol), generating $\text{H}_3\text{Ru}(\text{CO})_3(\text{CH}_2\text{OH})$ (**6b**²). Water desorption leads to the formation of $\text{H}_2\text{Ru}(\text{CO})_3\text{CH}_2$ (**6b**³) ($\Delta H_{\text{rxn}} = 300$ kJ/mol). The formation of the 16 valence electron transition-state species **6b**⁴ is less endothermic ($\Delta H_{\text{rxn}} = 160$ kJ/mol). This transition compound adsorbs another CO to form the chain starter (**7**) ($\Delta H_{\text{rxn}} = -500$ kJ/mol), making the overall conversion of the starter of the catalytic cycle (**3**) into species **7** highly exothermic. The formation of the chain starter (**7**) via the different intermediates generated by elementary reaction steps in mechanism **B** does not seem to be thermodynamically favoured due to high reaction energies of >250 kJ/mol.

Mechanism C

The C-O bond cleavage in the ruthenium-enol species (**5**) yielding a ruthenium-methylene intermediate (**6c**²) as proposed in mechanism **C** is endothermic ($\Delta H_{\text{rxn}} = 189$ kJ/mol). The ruthenium-methylene intermediate forms via a ruthenium-alkoxy species (**6c**¹) ($\Delta H_{\text{rxn}} = 285$ kJ/mol), creating again elementary reaction steps. However, the formation of **6c**¹ is highly endothermic. Starting from **6c**³, chain growth was also proposed by avoiding the highly exothermic formation of the chain starter **7**. H_2 -activation leads to **7c**¹

in a minor exothermic reaction. $7c^1$ tautomerises into $7c^2$ ($\Delta H_{\text{rxn}} = 285$ kJ/mol), before generating $\text{HRu}(\text{CO})_4\text{COCH}_3$ (**8**) by shifting the enol-ligand in the methylene group.

Conclusions

From a thermodynamic point of view reaction mechanisms *B* and *C* involve reaction intermediates with the lowest energy. The proposed reaction pathways in both mechanisms involve elementary reaction steps which can occur stepwise on a single ruthenium atom. However, the elementary reaction steps also involve the formation of 16 valence electron intermediates. Some of the steps require reaction energies of >200 kJ/mol; hence, the formation of the chain starter and thus FT synthesis on a monoatomic ruthenium centre is not feasible. The formation of $\text{H}_2\text{Ru}(\text{CO})_3(\text{CHOH})$ (**6b¹**) requires the least amount of energy and could be feasible at high reaction temperatures. However, the step to generate species **6b⁴** is not feasible with a reaction energy of >300 kJ/mol. From $\text{H}_2\text{Ru}(\text{CO})_3(\text{CHOH})$ (**6b¹**) desorption of methanol CH_3OH or formaldehyde CH_2O is thermodynamically favoured. The reverse reaction to generate the ruthenium-enol species (**4**) is highly exothermic and thermodynamically not favoured. This is in agreement with the experimental findings of Keim et al. (1980). The C_2 -alcohols and aldehydes, observed in the polar solvent NMP, are not formed from the FT reaction. The formation takes place via hydroformylation in the solvent under these high temperatures and pressures, which is a well-known reaction on single metal atoms.

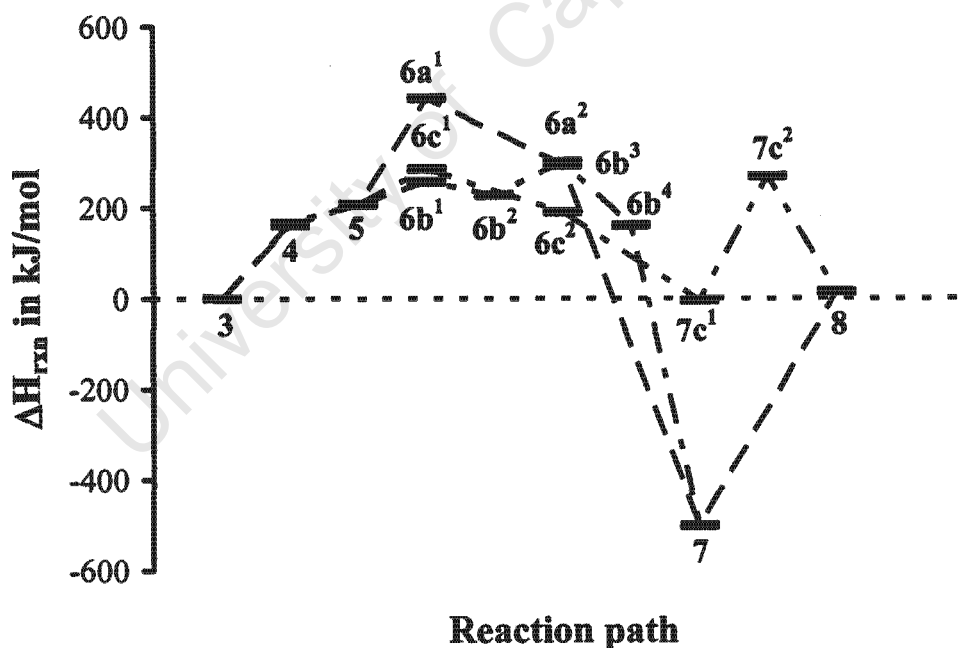


Figure 7.1: Enthalpy of reaction, ΔH_{rxn} , in kJ/mol for the different intermediates proposed in the monoatomic reaction mechanisms *A*, *B* and *C* at 475 K.

7.5 Diatomic Reaction Mechanism

Generation of the Chain Starter

Two different reaction mechanisms (mechanism **A1** and **A2** in Scheme 20) are proposed for the generation of the chain starter $\text{Ru}(\text{CO})_3\text{CH}_3\text{RuH}(\text{CO})_4$ (**4**). The change in enthalpy relative to the change in enthalpy of the starter of the catalytic chain, $\text{Ru}(\text{CO})_4(\mu\text{-CO})\text{RuH}_2(\text{CO})_4$ (**2**), ΔH_{rxn} , is illustrated in Figure 7.2.

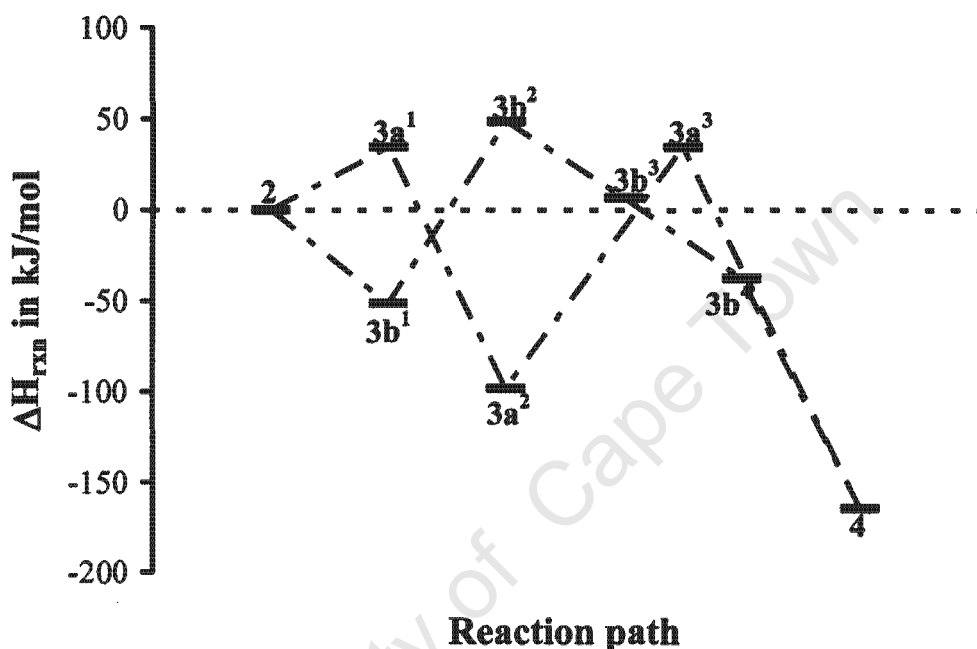


Figure 7.2: Enthalpy of reaction, ΔH_{rxn} , in kJ/mol for the different intermediates proposed in the diatomic reaction mechanisms **A1** and **A2** leading to the generation of the chain initiator at 475 K.

Mechanism A1

In mechanism **A1** all intermediates contain bridging C-ligands. The formation of the bridging ruthenium-alkoxy (**3a¹**) via activation of hydrogen on one ruthenium centre is endothermic ($\Delta H_{\text{rxn}} = +35$ kJ/mol) and therefore energetically demanding. The transformation of **3a¹** into the bridging ruthenium-alkyl (**3a²**) is exothermic ($\Delta H_{\text{rxn}} = -90$ kJ/mol), followed by a slightly endothermic tautomerisation to the terminal methylene ligand on one ruthenium and a bridging CO-ligand (**3a³**) ($\Delta H_{\text{rxn}} = +40$ kJ/mol) between the two. However, the energy difference between the local minimum **3a²** and species **3a³** is relatively high and the thermodynamic feasibility is questionable. The generation of the chain initiator (**4**) requires only the activation of a H_2 -molecule and releases a large amount of energy ($\Delta H_{\text{rxn}} = -170$ kJ/mol) making it thermodynamically very feasible. The energetic barriers of all these reaction steps are below typical FT activation energies of 100 to 120 kJ/mol, making the overall generation of the chain initiator thermodynamically feasible.

Mechanism A2

In comparison to mechanism *A1*, no bridging intermediates have been proposed for mechanism *A2*. The starter of the catalytic chain (**2**) transforms exothermically into the dihydrido-ruthenium species **3b¹** ($\Delta H_{\text{rxn}} = -50$ kJ/mol). The next reaction step to the ruthenium-enol (**3b²**) is, however, energetically demanding with ΔH_{rxn} of +50 kJ/mol. H₂-addition to generate **3b³** is slightly endothermic ($\Delta H_{\text{rxn}} = +5$ kJ/mol), whereas the water desorption step to the ruthenium-methylene (**3b⁴**) and the generation of the chain initiator (**4**) are both exothermic reactions ($\Delta H_{\text{rxn}} = -50$ kJ/mol and $\Delta H_{\text{rxn}} = -150$ kJ/mol). This reaction sequence does not include a local minimum as does mechanism *A1* and seems thermodynamically more preferred.

Chain Growth

Starting from the chain initiator **4** three different reaction mechanisms are proposed for the generation of the chain growth species Ru(CO)₄CH₂CH₃RuH(CO)₄ (**6**). Figure 7.3 shows the enthalpy of reaction relative to the enthalpy of reaction for the formation of the starting compound of the catalytic cycle **2**, ΔH_{rxn} , for the different intermediates proposed in mechanisms *B1*, *B2* and *B3* (see Scheme 22) at a 475 K reaction temperature.

Mechanism B1

In mechanism *B1* the generation of the methylene group occurs at the bridging ligand (see Scheme 21). The shift of a terminal CO-ligand from the chain initiator **4** into a bridging position forming **5a¹**, is exothermic ($\Delta H_{\text{rxn}} = -140$ kJ/mol), followed by a lower energy releasing H₂-activation to the bridging ruthenium-enol intermediate **5a²** ($\Delta H_{\text{rxn}} = -70$ kJ/mol). The H₂-addition and water desorption to **5a³** releases heat, having a ΔH_{rxn} value of -200 kJ/mol. Finally, the generation of the chain growth species **6** is even more exothermic with -260 kJ/mol.

Mechanism B2

The chain growth, as proposed in mechanism *B2*, follows a non-bridging methylene mechanism, starting from the slightly exothermic formation of the terminal ruthenium-enol intermediate **5b¹** ($\Delta H_{\text{rxn}} = -50$ kJ/mol). H₂-activation from **5b¹** to **5b²** releases a small amount of energy, having a ΔH_{rxn} value of -55 kJ/mol, followed by the water desorption step to the terminal ruthenium-methylene **5b³**, which is slightly more exothermic ($\Delta H_{\text{rxn}} = -85$ kJ/mol). As already described for mechanism *B1*, the formation of the ruthenium-ethyl **6** releases 260 kJ/mol.

Mechanism B3

The first postulated step in mechanism *B3* is a highly exothermic CO-insertion, generating **5c¹** ($\Delta H_{\text{rxn}} = -210$ kJ/mol). The reduction via H₂-addition to the ruthenium-alkoxyl (**5c²**) is slightly less exothermic ($\Delta H_{\text{rxn}} = -200$ kJ/mol). The transformation of the ruthenium-alkoxyl species to the ruthenium-ethylene (**5c³**) is not expected to be an elementary reaction step, due to the complexity of the reaction. The last step requires a H-shift and a CO-activation leading to the formation of the chain growth species **6** as already described for mechanisms *B1* and *B2*.

Further Chain Growth

For the second part of the chain growth, leading to the formation of the ruthenium-propyl species **8**, three different reaction mechanisms, respectively mechanisms *C1*, *C2* and *C3*,

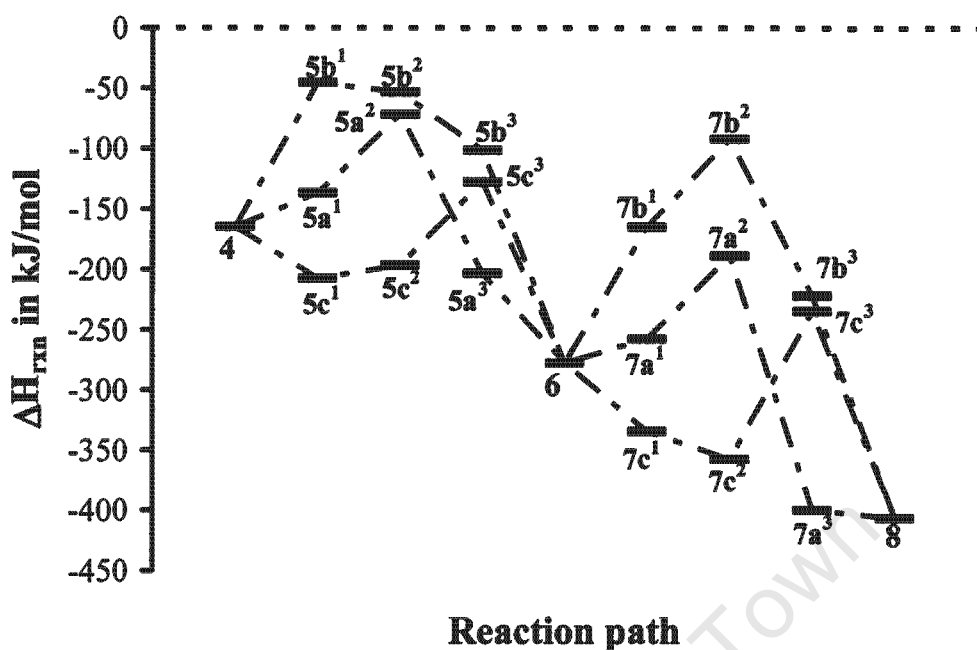


Figure 7.3: Enthalpy of reaction, ΔH_{rxn} , in kJ/mol for the different intermediates proposed in the diatomic reaction mechanisms for the first step of chain growth (mechanisms *B1*, *B2* and *B3*) and second step of chain growth (mechanisms *C1*, *C2* and *C3*) at 475 K.

can again be proposed. These reaction mechanisms follow the same reaction sequences as already described for the formation of the ruthenium-ethyl species **6**. The enthalpies of reaction for these different reactions show the same trend, whereas generally the enthalpy of reaction is more exothermic in comparison to the first part of chain growth. The origin of this trend is the typical product distribution for FT synthesis, namely that adsorbed longer chain hydrocarbons are more stable than shorter ones.

Conclusions

For the generation of the chain starter **4** both proposed reaction mechanisms, viz. *A* and *B*, are thermodynamic feasible with a maximal required activation energy of +50 kJ/mol. All proposed intermediates have 18 valence electrons and their formation is via elementary reaction steps. Mechanism *A* requires slightly less energy compared to mechanism *B*. However, the formation of **3a²** is in a local minimum, making mechanism *B* the preferred reaction pathway.

Mechanisms *C1* and *C2*, both based on the CO-insertion mechanism (see Section 2.1.4, p. 9), seem to be the thermodynamic most feasible reaction mechanisms for hydrocarbon chain growth on a diatomic ruthenium complex. However, all three proposed reaction pathways are thermodynamically feasible. The formation of all intermediates is exothermic, as it is known for the FT reaction. It has to be mentioned that with increase of hydrocarbon chain length the stability of the ruthenium compounds increases.

7.6 Conclusions of Theoretical Investigations

Thermodynamic analyses of different proposed reaction mechanisms to prove the thermodynamic feasibility of FT reactions on a mono- and diatomic ruthenium metal as model catalysts was investigated. By comparing the theoretically calculated reaction enthalpies with known FT activation energies it was shown that the C-O bond cleavage on a single ruthenium centre is thermodynamically not feasible. It requires more energy (>200 kJ/mol) than the typical FT activation energy of 100-120 kJ/mol and some of the proposed reaction steps are not elementary. Therefore, no formation of the chain initiator occurs on a monoatomic ruthenium centre and the FT reaction does not take place.

However, calculations on different proposed diatomic ruthenium mechanisms showed lower energy barriers, making the formation of the chain initiator thermodynamically feasible. The formation of reaction intermediates during chain growth is increasingly exothermic towards longer hydrocarbon chains. This is a known effect in FT product formation. Whereas all proposed reaction mechanisms, viz. the enol, the methylene and the CO-insertion mechanism, are thermodynamically feasible, the CO-insertion mechanism seems to be the most preferred one.

Due to its volatility the diatomic compound, $\text{Ru}_2(\text{CO})_9$, used in the calculations could not be run in experimental tests, and due to limited computing resources the experimentally tested compounds (Ru-2a, Ru-2b and Ru-2c) could not yet be theoretically investigated. The experiment on the diatomic compounds, however, indicated that C-O bond cleavage and C-C bond formation are feasible, whereas gas phase CO-activation for product formation may not have occurred. At this stage it is not known whether this is due to the structure of the tested compounds or due to experimental difficulties.

It may further be noted that interactions of the compounds with the alumina support, as reported in the literature (Brenner and Burwell (1978), Kuznetsov and Bell (1980), Guglielminotti and Zecchina (1982), Zecchina and Guglielminotti (1982)), have not been taken into account in the above theoretical study. These interactions might cause changes in the preferred theoretical reaction mechanism.

Chapter 8

Summary and Conclusions

This work presents an investigation on the effects of metal crystallite size in the nanometer range on Fischer-Tropsch synthesis. In addition, Ångström-sized metal frameworks, viz. organometallic compounds of varied nuclearity (two to six atoms) have been employed to study requirements of sites involved in FT synthesis. This work may also be seen as an attempt to “bridge” between heterogeneous and homogeneous FT synthesis. It includes the following three parts

- Preparation and characterisation of alumina supported model catalysts (nano-sized crystallites, 2 to 10 nm, and organometallic compounds with two to six ruthenium atoms)
- Fischer-Tropsch performance testing on the different model catalyst systems including characterisation of the spent catalysts
- Theoretical calculations on proposed reaction mechanisms to investigate the minimum amount of adjacent metal atoms necessary to show FT activity.

Catalyst preparation

The first challenge was the preparation of alumina supported nano-sized crystallites with narrow crystallite size distributions. This was successfully achieved by applying a reverse micelle technique. This novel technique, described in literature for the preparation of supported ruthenium crystallites with 2 and 4 nm in size, was modified to allow for preparation of narrowly distributed average crystallite sizes in the range of 2 to 10 nm. The size control was accomplished by varying the composition of the reverse micelle systems, which consisted of an aqueous phase, which contained dissolved ruthenium chloride, a surfactant and an organic solvent. Addition of the alumina support resulted in an “uptake” of the aqueous ruthenium ions onto the support after calcination, leading to the formation of the well-defined crystallites, the sizes of which remained almost unchanged upon reduction. These supported nano-sized crystallites were used as model catalysts for FT synthesis.

Model catalysts with cluster sizes in the Ångström-range were prepared by employing organometallic compounds. These compounds, with the number of ruthenium atoms varying from two to six, were synthesized by applying standard organometallic synthesis methods. Note that a monoatomic compound was excluded in the study as earlier

published experimental work indicated that a minimum of two adjacent metal atoms are required for FT activity. The compounds were deposited onto the alumina support via impregnation.

All supported model catalysts had a 3 wt% ruthenium loading.

Experimental

Fischer-Tropsch performance tests were carried out on all these model catalysts with different ruthenium crystallite sizes and on the organometallic compounds of different nuclearity. A fixed-bed reactor operated at 170°C, 4 bar and a 2:1 hydrogen to carbon monoxide synthesis gas feed ratio was used. These mild reaction conditions were chosen to minimise rapid decompositions of the organometallic compounds. Additionally, experiments at elevated temperature and pressure, 225°C and 20 bar, were conducted on the supported nano-sized crystallites to investigate crystallite size effects at more realistic FT conditions and high conversion levels.

Catalyst activity and product distributions were monitored at high temporal resolution over five hours of testing on supported organometallic compounds and over five days of testing on supported nano-sized crystallites using the ampoule sampling technique and adapted gas chromatography employing FID, TCD and MS detection.

Initial and steady-state Fischer-Tropsch testing of the supported **nano-sized crystallites** showed a decrease in activity for smaller crystallites at the two different reaction conditions applied and no constant niveau of specific catalyst activity was obtained for larger crystallites. Whereas no clear trend in product selectivity with varied metal crystallite size was monitored at initial stages of the reaction at steady-state conditions, larger crystallites showed decreased methane formation, increased C₅₊-product selectivity and, at elevated temperature and pressure, increased contents of olefins, particularly α -olefins, and oxygenates. In order to explain these changes in product selectivity, it was suggested that "ensembles" required for chain growth are more complex than those for methane formation and that more of these sites are generated on larger crystallites. Generally, a hydrogen richer product was obtained with decreasing crystallite size, indicating an increased relative hydrogen availability or respectively a decreased carbon monoxide inhibition on those crystallites.

All tested supported **organometallic compounds** displayed formation of C₁-C₄ hydrocarbons, indicating C-C bond formation and C-O bond cleavage. The activity of the clusters for product formation appears to depend on the nuclearity of the clusters and the chemical nature of the ligands. Very high methane selectivities, low chain growth probabilities and high olefin selectivities were obtained independently of cluster nuclearity. Diatomic clusters showed enhanced methane formation and some secondary olefin hydrogenation may take place on clusters with five or more ruthenium atoms. Although some activation of gas phase carbon monoxide to form carbon dioxide was found, it could not be shown whether or not gas phase carbon monoxide can be incorporated into hydrocarbon products on the clusters.

By comparing initial cluster and steady-state crystallite activities as function of number of exposed metal atoms, it was noted that the two series connect almost continuously. Therefore, it is concluded that the experiments on the organometallic model compounds

provide important clues on the site requirements for different reaction steps occurring during FT synthesis on nano-sized crystallites.

Theoretical work

Analysis of different proposed reaction mechanisms to theoretically prove the thermodynamic feasibility of the FT reaction on a mono- and diatomic ruthenium metal compound illustrated that a minimum of two adjacent metal atoms may be required for C-O bond cleavage and chain growth. This observation substantiates experimental results obtained in this work. Among the reaction mechanisms studied the CO-insertion mechanism appears to be thermodynamically the most feasible one.

University of Cape Town

University of Cape Town

Chapter 9

Recommendations and Future Work

It is recommended that future work built on this study should investigate:

- increased metal loadings on the support to enhance product concentration and simplify data analyses in low temperature experiments.
- continuing catalyst characterisation, viz. High-Resolution TEM and/or *in-situ* IR, to investigate causes of initial catalyst deactivation and changes in interaction of clusters with the support as function of runtime (e.g. crystallite reconstruction, carbon deposition).
- variation of cluster structures, including their ligand systems and their size, in order to understand the role of the “chemical environment” or steps of product formation better with the aim to improve selectivity of desired products (e.g. olefins versus paraffins).
- different support materials and/or support materials tested in different ways in order to affect interaction of the cluster with the support and to find more efficient ways of linking the clusters to supports.
- study into effects of crystallite size/structure-sensitivity of reaction steps such as olefin formation, hydrogenation and isomerisation, including (co-)feeding of olefins over crystallite of different size.
- do theoretical studies on experimentally tested dimers Ru-2a, Ru-2b and Ru-2c.

References

- Abrevaya, H.: 1990, 'Fischer-Tropsch Process employing a moderated Ruthenium Catalyst'. US Patent 4,945,116.
- Abrevaya, H., M. Cohn, W. Targos, and H. Robota: 1990, 'Structure-sensitive Reactions over supported Ruthenium Catalysts during Fischer-Tropsch Synthesis'. Catal. Lett. **1**(1-4), 183-196.
- Adesina, A.: 1996, 'Hydrocarbon Synthesis via Fischer-Tropsch Reaction: Travails and Triumphs'. Appl. Catal. A: Gen. **138**(2), 345-367.
- Anderson, K. and J. Ekerdt: 1985, 'Study of Fischer-Tropsch Synthesis over Fe/SiO₂: Effect of Diethylamine on Hydrocarbon and Alcohol Production'. J. Catal. **95**(2), 602-604.
- Anderson, R.: 1956, 'Catalysis for the Fischer-Tropsch Synthesis'. Catalysis **4**, 29-255.
- Anderson, R.: 1984, The Fischer-Tropsch Synthesis. New York: Academic Press.
- Asakura, K., M. Yamada, and Y. Iwasawa: 1985, 'Spectroscopic Studies on the Surface of Ruthenium Catalysts derived from Ru₃(CO)₁₂/γ-Al₂O₃ or SiO₂'. Chem. Lett. **14**(4), 511-514.
- Baetzold, R.: 1973, 'Molecular Orbital Description of Catalysis by Metal Clusters'. J. Catal. **29**(1), 129-137.
- Bahr, H. and V. Jessen: 1933, 'Fusion of Carbon Monoxide on Iron Oxide and Iron'. Ber. dts. chem. Gesell. **66B**, 1238-1247.
- Barkhuizen, D., I. Mabaso, E. Viljoen, C. Welker, M. Claeys, E. van Steen, and J. Fletcher: 2006, 'Experimental Approaches to the Preparation of supported Metal Nanoparticles'. Pure Appl. Chem. **78**(9), 1759-1769.
- Bartholomew, C.: 2001, 'Mechanisms of Catalyst Deactivation'. Appl. Catal. A: Gen. **212**(1-2), 17-60.
- BASF: 1913, 'Verfahren zur Darstellung von Kohlenwasserstoffen und deren Derivaten'. German Patent 293 787.
- BASF: 1914, 'Verfahren zur Darstellung von Kohlenwasserstoffen und deren Derivaten'. German Patent 295 202.
- BASF: 1921, 'Verfahren zur katalytischen Darstellung von Methan'. German Patent 366 791.

REFERENCES

- Becke, A.: 1988, 'A multicenter numerical Integretion Scheme for polyatomic Molecules'. J. Chem. Phys. **88**(4), 2547-2553.
- Bergner, A., M. Dolg, W. Küchle, H. Stoll, and H. Preuss: 1993, 'Ab initio Energy-adjusted Pseudopotentials for Elements of Groups 3-17'. Mol. Phys. **80**(6), 1431-1441.
- Bezemer, G., J. Bitter, H. Kuipers, H. Oosterbeek, J. Holewijn, X. Xu, F. Kapteijn, A. van Dillen, and K. de Jong: 2006, 'Cobalt Particle Size Effect in the Fischer-Tropsch Reaction studied with Carbon Nanofiber supported Catalysts'. J. Am. Chem. Soc. **128**(12), 3956-3964.
- Bian, G., A. Oonuki, N. Koizumi, H. Nomoto, and M. Yamada: 2002, 'Studies with a precipitated Iron Fischer-Tropsch Catalyst'. J. Mol. Catal. A: Chem. **186**(1-2), 203-213.
- Blyholder, G.: 1964, 'Molecular Orbital View of chemisorbed Carbon Monoxide'. J. Phys. Chem. **68**(10), 2772-2778.
- Boreskov, G. and A. Karnaukhov: 1952, 'The Adsorption Method of Measurement of the Surface of Platinum in platinized Silica Gels'. Zh. Fiz. Khim. **26**, 1814-1823.
- Boudart, M.: 1969, 'Catalysis by supported Metals'. Adv. Catal. **20**, 153-166.
- Boudart, M., A. Aldag, J. Benson, N. Dougharty, and C. Harkins: 1966, 'On the specific Activity of Platinum Catalysts'. J. Catal. **6**(1), 92-99.
- Boudart, M. and M. McDonald: 1984, 'Structure Sensitivity of Hydrocarbon Synthesis from CO and H₂'. J. Phys. Chem. **88**(11), 2185-2195.
- Boutonnet, M., J. Kizling, V. Minsta-Eya, A. Choplin, R. Touroude, and G. Maire: 1987, 'Monodisperse colloidal Metal Particles from nonaqueous Solutions: Catalytic Behavior in Hydrogenation of But-1-ene of Platinum, Palladium, and Rhodium Particles supported on Pumice'. J. Catal. **103**(1), 95-104.
- Boutonnet, M., J. Kizling, P. Stenius, and G. Maire: 1982, 'The Preparation of monodispersed colloidal Metal Particles from Microemulsions'. Colloid Surf. **5**(3), 209-225.
- Bradley, J.: 1979, 'Homogeneous Carbon Monoxide Hydrogenation to Methanol catalyzed by soluble Ruthenium Complexes'. J. Am. Chem. Soc. **101**(24), 7419-7421.
- Brenner, A. and R. Burwell: 1978, 'The Surface Chemistry of Molybdenum in States of lower Oxidation on Alumina'. J. Catal. **52**(3), 353-363.
- Bromfield, T. and N. Coville: 1999, 'The Effect of Sulfide Ions on a precipitated Iron Fischer-Tropsch Catalyst'. Appl. Catal. A: Gen. **186**(1-2), 297-307.
- Brown, M. and R. Gonzales: 1976, 'An Infrared Study of the Adsorption of Carbon Monoxide on the reduced and oxidized Form of Silica supported Ruthenium'. J. Phys. Chem. **80**(15), 1731-1735.
- Bruce, M., C. Jensen, and N. Jones: 1990, 'Polynuclear Ruthenium Complexes'. Vol. 28 of Inorganic Synthesis. New York: John Wiley and Sons, pp. 216-218.

- Bruce, M. and M. Williams: 1990, 'Polynuclear Ruthenium Complexes'. Vol. 28 of Inorganic Synthesis. New York: John Wiley and Sons, pp. 219–220.
- Calderazzo, F. and F. L'Eplattenier: 1967, 'The Pentacarbonyls of Ruthenium and Osmium - I. Infrared Spectra and Reactivity'. Inorg. Chem. **6**(6), 1120–1224.
- Calleja, G., A. De Lucas, and R. Van Grieken: 1991, 'Cobalt/HZSM-5 Zeolite Catalyst for the Conversion of Syngas to Hydrocarbons'. Appl. Catal. **68**(1), 11–29.
- Carter, E. and W. Goddard III: 1986, 'Bonding in Transition-Metal-Methylene Complexes. 2. $(\text{RuCH}_2)^+$, a Complex exhibiting low-lying Methylidene-like and Carbene-like States'. J. Am. Chem. Soc. **108**(9), 2180–2191.
- Carter, J. and J. Sinfelt: 1978, 'Catalyst Activation Process'. US Patent **4,088,603**.
- Che, O., O. Clause, and C. Marcilly: 1997, 'Impregnation and Ion Exchange'. Vol. 1 of Handbook of heterogeneous Catalysis. Weinheim, Germany: Ertl, G.; Knözinger, H.; Weitkamp, J., pp. 191–206.
- Choi, H. and E. Muetterties: 1981, 'Catalytic Carbon Monoxide Hydrogenation with $\text{Os}_3(\text{CO})_{12}$ and Boron Tribromide'. Inorg. Chem. **20**(8), 2664–2667.
- Ciobica, I., A. Kleyn, and R. van Santen: 2003, 'Adsorption and Coadsorption of CO and H_2 on Ruthenium Surfaces'. J. Phys. Chem. B **107**(1), 164–172.
- Ciobica, I. and R. van Santen: 2003, 'Carbon Monoxide Dissociation on planar and stepped Ru(0001) Surfaces'. J. Phys. Chem. B **107**(16), 3808–3812.
- Claeys, M.: 1997, 'Selektivität, Elementarschritte und kinetische Modellierung bei der Fischer-Tropsch-Synthese'. Ph.D. thesis, University of Karlsruhe, Karlsruhe.
- Claeys, M., M. Hearshaw, J. Moss, and E. van Steen: 2000a, 'Does mono-atomic Ru catalyse the Fischer-Tropsch Synthesis?'. In: 130A (ed.): Stud. Surf. Sci. Catal., Vol. 130A. Elsevier: Amsterdam: A. Corma, F.V. Felo, S. Mendioroz, J.L.G. Fierro, pp. 1157–1162.
- Claeys, M., M. Hearshaw-Timme, J. Moss, and E. van Steen: 2000b, 'Probing of the minimum required Ensemble Size in Ruthenium catalysed Fischer-Tropsch Synthesis'. In: DGMK Tagungsbericht, Vol. 2000-3. pp. 95–102, DGMK.
- Claeys, M. and H. Schulz: 2004, 'Effects of internal Mass Transfer on Activity and Selectivity in Iron based Fischer-Tropsch Synthesis'. Am. Chem. Soc., Div. Petro. Chem. **49**(2), 195–199.
- Claeys, M. and E. van Steen: 2002, 'On the Effect of Water during Fischer-Tropsch Synthesis with a Ruthenium Catalyst'. Catal. Today **71**(3-4), 419–427.
- Claeys, M. and E. van Steen: 2004, 'Basic Studies'. In: Stud. Surf. Sci. Catal., Vol. 152. Elsevier: Amsterdam: A. Steynberg and M. Dry, pp. 601–680.
- Cotton, F. and G. Wilkinson: 1973, Advanced Inorganic Chemistry. New York: John Wiley and Sons.

REFERENCES

- Craxford, S. and E. Rideal: 1939, 'Reactions of the Fischer-Tropsch Synthesis of Hydrocarbons and some related Reactions'. Trans. Farad. Soc. **35**, 946–958.
- Dalla Betta, R.: 1975, 'Carbon Monoxide Adsorption on supported Ruthenium'. J. Phys. Chem. **79**(23), 2519–2525.
- Dalla Betta, R., A. Piken, and M. Shelef: 1974, 'Heterogeneous Methanation: Initial Rate of CO Hydrogenation on supported Ruthenium and Nickel'. J. Catal. **35**(1), 54–60.
- Dalla Betta, R., A. Piken, and M. Shelef: 1975, 'Heterogeneous Methanation: Steady-state Rate of CO Hydrogenation on supported Ruthenium, Nickel and Rhenium'. J. Catal. **40**(2), 173–183.
- Daroda, R., J. Blackborrow, and G. Wilkinson: 1980, 'Synthesis of Methanol and derived Compounds by homogeneous Fischer-Tropsch type Reaction'. J. Chem. Soc., Chem. Comm. **22**, 1101–1102.
- Datye, A., X. Qing, K. Kharas, and J. McCarty: 2006, 'Particle Size Distributions in heterogeneous Catalysis: What do they tell us about the Sintering Mechanism?'. Catal. Today **111**(1-2), 59–67.
- Davies, D., A. Dyke, S. Knox, and M. Morris: 1984, 'Organic Synthesis of dinuclear Metal Centres. - Part 7. Ylides in the Synthesis of Organodiruthenium Complexes: X-ray Crystal Structure of $[\text{Ru}_2(\text{CO})_2(\mu\text{-CH}_2)(\eta\text{-C}_5\text{H}_5)_2]$ '. J. Chem. Soc., Dalton Trans. **10**(10), 2293–2299.
- De Koster, A. and R. Van Santen: 1991, 'Molecular Orbital Studies of the Adsorption of CH_3 , CH_2 , and CH on Rh(111) and Ni(111) Surfaces'. J. Catal. **127**(1), 141–166.
- Decker, S. and M. Klobukowski: 1998, 'The first Carbonyl Bond Dissociation Energies of $\text{M}(\text{CO})_5$ and $\text{M}(\text{CO})_4(\text{C}_2\text{H}_2)$ ($\text{M} = \text{Fe}, \text{Ru}, \text{Os}$): The Role of the Acetylene Ligand from a Density Functional Perspective'. J. Am. Chem. Soc. **120**(14), 9342–9355.
- Delley, B.: 1989, 'An All-Electron Numerical Method for Solving the Local Density Functional Theory'. J. Chem. Phys. **92**(1), 508–517.
- Delley, B.: 2000, 'From Molecules to Solids with the DMol³ Approach'. J. Chem. Phys. **113**(18), 7756–7764.
- Dictor, R. and A. Bell: 1986a, 'Fischer-Tropsch Synthesis over reduced and unreduced Iron Oxide Catalysts'. J. Catal. **97**(1), 121–136.
- Dictor, R. and A. Bell: 1986b, 'Studies of Fischer-Tropsch Synthesis over a fused Iron Catalyst'. Appl. Catal. **20**(1-2), 145–162.
- Doherty, N. and S. Knox: 1990, ' $(\eta^5\text{-Cyclopentadienyl})\text{-Diruthenium Complexes}$ '. Vol. 28 of Inorganic Synthesis. New York: John Wiley and Sons, pp. 185–187.
- Doherty, N., S. Knox, and M. Morris: 1990, ' $(\eta^5\text{-Cyclopentadienyl})\text{-Diruthenium Complexes}$ '. Vol. 28 of Inorganic Synthesis. New York: John Wiley and Sons, pp. 189–191.
- Dolg, M., U. Wedig, H. Stoll, and H. Preuss: 1987, 'Energy-adjusted ab initio Pseudopotentials for the first Row Transition Elements'. J. Chem. Phys. **86**(2), 886–872.

- Dombek, B.: 1980, 'Hydrogenation of Carbon Monoxide to Methanol and Ethylene Glycol by homogeneous Ruthenium Catalysts'. J. Am. Chem. Soc. **102**(22), 6855–6857.
- Dorling, T., M. Eastlake, and R. Moss: 1969, 'The Structure and Activity of supported Metal Catalysts'. J. Catal. **14**(1), 23–33.
- Dry, M.: 1981, 'The Fischer-Tropsch Synthesis'. In: Catal. Sci. Technol., Vol. 1. Springer Verlag: New York: J.R. Anderson, M. Boudart, pp. 159–255.
- Dry, M.: 1990, 'The Fischer-Tropsch Process - Commercial Aspects'. Catal. Today **6**(3), 183–206.
- Dry, M.: 1996, 'Practical and theoretical Aspects of the catalytic Fischer-Tropsch Process'. Appl. Catal. A: Gen. **138**(2), 319–344.
- Dry, M.: 1999, 'Fischer-Tropsch Reactions and the Environment'. Appl. Catal. A: Gen. **189**(2), 185–190.
- Dry, M.: 2002, 'The Fischer-Tropsch Process: 1950 - 2000'. Catal. Today **71**(3-4), 227–241.
- Duncan, T., P. Winslow, and A. Bell: 1985, 'The Characterization of Carbonaceous Species on Ruthenium Catalysts with ^{13}C Nuclear Magnetic Resonance Spectroscopy'. J. Catal. **93**(1), 1–22.
- Duvenhage, D. and N. Coville: 2006, 'Deactivation of a precipitated Iron Fischer-Tropsch Catalyst - A Pilot Plant Study'. Appl. Catal. A: Gen. **298**(1), 211–216.
- Ehlers, A. and G. Frenking: 1995, 'Structures and Bond Energies of the Transition-Metal Carbonyls $\text{M}(\text{CO})_5$ ($\text{M} = \text{Fe}, \text{Ru}, \text{Os}$) and $\text{M}(\text{CO})_4$ ($\text{M} = \text{Ni}, \text{Pd}, \text{Pt}$)'. Organomet. **14**(1), 423–426.
- Eriksson, S., U. Nylén, S. Rojas, and M. Boutonnet: 2004, 'Preparation of Catalysts from Microemulsions and their Applications in heterogeneous Catalysis'. Appl. Catal. A: Gen. **265**(2), 207–219.
- Erley, W. and P. McBreen: 1983, 'Evidence for CH_x Surface Species after the Hydrogenation of CO over an Fe(110) single Crystal Surface'. J. Catal. **84**(1), 229–234.
- Fahey, D.: 1981, 'Rational Mechanism for homogeneous Hydrogenation of Carbon Monoxide to Alcohols, Polyols, and Esters'. J. Am. Chem. Soc. **103**(1), 136–141.
- Feder, H. and J. Rathke: 1978, 'Catalysis of Carbon Monoxide Hydrogenation by soluble mononuclear Clusters'. J. Am. Chem. Soc. **100**(11), 3623–3625.
- Fischer, F. and H. Pichler: 1937, 'Über die Synthese von Benzin an Eisenkontakten bei erhöhtem Druck'. Ges. Abh. Kenntn. Kohle **13**, 407.
- Fischer, F., H. Pichler, and W. Lohmar: 1939, 'Wissenschaftliches Über die Synthese von Kogasin und Paraffin in wässriger Phase'. Brennstoff-Chemie **20**, 247–250.
- Fischer, F. and H. Tropsch: 1923a, 'The Reduction of Carbon Monoxide to Methane in the Presence of Iron and under Pressure'. Brennstoff-Chemie **4**, 193–197.

REFERENCES

- Fischer, F. and H. Tropsch: 1923b, 'Synthesis of higher Members of the aliphatic Series from Carbon Monoxide'. Ber. dts. chem. Ges. B: Abhandlungen **56B**, 2428–2443.
- Fischer, F. and H. Tropsch: 1926, 'The Synthesis of Petroleum at atmospheric Pressures from Gasification Products of Coal'. Brennstoff-Chemie **7**, 97–104.
- Fischer, F., H. Tropsch, and P. Dilthes: 1925, 'The Reduction of Carbon Monoxide to Methane in the Presence of various Metals'. Brennstoff-Chemie **6**, 265–271.
- Fischer, F., H. Tropsch, and W. Mohr: 1923, 'The Reduction of Carbon Monoxide to Methane in the Presence of Iron at ordinary Pressure'. Brennstoff-Chemie **4**, 197.
- Flory, P.: 1936, 'Molecular Size Distribution in linear Condensation Products'. J. Am. Chem. Soc. **58**(10), 1877–1885.
- Forzatti, P. and L. Lietti: 1999, 'Catalyst Deactivation'. Catal. Today **52**(2-3), 165–181.
- Freund, H.-J., M. Bäumer, and H. Kuhlenbeck: 2000, 'Catalysis and Surface Science: What do we learn from Studies of oxide-supported Cluster Model Systems?'. In: Adv. in Catal., Vol. 45. Elsevier: Amsterdam: B.C. Gates, H. Knözinger, pp. 333–384.
- Friedel, R. and R. Anderson: 1950, 'Composition of synthetic liquid Fuels. I. Product Distribution and Analysis of C₅-C₈-Paraffin Isomers from Cobalt Catalysts'. J. Am. Chem. Soc. **72**(3), 1212–1215.
- Friedrich, M., O. Roelen, and W. Feisst: 1939, 'Hydrocarbons from Hydrogenation of a Carbon Monoxide'. US Patent **2,127,127**.
- Fukushima, T., K. Fujimoto, and H. Tominaga: 1985, 'In-situ Infrared Studies of Ru/SiO₂: The Effect of Metal Dispersion and Pressure on the Chain Growth in the Fischer-Tropsch Reaction'. Appl. Catal. **14**(1), 95–99.
- Geerlings, J., M. Zonneville, and C. De Groot: 1991, 'Studies of the Fischer-Tropsch Reaction on Co(001)'. Surf. Sci. **241**(3), 302–314.
- Germain, J.: 1969, Catalytic Conversion of Hydrocarbons. London, New York: Academic Press.
- Geus, J. and A. van Dillen: 1997, 'Preparation of supported Catalysts by Deposition-Precipitation'. Vol. 1 of Handbook of heterogeneous Catalysis. Weinheim, Germany: G. Ertl, H. Knözinger, J. Weitkamp, pp. 240–257.
- Goodwin, J., D. Goa, S. Erdal, and F. Rogan: 1986, 'Reactive Metal Volatilization from Ru/Al₂O₃ as a Result of Ruthenium Carbonyl Formation'. Appl. Catal. **24**(1-2), 199–209.
- Guglielminotti, E. and A. Zecchina: 1982, 'Surface Characterization of the Ru₃(CO)₁₂/Al₂O₃ System'. J. Catal. **74**(2), 240–251.
- Gupta, B., B. Viswanathan, and M. Sastri: 1972, 'Interaction of Hydrogen and Carbon Monoxide on Cobalt Catalysts'. J. Catal. **26**(2), 212–217.
- Hall, A., A. Duangchan, and K. Smith: 1998, 'Characterisation of dispersed Hydroprocessing Catalysts prepared in Reverse Micelles'. Can. J. Chem. Eng. **76**(4), 744–752.

- Hayashi, H., L. Chen, T. Tago, M. Kishida, and K. Wakabayashi: 2002, 'Catalytic Properties of Fe/SiO₂ Catalysts prepared using Microemulsion for CO Hydrogenation'. Appl. Catal. A: Gen. **213**(1-2), 81-89.
- Henrici Olivé, G. and S. Olivé: 1979, 'Catalytical Alkylation of Benzene with Carbon Monoxide and Hydrogen: a homogeneously catalyzed Fischer-Tropsch Synthesis'. Angew. Chem. **91**(1), 83-84.
- Herrmann, W., J. Planck, E. Guggolz, and M. Ziegler: 1980, 'Transition Metal-Methylene Complexes. 11. Synthesis of the first Methylidyne-Rhodium Cluster by Acid induced Hydrogen/Methane Elimination from a μ -Methylene Complex'. Angew. Chem. **92**(8), 660-662.
- Hindermann, J., G. Hutchings, and A. Kiennemann: 1993, 'Mechanistic Aspects of the Formation of Hydrocarbons and Alcohols from CO Hydrogenation'. Cat. Rev. Sci. Eng. **35**(1), 1-127.
- Holmes, S., D. Clark, H. Turner, and R. Schrock: 1982, ' α -Hydride Elimination from Methylene and Neopentylidene Ligands. Preparation and Protonation of Tungsten (IV) Methylidyne and Neopentylidyne Complexes'. J. Am. Chem. Soc. **104**(23), 6322-6329.
- Honkala, K., A. Hellman, I. Remediakis, A. Logadottir, A. Carlsson, S. Dahl, C. Christensen, and J. Norskov: 2005, 'Ammonia Synthesis from First-Principles Calculation'. Science **307**(5709), 555-558.
- Huang, J., K. Hedberg, H. Davis, and R. Pomery: 1990, 'Structure and Bonding in Transition-Metal Carbonyls and Nitrosyls. 4. Molecular Structure of Ruthenium Pentacarbonyl by Gas-Phase Electron Diffraction'. Inorg. Chem. **29**(20), 3923-3925.
- Huang, Y. and J. Schwarz: 1987a, 'The Effect of Catalyst Preparation on catalytic Activity: I. The catalytic Activity of Ni/Al₂O₃ Catalysts prepared by wet Impregnation'. Appl. Catal. **30**(2), 239-253.
- Huang, Y. and J. Schwarz: 1987b, 'The Effect of Catalyst Preparation on catalytic Activity: II. The Design of Ni/Al₂O₃ Catalysts prepared by wet Impregnation'. Appl. Catal. **32**(2), 255-263.
- Huq, R., A. Poé, and S. Chawla: 1980, 'Kinetics of Substitution and oxidative Elimination Reactions of Pentacarbonylruthenium(0)'. Inorg. Chim. Acta **38**, 121-125.
- Iglesia, E.: 1997a, 'Design, Synthesis, and Use of Cobalt-based Fischer-Tropsch Synthesis Catalysts'. Appl. Catal. A: Gen. **161**(1-2), 59-78.
- Iglesia, E.: 1997b, 'Fischer-Tropsch Synthesis on Cobalt Catalysts: Structural Requirements and Reaction Pathways'. In: Stud. Surf. Sci. Catal., Vol. 107. Elsevier: Amsterdam: M. de Pontes, R.L. Espinoza, C.P. Nicolaidis, J.H. Scholz, M.S. Scurrrell, pp. 153-162.
- Iglesia, E., S. Reyes, and R. Madon: 1991, 'Transport-enhanced α -Olefin Readsorption in Ru-catalyzed Hydrocarbon Synthesis'. J. Catal. **129**(1), 238-256.

REFERENCES

- Iglesia, E., S. Reyes, R. Madon, and S. Soled: 1993, 'Selectivity Control and Catalyst Design in the Fischer-Tropsch Synthesis: Sites, Pellets and Reactors'. Adv. Catal. **39(2)**, 221–302.
- Iglesia, E., S. Soled, and R. Fiato: 1992, 'Fischer-Tropsch Synthesis on Cobalt and Ruthenium. Metal Dispersion and Support Effects on Reaction Rate and Selectivity'. J. Catal. **137(1)**, 212–224.
- Iyagba, E., T. Hoost, J. Nwalor, and J. Goodwin Jr.: 1990, 'The Effect of Chlorine Modification of Silica-supported Ru on its CO Hydrogenation Properties'. J. Catal. **123(1)**, 1–11.
- Jager, B.: 1997, 'Developments in Fischer-Tropsch Technology'. In: Stud. Surf. Sci. Catal., Vol. 107. Elsevier: Amsterdam: M. de Pontes, R.L. Espinoza, C.P. Nicolaides, J.H. Scholz, M.S. Scurrall, pp. 219–224.
- Jager, B. and R. Espinoza: 1995, 'Advances in low Temperature Fischer-Tropsch Synthesis'. Catal. Today **23(1)**, 17–28.
- Johnson, B., C. Bartholomew, and D. Goodman: 1991, 'The Role of Surface Structure and Dispersion in CO Hydrogenation on Cobalt'. J. Catal. **128(1)**, 231–247.
- Johnson, P. and R. Joyner: 1993, 'Structure-Function Relationships in heterogeneous Catalysis: the embedded Surface Molecule Approach and its Applications'. In: Stud. Surf. Sci. Catal., Vol. 75. Elsevier: Amsterdam: L. Guzzi, F. Solymosi, P. Tétényi, pp. 165–174.
- Johnston, P., G. Hutchings, N. Coville, K. Finch, and J. Moss: 1999, 'CO Hydrogenation using supported Iron Carbonyl Complexes'. Appl. Catal. A: Gen. **186(1-2)**, 245–253.
- Kaiser, R.: 1969, Chromatographie in der Gasphase. Mannheim: Bibliographisches Institut, 2 edition.
- Kaminsky, M., N. Winograd, and G. M. Geoffroy: 1986, 'Direct SIMS Observation of Methylidyne, Methylene and Methyl Intermediates on a Ni(III) Methanation Catalyst'. J. Am. Chem. Soc. **108(6)**, 1315–1316.
- Keim, W., M. Berger, and J. Schlupp: 1980, 'High-Pressure homogeneous Hydrogenation of Carbon Monoxide in polar and nonpolar Solvents'. J. Catal. **61(2)**, 359–365.
- Kellner, C. and A. Bell: 1981a, 'Infrared Studies of Carbon Monoxide Hydrogenation over Alumina-supported Ruthenium'. J. Catal. **71(2)**, 296–307.
- Kellner, C. and A. Bell: 1981b, 'Synthesis of oxygenated Products from Carbon Monoxide and Hydrogen over Silica- and Alumina-supported Ruthenium Catalysts'. J. Catal. **71(2)**, 288–295.
- Kellner, C. and A. Bell: 1982, 'Effects of Dispersion on the Activity and Selectivity of Alumina-supported Ruthenium Catalysts for Carbon Monoxide Hydrogenation'. J. Catal. **75(2)**, 251–261.
- King, D.: 1978, 'A Fischer-Tropsch Study of supported Ruthenium Catalysts'. J. Catal. **51(3)**, 386–397.

- King, R., M. Iqbal, and A. King Jr: 1979, 'Pentamethylcyclopentadienyl Derivatives of Transition Metals'. J. Organomet. Chem. **171**(1), 53–63.
- Kinugasa, T., A. Kondo, S. Nishimura, Y. Miyauchi, Y. Nishii, K. Watanabe, and H. Takeuchi: 2002, 'Estimation of Size of Reverse Micelles formed by AOT and SDEHP based on Viscosity Measurements'. Colloids and Surfaces A: Physicochem. Eng. Aspects **204**(1-3), 193–199.
- Kishida, M., K. Umakoshi, J. Ishiyama, H. Nagata, and K. Wakabayashi: 1996, 'Hydrogenation of Carbon Dioxide over Metal Catalysts prepared using Microemulsion'. Catal. Today **29**(1-2), 355–359.
- Klabunde, K., Y.-X. Li, and A. Khaleel: 1995, 'Building heterogeneous Catalysts an Atom at a Time'. Trans. Kan. Acad. Sci. **98**(1-2), 24–33.
- Knacke, O., O. Kubaschewski, and K. Hesselmann: 1991, Thermodynamic Properties of inorganic Substances. Düsseldorf: Springer Verlag, 2 edition.
- Kobayashi, M. and T. Shirasaki: 1973, 'The Chemisorption of CO on Ruthenium Metals and Ruthenium-Silica Catalysts'. J. Catal. **28**(2), 289–295.
- Koch, H. and F. Hilberath: 1941, 'Über die unterhalb von 100°C steigenden Kohlenwasserstoffe des synthetischen Benzins aus Kohlenoxyd und Wasserstoff (Kogasin)'. Brennstoff-Chemie **22**(135), 145–152.
- Kolbel, H., G. Patzschke, and H. Hammer: 1966, 'Reaction Mechanisms of the Fischer-Tropsch Synthesis. IX. Stoichiometric Chemisorption Complexes on Iron Catalysts.'. Brennstoff-Chemie **47**, 14–19.
- Koopman, P., A. Kieboom, and H. van Bekkum: 1981, 'Characterization of Ruthenium Catalysts as studied by Temperature Programmed Reduction'. J. Catal. **69**(1), 172–179.
- Kuznetsov, V. and A. Bell: 1980, 'An Infrared Study of Alumina- and Silica-supported Ruthenium Cluster Carbonyls'. J. Catal. **65**(2), 374–389.
- Lee, C., W. Yang, and R. Parr: 1988, 'Development of the Colle-Salvetti Correlation-Energy Formula into a Functional of the Electron Density'. Phys. Rev. B **37**(2), 785–789.
- Li, S., A. Krishnamoorthy, M. G. Li, A., and E. Iglesia: 2002, 'Promoted Iron-based Catalysts for Fischer-Tropsch Synthesis: Design, Synthesis, Site Densities and catalytic Properties'. J. Catal. **206**(2), 202–217.
- Lin, Z., T. Okuhara, M. Misono, K. Tohji, and Y. Udagawa: 1986, 'Pronounced Effect of Particle Size on Selectivity observed for Carbon Monoxide Hydrogenation over Ruthenium-Alumina Catalysts'. J. Chem. Soc., Chem. Commun. **22**, 1673–1675.
- Long, H., M. Turner, P. Fornasiero, J. Kaspar, M. Graziani, and P. Maitlis: 1997, 'Vinyllic Initiation of the Fischer-Tropsch Reaction over Ruthenium on Silica Catalysts'. J. Catal. **167**(1), 172–179.

REFERENCES

- Lynds, L.: 1964, 'Infrared Spectra of Carbon Monoxide chemisorbed on Iridium and Ruthenium'. Spectrochim. Acta **20**(9), 1369–1372.
- Mabaso, E.: 2005, 'Nanosized Iron Crystallites for Fischer-Tropsch Synthesis'. Ph.D. thesis, University of Cape Town, Cape Town.
- Mabaso, E., E. van Steen, and M. Claeys: 2006, 'Fischer-Tropsch Synthesis on supported Iron Crystallites of different Size'. In: DGMK-Tagungsbericht, Vol. 2006-4. pp. 93–100, DGMK.
- Madon, R., E. Iglesia, and S. Reyes: 1993, 'Non-Flory Product Distributions in Fischer-Tropsch Synthesis catalyzed by Ruthenium, Cobalt and Iron'. In: ACS Symposium Series No. 157, Vol. 517. S.C. Suib, M.E. Davis, pp. 385–391.
- Madon, R., S. Reyes, and E. Iglesia: 1995, 'Primary and secondary Reaction Pathways in Ruthenium-catalyzed Hydrocarbon Synthesis'. J. Phys. Chem. **95**(20), 7795–7804.
- Maitlis, P., H. Long, R. Quyoun, M. Turner, and Z.-Q. Whang: 1996, 'Heterogeneous Catalysis of C-C Bond Formation: Black Art or organometallic Science'. J. Chem. Soc., Chem. Comm. **1**, 1–8.
- Maitlis, P., R. Quyoun, H. Long, and M. Turner: 1999, 'Towards a chemical Understanding of the Fischer-Tropsch Reaction: Alkene Formation'. Appl. Catal. A: Gen. **186**(1-2), 363–374.
- Maitlis, P. M.: 1989, 'A new View of the Fischer-Tropsch Polymerization Reaction'. Pure Appl. Chem. **61**(10), 1747–1754.
- Mansker, L., Y. Dragomir, B. Bukur, and A. Datye: 1999, 'Characterisation of Slurry Phase Iron Catalysts for Fischer-Tropsch Synthesis'. Appl. Catal. A: Gen. **186**(1-2), 277–296.
- McKee, D.: 1967, 'Interaction of Hydrogen and Carbon Monoxide on Platinum Group Metals'. J. Catal. **8**(3), 240–249.
- Michalk, G., W. Moritz, H. Pfnuer, and D. Menzel: 1983, 'A LEED Determination of the Structures of Ru(001) and of CO/Ru(001)'. Surf. Sci. **129**(1), 92–106.
- Mills, G. and F. Steffgen: 1973, 'Catalytic Methanation'. Catal. Rev. **8**(2), 159–210.
- Moulijn, J., A. van Diepen, and F. Kapteijn: 2001, 'Catalyst Deactivation: Is it predictable? What to do?'. Appl. Catal. A: Gen. **212**(1-2), 3–16.
- Muetterties, E.: 1975, 'Metal Clusters in Catalysis. III. Clusters as Models for Chemisorption Processes in heterogeneous Catalysis'. Bull. Soc. Chim. Bel. **84**(10), 959–986.
- Nagy, J., A. Gougue, and G. Derouane: 1983, 'Preparation of monodispersed Nickel Boride Catalysts using reversed micellar Systems'. In: 16 (ed.): Stud. Surf. Sci. Catal. Elsevier: Amsterdam: P. Grange, P.A. Jacobs, pp. 193–202.
- Nicholls, J., Vargas, and M.D.: 1990, 'Carbido-Carbonyl Ruthenium Cluster Complexes'. Vol. 28 of Inorganic Synthesis. New York: John Wiley and Sons, pp. 280–285.

- Nie, Z.: 1996, 'Anfangsaktivität und -selektivität von modifizierten Kobalt- und Nickelkatalysatoren'. Ph.D. thesis, Universität Karlsruhe, Karlsruhe.
- Ojeda, M., S. Rojas, M. Boutonnet, F. Pérez-Alonso, F. García-García, and J. Fierro: 2004, 'Synthesis of Rh Nano-Particles by the Microemulsion Technology Particle Size Effect on the CO and H₂ Reaction'. Appl. Catal. A: Gen. **274**(1-2), 33–41.
- Okuhara, T., H. Tamura, and M. Misono: 1985, 'Effect of Potassium and Phosphorus on the Hydrogenation of CO over Alumina-supported Ruthenium Catalyst'. J. Catal. **95**(1), 41–48.
- Perdew, J., K. Burke, and M. Ernzerhof: 1996, 'Generalized Gradient Approximation made simple'. Phys. Rev. Lett. **77**(18), 3865–3868.
- Perdew, J. and Y. Wang: 1992, 'Accurate and simple analytic Representation of the Electron-Gas Correlation Energy'. Phys. Rev. B **45**(23), 13244–13249.
- Perry, R. and D. Green, Perry's Chemical Engineers' Handbook. 7 edition.
- Phala, N.: 2004, 'A theoretical Investigation in heterogeneous Gold Catalysis'. Ph.D. thesis, University of Cape Town, Cape Town.
- Pichler, H.: 1952, 'Twenty-five Years of Synthesis of Gasoline by Catalytic Conversion of Carbon Monoxide and Hydrogen'. In: IV (ed.): Adv. in Catal. New York: W. Frankenburg, E. Rideal, V. Komarewsky, p. 271.
- Pichler, H. and H. Buffleb: 1936, 'über das besondere Verhalten von Rutheniumkatalysatoren bei der Synthese von flüssigen Kohlenwasserstoffen'. Brennstoff-Chemie **19**(138), 226–230.
- Pichler, H. and O. Roelen: 1957, 'Mitteldrucksynthese'. In: 3 (ed.): Ullmanns Enzyklopädie der technischen Chemie. Munich: Urban and Schwarzenberg, p. 707.
- Pichler, H. and H. Schulz: 1970, 'Neue Erkenntnisse auf dem Gebiet der Synthese von Kohlenwasserstoffen aus CO und H₂'. Chem.-Ing. Techn. **42**(18), 1162–1174.
- Pichler, H., H. Schulz, and M. Elstner: 1967, 'Gesetzmässigkeiten bei der Synthese von Kohlenwasserstoffen aus Kohlenoxyd und Wasserstoff'. Brennstoff-Chemie **48**(3), 78–87.
- Pichler, H., H. Schulz, and F. Hojabri: 1964, 'Synthesis of α -Olefins from Carbon Monoxide and Hydrogen'. Brennstoff-Chemie **45**(7), 215–221.
- Pichler, H., H. Schulz, and B. Rao: 1968, 'Über Folgereaktionen bei der Fischer-Tropsch Synthese primär gebildeten Kohlenwasserstoffe'. Liebigs Ann. Chem. **719**(1), 61–68.
- Pileni, M.: 1993, 'Reverse Micelles as Microreactors'. J. Phys. Chem. **97**(27), 6961–6973.
- Pillai, V., P. Kumar, M. Hou, and S. O. Ayyub, P.: 1995, 'Preparation of Nanoparticles of Silver Halides, Superconductors and magnetic Materials using Water-in-Oil Microemulsions as Nano-Reactors'. Adv. Colloid Interface Sci. **55**, 241–269.

REFERENCES

- Ragaini, V., R. Carli, C. Bianchi, D. Lorenzetti, G. Predieri, and P. Moggi: 1996, 'Fischer-Tropsch Synthesis on Alumina-supported Ruthenium Catalysts: II. Influence of morphological Factors'. Appl. Catal. A: Gen. **139**(1-2), 31-42.
- Rainer, D., M. Wu, D. Mahon, and D. Goodman: 1996, 'Adsorption of CO on Pd/Al₂O₃/Ta(110) Model Catalysts'. J. Vac. Sci. Technol. A **14**(3), 1184-1188.
- Reuel, R. and C. Bartholomew: 1984, 'Effects of Support and Dispersion on the CO Hydrogenation Activity/Selectivity Properties of Cobalt'. J. Catal. **85**(1), 78-88.
- Roginski, S.: 1965. In: 3rd Congr. on Catal. Amsterdam, p. 939.
- Sabatier, P. and J. Senderens: 1902, 'New Syntheses of Methane'. J. Soc. Chem. Ind. **21**, 504.
- Schulman, J. and J. Friend: 1949, 'Light-Scattering Investigation of the Structure of transparent Oil-Water dispersed Systems'. J. Colloid Sci. **4**(5), 497-509.
- Schulz, G.: 1930, 'Highly polymerized Compounds. CXXII The Relation between Reaction Rate and Composition of the Reaction Product in Macropolymerization Processes'. Z. Physik. Chem. **B30**, 379-98.
- Schulz, H.: 1999, 'Short History and present Trends of Fischer-Tropsch Synthesis'. Appl. Catal. A: Gen. **186**(1-2), 3-12.
- Schulz, H.: 2003, 'Major and minor Reactions in Fischer-Tropsch Synthesis on Cobalt Catalysts'. Top. Catal. **26**(1-4), 73-85.
- Schulz, H.: 2006. personal communication.
- Schulz, H., K. Beck, and E. Erich: 1988, 'Mechanism of the Fischer-Tropsch Process'. In: Stud. Surf. Sci. Catal., Vol. 36. Elsevier: Amsterdam: D. Bibby, C. Chang, R. Howe and S. Yurchak, p. 457.
- Schulz, H., W. Böhringer, C. Kohl, N. Rahman, and A. Will: 1984, 'Entwicklung und Anwendung der Kapillar-GC-Gesamtprobentechnik für Gas/Dampf-Vielstoffgemische'. In: DGMK Forschungsbericht, Vol. 1984-3. p. 320, DGMK.
- Schulz, H. and M. Claeys: 1999a, 'Kinetic Modelling of Fischer-Tropsch Product Distributions'. Appl. Catal. A: Gen. **186**(1-2), 91-107.
- Schulz, H. and M. Claeys: 1999b, 'Reactions of α -Olefins of different Chain Length added during Fischer-Tropsch Synthesis on a Cobalt Catalyst in a Slurry Reactor'. Appl. Catal. A: Gen. **186**(1-2), 71-90.
- Schulz, H. and J. Cronjé: 1977, 'Kohle, Fischer-Tropsch Synthese'. In: 14 (ed.): Ullmanns Enzyklopädie der technischen Chemie. Weinheim: Verlag Chemie, 4 edition, pp. 329-350.
- Schulz, H. and H. Gökcebay: 1984, 'Fischer-Tropsch CO-Hydrogenation as a Means of linear Olefins Productions'. In: Catalysis of organic Reactions, Vol. 153. New York: J.R. Kosak; M. Dekker, p. 153.

- Schulz, H., Z. Nie, and F. Ousmanov: 2002, 'Construction of the Fischer-Tropsch Regime with Cobalt Catalysts'. Catal. Today **71**(3-4), 351-360.
- Schulz, H., G. Schaub, M. Claeys, and T. Riedel: 1999, 'Transient initial kinetic Regimes of Fischer-Tropsch Synthesis'. Appl. Catal. A: Gen. **186**(1-2), 215-227.
- Schulz, H., E. van Steen, and M. Claeys: 1994, 'Selectivity and Mechanism of Fischer-Tropsch Synthesis with Iron and Cobalt Catalysts'. In: Stud. Surf. Sci. Catal., Vol. 81. Elsevier: Amsterdam: H.E. Curry-Hyde, R.F. Howe, p. 455.
- Schulz, H., E. van Steen, and M. Claeys: 1995, 'Specific Inhibition as the kinetic Principle of Fischer-Tropsch Synthesis'. Topics in Catal. **2**(1-4), 223-234.
- Shen, W., J. Dumesic, and C. Hill: 1981, 'Criteria of stable Ni Particle Size under Methanation Reaction Conditions: Nickel Transport and Size Growth via Nickel Carbonyl'. J. Catal. **68**(1), 152-165.
- Shultz, J., L. Hofer, F. Karn, and R. Anderson: 1962, 'Studies of the Fischer-Tropsch Synthesis'. J. Phys. Chem. **66**(3), 501-506.
- Shultz, J., F. Karn, and R. Anderson: 1967, 'Noble Metals, Molybdenum, and Tungsten in Hydrocarbon Synthesis'. Bureau of Mines Report of Investigations (6974), pp. 20.
- Song, K. and Y. Kang: 2000, 'Preparation of high Surface Area Tin Oxide Powders by a homogeneous precipitation Method'. Mat. Lett. **42**(5), 283-289.
- Stenius, P., J. Kizling, and M. Boutonnet: 1984, 'Liquid Suspension of Particles of a Metal belonging to the Platinum Group and a Method for the Manufacture of such a Suspension'. US Patent **4,425,261**.
- Sternberg, A. and J. Wender: 1959. In: Proc. Intern. Conf. Coord. Chem. London, p. 53, The Chemical Society.
- Steynberg, A.: 2004, 'Introduction to Fischer-Tropsch Technology'. In: Stud. Surf. Sci. Catal., Vol. 152. Elsevier: Amsterdam: A. Steynberg and M. Dry, p. 1.
- Steynberg, A., M. Dry, B. Davis, and B. Breman: 2004, 'Fischer-Tropsch Reactors'. In: Stud. Surf. Sci. Catal., Vol. 152. Elsevier: Amsterdam: A. Steynberg and M. Dry, p. 64.
- Steynberg, A., R. Espinoza, and A. Vosloo: 1999, 'High Temperature Fischer-Tropsch Synthesis in commercial Practice'. Appl. Catal. A: Gen. **186**(1-2), 41-54.
- Storch, H., N. Golumbic, and R. Anderson: 1951, The Fischer-Tropsch and related Synthesis. New York: John Wiley and Sons.
- Sweet, J. and W. Graham: 1979, 'Reduction of coordinated Carbon Monoxide, Formyl, and Hydroxymethyl Ligands: Models for Fischer-Tropsch and related Reactions'. J. Organomet. Chem. **173**(3), C9-C12.
- Tanford, C.: 1972, 'Micelle Shape and Size'. J. Phys. Chem. **76**(21), 3020-3026.
- Targos, W.: 1987, 'Method of Making a Catalyst Composition comprising uniform Size Metal Components on Carrier'. US Patent **4,714,693**.

REFERENCES

- Tau, L., H. Dabbagh, S. Bao, B. Chawla, J. Halasz, and B. Davies: 1988, 'Incorporation of Carbon-14 labeled Compounds during Fischer-Tropsch Synthesis'. In: Proc. - Int. Congr. Catal., Vol. 2. Chem. Inst. Can.: Ottawa: M.J. Phillips, M. Ternan, p. 861.
- Tropsch, H. and H. Koch: 1929, 'Über das synthetische Benzin aus Wassergas'. Brennstoff-Chemie **10**, 337.
- van der Laan, G.: 1999, 'Kinetics, Selectivity and Scale-up of the Fischer-Tropsch Synthesis'. Ph.D. thesis, University of Groningen, Groningen.
- van Hardeveld, R. and F. Hartog: 1969, 'The Statistics of Surface Atoms and Surface Sites of Metal Crystals'. Surf. Sci. **15**(2), 189–230.
- van Steen, E., M. Claeys, M. Dry, J. van de Loosdrecht, E. Viljoen, and J. Visagie: 2005, 'Stability of Nanocrystals: Thermodynamic Analysis of Oxidation and Re-reduction of Cobalt in Water/Hydrogen Mixtures'. J. Phys. Chem. B **109**(8), 3575–3577.
- van Steen, E. and H. Schulz: 1999, 'Polymerization Kinetics of the Fischer-Tropsch CO Hydrogenation using Iron and Cobalt based Catalysts'. Appl. Catal. A: Gen. **186**(1-2), 309–320.
- Vannice, M.: 1975a, 'The catalytic Synthesis of Hydrocarbons from H₂/CO Mixtures'. J. Catal. **37**(3), 449–461.
- Vannice, M.: 1975b, 'The catalytic Synthesis of Hydrocarbons from H₂/CO Mixtures over the Group VIII Metals - The Kinetics of the Methanation Reaction over supported Metals'. J. Catal. **37**(3), 462–473.
- Wang, C. and J. Ekerdt: 1984, 'Evidence for Alkyl Intermediates during Fischer-Tropsch Synthesis and their Relation to Hydrocarbon Products'. J. Catal. **86**(2), 239–244.
- Wang, H.-K., H. Choi, and E. Muetterties: 1981, 'Catalytic Hydrogenation of Carbon Monoxide with Ir₄(CO)₁₂ and AlCl₃'. Inorg. Chem. **20**(8), 2661–2663.
- Wang, Y.-N., W.-P. Ma, Y.-J. Lu, J. Yhang, Y.-Y. Xu, H.-W. Xiang, Y.-W. Li, Y.-L. Zhao, and B.-J. Zhang: 2003, 'Kinetics Modelling of Fischer-Tropsch Synthesis over an industrial Fe-Cu-K Catalyst'. Fuel **82**(2), 195–213.
- Wanke, S. and P. Flynn: 1975, 'A Model of supported Metal Catalysts Sintering. I. Development of Model'. Cat. Rev. Sci. Eng. **12**(1), 93–135.
- Winslow, P. and A. Bell: 1985, 'Studies of Carbon- and Hydrogen-containing Adspecies present during CO Hydrogenation over unsupported Ru, Ni, and Rh'. J. Catal. **94**(2), 385–399.
- Yamasaki, H., Y. Kobori, S. Naito, T. Onishi, and K. Tamaru: 1981, 'Infrared Studies of the Reaction of H₂ + CO on a Ru/SiO₂ Catalyst'. J. Chem. Soc., Faraday Trans. 1 **77**(12), 2913–2925.
- Zaera, F.: 2004, 'Mechanistic Requirements for catalytic active Species'. J. Phys.: Cond. Matter **16**(22), S2299–S2310.

- Zecchina, A. and E. Guglielminotti: 1982, 'Surface Characterization of the $\text{Ru}_3(\text{CO})_{12}/\text{Al}_2\text{O}_3$ System'. J. Catal. **74**(2), 225–239.
- Zhou, X. and E. Gulari: 1987, 'CO Hydrogenation on $\text{Ru}/\text{Al}_2\text{O}_3$: Selectivity under transient Conditions'. J. Catal. **105**(2), 499–510.
- Ziegler, T., V. Tschinke, and C. Ursenbach: 1987, 'Thermal Stability and kinetic Lability of the Metal-Carbonyl Bond. - A theoretical Study on $\text{M}(\text{CO})_6$ ($\text{M} = \text{Cr}, \text{Mo}, \text{W}$), $\text{M}(\text{CO})_5$ ($\text{M} = \text{Fe}, \text{Ru}, \text{Os}$), and $\text{M}(\text{CO})_4$ ($\text{M} = \text{Ni}, \text{Pd}, \text{Pt}$)'. J. Am. Chem. Soc. **109**(16), 4825–4837.

University of Cape Town

Appendix A

Preparation and Characterisation of Model Catalysts

University of Cape Town

A.1 Chemicals for Model Catalyst Preparation

Table A.1: Chemicals used for model catalyst preparation.

Compound	Details
Acetone	Kimix (Ar, 99.5% purity)
Aluminium oxide	Puralox (Batch 9574), SCCa 5-150; Sasol Germany; $S_{\text{BET}} = 162 \text{ m}^2/\text{g}$; $V_{\text{pore}} = 0.47 \text{ cm}^3/\text{g}$; $\bar{d}_{\text{pore}} = 11.5 \text{ nm}$ particle size: 150-200 μm
Air, synthetic	Air products (21% O_2 in N_2)
Carbon monoxide	Afrox (99.97% purity)
Carbon dioxide	Air liquide (99.999% purity)
Chloroform-d	Fluka (99.8 atom % D, contains 1% (v/v) TMS)
Cyclohexane (D_6)	Aldrich (99% purity)
n-Decane	Aldrich (>99% purity)
Dicyclopentadiene	Aldrich (stabilized with BHT)
n-Heptane	Riedel de Haën (99% purity)
n-Hexane	Kimix (Ar, 98% purity)
Hydrogen	Air liquide (99.999% purity)
Hydrochloric acid	Fluka (puriss. p.a., >32%)
Methanol	Merck (Ar, >99.5% purity)
Methylene dichloride	Merck (>99% purity)
Methyltium, solution	Merck (5% in diethylether)
Nitrogen	Air liquide (99.999% purity)
Penta-ethyleneglycol-dodecylether, Berol 50	Akzo Nobel
Pentamethylenecyclopentadiene	Aldrich (95% purity)
n-Pentane	Merck (p.a., >99% purity)
Potassium chloride	Fluka (puriss. p.a., >99.5% purity)
Potassium hydroxide	Fluka (puriss. p.a., >99.5% purity)
Potassium hydroxide, pellets	Fluka (purum p.a., >85% purity)
Ruthenium-(III)-chloride hydrate	Fluka ($\approx 41\%$ Ru, purum)
Sodium borohydride	Sigma Aldrich (granular, 99.999% purity)
Tetrafluoroboric acid, solution	Merck ($\approx 54\%$ in diethylether)
Tetrahydrofuran	Kimix (Ar, >99% purity)

A.2 Metal Crystallite Size Distributions

University of Cape Town

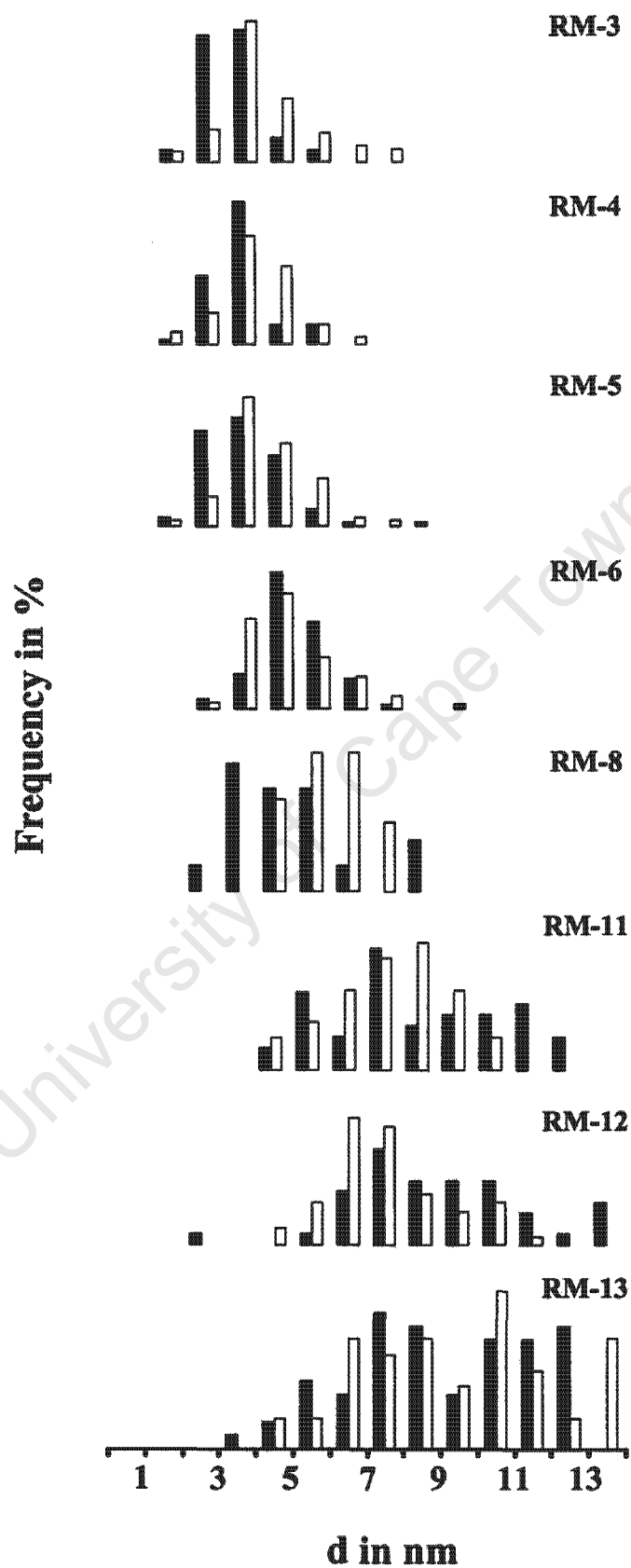


Figure A.1: Crystallite size distributions of calcined (*closed bars*) and reduced (*open bars*) alumina supported nano-sized crystallites as determined by means of TEM analysis.

A.2. METAL CRYSTALLITE SIZE DISTRIBUTIONS

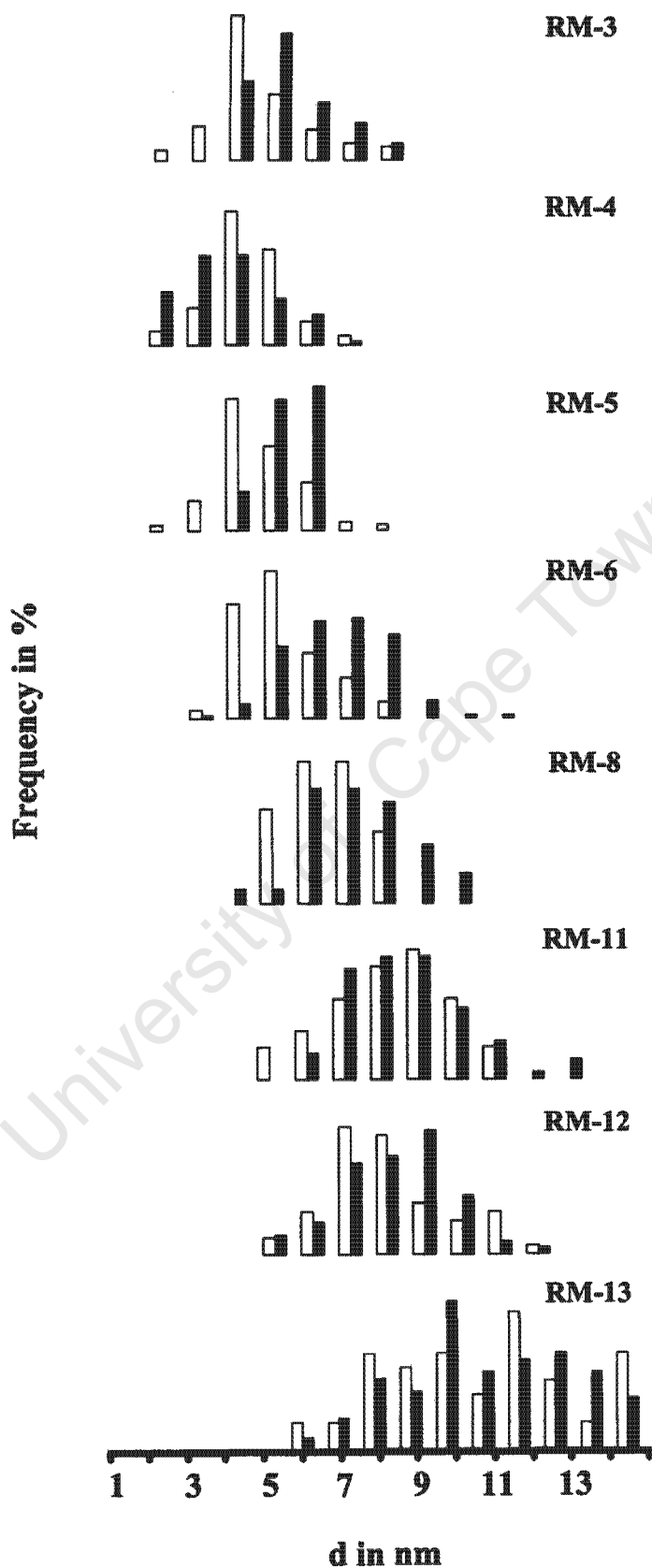


Figure A.2: Crystallite size distributions of reduced (*open bars*) and spent (*closed bars*) alumina supported nano-sized crystallites as determined by means of TEM analysis.

A.3 Chemisorption Reading

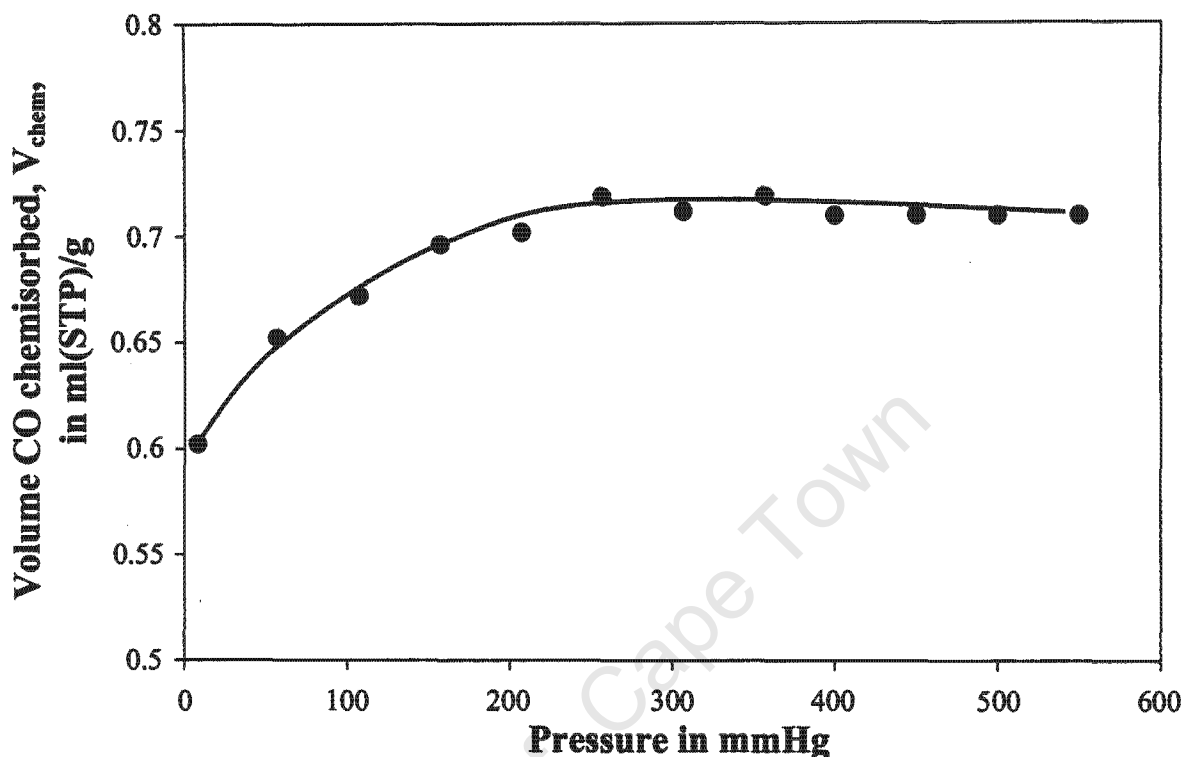


Figure A.3: Example of typical chemisorption reading; sample: RM-2.

A.4 Calculation of the Number of Exposed Surface Atoms

The calculation of the number of exposed surface atoms follows a method described by van Hardeveld and Hartog (1969). The surface atoms of a metal crystallite can be differentiated by the number and the arrangement of their nearest neighbours.

The total number of atoms, N_{total} , can be divided into the number of bulk atoms, N_{bulk} , and the number of surface atoms, N_s . Surface atoms differ from atoms in the bulk of the crystal in that they have an incomplete set of nearest neighbours, varying with the place where that atom is situated. The amount of surface and bulk atoms is dependent on the geometry of the crystal structure. The crystallite size, expressed as a dimensionless quantity (d_{cryst}) for a certain amount of surface atoms, can be calculated using the following equation:

$$d_{cryst} = d_{atom}^{-1} \cdot \left(\frac{6}{\pi} \cdot N_{total} \cdot \frac{V_u}{N_u} \right)^{1/3} \quad (A.1)$$

with V_u being the volume of the cell unit and N_u being the number of atoms in the unit cell.

For a hexagonal cubic packing such as typically found for ruthenium the following set of equations was used to calculate the different atoms. N_{total} and N_{bulk} are given by a polynomial of the third degree in j (with j being the number of atoms lying on an

A.4. CALCULATION OF THE NUMBER OF EXPOSED SURFACE ATOMS

equivalent edge with corner atoms included and N_{exp} being given by a polynomial of the second degree of j).

Total number of atoms

$$N_{\text{total}} = \frac{1}{2} \cdot j \cdot (j^2 + 1) \quad (\text{A.2})$$

Number of bulk atoms

$$N_{\text{bulk}} = \frac{1}{2} \cdot (j - 2) \cdot (j^2 - 4 \cdot j + 5) \quad (\text{A.3})$$

Number of exposed surface atoms

$$N_{\text{exp}} = 3 \cdot j^2 - 6 \cdot j + 5 \quad (\text{A.4})$$

Using this set of equations, the number of exposed surface metal atoms for a given number of total metal atoms can be calculated (see Figure A.4). The transformation from number of exposed metal atoms to crystallite size diameter is achieved by using equation A.1^a. The volume of the unit cell, V_u , was calculated using equation A.5.

$$V_u = \frac{6}{(\pi \cdot d_{\text{lattice}})^{1/3}} \quad (\text{A.5})$$

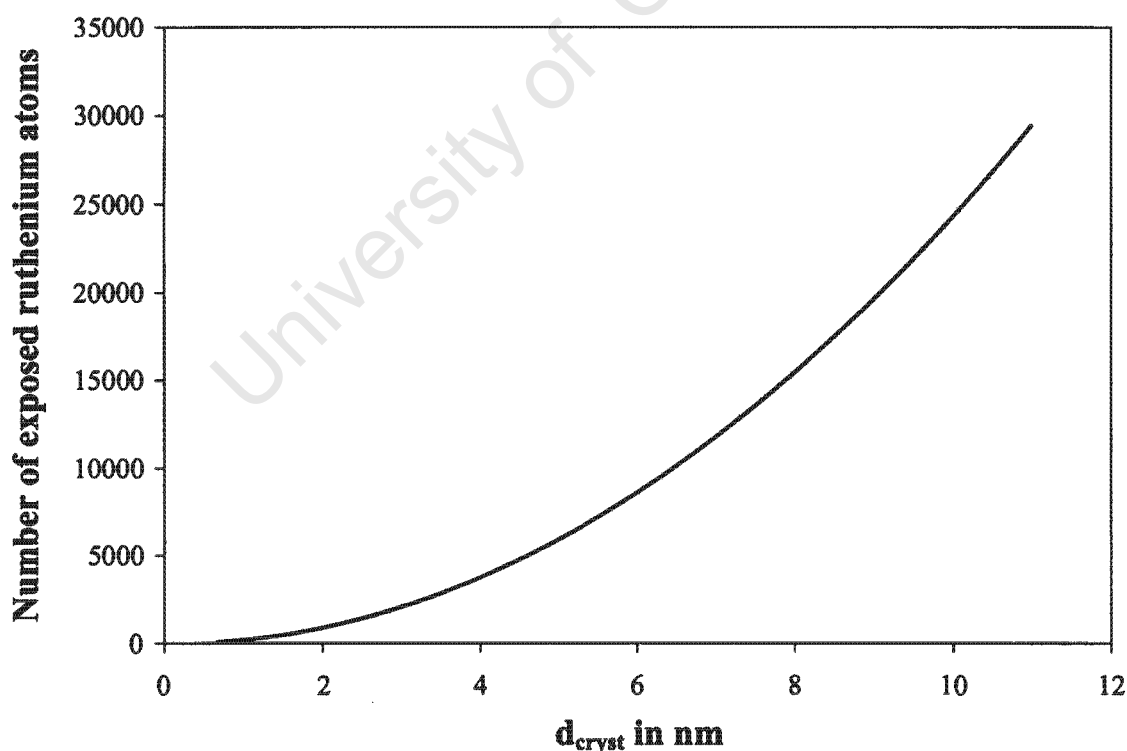


Figure A.4: Number of exposed ruthenium atoms as function of crystallite size of ruthenium.

^aThe lattice parameter (d_{lattice}) for Ru is 2.6 Å.

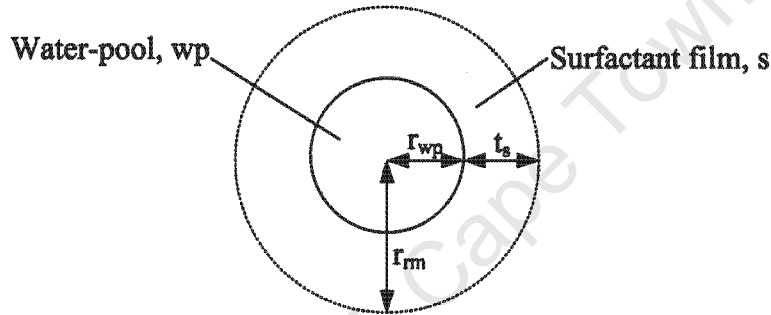
A.5 Theoretical Modelling of Reverse Micelle Size

The theoretical size of a reverse micelle was calculated based on viscosity measurements (see Section 5.1.1, p. 51). The viscosity η of a suspension is related to the volume fraction of suspended particles.

In this work the volume fraction of the suspended particles, Φ , was determined using the following equation developed by Cheng and Schachmann in 1955 (Kinugasa et al., 2002):

$$\frac{\eta - \eta_0}{\eta} = 2.5 \cdot \Phi + 14.1 \cdot \Phi^2 \quad (\text{A.6})$$

with η being the viscosity of the suspension (in this case the microemulsion suspension) and η_0 being the viscosity of the suspending medium (n-hexane in this case). Scheme 23 shows an ideal reverse micelle diagram illustrating the water-pool part and the surfactant film separated from the surrounding oil phase.



Scheme 23: Description of the reverse micelle dimensions.

The micelles are assumed to be spherical particles with uniform particle size at a particular water-to-surfactant weight ratio, ω_{wt} , and the aggregation number, n_{ag} , is assumed to be constant. The volume fraction, Φ , of the particles is defined by Kinugasa et al. (2002) as:

$$\Phi = N_A \cdot V_{rm} \cdot c_{rm} = \frac{N_A \cdot V_{rm} \cdot c_s}{n_{ag}} \quad (\text{A.7})$$

with V_{rm} being the volume of the reverse micelle, c_{rm} the concentration of reverse micelles, c_s the concentration of the surfactant and N_A the Avogadro constant.

From Scheme 23, V_{rm} and V_{wp} , may be expressed in terms of the radius of the micelle, r_{rm} , the radius of the water-pool, r_{wp} , and the thickness of the surfactant layer^b, t_s , as shown in the following equations:

$$V_{rm} = \frac{4 \cdot \pi \cdot r_{rm}^3}{3} \quad (\text{A.8})$$

$$V_{wp} = \frac{4 \cdot \pi \cdot r_{wp}^3}{3} \quad (\text{A.9})$$

$$r_{rm} = r_{wp} + t_s \quad (\text{A.10})$$

By putting equations A.9 and A.10 in equation A.8, V_{rm} can be rewritten as:

^bThe thickness of the surfactant layer, t_s , is equivalent to the length of the surfactant and is defined as $t_s = 1.5 + 1.265 \cdot N_C$.

$$V_{rm} = \frac{4 \cdot \pi}{3} \cdot \left[\left(\frac{3 \cdot V_{wp}}{4 \cdot \pi} \right)^{1/3} + t_s \right]^3 \quad (A.11)$$

V_{wp} can be expressed based on the volume of water present, V_w , and the total number of reverse micelles present in the solution, N_{rm} :

$$V_{wp} = \frac{V_w}{N_{rm}} = \frac{V_w \cdot n_{ag}}{N_A \cdot V_{total} \cdot c_s} \quad (A.12)$$

with V_{total} defined as the total volume of the reverse micelle system. Substituting equation into equation A.12 gives:

$$V_{rm} = \frac{4 \cdot \pi}{3} \cdot \left[\left(\frac{3 \cdot V_w \cdot n_{ag}}{4 \cdot \pi \cdot N_A \cdot c_s \cdot V_{total}} \right)^{1/3} + t_s \right]^3 \quad (A.13)$$

Equation A.7 can be rewritten as:

$$\Phi = \frac{4 \cdot \pi \cdot N_A \cdot c_s}{3 \cdot n_{ag}} \cdot \left[\left(\frac{3 \cdot V_w \cdot n_{ag}}{4 \cdot \pi \cdot N_A \cdot c_s \cdot V_{total}} \right)^{1/3} + t_s \right]^3 \quad (A.14)$$

If the volume fraction of the dispersed particles, Φ , is known from the viscosity correlations, the aggregation number, n_{ag} , can be calculated using equation A.14. This in turn permits the determination of the water-pool radius, r_{wp} as shown in the following equation:

$$r_{wp} = \left(\frac{3 \cdot V_w \cdot n_{ag}}{4 \cdot \pi \cdot N_A \cdot c_s \cdot V_{total}} \right)^{1/3} \quad (A.15)$$

The rearrangement of equation A.14 and substitution in equation A.15 results in:

$$r_{wp} = \left(\frac{V_w}{V_{total}} \right)^{1/3} \cdot \left(\frac{t_s}{\Phi^{1/3} - \left(\frac{V_w}{V_{total}} \right)^{1/3}} \right) \quad (A.16)$$

The volume fraction of the suspended particles can also be estimated from known compositions of the microemulsions and densities of the respective aqueous and surfactant phases as derived from Mabaso (2005). This approach does not include particle-particle and particle-medium interactions. The known mass of water, m_w , and the surfactant phase, m_s , are given by:

$$m_w = V_w \cdot \rho_w = \frac{4}{3} \cdot \pi \cdot r_{wp}^3 \cdot \rho_w \quad (A.17)$$

$$m_s = V_s \cdot \rho_s = \frac{4}{3} \cdot \pi \cdot (r_{rm}^3 - r_{wp}^3) \cdot \rho_s \quad (A.18)$$

where ρ_w is the density of water and ρ_s is the density of the surfactant. The water-to-surfactant weight ratio, ω_{wt} , is defined as:

$$\omega_{wt} = \frac{m_w}{m_s} = \frac{r_{wp}^3 \cdot \rho_w}{(r_{rm}^3 - r_{wp}^3) \cdot \rho_s} \quad (A.19)$$

Rearranging equation A.19 and substituting equation A.9 for r_{wp} leads to:

$$r_{rm}^3 = \frac{\rho_w + \omega_{wt} \cdot \rho_s}{\omega_{wt} \cdot \rho_s} \cdot r_{wp}^3 = \frac{\rho_w + \omega_{wt} \cdot \rho_s}{\omega_{wt} \cdot \rho_s} \cdot \frac{3}{4 \cdot \pi} \cdot V_{wp} \quad (A.20)$$

Substituting equation A.20 into A.8 and then substituting equation A.12 for V_{wp} :

$$V_{rm} = \frac{\rho_w + \omega_{wt} \cdot \rho_s}{\omega_{wt} \cdot \rho_s} \cdot \frac{V_w \cdot n_{ag}}{N_A \cdot c_s \cdot V_{total}} \quad (A.21)$$

Accordingly, equation A.7 can be re-written as:

$$\Phi = \frac{\rho_w + \omega_{wt} \cdot \rho_s}{\omega_{wt} \cdot \rho_s} \cdot \frac{V_w}{V_{total}} \quad (A.22)$$

This equation is independent on the aggregation number, n_{ag} . Therefore, the reverse micelle size can be estimated directly by substituting equation A.22 in equation A.16 without requiring the viscosity (see equation A.23).

$$r_{wp} = \frac{t_s}{\left(\frac{\rho_w + \omega_{wt} \cdot \rho_s}{\omega_{wt} \cdot \rho_s} \right)^{1/3} - 1} \quad (A.23)$$

A.6 Thermogravimetric Analysis

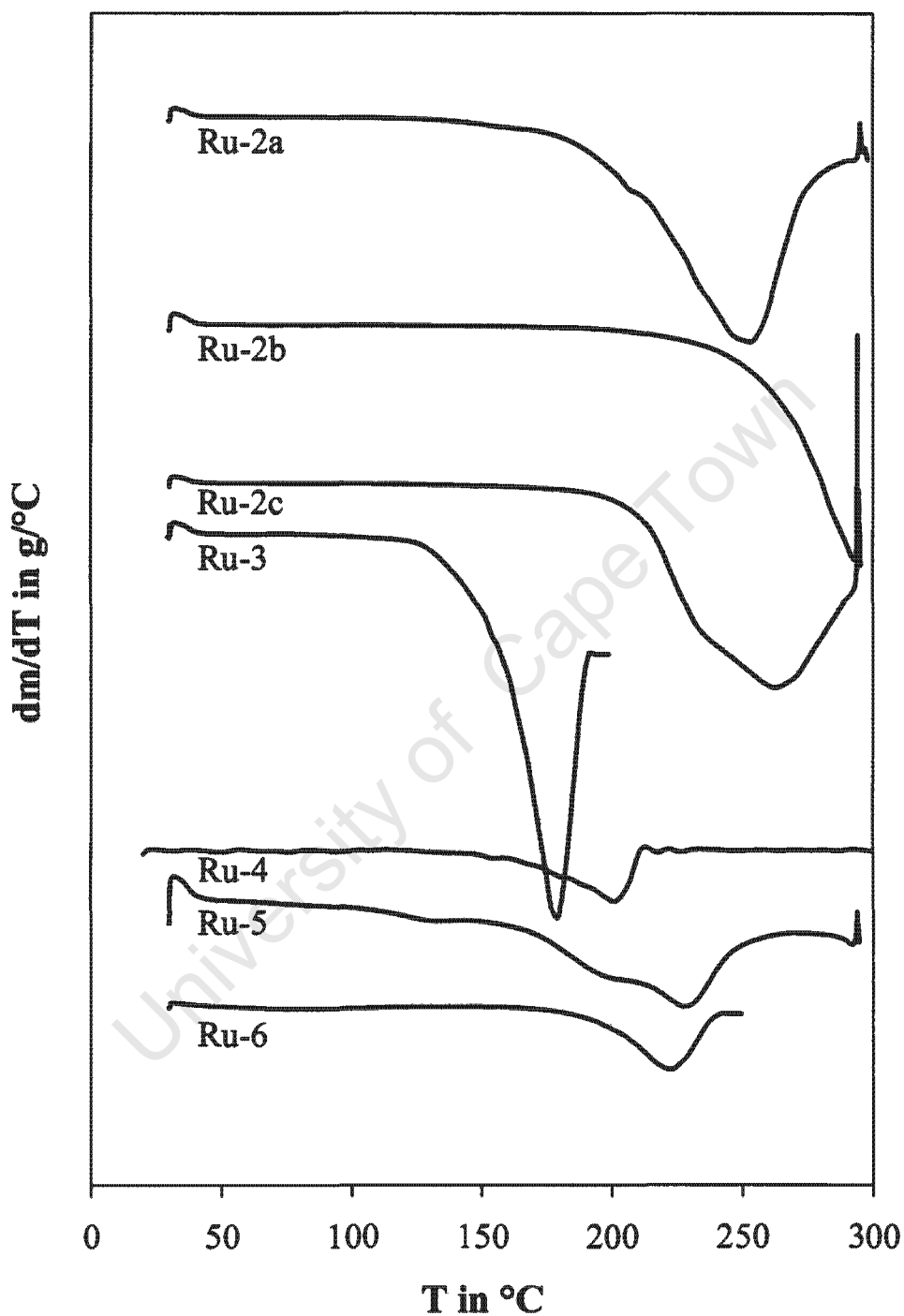


Figure A.5: First derivative of weight vs. temperature profile from TGA analysis for the different organometallic complexes in 5 vol% hydrogen in argon.

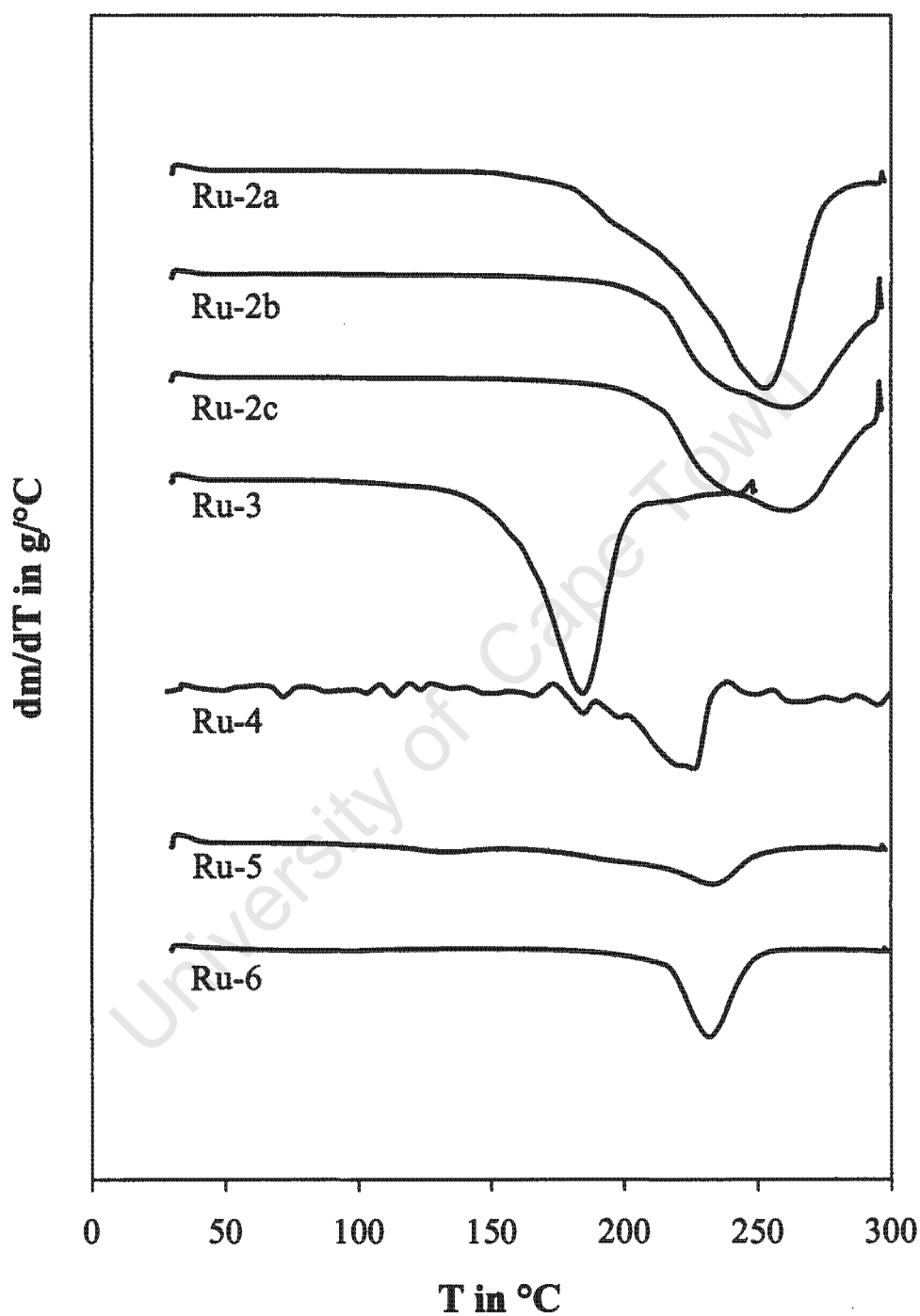


Figure A.6: First derivative of weight vs. temperature profile from TGA analysis for the different organometallic complexes in 5 vol% carbon monoxide in nitrogen.

Appendix B

Fischer-Tropsch Performance Tests

B.1 TCD and FID Chromatograms

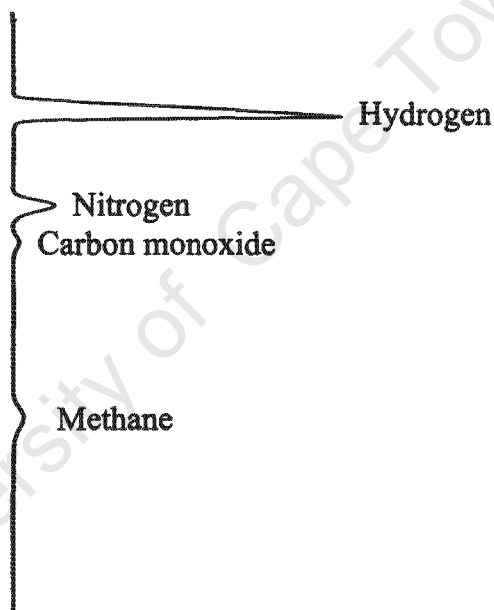


Figure B.1: A typical chromatogram obtained from GC-TCD analysis in FT synthesis (225°C/20 bar); catalyst sample RM-10 after 3 hours runtime.

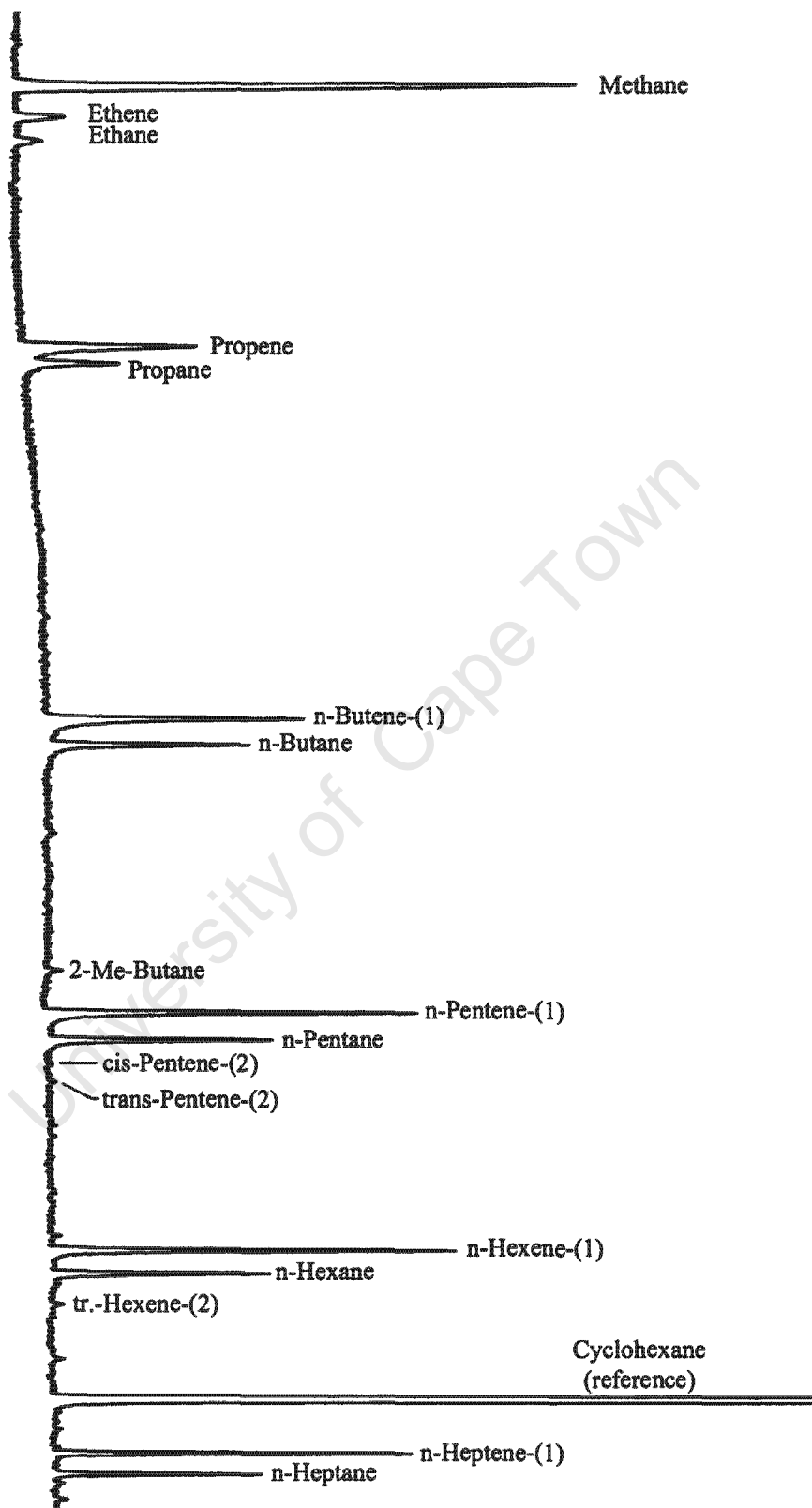


Figure B.2: A typical chromatogram obtained from GC-FID analysis in FT synthesis at 170°C/4 bar; catalyst sample RM-10 after 3 minutes runtime.

B.2 Tables of Selected Results

University of Cape Town

Table B.1: Results of FT experiments in synthesis gas after 1-3 minutes runtime on different alumina supported nano-sized crystallites. ($T_{\text{Reaction}} = 170^{\circ}\text{C}$, $P = 4$ bar)

Sample code	RM-1	RM-2	RM-3	RM-4	RM-5	RM-6	RM-7	RM-8	RM-9	RM-10	RM-11	RM-12	RM-13
$\bar{d}_{\text{red-TEM}}^{\text{a}}$, nm	1.5	3.9	4.1	3.8	4.1	4.7	4.9	6.3	6.7	6.7	8.3	7.7	9.6
$N_{\text{exp-red}}^{\text{b}}$	510	3680	3690	3550	3680	5050	5600	9700	10500	10500	16500	14300	22000
$\bar{d}_{\text{spent-TEM}}^{\text{c}}$, nm	4.0	5.6	4.9	3.2	4.9	6.7	6.5	7.1	6.7	6.7	9.3	7.8	9.8
$N_{\text{exp-spent}}^{\text{d}}$	3700	7300	5600	2250	5500	10500	10200	11200	11100	11000	20670	14500	23500
$x_{\text{Ru-TPR}}^{\text{e}}$, wt%	2.8	2.8	1.7	1.4	2.2	2.1	2.8	3.1	3.0	3.0	3.2	2.5	1.8
Activity, s^{-1}													
$\text{TOF}_{\text{VOC's}} \cdot 10^{5\text{f}}$	1.9	5.1	3.0	8.4	0.5	2.5	3.4	17.0	15.9	33.4	3.3	11.5	5.4
$\text{TOF}(\text{C}_{2+})_{\text{VOC's}} \cdot 10^{5\text{g}}$	0.3	1.3	1.8	0.7	0.2	1.5	1.7	1.6	2.8	2.7	1.7	2.5	2.0
Selectivity, C%													
$\text{C}_1(\text{VOC's})^{\text{h}}$	87.4	81.4	79.5	94.8	74.7	74.7	86.4	94.5	90.1	93.0	66.8	86.5	73.1
$\text{C}_{5+}(\text{VOC's})^{\text{h}}$	1.7	1.3	1.9	0.6	3.3	4.2	0.0	0.9	1.5	1.4	8.8	1.7	0.0
Olefins, mol%													
C_2^{i}	23.1	0.5	40.2	14.4	35.3	35.4	12.0	15.3	0.0	10.7	32.6	13.0	38.9
C_3^{i}	13.5	12.6	38.8	20.7	8.3	18.6	1.3	29.3	15.0	39.9	36.9	28.4	57.5
C_5^{i}	13.7	13.2	43.5	36.0	16.5	10.0	4.0	33.0	11.0	35.0	46.5	18.0	43.0
$\alpha\text{-C}_5$ in lin. O^{j}	0.0	14.0	31.5	35.0	16.5	19.0	14.0	25.0	35.0	19.5	47.0	24.0	39.5
Chain growth probability													
$P_{\text{g, C3-C7}}^{\text{k}}$	0.59	0.44	0.43	0.47	0.47	0.54	0.61	0.48	0.46	0.56	0.61	0.50	0.54

^a average crystallite size obtained from TEM micrographs of the reduced catalysts

^b number of exposed ruthenium surface atoms per crystallite of average size in reduced catalysts

^c average crystallite size obtained from TEM micrographs of the spent catalysts

^d number of exposed ruthenium surface atoms per crystallite of average size in spent catalysts

^e ruthenium loading obtained from TPR measurements

^f turnover frequency of volatile organic products (VOC's) formed

^g turnover frequency of C_{2+} hydrocarbons in VOC's formed

^h selectivity in VOC's

ⁱ molar content of olefins in linear hydrocarbon-fraction

^j molar content of α -olefins in linear C_5 -olefins

^k chain growth probability determined from slopes between C_3 to C_7 in ASF distribution

Table B.2: Results of FT experiments in synthesis gas after 10-20 minutes runtime on different alumina supported nano-sized crystallites. ($T_{\text{Reaction}} = 170^{\circ}\text{C}$, $P = 4$ bar)

Sample code	RM-1	RM-2	RM-3	RM-4	RM-5	RM-6	RM-7	RM-8	RM-9	RM-10	RM-11	RM-12	RM-13
$\bar{d}_{\text{red-TEM}}^{\text{a}}$, nm	1.5	3.9	4.1	3.8	4.1	4.7	4.9	6.3	6.7	6.7	8.3	7.7	9.6
$N_{\text{exp-red}}^{\text{b}}$	510	3680	3690	3550	3680	5050	5600	9700	10500	10500	16500	14300	22000
$\bar{d}_{\text{spent-TEM}}^{\text{c}}$, nm	4.0	5.6	4.9	3.2	4.9	6.7	6.5	7.1	6.7	6.7	9.3	7.8	9.8
$N_{\text{exp-spent}}^{\text{d}}$	3700	7300	5600	2250	5500	10500	10200	11200	11100	11000	20670	14500	23500
$x_{\text{Ru-TPR}}^{\text{e}}$, wt%	2.8	2.8	1.7	1.4	2.2	2.1	2.8	3.1	3.0	3.0	3.2	2.5	1.8
Activity, s^{-1}													
$\text{TOF}_{\text{VOC's}} \cdot 10^{5\text{f}}$	0.9	1.7	1.7	4.7	0.5	1.2	1.6	3.3	4.1	5.1	1.8	3.1	7.9
$\text{TOF}_{(\text{C}_{2+})\text{VOC's}} \cdot 10^{5\text{g}}$	0.3	0.9	0.9	2.0	0.3	0.6	0.9	1.9	2.0	3.0	0.9	1.2	4.5
Selectivity, C%													
$\text{C}_1(\text{VOC's})^{\text{h}}$	64.6	45.3	43.1	57.5	52.8	48.2	36.6	40.5	54.9	41.3	48.2	59.9	43.0
$\text{C}_{5+}(\text{VOC's})^{\text{h}}$	12.5	18.0	25.3	14.9	24.3	15.2	23.0	13.4	13.3	17.4	21.0	12.4	20.6
Olefins, mol%													
C_2^{i}	65.1	40.5	56.8	50.6	n/a	33.5	33.4	61.1	10.7	57.7	76.9	n/a	21.0
C_3^{i}	13.9	11.2	77.9	50.3	n/a	26.8	12.0	48.3	36.2	56.3	62.4	34.1	64.7
C_5^{i}	27.0	13.0	63.0	61.0	32.0	20.0	11.0	51.0	19.0	58.0	57.0	26.0	58.0
$\alpha\text{-C}_5$ in lin. O^{j}	36.0	26.0	38.0	43.0	34.0	22.0	38.0	40.0	41.0	77.0	28.0	25.0	25.0
Chain growth probability													
$P_{\text{g, C3-C7}}^{\text{k}}$	0.67	0.76	0.82	0.77	0.73	0.77	0.78	0.63	0.70	0.77	0.78	0.66	0.72

^a average crystallite size obtained from TEM micrographs of the reduced catalysts

^b number of exposed ruthenium surface atoms per crystallite of average size in reduced catalysts

^c average crystallite size obtained from TEM micrographs of the spent catalysts

^d number of exposed ruthenium surface atoms per crystallite of average size in spent catalysts

^e ruthenium loading obtained from TPR measurements

^f turnover frequency of volatile organic products (VOC's) formed

^g turnover frequency of C_{2+} hydrocarbons in VOC's formed

^h selectivity in VOC's

ⁱ molar content of olefins in linear hydrocarbon-fraction

^j molar content of α -olefins in linear C_5 -olefins

^k chain growth probability determined from slopes between C_3 to C_7 in ASF distribution

Table B.3: Results of FT experiments in synthesis gas after 60 minutes runtime on different alumina supported nano-sized crystallites. ($T_{\text{Reaction}} = 170^{\circ}\text{C}$, $P = 4$ bar)

Sample code	RM-1	RM-2	RM-3	RM-4	RM-5	RM-6	RM-7	RM-8	RM-9	RM-10	RM-11	RM-12	RM-13
$\bar{d}_{\text{red-TEM}}^{\text{a}}$, nm	1.5	3.9	4.1	3.8	4.1	4.7	4.9	6.3	6.7	6.7	8.3	7.7	9.6
$N_{\text{exp-red}}^{\text{b}}$	510	3680	3690	3550	3680	5050	5600	9700	10500	10500	16500	14300	22000
$\bar{d}_{\text{spent-TEM}}^{\text{c}}$, nm	4.0	5.6	4.9	3.2	4.9	6.7	6.5	7.1	6.7	6.7	9.3	7.8	9.8
$N_{\text{exp-spent}}^{\text{d}}$	3700	7300	5600	2250	5500	10500	10200	11200	11100	11000	20670	14500	23500
$x_{\text{Ru-TPR}}^{\text{e}}$, wt%	2.8	2.8	1.7	1.4	2.2	2.1	2.8	3.1	3.0	3.0	3.2	2.5	1.8
Activity, s^{-1}													
$\text{TOF}_{\text{VOC's}} \cdot 10^{5\text{f}}$	0.7	1.3	1.4	3.1	-	1.1	0.9	2.2	2.8	3.1	1.9	2.1	4.8
$\text{TOF}(\text{C}_{2+})_{\text{VOC's}} \cdot 10^{5\text{g}}$	0.3	0.7	0.8	2.3	-	0.5	0.5	1.0	1.5	2.0	1.1	1.1	3.3
Selectivity, C%													
$\text{C}_1(\text{VOC's})^{\text{h}}$	63.5	45.0	42.7	27.1	-	54.6	38.8	53.2	46.1	39.3	39.9	46.3	31.9
$\text{C}_{5+}(\text{VOC's})^{\text{h}}$	15.1	13.1	32.4	26.1	-	13.0	16.6	16.5	14.3	20.2	28.6	15.4	33.0
Olefins, mol%													
C_2^{i}	64.8	71.6	n/a	50.6	-	79.6	64.7	64.3	67.1	67.8	92.8	37.9	68.2
C_3^{i}	19.4	47.8	66.7	43.9	-	45.9	52.8	57.7	48.1	53.7	64.1	48.9	71.3
C_5^{i}	24.0	56.5	64.0	67.5	-	29.4	61.8	59.8	60.7	62.6	62.2	51.9	59.2
$\alpha\text{-C}_5$ in lin. O^{j}	19.0	80.0	78.0	90.0	-	82.0	90.0	90.0	79.0	88.0	84.0	75.0	80.0
Chain growth probability													
$P_{\text{g, C3-C7}}^{\text{k}}$	0.78	0.79	0.76	0.82	-	0.77	0.81	0.86	0.84	0.87	0.80	0.70	0.79

^a average crystallite size obtained from TEM micrographs of the reduced catalysts

^b number of exposed ruthenium surface atoms per crystallite of average size in reduced catalysts

^c average crystallite size obtained from TEM micrographs of the spent catalysts

^d number of exposed ruthenium surface atoms per crystallite of average size in spent catalysts

^e ruthenium loading obtained from TPR measurements

^f turnover frequency of volatile organic products (VOC's) formed

^g turnover frequency of C_{2+} hydrocarbons in VOC's formed

^h selectivity in VOC's

ⁱ molar content of olefins in linear hydrocarbon-fraction

^j molar content of α -olefins in linear C_5 -olefins

^k chain growth probability determined from slopes between C_3 to C_7 in ASF distribution

Table B.4: Results of FT experiments in synthesis gas at steady-state on different alumina supported nano-sized crystallites.
($T_{\text{Reaction}} = 170^{\circ}\text{C}$, $P = 4$ bar)

Sample code	RM-1	RM-2	RM-3	RM-4	RM-5	RM-6	RM-7	RM-8	RM-9	RM-10	RM-11	RM-12	RM-13
$\bar{d}_{\text{red-TEM}}^{\text{a}}$, nm	1.5	3.9	4.1	3.8	4.1	4.7	4.9	6.3	6.7	6.7	8.3	7.7	9.6
$N_{\text{exp-red}}^{\text{b}}$	510	3680	3690	3550	3680	5050	5600	9700	10500	10500	16500	14300	22000
$\bar{d}_{\text{spent-TEM}}^{\text{c}}$, nm	4.0	5.6	4.9	3.2	4.9	6.7	6.5	7.1	6.7	6.7	9.3	7.8	9.8
$N_{\text{exp-spent}}^{\text{d}}$	3700	7300	5600	2250	5500	10500	10200	11200	11100	11000	20670	14500	23500
$x_{\text{Ru-TPR}}^{\text{e}}$, wt%	2.8	2.8	1.7	1.4	2.2	2.1	2.8	3.1	3.0	3.0	3.2	2.5	1.8
Activity, s^{-1}													
$\text{TOF}_{\text{VOC's}} \cdot 10^{5\text{f}}$	0.6	0.6	0.6	0.5	0.7	0.9	0.8	1.1	1.2	2.3	1.3	1.1	2.5
$\text{TOF}_{\text{prod.}} \cdot 10^{5\text{f}}$	0.7	0.9	1.1	1.1	1.0	1.4	1.1	1.5	1.6	2.8	1.9	2.8	3.6
$\text{TOF}(\text{C}_{2+})_{\text{VOC's}} \cdot 10^{5\text{g}}$	0.2	0.2	0.2	0.1	0.2	0.3	0.4	0.5	0.6	1.3	0.7	0.4	1.7
$\text{TOF}(\text{C}_{2+})_{\text{prod.}} \cdot 10^{5\text{g}}$	0.4	0.5	0.7	0.6	0.6	0.8	0.8	0.9	1.0	1.9	1.3	2.1	2.8
Selectivity, C%													
$\text{C}_1(\text{VOC's})^{\text{h}}$	64.0	69.8	49.5	64.8	60.0	63.6	48.2	55.8	54.8	41.1	48.1	44.2	33.0
$\text{C}_1(\text{prod.})^{\text{h}}$	52.4	47.6	38.6	45.9	41.2	43.2	33.2	40.6	37.3	33.6	48.5	24.4	22.8
$\text{C}_{5+}(\text{VOC's})^{\text{h}}$	5.2	18.1	9.7	10.7	16.6	13.1	23.8	30.7	30.2	21.6	28.2	29.1	26.1
$\text{C}_{5+}(\text{prod.})^{\text{h}}$	35.2	49.1	57.9	47.8	52.4	52.9	60.2	55.9	54.2	56.3	29.5	73.6	67.0
Olefins, mol%													
C_2^{i}	51.5	61.4	62.1	55.0	71.2	61.7	68.1	62.2	68.0	65.5	75.1	61.6	70.0
C_3^{i}	48.1	71.2	53.5	42.9	78.1	77.8	75.1	58.0	63.5	74.9	76.7	60.0	70.4
C_5^{i}	65.0	55.2	59.7	67.1	64.6	57.9	63.7	57.9	59.3	63.6	68.3	57.1	77.0
$\alpha\text{-C}_5$ in lin. O^{j}	83.0	90.0	82.5	80.0	96.0	88.6	96.3	94.5	93.0	93.0	87.0	90.0	40.9
Chain growth probability													
$P_{\text{g, C3-C7}}^{\text{k}}$	0.69	0.88	0.77	0.71	0.84	0.92	0.96	0.94	0.79	0.93	0.88	0.92	0.87

^a average crystallite size obtained from TEM micrographs of the reduced catalysts

^b number of exposed ruthenium surface atoms per crystallite of average size in reduced catalysts

^c average crystallite size obtained from TEM micrographs of the spent catalysts

^d number of exposed ruthenium surface atoms per crystallite of average size in spent catalysts

^e ruthenium loading obtained from TPR measurements

^f turnover frequencies of volatile organic products (VOC's) or total product (prod.) formed

^g turnover frequency of C_{2+} hydrocarbons of VOC's or total product formed

^h selectivity in VOC's or total product

ⁱ molar content of olefins in linear hydrocarbon-fraction

^j molar content of α -olefins in linear C_5 -olefins

^k chain growth probability determined from slopes between C_3 to C_7 in ASF distribution

APPENDIX B. FISCHER-TROPSCH PERFORMANCE TESTS

Table B.5: Steady-state results of FT synthesis at 225°C/20 bar for five selected alumina supported nano-sized crystallites.

($T_{\text{Reaction}} = 225^{\circ}\text{C}$, $P = 20$ bar, $\text{GHSV} = 7 \text{ ml(STP)}/(\text{min}\cdot\text{g}_{\text{cat}})$, $(\text{H}_2/\text{CO})_{\text{in}} = 2:1$)

Sample code	RM-2	RM-3	RM-7	RM-9	RM-10
$\bar{d}_{\text{red-TEM}}$, ^a nm	3.9	4.1	4.9	6.7	8.3
$N_{\text{exp-red}}$ ^b	3680	3690	5600	10500	16500
$\bar{d}_{\text{spent-TEM}}$, ^a nm	4.1	4.5	6.6	7.1	9.6
$N_{\text{exp-spent}}$ ^b	4110	4950	10445	12000	22700
$x_{\text{Ru-TPR}}$, ^c wt%	2.8	1.7	2.8	3.0	3.2
Activity, s⁻¹					
$\text{TOF}_{\text{VOC's}} \cdot 10^{3\text{d}}$	22.1	20.0	22.4	25.3	31.4
$\text{TOF}_{\text{prod.}} \cdot 10^{3\text{d}}$	23.3	23.4	21.9	26.7	31.8
$\text{TOF}(\text{C}_{2+})_{\text{VOC's}} \cdot 10^{3\text{e}}$	6.1	8.2	11.8	13.3	17.2
$\text{TOF}(\text{C}_{2+})_{\text{prod.}} \cdot 10^{3\text{e}}$	7.4	11.9	15.2	14.2	20.9
Selectivity, C%					
$\text{C}_1(\text{VOC's})$ ^f	69.0	63.0	46.2	47.1	47.3
$\text{C}_1(\text{prod.})$ ^f	51.5	30.6	8.3	16.1	12.4
$\text{C}_{5+}(\text{VOC's})$ ^f	16.2	19.5	30.9	29.7	30.7
$\text{C}_{5+}(\text{prod.})$ ^f	38.7	59.7	84.7	76.5	81.8
Olefins, mol%					
C_2 ^g	30.6	39.1	64.3	70.1	55.4
C_3 ^g	39.4	48.9	64.7	62.9	61.3
C₅-Fraction, mol%					
Ol in lin. prod. ^h	33.1	45.2	54.1	55.3	55.4
α -Ol in lin. prod. ⁱ	86.0	96.3	97.0	95.0	94.0
iso/n ^j	0.06	0.05	0.06	0.05	0.04
Ox. in lin. prod. ^k	0.29	0.82	0.70	1.08	1.35
Alc. in Ox. ^l	100	100	64	53	84
Chain growth probability					
$P_g, \text{C}_3\text{-C}_7$ ^m	0.84	0.89	0.90	0.86	0.94

^a average crystallite size obtained from TEM micrographs of the reduced catalysts

^b number of exposed metal atoms of the reduced catalysts

^c ruthenium loading obtained from TPR measurements

^d turnover frequencies of volatile organic compounds (VOC's) or total product formed (prod.)

^e turnover frequencies of C₂₊ hydrocarbons in VOC's or total product

^f selectivities in VOC's and total product

^g molar content of olefins in linear hydrocarbon-fractions

^h molar content of pentenes in linear C₅ hydrocarbons

ⁱ molar content of α -olefins in linear C₅ hydrocarbons

^j molar ratio of branched to linear products in C₅-fraction

^k molar content of pentanol and pentanal in linear C₅-products

^l molar content of pentanol in linear C₅-oxygenates

^m chain growth probability determined from slopes between C₃ to C₇ in ASF distribution

B.2. TABLES OF SELECTED RESULTS

Table B.6: Selected results of FT experiments in synthesis gas ($(\text{H}_2/\text{CO})_{\text{in}} = 2:1$) and in hydrogen after 1-3 minutes runtime on different supported organometallic compounds.
($T_{\text{Reaction}} = 170^\circ\text{C}$, $P = 4$ bar, $\text{GHSV} = 7 \text{ ml(STP)}/(\text{min}\cdot\text{g}_{\text{cat}})$)

Sample code	Ru-2a	Ru-2b	Ru-2c	Ru-3	Ru-4	Ru-5	Ru-6
<i>in synthesis gas (1-3 min)</i>							
N_{exp}	2	2	2	3	4	5	6
$x_{\text{Ru}}(\text{spent})^{\text{a}}$	0.92	0.45	1.99	2.64	2.75	1.17	1.95
Activity, s^{-1}							
TOF $\cdot 10^{6\text{b}}$	6.8	3.0	3.0	3.5	4.9	5.7	8.9
TOF(C_{2+}) $\cdot 10^{6\text{c}}$	0.6	0.4	0.9	1.0	1.5	1.8	1.5
Selectivity $^{\text{d}}$, C%							
C_1	87.8	89.6	83.0	77.3	77.9	71.1	85.4
Olefins, mol%							
C_2^{e}	63.0	79.9	74.9	67.0	69.7	19.5	31.8
C_3^{e}	91.5	73.7	80.9	65.2	59.2	56.0	66.0
Chain growth probability							
$P_{\text{g}, 1-2}^{\text{f}}$	0.09	0.08	0.39	0.15	0.11	0.37	0.25
$P_{\text{g}, 3-4}^{\text{g}}$	0.28	0.16	(>1)	0.34	0.03	0.56	0.46
<i>in hydrogen (1-3 min)</i>							
N_{exp}	2	2	2	3	4	5	6
$x_{\text{Ru}}(\text{spent})^{\text{a}}$	2.47	2.96	1.96	2.68	2.92	2.25	1.24
Activity, s^{-1}							
TOF $\cdot 10^{6\text{b}}$	1.9	3.5	1.4	2.7	10.7	1.4	9.0
TOF(C_{2+}) $\cdot 10^{6\text{c}}$	0.2	0.7	0.6	1.1	2.5	0.1	1.5
Selectivity $^{\text{d}}$, C%							
C_1	89.3	72.8	59.4	60.0	76.4	94.6	83.4
Olefins, mol%							
C_2^{e}	66.7	65.5	0.0	50.9	0.0	0.0	0.0
C_3^{e}	19.6	0.0	23.1	38.5	17.1	0.0	0.0
Chain growth probability							
$P_{\text{g}, 1-2}^{\text{f}}$	0.28	0.32	0.63	0.39	0.31	0.11	0.3
$P_{\text{g}, 3-4}^{\text{g}}$	n/a	0.16	(>1)	0.55	0.77	n/a	0.30

^a ruthenium loading obtained from ICP analysis of the spent catalyst

^b turnover frequency for C_1 - C_4 hydrocarbons formed

^c turnover frequency for C_2 - C_4 hydrocarbons formed

^d methane content in C_1 - C_4 -fraction

^e molar content of olefins in linear hydrocarbon-fraction

^f chain growth probability determined from slopes between C_1 to C_2 in ASF distribution

^g chain growth probability determined from slopes between C_3 to C_4 in ASF distribution

APPENDIX B. FISCHER-TROPSCH PERFORMANCE TESTS

Table B.7: Selected results of FT experiments in synthesis gas after 10-20 minutes runtime in synthesis gas ($(\text{H}_2/\text{CO})_{\text{in}} = 2:1$) and at maximal activities for performances in hydrogen (runtimes between 10-100 minutes) on different supported organometallic compounds.
($T_{\text{Reaction}} = 170^\circ\text{C}$, $P = 4$ bar, $\text{GHSV} = 7$ ml(STP)/(min·g_{cat}))

Sample code	Ru-2a	Ru-2b	Ru-2c	Ru-3	Ru-4	Ru-5	Ru-6
<i>in synthesis gas (10-20 min)</i>							
N_{exp}	2	2	2	3	4	5	6
$x_{\text{Ru}}(\text{spent})^{\text{a}}$	0.92	0.45	1.99	2.64	2.75	1.17	1.95
Activity, s^{-1}							
TOF·10 ^{6b}	0.1	0.3	1.3	0.7	1.2	1.3	5.0
TOF(C ₂₊)·10 ^{6c}	0.06	0.06	0.3	0.1	0.4	0.1	0.6
Selectivity ^d , C%							
C ₁	64.4	80.7	75.9	79.3	66.7	89.1	87.4
Olefins, mol%							
C ₂ ^e	64.6	59.2	91.5	69.4	72.8	14.6	51.2
C ₃ ^e	n/a	80.0	67.9	69.0	89.0	82.9	37.5
Chain growth probability							
$P_{\text{g}, 1-2}^{\text{f}}$	0.09	0.08	0.39	0.15	0.11	0.37	0.25
$P_{\text{g}, 3-4}^{\text{g}}$	0.28	0.16	(>1)	0.34	0.03	0.56	0.46
<i>in hydrogen (10-100 min)</i>							
N_{exp}	2	2	2	3	4	5	6
$x_{\text{Ru}}(\text{spent})^{\text{a}}$	2.47	2.96	1.96	2.68	2.92	2.25	1.24
Activity, s^{-1}							
TOF·10 ^{6b}	157.3	5.0	148.0	37.8	29.0	58.6	21.7
TOF(C ₂₊)·10 ^{6c}	16.0	0.2	1.6	3.2	2.6	5.9	3.7
Selectivity ^d , C%							
C ₁	89.8	86.3	80.6	91.6	91.2	90.0	83.1
Olefins, mol%							
C ₂ ^e	0.0	0.0	1.0	0.0	0.0	5.0	3.9
C ₃ ^e	11.8	0.0	9.5	6.1	7.9	8.9	10.0
Chain growth probability							
$P_{\text{g}, 1-2}^{\text{f}}$	0.23	0.29	0.41	0.07	0.21	0.19	0.27
$P_{\text{g}, 3-4}^{\text{g}}$	n/a	0.28	0.67	0.27	n/a	0.31	0.30

^a ruthenium loading obtained from ICP analysis of the spent catalyst

^b turnover frequency for C₁-C₄ hydrocarbons formed

^c turnover frequency for C₂-C₄ hydrocarbons formed

^d methane content in C₁-C₄-fraction

^e molar content of olefins in linear hydrocarbon-fraction

^f chain growth probability determined from slopes between C₁ to C₂ in ASF distribution

^g chain growth probability determined from slopes between C₃ to C₄ in ASF distribution

B.2. TABLES OF SELECTED RESULTS

Table B.8: Selected results of FT experiments in synthesis gas after 300 minutes runtime on different supported organometallic compounds.

($T_{\text{Reaction}} = 170^{\circ}\text{C}$, $P = 4$ bar, $\text{GHSV} = 7 \text{ ml(STP)}/(\text{min}\cdot\text{g}_{\text{cat}})$, $(\text{H}_2/\text{CO})_{\text{in}} = 2:1$)

Sample code	Ru-2a	Ru-2b	Ru-2c	Ru-3	Ru-4	Ru-5	Ru-6
<i>in synthesis gas (300 min)</i>							
N_{exp}	2	2	2	3	4	5	6
$x_{\text{Ru}}(\text{spent})^{\text{a}}$	0.92	0.45	1.99	2.64	2.75	1.17	1.95
Activity, s^{-1}							
TOF $\cdot 10^{6\text{b}}$	1.3	0.7	5.3	1.1	2.9	14.0	24.2
TOF(C_{2+}) $\cdot 10^{6\text{c}}$	0.3	0.1	1.0	0.5	0.6	0.8	0.3
Selectivity^d, C%							
C_1	83.5	84.7	81.8	62.8	60.6	94.0	98.9
Olefins, mol%							
C_2^{e}	74.8	100	68.7	73.9	62.9	71.4	28.7
C_3^{e}	100	100	100	61.8	51.7	65.1	53.2
Chain growth probability							
$P_{\text{g}, 1-2}^{\text{f}}$	0.37	0.31	0.21	0.54	0.49	0.21	0.18
$P_{\text{g}, 3-4}^{\text{g}}$	n/a	n/a	(>1)	0.19	n/a	0.78	0.18

^a ruthenium loading obtained from ICP analysis of the spent catalyst

^b turnover frequency for C_1 - C_4 hydrocarbons formed

^c turnover frequency for C_2 - C_4 hydrocarbons formed

^d methane content in C_1 - C_4 -fraction

^e molar content of olefins in linear hydrocarbon-fraction

^f chain growth probability determined from slopes between C_1 to C_2 in ASF distribution

^g chain growth probability determined from slopes between C_3 to C_4 in ASF distribution

University of Cape Town

B.3 Additional Fischer-Tropsch Graphs

B.3.1 Supported Nano-sized Crystallites

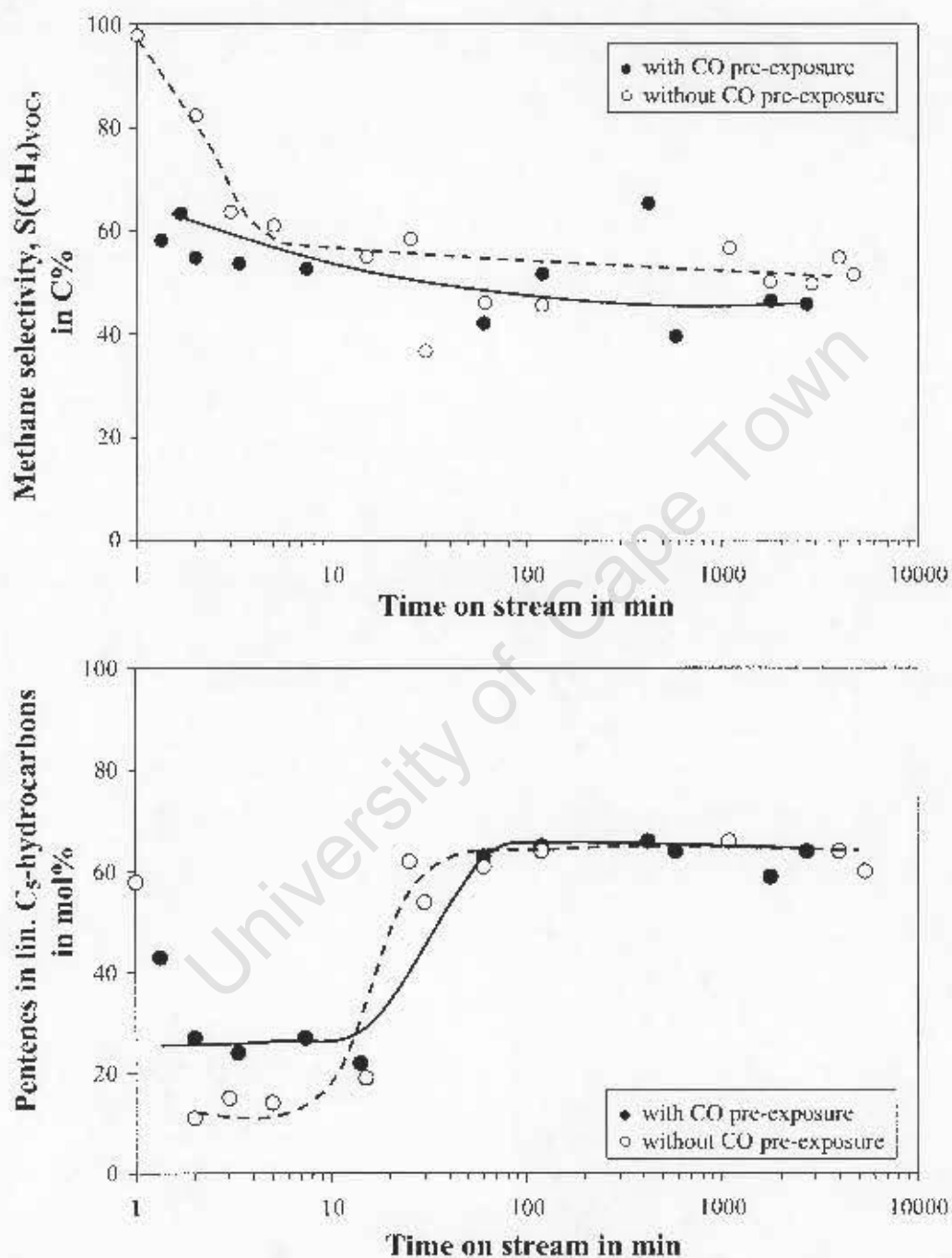


Figure B.3: *top:* Changes in methane selectivities in volatile organic compounds in FT synthesis at $170^\circ\text{C}/4$ bar as function of time on stream for catalyst sample RM-2, with (●) and without (○) carbon monoxide pre-exposure after reduction prior to FT experiment. *bottom:* Changes in molar contents of pentenes in C_5 -fraction of linear hydrocarbons in FT synthesis as function of time on stream for catalyst sample RM-2, with (●) and without (○) carbon monoxide pre-exposure after reduction prior to FT experiments. ($T_{\text{Reactor}} = 170^\circ\text{C}$, $P = 4$ bar, $\text{GHSV} = 7$ ml(STP)/(min \cdot g $_{\text{cat}}$), $(\text{H}_2/\text{CO})_{\text{in}} = 2:1$)

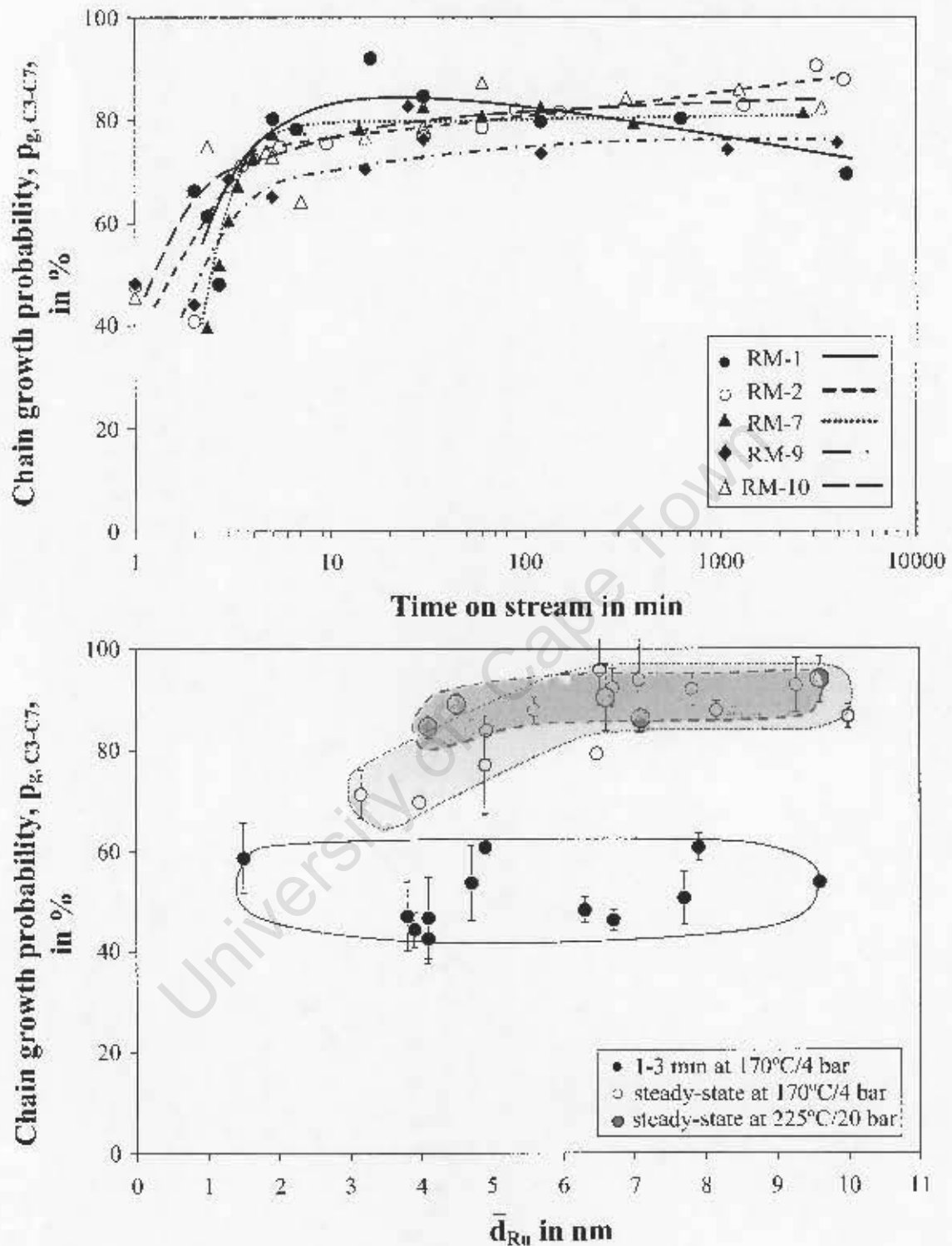


Figure B.4: *top:* Changes in chain growth probabilities in C_4 - C_7 hydrocarbons in FT synthesis at $170^\circ\text{C}/4$ bar for five selected supported nano-sized ruthenium crystallites.

bottom: Average chain growth probabilities (C_4 - C_7) in FT synthesis at $170^\circ\text{C}/4$ bar versus average ruthenium crystallite size of fresh (1-3 minutes runtime) or, respectively, spent (steady-state) model catalysts.

(Note: Average crystallite sizes obtained from TEM micrographs of freshly reduced and spent catalysts.)

($T_{\text{Reaction}} = 170^\circ\text{C}/225^\circ\text{C}$, $P = 4$ bar/20 bar, $\text{GHSV} = 7$ ml(STP)/(min \cdot g $_{\text{cat}}$), $(\text{H}_2/\text{CO})_n = 2:1$)

University of Cape Town

B.3.2 Supported Organometallic Compounds

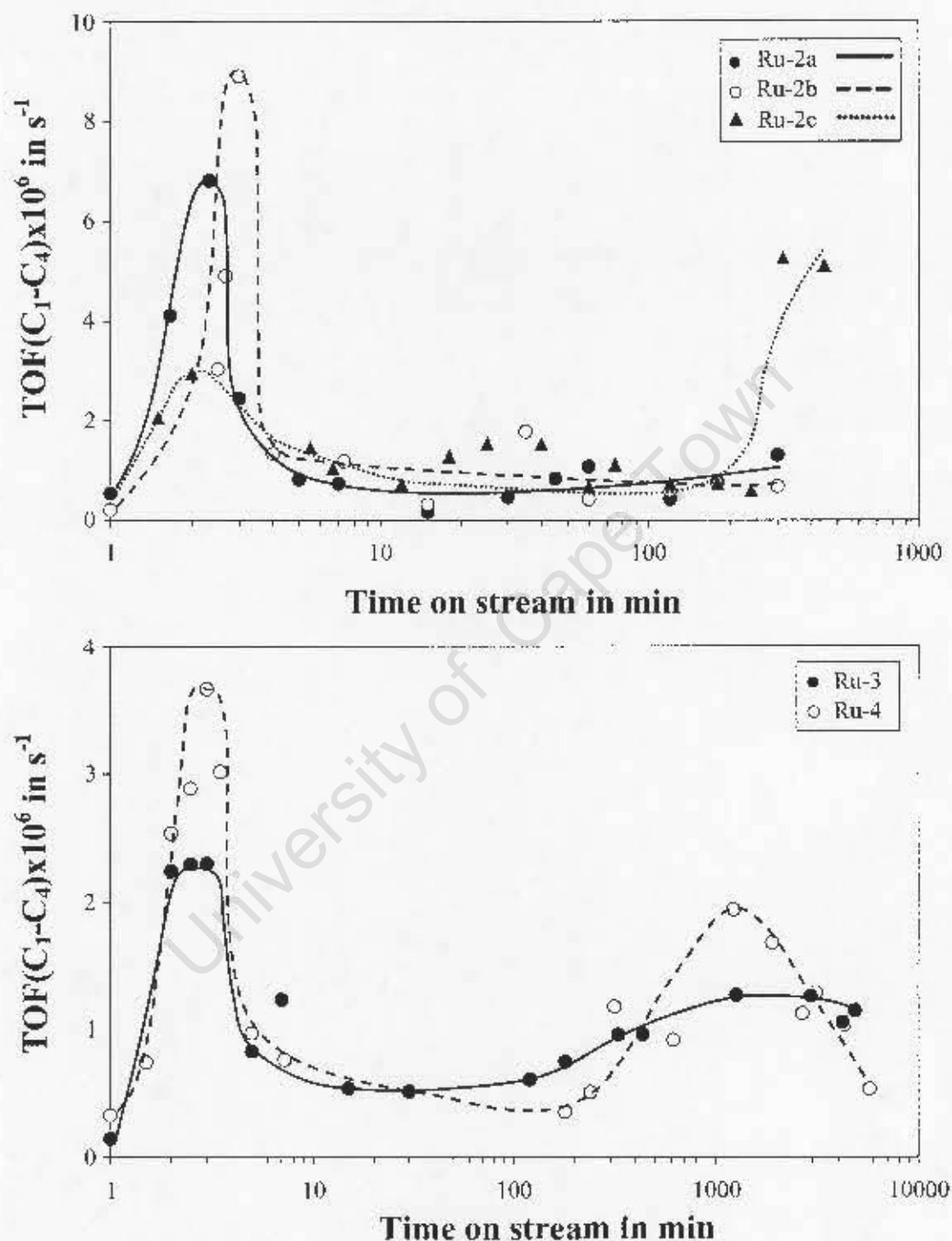


Figure B.5: *top*: Changes in turnover frequencies of C₁-C₄ hydrocarbons in FT synthesis at 170°C/4 bar as function of time on stream for the different alumina supported diatomic organometallic compounds.

bottom: Changes in turnover frequencies in FT synthesis at 170°C/4 bar as function of time on stream at extended runtimes for the alumina supported organometallic compounds Ru-3 and Ru-4.

(T_{reaction} = 170°C, P = 4 bar, GHSV = 7 ml(STP)/(min·g_{cat}), (H₂/CO)_{in} = 2:1)

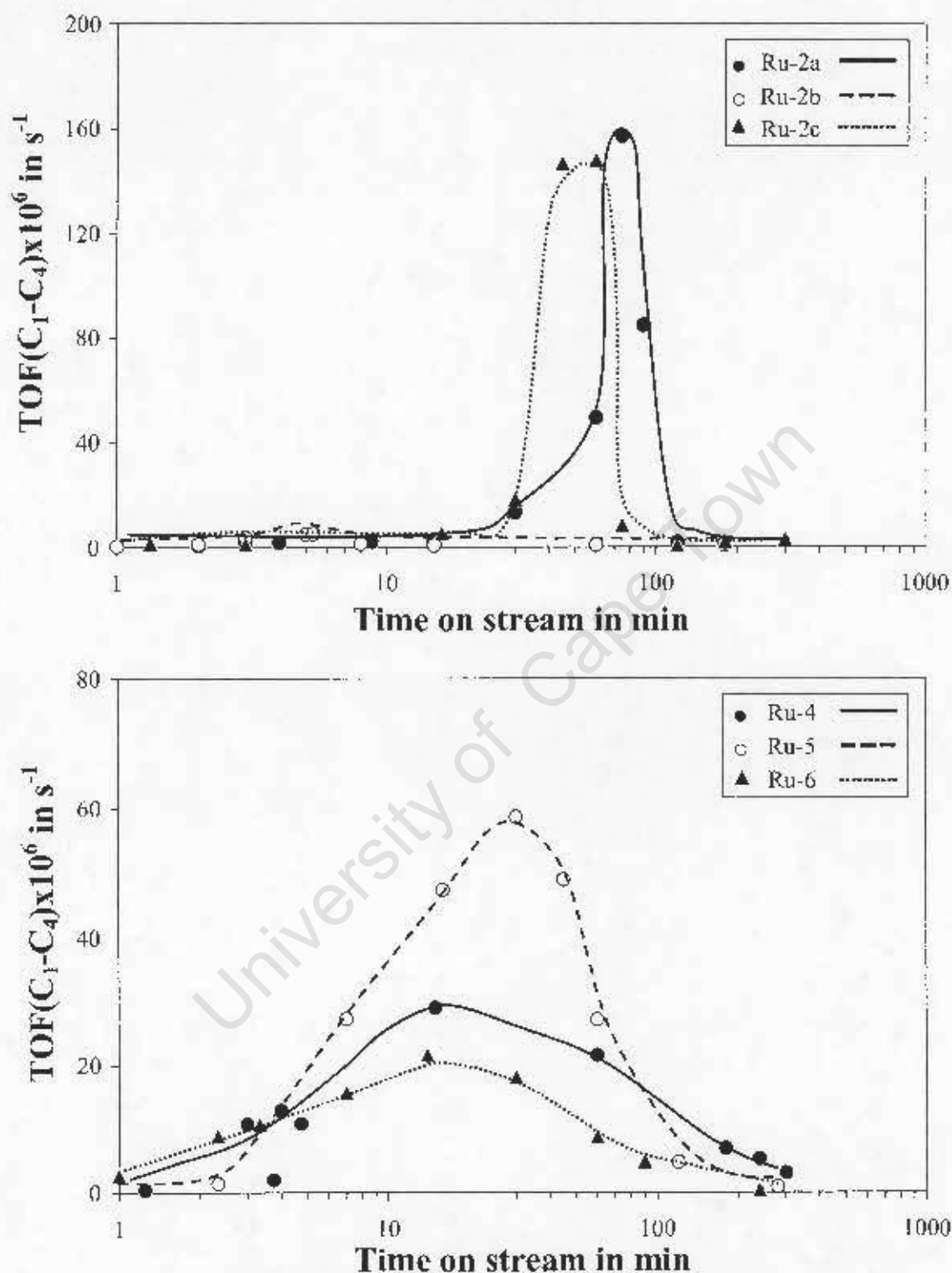


Figure B.6: *top*: Changes in turnover frequencies of C₁-C₄ hydrocarbons in FT synthesis at 170°C/4 bar in hydrogen as function of time on stream for different alumina supported diatomic organometallic compounds.

bottom: Changes in turnover frequencies in FT synthesis at 170°C/4 bar in hydrogen as function of time on stream for selected alumina supported organometallic compounds.

($T_{\text{Reaction}} = 170^{\circ}\text{C}$, $P = 4$ bar, $\text{GHSV} = 7 \text{ ml(STP)}/(\text{min}\cdot\text{g}_{\text{cat}})$)

B.4 Additional Characterisation Data of Supported Organometallic Compounds

Table B.9: Metal loadings of spent supported organometallic compounds after FT testing in hydrogen observed by means of ICP analyses (loading of fresh samples: 3 wt%).

Sample code	x_{Ru} (spent) in wt%
Ru-2a	2.47
Ru-2b	2.96
Ru-2c	1.96
Ru-3	2.68
Ru-4	2.92
Ru-5	2.25
Ru-6	1.24

Appendix C

Theoretical Calculations

University of Cape Town

C.1 The Density Functional Theory

The Schrödinger equation is solved to obtain the energy of a system. The general form of the time-dependent Schrödinger equation is:

$$\left(-\frac{\hbar}{2m} \cdot \nabla^2 + V\right) \cdot \psi(\mathbf{r}) = E \cdot \psi(\mathbf{r}) \quad (\text{C.1})$$

The wavefunction, ψ , describes the motion of a particle through space, V represents the external field and E represents the energy of the particle. ∇^2 is the second-derivative operator with respect to the x , y and z coordinates, known as ‘‘Laplace operator’’. The first term left represents the kinetic energy operator. The term in brackets can be described as the Hamiltonian operator, \hat{H} , viz. the total energy operator. \hbar is the Planck’s constant, h , divided by 2π ^a.

The energy, E , or the so-called ‘‘Eigenvalues’’ of the system can be calculated by:

$$E = \frac{\int \psi^* \cdot \hat{H} \psi d\tau}{\int \psi^* \cdot \psi d\tau} \quad (\text{C.2})$$

If the wavefunction is known, these energies of the particles can be calculated.

The density functional theory (DFT) is one way of solving the Schrödinger equation. It solves very accurately without too many approximations. Consequently, however, a complex, time-consuming calculation path is required and DFT is thus only reasonable with respect to small cluster systems. The fundamental idea behind the DFT calculations is the dependency of the total electron system on the electron density, ρ . The total energy for the overall system, $E(\rho)$, is expressed as:

$$E(\rho) = T(\rho) + U(\rho) + E_{xc}(\rho) \quad (\text{C.3})$$

with the following parameters:

$T(\rho)$ = kinetic energy

$U(\rho)$ = classical Coulomb interaction between all particles

$E_{xc}(\rho)$ = exchange correlation energy

The exchange correlation energy, E_{xc} , comprises all particle interactions that are not taken into consideration by the Hartree Fock approximation.

It contains all the other interactions for an exact representation of the total energy in the atom. However, the form of this exchange-correlation energy function is not known and different DFT functionals differ in its representation. The derivative of the exchange-correlation energy with respect to the electron density yields the exchange-correlation potential, μ_{xc} (equation C.4).

$$\mu_{xc} = \frac{\partial E_{xc}[\rho]}{\partial \rho} \quad (\text{C.4})$$

The exchange-correlation potential is added to the Hamiltonian operator in the Schrödinger equation (equation C.5).

^aPlanck’s constant, h , equals $6.626 \cdot 10^{-34}$ J.s.

$$\left(-\frac{\hbar}{2m}\nabla^2 + V(r) + \mu_{xc}(r)\right) \cdot \psi(r) = E_i \cdot \psi(r) \quad (\text{C.5})$$

The Kohn-Sham (or one-electron) orbitals can be used to solve the Schrödinger equation. Using these solutions, the electron density, ρ , can be calculated at any point, r , in the three dimensional system using the following equation:

$$\rho(r) = \sum_{i=1}^N |\psi_i(r)|^2 \quad (\text{C.6})$$

These DFT equations can be solved with an iterative procedure, from guessed initial wavefunctions although, in principle, the wavefunctions are not necessary for evaluation of equation C.3. The so-called self-consistent field (SCF) procedure in DFT consists of choosing an initial set of coefficients to expand the basis set, constructing a set of molecular orbitals (wave functions), using the trial set of molecular orbitals to construct the electronic density according to equation C.6 and using the obtained density to calculate the Coulomb and the exchange-correlation potentials, a new set of molecular orbitals and the electronic density. This procedure is repeated until the input and the output densities differ by less than or equal to a present tolerance.

Two different forms of the exchange-correlation energy must be pointed out. In the local density approximation (LDA) the exchange-correlation energy at a point r is only dependant on the local density, ρ . In the gradient generalized approximation (GGA) the exchange-correlation energy also depends on the density gradients. This approximation can be also classified as “gradient-corrected”.

C.2 Calculation of Thermodynamic Data

The values obtained via the DFT method were used to calculate thermodynamic data at different temperatures.

At a reaction temperature of 0 K, the atoms have only the electronic energy, E_{elec} . All the other modes of movement are frozen: viz. non-Heisenberg forced vibrations, translations and rotations. This results in a total energy at 0 K, $E(0\text{ K})$, of:

$$E(0\text{K}) = E_{\text{elec}} + \text{ZPVE} \quad (\text{C.7})$$

The ZPVE term represents the “Zero point vibrational energy”. This energy results from the vibrational motion of molecular systems at 0 K.

Additional molecular vibrations, rotations and translations appear only at temperatures above 0 K. These energies are computed from vibrational, translational and rotational partition functions. Therefore the total energy of the molecule, $E(T)$, at any reaction temperature is defined as:

$$E(T) = E(0\text{K}) + E_{\text{vib}} + E_{\text{rot}} + E_{\text{trans}} \quad (\text{C.8})$$

from C.7 it follows:

$$E(T) = E_{\text{elec}} + \text{ZPVE} + E_{\text{vib}} + E_{\text{rot}} + E_{\text{trans}} \quad (\text{C.9})$$

The enthalpy of a compound at a certain temperature, $H(T)$, was calculated directly by the Materials Studio program by using the following equation:

$$H(T) = ZPVE + E_{\text{vib}} + E_{\text{rot}} + E_{\text{trans}} + R \cdot T \quad (\text{C.10})$$

However, this equation does not include the E_{elec} term and had to be modified to obtain the “real” enthalpy value, $H(T)_{\text{corrected}}$. The electronic energy, E_{elec} , also had to be thermally corrected for temperatures above 0 K, by subtraction of an $R \cdot T$ term^b. The same correction was necessary for the enthalpy of reaction at a certain temperature T , $H(T)_{\text{corrected}}$. Similarly, the “real” $H(T)_{\text{corrected}}$ value was calculated by subtracting the $R \cdot T$ term at the desired temperature from the $H(T)$ value, supplied by the program.

$$H(T)_{\text{correction}} = H(T) - R \cdot T \quad (\text{C.11})$$

By taking the stoichiometric factors of the different reaction equations into account, $\Delta H(T)_{\text{corrected}}$ was obtained by using:

$$\Delta H(T)_{\text{corrected}} = \sum_i \nu_i \cdot H(\text{products})_{\text{corrected}} - \sum_i \nu_i \cdot H(\text{reagents})_{\text{corrected}} \quad (\text{C.12})$$

In a similar matter ΔE_{elec} was calculated using:

$$\Delta E_{\text{elec}} = \sum_i \nu_i \cdot E(\text{products})_{\text{elec}} - \sum_i \nu_i \cdot E(\text{reagents})_{\text{elec}} \quad (\text{C.13})$$

Finally, the addition of ΔE_{elec} and $\Delta H(T)$ led to the real $\Delta H(T)$ values as shown in equation C.14.

$$\Delta H = \Delta H(T)_{\text{corrected}} + \Delta E_{\text{elec}} \quad (\text{C.14})$$

However, the obtained entropy values from the program at a certain temperature for each compound, $S(T)$, could be used directly to calculate $\Delta S(T)$ with the following equation:

$$\Delta S(T) = \sum_i \nu_i \cdot S(\text{products}) - \sum_i \nu_i \cdot S(\text{reagents}) \quad (\text{C.15})$$

^b R is the universal gas constant (8.314 J/mol·K) and T is the reaction temperature.

C.3 Entropy of Reaction

C.3.1 Monoatomic Reaction Mechanisms

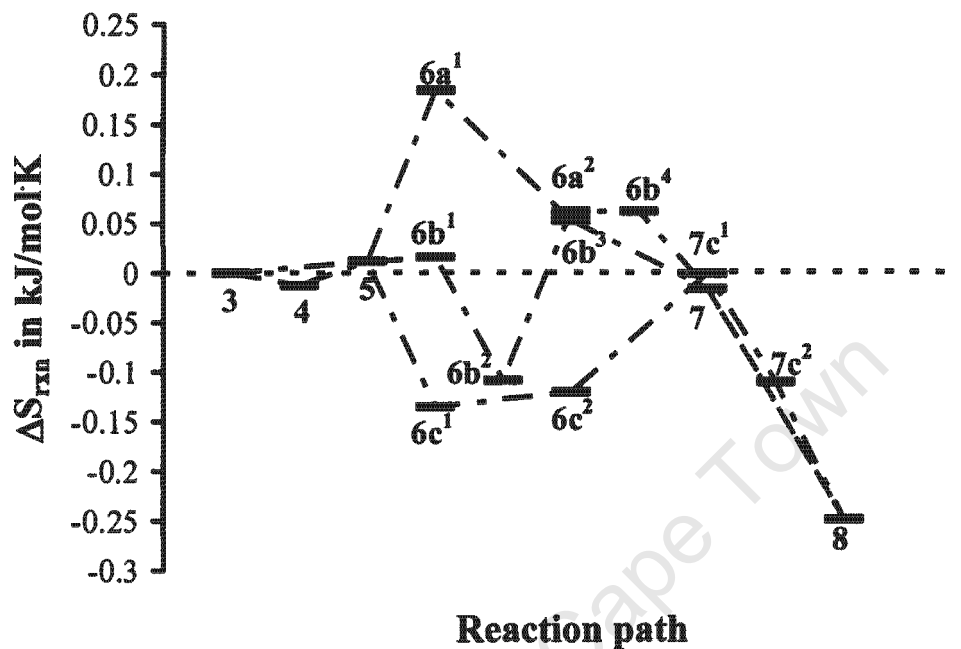


Figure C.1: Entropy of reaction, ΔS_{rxn} , in $\text{kJ}/(\text{mol}\cdot\text{K})$ for the different intermediates proposed in the monoatomic reaction mechanisms A, B and C at 475 K.

C.3.2 Diatomic Reaction Mechanisms

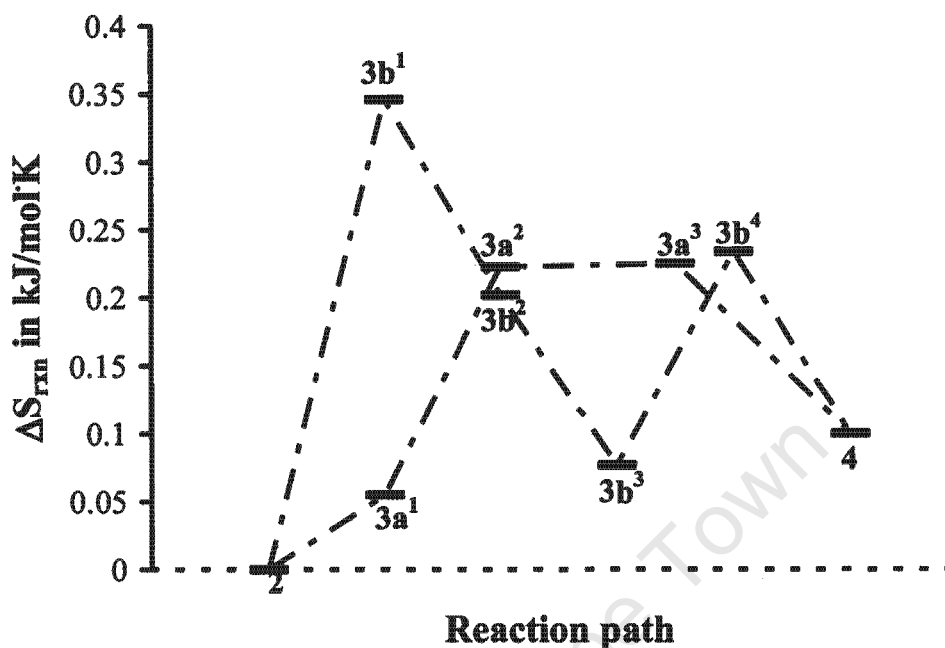


Figure C.2: Entropy of reaction, ΔS_{rxn} , in $\text{kJ}/(\text{mol}\cdot\text{K})$ for the different intermediates proposed in the diatomic reaction mechanisms A, B and C leading to the generation of the chain initiator at 475 K.

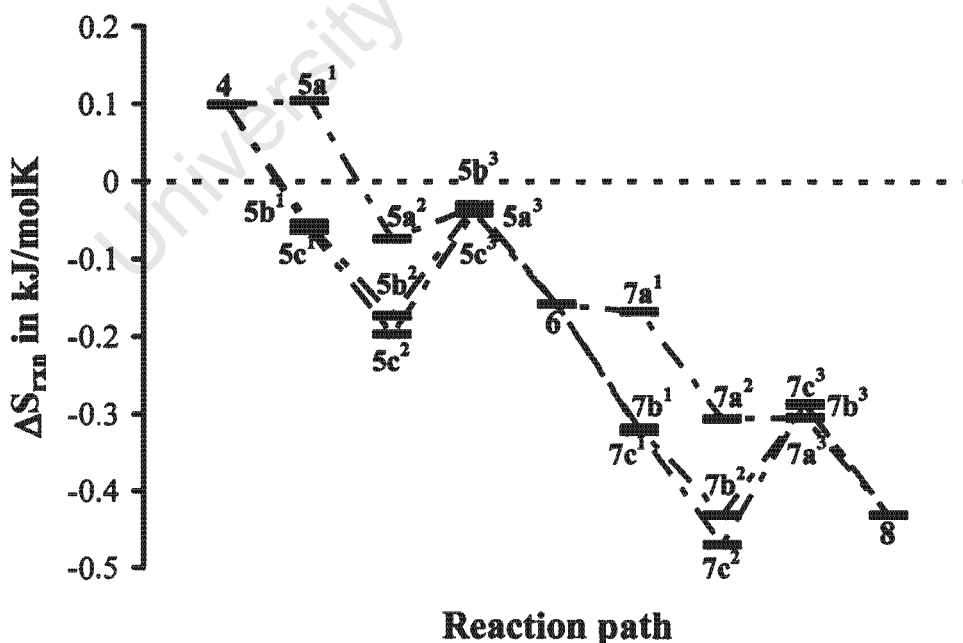


Figure C.3: Entropy of reaction, ΔS_{rxn} , in $\text{kJ}/(\text{mol}\cdot\text{K})$ for the different intermediates proposed in the diatomic reaction mechanisms A, B and C leading to the first step of chain growth at 475 K.

Appendix D

Curriculum Vitae

University of Cape Town

APPENDIX D. CURRICULUM VITAE

Personal Details

Name: Cathrin Alexandra Welker
Date of Birth: 23.03.1979
Place of Birth: Ostfildern, Germany
Nationality: German
Family Status: Single

School Education

1985-1989 Primary School Education (Friedrich-Glück Schule Oberensingen)
in Nürtingen, Germany
1989-1998 Secondary School Education (Max-Planck-Gymnasium
Nürtingen) in Nürtingen, Germany
1998 Abitur ("A-levels")

University Education

1998-2003 Study of Chemistry (Vordiplom ("Prediploma") 2000,
Diplom ("Diploma") 2003), University of Stuttgart, Germany
Aug.-Sept. 2001 Summer Student Program, Hahn-Meitner-Institut,
Berlin, Germany
May-July 2002 Exchange Student, Catalysis Research Unit,
Department of Chemical Engineering, University of
Cape Town, South Africa
Mar.-Sept. 2003 Diploma Thesis, Institute of Chemical Technology,
University of Stuttgart, Germany
30.09.2003 Diplom in Chemistry

Scientific and Teaching Jobs

2001-2002 Scientific Assistant (HIWI),
Institute of Chemical Technology, University of Stuttgart, Germany
2004-2006 Teaching Assistant and Senior Teaching Assistant,
Department of Chemical Engineering,
University of Cape Town
2004 and 2006 Supervisor "Final Student Project",
Department of Chemical Engineering, University of Cape Town
2006 Part-time lecturer CHE3046f (Thermodynamics 2),
Department of Chemical Engineering, University of Cape Town

Awards/Scholarships

2004-current	DST-NRF Centre of Excellence in Catalysis (c*change) Bursary
2005 and 2006	“Research Fellowship Associate Award”, University of Cape Town, South Africa
2006	“Best Poster Award”, Research and Development Day, South African Institution of Chemical Engineers, Stellenbosch
2006	“Merit-Award” for Sports Administration, University of Cape Town, South Africa
2006	“CATSA International Student Travel Grant”, Catalytic Society of South Africa

University of Cape Town

Appendix E

List of Publications

University of Cape Town

Journal Publications

D. Barkhuizen, I. Mabaso, E. Viljoen, C. Welker, M. Claeys, E. van Steen, J. Fletcher
"Supported metal-nanoparticle catalyst preparation"
Pure Appl. Chem., Vol. 78, No 9 (2006) 1759-1769

C. Welker, J.R. Moss, E. van Steen, M. Claeys
"Closing the Gap between homo- and heterogeneous Fischer-Tropsch Synthesis"
DGMK Tagungsbericht, Vol. 2006-4 (2006) 223-230

Conference Presentations

2005

C. Welker, M. Claeys, E. van Steen, J.R. Moss
"Modelling of reaction mechanisms for different Ru model catalysts for Fischer-Tropsch synthesis"
Lecture held at "South African Chemical Institute Conference 2005 in Inorganic Chemistry (INORG 2005)", Durban, South Africa, April 2005, S6 in book of abstracts

C. Welker, J.R. Moss, E. van Steen, M. Claeys
"Closing the gap between homo- and heterogeneous Fischer-Tropsch synthesis - Modelling Approach"
Lecture held at "Research and Development Day", Cape Town, South Africa, June 2005, OR09 in book of abstracts

C. Welker, J.R. Moss, E. van Steen, M. Claeys
"Fischer-Tropsch synthesis on organometallic model catalysts"
Poster presented at "3rd Cape Organometallic Symposium", Cape Town, South Africa, October 2005, P16 in book of abstracts

C. Welker, J.R. Moss, E. van Steen, M. Claeys,
"Closing the gap between homo- and heterogeneous Fischer-Tropsch synthesis"
Lecture held at "DST-NRF Centre of Excellence in Catalysis (c*change) Workshop", Midrand, South Africa, November 2005

C. Welker, J.R. Moss, E. van Steen, M. Claeys,
"Effect of crystallite size in Ru-based Fischer-Tropsch synthesis"
Lecture held and poster presented at "Catalysis Society of South Africa Conference 2005 (CATSA 2005)", Midrand, South Africa, November 2005, P24 in book of abstracts

2006

C. Welker, J.R. Moss, E. van Steen, M. Claeys
"Effect of crystallite size in Ru-based Fischer-Tropsch synthesis"
Poster presented at "Research and Development Day 2006", Stellenbosch, South Africa, June 2006, P1 in book of abstracts

Journal Publications

D. Barkhuizen, I. Mabaso, E. Viljoen, C. Welker, M. Claeys, E. van Steen, J. Fletcher
"Supported metal-nanoparticle catalyst preparation"
Pure Appl. Chem., Vol. 78, No 9 (2006) 1759-1769

C. Welker, J.R. Moss, E. van Steen, M. Claeys
"Closing the Gap between homo- and heterogeneous Fischer-Tropsch Synthesis"
DGMK Tagungsbericht, Vol. 2006-4 (2006) 223-230

Conference Presentations

2005

C. Welker, M. Claeys, E. van Steen, J.R. Moss
"Modelling of reaction mechanisms for different Ru model catalysts for Fischer-Tropsch synthesis"
Lecture held at "South African Chemical Institute Conference 2005 in Inorganic Chemistry (INORG 2005)", Durban, South Africa, April 2005, S6 in book of abstracts

C. Welker, J.R. Moss, E. van Steen, M. Claeys
"Closing the gap between homo- and heterogeneous Fischer-Tropsch synthesis - Modelling Approach"
Lecture held at "Research and Development Day", Cape Town, South Africa, June 2005, OR09 in book of abstracts

C. Welker, J.R. Moss, E. van Steen, M. Claeys
"Fischer-Tropsch synthesis on organometallic model catalysts"
Poster presented at "3rd Cape Organometallic Symposium", Cape Town, South Africa, October 2005, P16 in book of abstracts

C. Welker, J.R. Moss, E. van Steen, M. Claeys,
"Closing the gap between homo- and heterogeneous Fischer-Tropsch synthesis"
Lecture held at "DST-NRF Centre of Excellence in Catalysis (c*change) Workshop", Midrand, South Africa, November 2005

C. Welker, J.R. Moss, E. van Steen, M. Claeys,
"Effect of crystallite size in Ru-based Fischer-Tropsch synthesis"
Lecture held and poster presented at "Catalysis Society of South Africa Conference 2005 (CATSA 2005)", Midrand, South Africa, November 2005, P24 in book of abstracts

2006

C. Welker, J.R. Moss, E. van Steen, M. Claeys
"Effect of crystallite size in Ru-based Fischer-Tropsch synthesis"
Poster presented at "Research and Development Day 2006", Stellenbosch, South Africa, June 2006, P1 in book of abstracts

C. Welker, M. Claeys, E. van Steen, J.R. Moss
"Fischer-Tropsch synthesis on organometallic model catalysts"
Lecture held at "Organometallic chemistry and their application 2006" (OATA), Cape Town, South Africa, August 2006, L8 in book of abstracts

C. Welker, M. Claeys, E. van Steen, J.R. Moss
"Fischer-Tropsch synthesis on organometallic model catalysts"
Poster presented at "37th International Conference on Coordination Chemistry (ICCC)", Cape Town, South Africa, August 2006, p. 449 in book of abstracts (ISBN: 1-920-01705-4); Eds.: D.J. Robinson and J.M. Robinson

C. Welker, M. Claeys, E. van Steen, J.R. Moss
"Fischer-Tropsch synthesis on organometallic model catalysts"
Poster presented at "17th International Homogeneous Catalysis Symposium", Sun City, South Africa, August 2006, A56 in book of abstracts

C. Welker, J.R. Moss, E. van Steen, M. Claeys
"Closing the Gap between homo- and heterogeneous Fischer-Tropsch synthesis"
Poster presented at "DGMK/SCI conference, Synthesis Gas Chemistry", Dresden, Germany, October 2006, p. 223-230 in "DGMK Tagungsbericht 2006-4" (ISBN: 3-936418-57-8), Eds.: S. Ernst, A. Jess, F. Ness, C. Perego, M. Rupp, E. Santacesaria

C. Welker, J.R. Moss, E. van Steen, M. Claeys
"Closing the Gap between homo- and heterogeneous Fischer-Tropsch synthesis"
Lecture held at "DST-NRF Centre of Excellence in Catalysis (c*change) Workshop", Mossel Bay, South Africa, November 2006

C. Welker, J.R. Moss, E. van Steen, M. Claeys
"Closing the Gap between homo- and heterogeneous Fischer-Tropsch synthesis"
Poster presented at "Catalytic Society of South Africa Conference 2006 (CATSA 2006)", Mossel Bay, South Africa, November 2006, FTS-7 in book of abstracts